Leibniz-Institut für Astrophysik Potsdam
Cosmology and Large-scale Structure

Unveiling the Epoch of Reionization by simulations and high-redshift galaxies

Anne Hutter

Published online at the
Institutional Repository of the University of Potsdam:
URN urn:nbn:de:kobv:517-opus4-76998
http://nbn-resolving.de/urn:nbn:de:kobv:517-opus4-76998

Abstract

The Epoch of Reionization marks after recombination the second major change in the ionization state of the universe, going from a neutral to an ionized state. It starts with the appearance of the first stars and galaxies; a fraction of high-energy photons emitted from galaxies permeate into the intergalactic medium (IGM) and gradually ionize the hydrogen, until the IGM is completely ionized at $z \simeq 6$ (Fan et al., 2006). While the progress of reionization is driven by galaxy evolution, it changes the ionization and thermal state of the IGM substantially and affects subsequent structure and galaxy formation by various feedback mechanisms. Understanding this interaction between reionization and galaxy formation is further impeded by a lack of understanding of the high-redshift galactic properties such as the dust distribution and the escape fraction of ionizing photons. Lyman Alpha Emitters (LAEs) represent a sample of high-redshift galaxies that are sensitive to all these galactic properties and the effects of reionization. In this thesis we aim to understand the progress of reionization by performing cosmological simulations, which allows us to investigate the limits of constraining reionization by high-redshift galaxies as LAEs, and examine how galactic properties and the ionization state of the IGM affect the visibility and observed quantities of LAEs and Lyman Break galaxies (LBGs).

In the first part of this thesis we focus on performing radiative transfer calculations to simulate reionization. We have developed a mapping-sphere-scheme, which, starting from spherically averaged temperature and density fields, uses our 1D radiative transfer code and computes the effect of each source on the IGM temperature and ionization (H II, He II, He III) profiles, which are subsequently mapped onto a grid. Furthermore we have updated the 3D Monte-Carlo radiative transfer pCRASH, enabling detailed reionization simulations which take individual source characteristics into account.

In the second part of this thesis we perform a reionization simulation by post-processing a smoothed-particle hydrodynamical (SPH) simulation (GADGET-2) with 3D radiative transfer (pCRASH), where the ionizing sources are modelled according to the characteristics of the stellar populations in the hydrodynamical simulation. Following the ionization fractions of hydrogen (H I) and helim (He II, He III), and temperature in our simulation, we find that reionization starts at $z \simeq 11$ and ends at $z \simeq 6$, and high density regions near sources are ionized earlier than low density regions far from sources. The sizes of the ionized regions depend primarily on the evolution time and the stellar masses of the enclosed galaxies. Accounting for the clumpiness of the IGM locally, our simulation contains self-shielded partially neutral regions even at the end of reionization.

In the third part of this thesis we couple the cosmological SPH simulation and the radiative transfer simulations with a physically motivated, self-consistent model for LAEs, in order to understand the importance of the ionization state of the IGM, the escape fraction of ionizing photons from galaxies and dust in the interstellar medium (ISM) on the visibility of LAEs. Comparison of our models results with the LAE Lyα and UV luminosity functions at $z \simeq 6.6$ reveals a three-dimensional degeneracy between the ionization state of the IGM, the ionizing photons escape fraction and the ISM dust distribution, which implies that LAEs act not only as tracers of reionization but also of the ionizing photon escape fraction and of the ISM dust distribution. This degeneracy does not even break down when we compare simulated with observed clustering of LAEs at $z \simeq 6.6$. However, our results show that reionization has the largest impact on the amplitude of the LAE angular correlation functions, and its imprints are clearly distinguishable from those of properties on galactic scales (ionizing photon escape fraction, ISM dust distribution). These results show that reionization cannot be constrained tightly by exclusively using LAE observations. Further observational constraints, e.g. tomographies of the redshifted hydrogen 21 cm line, are required.

In addition we also use our LAE model to probe the question when a galaxy is visible as a LAE or a LBG. Within our model galaxies above a critical stellar mass can produce enough luminosity to be visible as a LBG and/or a LAE. By finding an increasing duty cycle of LBGs with Lyα emission as the UV magnitude or stellar mass of the galaxy rises, our model reveals that the brightest (and most massive) LBGs most often show Lyα emission. Predicting the Lyα equivalent width (Lyα EW) distribution and the fraction of LBGs showing Lyα emission at $z \simeq 6.6$, we reproduce the observational trend of the Lyα EWs with UV magnitude. However, the Lyα EWs of the UV brightest LBGs exceed observations and can only be reconciled by accounting for an increased Lyα attenuation of massive galaxies, which implies that the observed Lyα brightest LAEs do not necessarily coincide with the UV brightest galaxies. Applying our LAE model with an increased Lyα attenuation allows us to reproduce the observed fraction of LBGs showing Lyα emission for an EW selection criterion of > 55Å. We have analysed the dependencies of LAE observables on the properties of the galactic and intergalactic medium and the LAE-LBG connection, and this enhances our understanding of the nature of LAEs.

Zusammenfassung

Die Epoche der Reionisation markiert die nach der Rekombination zweite grundlegende Änderung des Ionisationszustandes des Universums, nämlich den Übergang von einem neutralen zu einem ionisierten Zustand. Die Epoche der Reionisation beginnt mit dem Erscheinen der ersten Sterne und Galaxien. Von den Galaxien ausgesendete energiereiche Photonen durchdringen das intergalaktische Medium (IGM) und ionisieren den vorhandenen Wasserstoff schrittweise, bis das IGM bei $z \simeq 6$ (Fan et al., 2006) vollständig ionisiert ist. Während der Verlauf der Reionisation zum einen durch die Galaxienentwicklung bestimmt wird, verändert die Reionisation zum anderen den Ionisations- und thermischen Zustand des IGMs und beeinflusst damit die darauffolgende Struktur- und Galaxienentwicklung durch verschiedene Rückkopplungsmechanismen. Die geringen Kenntnisse der Eigenschaften von Galaxien bei hohen Rotverschiebungen wie der Staubverteilung und des Anteils an ionisierenden Photonen, die die Galaxien verlassen können, erschweren jedoch das Verständnis des Wechselspiels zwischen Reionisation und Galaxienentwicklung. Lyman Alpha Emitter (LAE) stellen Galaxien bei hoher Rotverschiebung dar, deren Sichtbarkeit diesen Eigenschaften und den Effekten der Reionisation unterliegen. Diese Arbeit zielt darauf ab, den Verlauf der Reionisation anhand von kosmologischen Simulationen zu verstehen. Insbesondere interessiert, inwieweit der Verlauf der Reionisation durch Galaxien bei hohen Rotverschiebungen eingeschränkt werden kann, und wie die Eigenschaften der Galaxien und der Ionisationszustand des IGMs die Sichtbarkeit und die beobachtbaren Größen der LAE und Lyman Break Galaxien (LBG) beeinflussen können.

Im ersten Teil dieser Arbeit werden verschiedene Ansätze zur Lösung des Strahlungstransportes neu- und weiterentwickelt mit dem Ziel, die Epoche der Reionisation zu simulieren. Dazu wurde zum einen eine Methode entwickelt, die als Berechnungsgrundlage sphärisch gemittelte Temperatur- und Dichtefelder benutzt. Mithilfe des in dieser Arbeit entwickelten eindimensionalen Strahlungstransportcodes werden die Auswirkungen jeder Quelle auf die dementsprechenden Temperatur- und Ionisationsprofile (H II, He II, He III) berechnet und diese auf ein Gitter abgebildet. Zum anderen wurde der dreidimensionale Monte-Carlo-Strahlungstransportcode pCRASH so erweitert, sodass detaillierte Reionisationsimulationen, die individulle Quelleneigenschaften berücksichtigen, durchgeführt werden können.

Im zweiten Teil dieser Arbeit wird die Epoche der Reionisation in sich konsistent simuliert, indem aufbauend auf einer gasdynamischen Simulation (smoothed particle hydrodynamics (SPH), GADGET-2) mithilfe von pCRASH Strahlungstransportrechnungen ausgeführt werden. Dabei werden die ionisierenden Quellen gemäß der Eigenschaften der Sternpopulationen in der gasdynamischen Simulation modelliert. Die Entwicklung der IGM-Ionisationsanteile an Wasserstoff (H II) und Helium (He II, He III) sowie der Temperatur werden in der Simulation verfolgt. Es zeigt sich, dass Reionisation erstens bei $z \simeq 11$ beginnt und bei $z \simeq 6$ endet, und zweitens von überdichten zu unterdichten Gebieten des Kosmos hin verläuft, wobei die Größe der ionisierten Gebiete hauptsächlich von der Entwicklungszeit und der stellaren Masse der beinhaltenden Galaxien abhängt. Desweiteren zeigt sich durch die Miteinbeziehung eines lokalen Verklumpungsfaktors, dass es abgeschirmte, teilneutrale Gebiete gibt, die selbst am Ende der Reionisierungsepoche verbleiben.

Im dritten Teil der Arbeit werden kosmologische SPH - und Strahlungstransportsimulationen mit einem physikalisch motivierten, selbst-konsistenten Modell für LAEs kombiniert, um den Einfluss des Ionisationszustandes des IGMs, des Anteils der ionisierenden Photonen, die die Galaxien verlassen können, und der Staubverteilung im interstellaren Medium (ISM) auf die sichtbaren Eigenschaften der LAEs zu verstehen. Der Vergleich der Simulationsergebnisse mit den beobachteten LAE Lyα- und UV-Leuchtkraftfunktionen bei $z \simeq 6.6$ offenbart eine dreidimensionale Entartung zwischen dem Ionisationszustand des IGMs, dem Anteil der ionisierenden Photonen, die die Galaxien verlassen können, und der Staubverteilung im ISM. Dies bedeutet, dass die Sichtbarkeit von LAEs nicht nur ein Indikator für den Ionisationszustand des IGM ist, sondern auch für den Anteil an ionisierenden Photonen, die die Galaxien verlassen können, und für die Staubverteilung im ISM. Diese Entartung lässt sich auch nicht auflösen, wenn Simulations- und Beobachtungsdaten der räumlichen Verteilung der LAEs bei $z \simeq 6.6$ gemessen mit der winkelabhängigen Zweipunktkorrelationsfunktion verglichen werden. Jedoch zeigt unser Modell, dass die Reionisation den größten Effekt auf die Amplitude der Winkelkorrelation hat und dass sich ihre Spuren klar von den Effekten auf galaktischen Skalen (den Anteil der ionisierenden Photonen, die die Galaxien verlassen können, und der Staubverteilung im ISM) unterscheiden lassen. Somit kann Reionisation nicht alleine durch LAE Beobachtungen eingeschränkt werden, und es werden weitere Beobachtungen, wie z.B. die Tomographie der rotverschobenen 21 cm Wasserstofflinie, benötigt.

Anhand des konstruierten LAE Modells wird auch die Frage erörtert, wann eine Galaxie als LAE oder als LBG sichtbar ist. Vom Modell ausgehend produzieren Galaxien oberhalb einer kritischen stellaren Masse ausreichend Leuchtkraft, um als LBG oder LAE sichtbar zu werden. Der Anteil der Lebenszeit einer Galaxie, zu der sie als LBG mit Lyα-Emission identifiziert wird, nimmt mit der UV-Leuchtkraft (stellaren Masse) zu. Damit zeigen in unserem Modell die leuchtstärksten (und massereichsten) LBGs am häufigsten Lyα-Emissionen. Ferner werden Lyα-Äquivalentbreitenverteilungen und die Anteile an LBGs mit Lyα-Emissionen bei $z \simeq 6.6$ bestimmt. Es zeigt sich, dass der beobachtete Trend der Beziehung zwischen der Lyα - Äquivalentbreite und der UV-Leuchtkraft reproduziert wird. Jedoch überschreiten die Äquivalentbreitenwerten UV-leuchtkräftiger Galaxien die Beobachtungen und können nur dann in Übereinstimmung gebracht werden, wenn eine mit der Galaxienmasse zunehmende Abschwächung der Lyα-Strahlung postuliert wird. Unter dieser Annahme können auch die beobachteten LAE-Anteile für ein Äquivalentbreitenselektionskriterium > 55Å reproduziert werden. Durch diese Analyse der Abhängigkeit der beobachtbaren Größen der LAEs von den Eigenschaften des galaktischen und intergalaktischen Mediums und des Zusammenhangs zwischen LAEs und LBGs trägt diese Arbeit zum allgemeinen Verständnis der Natur von LAEs bei.

Leibniz-Insitut für Astrophysik Potsdam
Cosmology and Large-scale Structure

Unveiling the Epoch of Reionization by simulations and high-redshift galaxies

Dissertation
zur Erlangung des akademischen Grades
Doktor der Naturwissenschaften (Dr. rer. nat.)
in der Wissenschaftsdisziplin Theoretische Astrophysik

eingereicht an der
Mathematisch-Naturwissenschaftlichen Fakultät
der Universität Potsdam

von
Anne Hutter

Potsdam, im November 2014

Contents

Chapter

1

Introduction

The Lambda Cold Dark Matter (LCDM) model has been exceptionally successful in explaining the large scale structure in the distribution of galaxies as well as the accelerated expansion of the Universe and the abundances of the primordial elements. The LCDM model contains a cosmological constant (Λ) which is associated with dark energy, and cold dark matter (CDM). A cosmological constant has negative pressure which causes an accelerated expansion, also referred to as "gravitational repulsion", and currently contributes 68.3% to the total energy density of our flat Universe. Cold dark matter is described by being cold, non-baryonic, dissipationless and collisionless, i.e. its particles only interact via gravitation and possibly the weak force. Evidence for the existence of dark matter has been indicated by several observations. Firstly, when the mass of galactic clusters is inferred from the velocities of their galaxies, a larger mass is obtained than the mass evaluated from the light of galaxies (Zwicky, 1933, 1937; Faber and Gallagher, 1979; Carlberg et al., 1997). Secondly, the observed flat rotation curves of spinning galaxies would be in contradiction with Kepler's law if only the visible matter contributed (Volders, 1959; Rubin et al., 1978, 1980; Persic et al., 1996). Thirdly, shapes of galaxies can be distorted by gravitational lensing which is only possible if invisible accumulations of mass act as lenses (Tyson et al., 1990; Clowe et al., 2006). Cold dark matter provides a solution to these issues and within LCDM it provides 26.8% of the energy density of the Universe today. The remaining 4.9% are provided by baryons, the visible matter consisting of leptons and hadrons.

The physical description of the Universe is based upon the "cosmological principle", i.e. the distribution of matter and energy must be homogeneous and isotropic on the largest scales. Indeed the observed distribution of galaxies, the X-ray and cosmic microwave background (CMB) suggest that our Universe is isotropic on large scales (Wu et al., 1999; Bennett et al., 1996), while its homogeneity is not strictly constrained. Nevertheless, an inhomogeneous and isotropic universe can be excluded (Goodman, 1995). For a homogeneous and isotropic space the Friedmann equation that is derived from the Einstein field equations describes the expansion of space time by means of the scale factor $a(z) = 1/(1+z)$ by which the physical distance between objects at rest (i.e. constant comoving coordinates) is increasing with time.

$$H(t) \quad = \quad \frac{\dot{a}(t)}{a(t)} = \left[\Omega_r a^{-4} + \Omega_m a^{-3} + \Omega_\Lambda + \Omega_k a^{-2}\right]^{1/2} \tag{1.1}$$

The time-dependent expansion rate of the universe $H(t)$ is related to its matter-energy contents in form of radiation (Ω_r), matter including dark matter and baryons (Ω_m), vacuum (Ω_Λ), and a term accounting for the curvature of the universe (Ω_k). The geometry of the universe is determined by whether Ω_k is greater than, less than or equal to zero and corresponds to a spherical (closed), hyperbolic (open) or flat universe respectively. By means of the present energy density contents $\Omega_k = 1 - \Omega_r - \Omega_m - \Omega_\Lambda$ our Universe turns out to be rather flat (Hinshaw et al., 2013; Planck Collaboration et al., 2014a).

The evolution of the Universe is determined by the time evolution of the different energy contents (radiation, matter, vacuum). After the big bang the Universe emerges in a hot and dense state, the Universe expands and cools adiabatically. During inflation the expansion is strongly accelerated due

to the change of state of the inflaton field. Inflation provides the necessary expansion of space time to generate a homogeneous, isotropic and flat Universe. The exponential growth of the scale factor during inflation causes the quantum fluctuations of the inflaton field to be expanded to macroscopic scales and to become superhorizon, where the horizon depicts the distance light could have travelled, $r_H = ct$. At later times of radiation and matter domination these scales become subhorizon again and set the initial conditions for structure formation. In the first three minutes after inflation atomic nuclei as hydrogen, deuterium and helium form. At a redshift of $z \sim 3600$ (Ryden, 2006) the Universe passes from the radiation- into the matter dominated epoch. Due to the expansion of the Universe, the Jeans length, which defines the smallest structures that can form, decreases and dark matter perturbations can grow in amplitude; baryons remain in thermal equilibrium with photons via scattering. The recombination of electrons with atomic nuclei does not take place until the Universe has expanded and cooled down sufficiently at a redshift of $z \sim 1100$ (Ryden, 2006), so that the photons' mean free path becomes effectively infinite and photons can propagate freely. These photons are seen as the CMB today. Before recombination the electron-baryon plasma is subject to pressure-waves or oscillations: due to gravity baryons fall into the dark matter gravitational potential but as their density increases, radiative pressure drives them apart. Thus the existing pressure-waves at the time of decoupling are imprinted in the CMB and depict the initial conditions for the subsequent large-scale structure of our Universe. After recombination dark matter as well as baryons are subject to gravitational instability. Density perturbations grow in amplitude and collapse to sheets (along one axis), filaments (along two axes) and subsequently halos (along three axes) forming the cosmic web (Zel'dovich, 1970; Shandarin and Zeldovich, 1989).

As the Universe becomes transparent by forming neutral hydrogen and helium during recombination, the Universe enters the era of dark ages, which is characterised by the absence of light sources other than the background radiation. Yet primordial density fluctuations grow, until nonlinear gravitational collapse leads to the formation of the first dark matter halos, in which gas could collapse and radiatively cool. The appearance of the first stars in those halos at $z \simeq 15 - 30$ marks the end of the dark ages and heralds the Epoch of Reionization. Ionizing photons start to permeate the Universe and gradually ionize the hydrogen in the intergalactic medium (IGM), until the Universe is reionized by $z \simeq 6$ (Fan et al., 2006). The Epoch of Reionization marks an important point in the history of the Universe: ionization of hydrogen and corresponding heating of the IGM influence subsequent galaxy formation; reionization has influence on the physical processes that shaped the galaxies of various luminosities and masses today, as the first sources provide seeds for subsequent formation of larger galaxies due to the hierarchical structure formation in our Universe; and reionization represents the evolutionary link between the smooth matter distribution at early times (of recombination) and a highly structured Universe at $z < 6$. Hence, it is of great interest to study reionization, its progress, duration, effects on structure formation and how accurately it can be probed observationally. In the remainder of this Chapter we briefly elaborate on theoretical descriptions of structure formation, describe the sources of reionization, the progress of reionization and relevant feedback mechanisms on galaxy formation, explain observational probes of reionization, and give a short outline of this thesis.

1.1 Theory of structure formation

The growth of perturbations is divided into a linear and a non-linear regime, where the relative density perturbations $\delta = \varrho(\vec{r})/\bar{\varrho} - 1$ are small ($\ll 1$) in the linear regime, while they are larger than unity in the non-linear regime. In the linear regime the absence of dark matter particle stream crossings and baryonic shocks allow us to describe the universe as an ideal pressure-less fluid of particles. Solving the linearised fluid equations (continuity and Euler equations) two solutions for the evolution of the perturbations are obtained of which the growing one dominates. Density perturbations maintain their shapes and grow self-similarly according to a growth factor until they become non-linear.

When perturbations become non-linear, the full gravitational problem needs to be considered. Analytical calculations of a spherical collapse capture some of the physics of halo formation, but to follow non-linear structure formation entirely numerical simulations are necessary. From numerical simulations it is found that structure formation in cold dark models proceed hierarchically, i.e. while at early times most of dark matter resides in low mass halos, they accrete more matter with time, merge and form high-mass halos. While Press and Schechter (1974) found an analytical description for the abundance of halos, numerical simulations yielded a universal spherically-averaged density profile which was successfully fitted by the Navarro-Frenk-White profile (Navarro et al., 1996). Nevertheless

these descriptions include only dark matter, including baryons into the calculations - taking into account a variety of additional effects as collisions - alters the derived observational quantities.

To generate the appropriate initial density fluctuations for numerical simulation the density contrast of the universe as a function of scale is required. From theory it is given by the matter power spectrum $P(k)$, the Fourier transform of the matter correlation function $\xi(r)$

$$P(k) = \left\langle |\delta(k)|^2 \right\rangle \quad \text{with} \tag{1.2}$$

$$\delta(k) \propto \int \delta(\vec{x}) \, \exp(i\vec{k}\vec{x}) \, \mathrm{d}^3x. \tag{1.3}$$

Inflation generates perturbations given by a Gaussian field, i.e. phases are statistically independent. Furthermore the power spectrum of density fluctuations in the gravitational potential needs to be scale-invariant. Harrison (1970) and Zeldovich (1972) showed that such a spectrum is given by $P(k) \propto k^n$ with $n \sim 1$. To derive the total matter power spectrum the growth of scales and the times they enter the horizon needs to be considered. As the horizon increases faster than perturbations grow, larger scales come into communication with time, i.e. they re-enter the horizon. Thus the final power spectrum is given by the large scale fluctuations that become subhorizon in the matter-dominated area, $P(k) \propto k$, and the smaller scale fluctuations that have already become subhorizon in the radiation-dominated area, $P(k) \propto k^{-3}$. Thus at scale of order the horizon at matter-radiation equality, $k_{eq}^{-1} = cH^{-1}$, the power spectrum is characterised by a turnover. On small scales the power spectrum deviates from $P(k) \propto k^{-3}$ due to the additional non-linear growth of perturbations.

1.2 Early star and galaxy formation

Although most of the matter in the Universe is represented by dark matter, only baryonic matter forms the visible stars, galaxies and clusters. The baryonic matter distribution follows predominantly the dark matter distribution as long as the baryonic gas pressure and the gravitational forces settle to an equilibrium state. Thus the large scale structure of matter - the cosmic web - is given by the collapse of dark matter which the baryons follow. Nevertheless, in collapse regions, i.e. in halos, the baryonic pressure becomes essential. A cloud of gas becomes Jeans unstable (Jeans, 1902) if its sound crossing time drops below its gravitational free fall time, the corresponding Jeans mass increases with temperature and decreases with density according to $M_J \propto T^{3/2}\varrho^{-1/2}$. As the Universe expands and cools adiabatically, the declining temperature causes a decrease of the Jeans mass. Since the Jeans mass depends directly on the temperature, cooling processes determine substantially the collapse mass. In the early Universe shock-heated primordial gas cools via molecular and atomic hydrogen. While ionized gas can cool down to 10^4K via recombination radiation, collisional excitation and Bremsstrahlung (atomic cooling), neutral gas can be cooled down to a few 10^2 K via vibrational and rotational transitions in molecular hydrogen (which forms via gas-phase reactions) (Wise and Abel, 2007; Stiavelli, 2009). Cooling by molecular hydrogen is essential for the formation of the first stars. While more massive halos form even higher H_2 fractions than they need to cool efficiently, lower mass halos are not able to form a sufficient H_2 fractions. Thus for star formation a minimum halo mass is required to ensure cooling by a sufficient H_2 content (Stiavelli, 2009). Hence, there exist two independent mass thresholds for star formation, the Jeans mass and the cooling mass, where for the very first objects the cooling threshold is higher.

Nevertheless in presence of Lyman-Werner photons (ultraviolet (UV) photons) H_2 can be easily photo-dissociated. The formation of stars by H_2 cooling is already suppressed after stars have build up a Lyman-Werner background (Wise and Abel, 2008; Johnson et al., 2007; Ahn et al., 2009; Trenti and Stiavelli, 2009; Pawlik et al., 2013), and objects can only fragment further by atomic cooling which becomes effective in objects with higher virial temperatures $T_{vir} > 10^4$ K.

1.3 Epoch of Reionization

With the formation of the first stars the Universe starts to be permeated by hydrogen ionizing photons. As these photons escape from the interstellar medium (ISM) of galaxies into IGM, they gradually ionize the hydrogen in the IGM; this period of time is also referred to as the Epoch of Reionization which is visualised in Fig. 1.1. In this section we describe the sources of ionizing photons, how the IGM is reionized and how galaxy formation is affected by reionization.

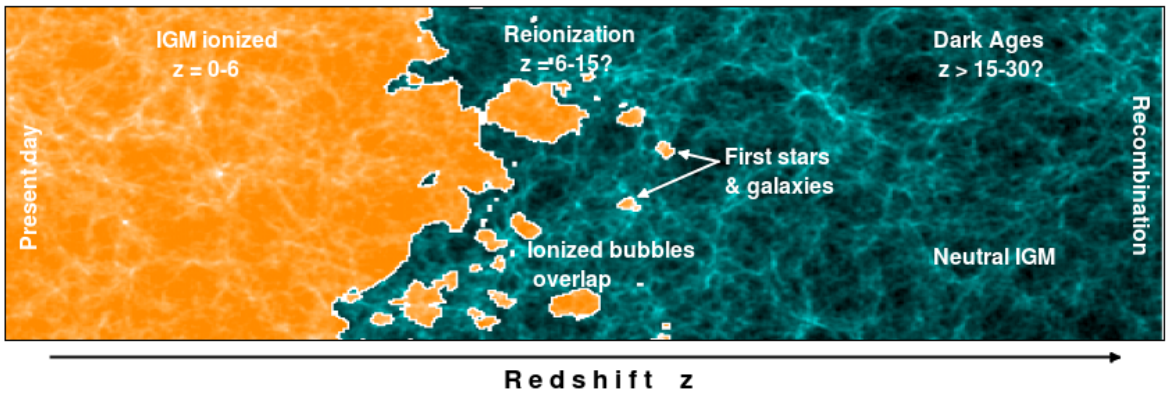

Figure 1.1: Cosmic recombination depicts the transition from the neutral IGM after the Universe recombined at $z \simeq 1100$ to the ionized IGM. After recombination, when CMB radiation was released, hydrogen in the Universe remained neutral until the first stars and galaxies appeared. The first light sources emit ionizing UV radiation which gradually ionized their surrounding. As the number of galaxies increases with cosmic time, the ionized bubbles grow, merge, increasing the ionized volume until the Universe is reionized at $z \simeq 6$. At lower redshifts the Universe remains highly ionized due to the ionizing radiation emitted by galaxies and quasars.

1.3.1 Escape of ionizing radiation from galaxies

The progress and duration of reionization is determined by the fraction of emitted number of ionizing photons that are able to escape from the galaxies into the IGM ($f_{\rm esc}$). Within the galaxies stellar populations produce ionizing photons which are subsequently partly absorbed by the hydrogen in the ISM. Since we have no observational constraints on the escape fraction during the Epoch of Reionization, numerical simulations have been exploited to constrain the possible values of $f_{\rm esc}$ as well as the respective dependencies on galaxy properties and redshift. Little consensus has been reached, however as some authors find $f_{\rm esc}$ to increase with halos mass (Gnedin et al., 2008; Wise and Cen, 2009), and others yield the opposite trend (Razoumov and Sommer-Larsen, 2010; Yajima et al., 2011; Ferrara and Loeb, 2013; Wise et al., 2014; Kimm and Cen, 2014). Similarly the estimated values of $f_{\rm esc}$ vary significantly, ranging from a few percent (Gnedin et al., 2008) up to $10-30\%$ (Mitra et al., 2013; Kimm and Cen, 2014) or even higher (Wise and Cen, 2009; Wise et al., 2014). Recently Kimm and Cen (2014) have shown by using radiative hydrodynamical simulations that the escape fraction is driven by SN explosions and subsequent star formation: ~ 10 Myr after stars have formed in a dense cloud (showing a negligible escape fraction), star-forming gas is blown away by energetic SN explosions, increasing the instantaneous $f_{\rm esc}$ value to $> 10\%$. Subsequent star formation is suppressed, leading to a reduced $f_{\rm esc}$. Consequently, the actual escape probability of ionizing photons is affected by this time delay between the peak of star formation and escape fraction, and can vary between $\sim 1-30\%$. Since less dense and smaller galaxies are more susceptible to supernovae explosions, there is a trend of $f_{\rm esc}$ to decrease with increasing halo mass, continuing the trend found in Wise et al. (2014). An accurate prediction for the escape fraction from galaxies can only be made if the ISM density structure is properly resolved, as clumping has a significant effect on the penetration and escape of ionizing radiation from an inhomogeneous medium. If less massive galaxies indeed show lower $f_{\rm esc}$ values, the mean escape fraction would increase towards higher redshifts, since radiative feedback is expected to deplete the low-mass galaxy population (Ferrara and Loeb, 2013). Indeed according to observations at $z \simeq 1-3$ galaxies at higher redshift exhibit a larger relative escape fraction (900Å to 1500Å) than at lower redshift (Siana et al., 2010). While there are no direct observational constraints at $z > 6$, theoretical models aiming to reproduce other observables at $z > 6$, in particular the number of galaxies, also require rising $f_{\rm esc}$ values towards higher redshifts (Mitra et al., 2013; Dijkstra et al., 2014).

1.3.2 Reionization of the IGM

The fraction of ionizing photons that escape from the galaxies contributes to the ionization of the IGM. In common reionization scenarios galaxies are assumed to be isotropic point sources of ionizing

photons. During reionization the ionized regions grow around the sources, merge and expand until the IGM is fully ionized. The velocity of the ionization fronts depends on the optical depth: while ionization fronts expand slowly in dense regions ($\mathrm{Log}(1+\delta) \gtrsim 1$), they spread more rapidly in less dense regions.

According to Gnedin (2000) three different stages of reionization can be identified: In the pre-overlap phase the individual ionizing sources turn on and start to ionized their surrounding. Due to hierarchical structure formation star-forming galaxies are preferentially located in high-density regions, where high recombination rates moderate the propagation of the ionization fronts. Once the ionizing photons emerge from high-density regions, they start to ionize low-density voids and dense regions without sources remain neutral. The IGM develops into a two-phase medium consisting of highly-ionized and neutral regions. The photon density is very inhomogeneous within the ionized regions and depends on the distance to neighbouring sources.

As soon as neighbouring ionized regions start to merge, reionization enters the overlap phase. Each point within the ionized region is exposed to all included sources and consequently the ionizing intensity rises rapidly, ionized regions expand into high-density gas that had remained neutral at lower intensities of ionizing photons. In this phase the process of reionization occurs rapidly as with each merger of ionized regions the ionizing intensity rises and gradually becomes more homogeneous. This phase transition is accelerated by the hierarchical structure formation: at the respective redshift range the galaxy formation rate rises rapidly with time increasing the ionizing intensity. This process leaves the IGM in a state where low-density regions have become highly-ionized, ionizing radiation has propagated everywhere except into self-shielded high-density regions that remain neutral. Reionization has occurred.

In the post-overlap phase neutral self shielded high-density regions represent Lyman Limit systems or damped Lyman-α systems. Nevertheless as galaxy formation proceeds, the mean ionizing intensity rises, gradually ionizes these previously self shielded high-density regions and becomes more uniform.

1.3.3 Feedback from radiation

Photoevaporation of gaseous halos after reionization

During the progress of reionization an intense UV background builds up which not only ionizes, but also heats the IGM above 10^4K via photoionization. A major fraction of collapsed gas resides in halos where due to a lack of atomic cooling the formation of galactic disks and stars is prevented, in so-called minihalos (Shapiro et al., 2004). Photoionization heating increases the temperature of the gas residing in these halos, whereas a fraction may obtain such high temperatures that it becomes unbound, i.e. it can expand due to the pressure gradient and evaporate into the IGM. The less the gas is bound in the halo, i.e. the less massive the halo is or the lower its circular velocity, the higher is the fraction of unbound gas (Barkana and Loeb, 1999). Thus photoevaporation causes gas depletion in predominantly low-mass halos (minihalos), decreasing the gas reservoir for star formation. The rising UV background during reionization can have several feedback effects by suppressing star formation within ionized regions: the completion of reionization is delayed, and the distribution of ionized regions becomes more uniform (Sobacchi and Mesinger, 2013b,a). The impact of this radiative feedback mechanism is highly debated. While some authors find its impact on reionization modest (Dijkstra et al., 2004b; Sobacchi and Mesinger, 2013a), others claim that all baryonic gas is removed from minihalos delaying reionization (Shapiro et al., 2004; Iliev et al., 2005).

Suppression of the formation of low mass galaxies

Photoionization heating causes the Jeans mass to increase dramatically, changing the minimum mass for galaxy formation. While the minimum mass for galaxy formation was set by cooling in non-photoheated regions, it is set by the Jeans mass in photoheated regions: in halos that show low circular velocities and low masses the gas infall becomes limited due to heating which leads to a suppression of the formation of low mass galaxies.

1.3.4 Feedback from galactic outflows

In addition to radiative feedback mechanisms kinetic feedback can also affect subsequent structure formation. Star formation comes along with the death of massive stars in supernovae explosions. The hydrodynamic energy injected by the supernovae can be enough to eject gas from the galaxy leading

to outflows (Larson, 1974). While the total energy in supernovae outflows is proportional to the halo mass, assuming a constant baryon fraction that is turned into massive stars, the binding energies of the supernovae ejecta and of all gas is proportional to the halo mass squared. Thus outflows can escape more easily from low mass galaxies and expel a larger fraction of gas (Rees and Ostriker, 1977; White and Rees, 1978; White and Frenk, 1991). As outflows reduce the gas content inside the galaxy, star formation is suppressed. This affects galaxy formation and could have a high impact especially at high redshifts (Wise and Abel, 2008), since high redshift galaxies first form in low mass halos and secondly merge with other halos causing regions of high star formation. Furthermore supernovae are the production sites for metals in the Universe. Supernovae explosions expel metal-enriched gas from the galaxies (outflows) which enhances the metal content of the IGM (Cen and Ostriker, 1999; Aguirre et al., 2001, 2005; Theuns et al., 2002; Oppenheimer and Davé, 2006; Tescari et al., 2011). This metal enrichment allows later generation of stars to form more easily due to metal-enhanced cooling. Moreover the expanding shocks from supernovae can also strip off gas from neighbouring galaxies and suppress their star formation respectively (Scannapieco et al., 2000; Scannapieco and Broadhurst, 2001).

1.3.5 Sources of reionization

The first stars in the Universe must have formed from the primordial elements which are primarily hydrogen and helium. Due to the absence of metals in the Universe, the first gas clouds cool by molecular hydrogen. Since molecular hydrogen cooling is less efficient than metal-enhanced cooling, the temperature in the gas clouds forming the first stars is higher than those of later type stars. Thus the respective Jeans mass is higher, fragmentation is lower and the first stars turn out to be more massive and hot, ranging between $30 - 300\,\mathrm{M}_\odot$ (Abel et al., 2002; Bromm et al., 2002; Yoshida et al., 2006). These metal-free stars are also referred to as Population III stars. The UV radiation of neighbouring Population III stars is able to destroy the main coolant of a potentially forming Population III star, i.e. molecular hydrogen; however, this can be ignored if the molecular hydrogen is inside giant hydrogen clouds and thus shielded against the UV radiation. As soon as star forming regions are metal-enriched by the first Population III supernovae, the subsequent generation of stars, Population II stars, form. Although Population II stars are still metal-poor, the available metals allow a more efficient cooling leading to lower stellar masses. Since Population III and II stars dominate the early star formation they are considered to be the main sources of reionization (Choudhury and Ferrara, 2007; Sokasian et al., 2003, 2004; Wyithe and Loeb, 2003; Yajima and Khochfar, 2014). Stellar radiation of hot stars can provide a sufficient number of ionizing photons. Nevertheless an even harder ionizing spectrum than that of the hottest stars is provided by quasars which present an interesting alternative reionization source. Nevertheless, it turns out that their number inferred from observations is not high enough to provide enough UV photons for reionization (Fan et al., 2001; Dijkstra et al., 2004a; Meiksin, 2005; Bolton and Haehnelt, 2007; Srbinovsky and Wyithe, 2007; Salvaterra et al., 2005, 2007) and furthermore the number of quasars is constrained by the observed X-ray background, making only a contribution of up to 10% possible (McQuinn, 2012).

1.4 Observational probes of the Epoch of Reionization

The epoch of reionization marks a watershed event in the evolution of the Universe. With the appearance of the first stars hydrogen ionizing photons carve out ionized spheres in the neutral IGM around themselves and ends when all neutral hydrogen in the IGM is ionized. Since reionization affects subsequent structure formation through a number of radiative feedback effects, it is of particular interest to gain knowledge about the detailed progress of reionization and its time of occurrence. While simulations can provide a variety of possible reionization scenarios, only a few of them will be allowed by observational constraints. Clear hints on reionization have been found in the CMB and in quasar absorption spectra, whilst to detect the decrease of galaxies with strong Lyman α (Lyα) emission towards higher redshifts is observational challenging. Future hopes lie in deeper surveys searching for strong Lyα emissions at high redshifts ($z > 6$) and in detections of the redshifted hydrogen line (21cm line). In this Section we elaborate on the different observational probes of reionization: the CMB, the 21cm line, and the attenuation of Lyα radiation.

1.4.1 Cosmic microwave background

Reionization has left multiple traces in the CMB. After recombination electrons are bound in hydrogen or helium atoms and the length of the mean free path of CMB photons becomes so large that they propagate freely. As reionization starts hydrogen becomes ionized and electrons unbound, increasing the effective number of free particles. Due to the recurrence of free electrons, CMB photons - having the temperature fluctuations at redshift $z \simeq 1100$ imprinted - are rescattered out of their lines of sight and statistically replaced by photons with random temperature fluctuations. This rescattering leads to a damping of the temperature anisotropies on all scales smaller than the horizon at reionization, i.e. all modes $l \lesssim 40$ (Dunkley et al., 2009; Larson et al., 2011; Planck Collaboration et al., 2014b).

Furthermore reionization enhanced the large-scale polarization signal of the CMB. While only local temperature quadrupoles cause a polarization of the CMB photons at the end of recombination, these local quadrupoles have grown by free streaming to large-scale quadrupoles at the time of reionization. Scattering at reionization generates a polarization signal from these enhanced temperature quadrupoles, increasing the power of large-scale polarization and suppressing the power of small-scale polarization due to the overall damping of the temperature anisotropies. The position and height of the peak in the polarization power spectrum gives hints on the redshift of reionization and the associated optical depth (Zaldarriaga, 1997). Measurements by Planck have revealed the optical depth and the redshift of reionization to be $\tau_e = (0.089^{+0.012}_{-0.014})$ and $z_{reion} = (11.1 \pm 1.1)$ respectively (Planck Collaboration et al., 2014a).

At scales $l > 3000$ the reionization history is also imprinted in the secondary temperature anisotropies of the CMB by the kinetic Sunyaev-Zeldovich (kSZ) effect. Since high energy electrons interact with the CMB photons by inverse Compton scattering, CMB photons in ionized regions receive energy boosts by bulk peculiar velocities of electrons. Thus the kSZ power spectrum on small scales reflects the topology of the ionized regions during reionization. As reionization scenarios become more patchy, the amplitude of the kSZ signal increases, whereas maximum contribution to the kSZ signal occurs when the angular sizes of the ionized regions are close to those corresponding to a given multipole (Park et al., 2013). However Park et al. (2013) found that extended periods of low-level ionization contribute marginally to the kSZ power spectrum at $l \approx 3000$.

1.4.2 The hydrogen 21 cm line

The 21 cm hydrogen line is sensitive to neutral hydrogen (H I) and thus represents a powerful tool to study the epoch of reionization, as well as the dark ages that preceded reionization. It corresponds to the transition from the triplet to the singlet hyperfine state of neutral hydrogen which differ only in the value of the total spin angular momentum. The relative population of these two states, i.e. the number of hydrogen atoms in the singlet (n_0) or triplet state (n_1), is determined by the spin temperature (T_S)

$$\frac{n_1}{n_0} = 3 \exp\left(-\frac{T_{21cm}}{T_S}\right), \tag{1.4}$$

where $T_{21cm} = h\nu_0/k$, and $h\nu_0 = hc/\lambda_0$ corresponds to the energy of 21 cm photons. Different excitation mechanisms, collisional and radiative, cause a change in the relative population of singlet and triplet states, where each of them can excite the transition by exchange of a quantum of energy $h\nu_0$: Although high energy collisions could alternate the hydrogen hyperfine state by excitation and de-excitation of Lyα photons, the required kinetic temperature of electrons and protons (T_K) is so high that respective regions are ionized and thus unobservable in 21 cm. In contrast low energy collisions excite the transition directly by absorption or emission of a 21 cm photon and thus drive T_S towards T_K. Low energy radiation, i.e. 21 cm radiation, induces transitions by absorption, its intensity is given by the so-called brightness temperature $T_R = \lambda^2/(2k)I_\nu$. In the presence of high energy radiation, e.g. the UV background, hydrogen atoms absorb and reemit Lyα photons, leading to a redistribution of singlet and triplet according to the radiation spectrum near Lyα energy, which is described by the colour temperature of the UV background (T_L). This effect is also known as the Wouthuysen-Field effect (Wouthuysen, 1952; Field, 1959a,b). Considering all these effects the spin temperature is given by Field (1958)

$$T_S = \frac{T_R + y_c T_K + y_L T_L}{1 + y_c + y_L} \tag{1.5}$$

where y_c and y_L are the coupling factors for collisions and UV radiation respectively.

In the low density IGM scattering by Lyα photons dominates as continuum photons from early sources redshift into Lyα and provide a sufficient Lyα background. Since the neutral IGM is opaque to resonant scattering, the colour temperature T_R is driven to the kinetic temperature of the gas T_K, while $y_c \approx 0$.

However the intensity of the 21 cm signal of the IGM can only be measured relative to a background radiation, e.g. the CMB. In a cloud of neutral hydrogen the background radiation (T_R) is partially absorbed and a fraction $T_R \exp(-\tau)$ is transmitted, whereas τ reflects the optical depth for 21 cm radiation. The absorbed background radiation translates into a 21 cm emission of the cloud with an intensity $T_S(1-\exp(-\tau))$. To obtain the intensity with which the cloud emits in 21 cm, the difference in intensity between the undiminished background radiation and the diminished background radiation with the resonance 21 cm radiation of the cloud can be calculated (e.g. Iliev et al., 2011)

$$\begin{aligned} \delta T_b &= \frac{T_S - T_R}{1+z}(1-\exp^{-\tau}) \\ &\approx \frac{T_S - T_R}{1+z}\frac{3\lambda_0^3\ A_{10}\ T_{21cm}\ n_{HI}(z)}{32\pi\ T_S\ H(z)} \end{aligned} \tag{1.6}$$

whereas δT_b is also referred to as the differential brightness temperature, $\lambda_0 = 21.16$ cm is the rest-frame wavelength of the 21 cm line, $A_{10} = 2.85 \times 10^{-15}\mathrm{s}^{-1}$ the Einstein coefficient for spontaneous emission, $T_{21cm} = 0.068$K the energy difference between the two levels, $n_{HI}(z)$ the neutral hydrogen density and $H(z)$ the Hubble constant at redshift z. In our Universe only the CMB poses such a prevailing low energy background radiation, $T_R = T_{CMB}$. As the 21 cm signal of the IGM is measured relative to the CMB, the IGM can be either seen in emission ($T_S > T_{CMB}$) or in absorption ($T_S < T_{CMB}$). If $T_S \gg T_{CMB}$, the IGM is observed in emission at a level that is independent of T_S, while in absorption at a level that is a factor T_{CMB}/T_S larger than in emission, if $T_S \ll T_{CMB}$.

During the dark ages and the epoch of reionization the 21 cm signal depends on the neutral hydrogen densities and the prevailing mechanisms driving the spin temperature (Mesinger et al., 2011). At very early times the IGM is so dense that T_S is collisionally coupled to T_K ($T_K = T_S < T_{CMB}$). After decoupling the gas temperature cools adiabatically and thus faster than the CMB (T_{CMB}). The 21 cm signal appears in absorption and its fluctuations are driven by the density fluctuations. As the Universe expands, the mean IGM density and thus the number of collisions decreases, T_S decouples from T_K and approaches T_{CMB} ($T_K < T_S < T_{CMB}$), whereas underdense regions decouple first due to their smaller number of atoms. With the appearance of light sources the Universe is permeated by Lyα and T_S couples again to T_K via the Wouthuysen-Field effect ($T_K < T_S < T_{CMB}$). Since heating by Lyα is more modest than by X-rays, T_K keeps decreasing as the Universe expands. Soon after the first sources have turned on X-rays from early quasars or star-forming regions start to heat the IGM and T_K increases. As soon as T_K rises above T_{CMB} the 21 cm signal is seen in emission, since T_S remains coupled to T_K. Once UV photons start to ionize the IGM, the 21 cm signal first becomes insensitive to T_S and disappears afterwards as soon as the respective region is completely ionized.

To compute the differential brightness temperature of the 21 cm signal during the Epoch of Reionization Equation 1.6 can be simplified. As the spin temperature T_S is coupled to the kinetic temperature of the gas T_K and $T_S \gg T_R$, the term $(T_S - T_R)/T_S$ in Equation 1.6 with $T_R = T_{CMB}$ converges to 1. The assumption $T_S \approx T_K$ does not hold during the early stages of reionization when only a few sources have turned on. Nevertheless it provides a useful tool to compute the 21 cm signal from numerical reionization simulation as the complicated computation of the spin temperature can be omitted. The overall strength of the 21 cm signal consists in the free propagation and redshifting after its emission. Thus when the frequency range that corresponds to the emitted signal during reionization is detected, we can not only trace the distribution of the ionized regions but also their time evolution.

A number of radio interferometers including PAPER (Parsons et al., 2010), 21CMA (Wang et al., 2013), GMRT (Pen et al., 2008; Ali et al., 2008), LOFAR (van Haarlem et al., 2013), MWA (Tingay et al., 2013), are just beginning observations with the objective to detect the redshifted 21 cm signal from reionization. For analyzing upcoming 21 cm observations, it is necessary to consider the foreground and noise contaminations and filter the primary 21 cm signal. Despite low signal-to-noise, prominent foregrounds and instrumental response were shown to be extractable from the data in cases of LOFAR (Jelić et al., 2008; Harker et al., 2010; Chapman et al., 2012) and MWA (Geil et al., 2008, 2011). Although small scales are blurred by thermal noise of the telescope, large-scale ionized regions at the end of reionization are likely to be detectable due to their coherent signature over well-resolved

observing angles (Zaroubi et al., 2012), provided that LOFAR and MWA reach low enough noise levels by long observation times (Datta et al., 2012; Zaroubi et al., 2012; Malloy and Lidz, 2013; Chapman et al., 2013). Nevertheless, besides the possibility of imaging the largest structures during reionization this generation of telescopes focuses on the statistics of the 21 cm signal as its power spectrum (e.g. Pritchard and Loeb, 2008). Even after foreground and noise removal the resulting 21 cm tomography will not reflect the unperturbed evolution of the ionized regions distribution as peculiar velocities of the IGM gas introduce non-random distortion to the 21 cm signal. The contrast of the signal increases and anisotropies are introduced (Barkana and Loeb, 2005; Lidz et al., 2007; Mao et al., 2008, 2012; Jensen et al., 2013a). Since only the signal along the line of sight is affected by redshift distortions, anisotropies can also help to remove secondary contributions to the power spectrum and extract pure cosmological information (Barkana and Loeb, 2005; Mao et al., 2012). Furthermore the anisotropies introduced by redshift distortions may be used to constrain reionization models. This approach seems to be promising as Jensen et al. (2013a) showed that for two extreme cases of reionization topology, inside-out and outside-in models, different evolutions of the anisotropies are expected.

1.4.3 Lyman Alpha

Lyα photons represent a powerful tool in understanding the ionizing state of the IGM given by their high optical depth (τ) to H I (e.g. Madau and Rees, 2000)

$$\tau = 1.5 \times 10^5 h^{-1} \Omega_m^{-1} \frac{\Omega_b h^2}{0.019} \left(\frac{1+z}{8} \right)^{3/2} (1+\delta_H) \chi_{HI}, \tag{1.7}$$

where h is the Hubble parameter, Ω_m and Ω_b the matter and baryon density, $(1+\delta_H) = n_H / \langle n_H \rangle$ the hydrogen overdensity, and χ_{HI} the mean fraction of neutral hydrogen. As can be seen from Equation 1.7 already small fractions of neutral hydrogen as low as 10^{-5} can cause a significant absorption of the Lyα photons making them a sensitive probe of neutral hydrogen in the IGM.

Gunn-Peterson Trough: During the progress of reioization Lyα radiation is absorbed by neutral hydrogen in the IGM. Thus, as the radiation of a source at z_{em} propagates through space, it is redshifted and radiation is always absorbed at Lyα resonance. For a neutral IGM at $z > z_{reion}$ such a spectrum shows a Gunn-Peterson trough (Gunn and Peterson, 1965) at wavelengths shorter than the local Lyα resonance $\lambda_{obs} < \lambda_\alpha (1 + z_{em})$ with $\lambda_\alpha = c/\nu_\alpha = 1216$Å. Indeed Fan et al. (2006) deduced the evolution of the Gunn-Peterson optical depth τ from a sample of 19 quasars at $5.74 < z_{em} < 6.42$. Towards higher redshifts the optical depth increases and ionized hydrogen (H II) regions around the luminous quasars decrease rapidly which suggests an accelerated evolution of the ionization state of the IGM at $z > 5.7$. Based on their observations Fan et al. (2006) concludes that $z \sim 6$ seems to be the end of the overlap stage of reionization. The results of Becker et al. (2014) are consistent with the conclusions of Fan et al. (2006) but present evidence for ionzation-driven fluctuations in the IGM neutral fractions near $z \sim 6$ from a set of 42 quasars at $4.5 < z_{em} < 6.4$.

Lyman Alpha emitters: Based on different selection techniques observations have yielded two types of high-redshift star-forming galaxies. On the one hand Lyman Break galaxies (LBGs) are identified by means of colours near the Lyman continuum discontinuity at 912 Å (e.g. Bouwens et al., 2011). Their selection technique is based on the fact that photons bluewards of the Lyman limit (912 Å) are almost completely absorbed by the neutral gas around star-forming regions of galaxies. On the other hand Lyman Alpha emitters (LAEs) are detected by their Lyα emission, which is identified by an excess in a narrowband filter with respect to the nearby continuum (Cowie and Hu, 1998; Ouchi et al., 2008). LAEs provide an excellent tool of tracing the ionization state of the IGM and high-redshift galaxy evolution for two reasons: (1) the strength, width and continuum break bluewards of Lyα line makes their detection unambiguous, and (2) Lyα photons are very sensitive to the attenuation by H I. Observations indicate that LAEs are young star-forming galaxies at high redshifts with low dust content (Yuma et al., 2010; Wiklind et al., 2013), whereupon bluer UV continuum slopes (Shapley et al., 2003; Vanzella et al., 2009; Pentericci et al., 2009; Kornei et al., 2010; Stark et al., 2010) indicate lower dust extinction (Meurer et al., 1999; Stark et al., 2010; McLure et al., 2011; Bouwens et al., 2012; Wilkins et al., 2013) than in LBGs.

These star-forming galaxies produce hydrogen ionizing UV radiation corresponding to the stellar masses, ages and metallicities of their stellar populations. The ionizing photons are partly absorbed

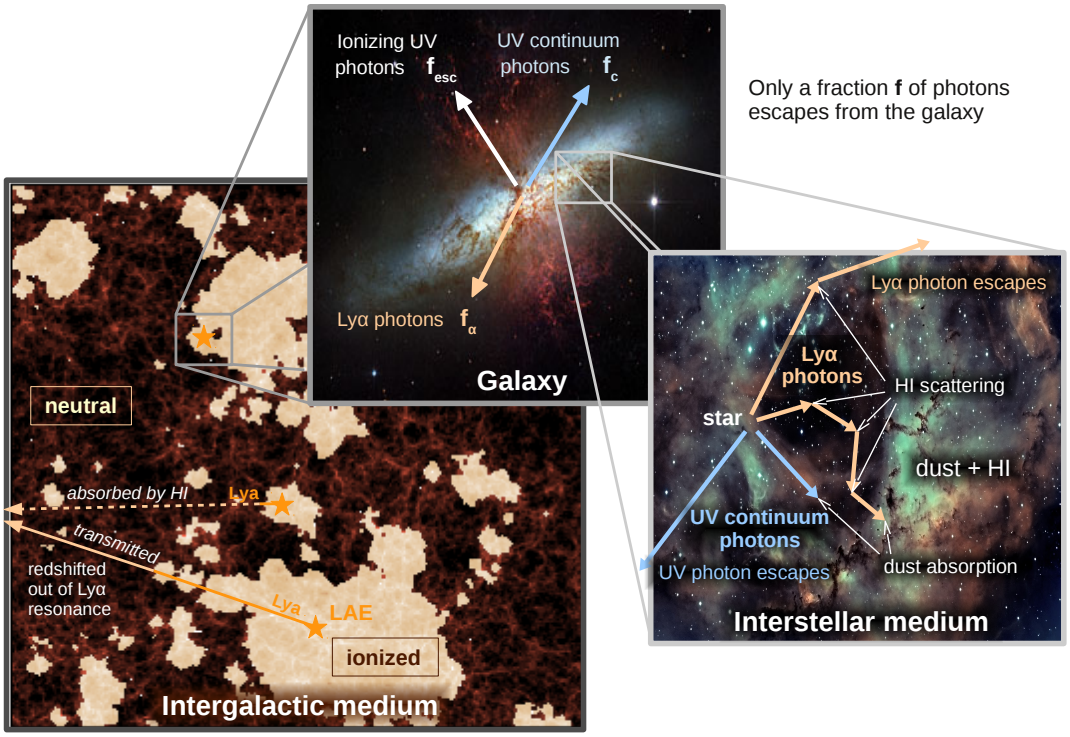

Figure 1.2: Physics of Lyman Alpha emitters: ionizing UV radiation is emitted by stars, a fraction $(1 - f_{\rm esc})$ is absorbed in the ISM, and Lyα photons are produced by the respective H I recombination radiation. The emitted Lyα photons propagate in the ISM until they are either scattered by H I or absorbed by dust; a fraction f_α can escape unattenuated from the galaxy into the IGM. UV continuum photons below the ionization threshold propagate until they are absorbed by dust within the ISM or reach the IGM where they propagate freely; the respective escape fraction from the galaxy is f_c. The fraction of ionizing UV photons escaping from the galaxy $f_{\rm esc}$ ionizes the IGM around the galaxy. Lyα radiation propagates unattenuated in the IGM as long as the IGM is ionized or the emitted Lyα line is out of Lyα resonance; otherwise H I leads to severe attenuation. Based on the transmitted Lyα flux, a galaxy is identified as a LAE or not. (Image credits: NASA, ESA and The Hubble Heritage Team (STScI/AURA) via `http://www.spacetelescope.org/images/heic0604a/` and Andrew Harrison via `http://interstellar-medium.blogspot.com/`)

by the neutral hydrogen in the ISM, and Lyα photons are emitted due to the recombinations in these high densities of hydrogen. The remaining fraction of ionizing photons can escape the galaxy and contribute to the ionization of the IGM. While softer UV continuum photons (non-ionizing and below the Lyα energy) are attenuated by dust in the ISM, Lyα photons are also scattered by neutral hydrogen leading to differing escape fractions of UV continuum and Lyα photons. Thus the Lyα escape fraction depends on the dust distribution, but it depends also on the kinematics and geometry of the ISM. It determines the strength of Lyα line that can leave the galaxy and propagate through the IGM while being redshifted. Star-forming galaxies showing detectable Lyα emission are identified as LAEs, while all galaxies showing an almost complete absorption bluewards of the Lyman limit are identified as LBGs.

As long as the medium is ionized, the Lyα photons propagate unattenuated, but are attenuated in presence of neutral hydrogen. Due to the low densities in the IGM, the respective recombination time scales are so long that Lyα radiation is only absorbed but not re-emitted. Hence, as long as ionized regions around sources are sufficiently extended, the emitted Lyα line has redshifted out of resonance when reaching regions of neutral hydrogen, the Lyα line can be detected. The more reionization proceeds, the more Lyα radiation is transmitted through the IGM and the higher becomes the number of observed LAEs. Hence, the Lyα luminosity function (Lyα LF) can be used to reconstruct, at least piecewise, the cosmic reionization history. A drop of the Lyα LF from $z \sim 5.7$ to 6.6 (Kashikawa et al., 2011) and from $z \sim 6.6$ to 7.3 (Konno et al., 2014) has been found indicating ongoing reionization,

while the respective LAE UV luminosity function remains constant at $z \simeq 5.7-6.6$ (Kashikawa et al., 2011). However, this drop in the Lyα LF could also be caused by intrinsic galaxy evolution (Dijkstra et al., 2007; Dayal et al., 2008; Samui et al., 2009; Dijkstra et al., 2014), or a combination of galaxy evolution and reionization (Dayal et al., 2011).

Several physical effects complicate the interpretation of LAE data as illustrated in Fig. 1.2: First the intrinsic Lyα luminosity of a galaxy depends on the total number of ionizing photons produced in the galaxy which in turn depends on the star formation rates, stellar masses, ages and metallicities of the stellar populations (Santos, 2004). Secondly the fraction of ionizing photons that are not absorbed by H I or dust and thus can escape from the galaxy and ionize the H I in the IGM, depends on the H I and dust content of the galaxy. Thirdly only a fraction of the Lyα radiation is not attenuated by dust and can escape from the galaxy. How the distribution of dust affects the Lyα escape fraction is still under debate. While Neufeld (1991) suggested that clumped dust can lead to enhanced Lyα emissions, numerical simulations (Laursen et al., 2013) reveal that such an enhancement is not possible for reasonable physical conditions. Fourthly peculiar velocities lead to a shift of the Lyα line; inflows (outflows) from the emitter red-shift (blue-shift) the Lyα line, leading to an increase (decrease) in the transmission of the Lyα line. Finally only a fraction of the Lyα radiation escaping from the galaxy is transmitted through the IGM. As mentioned above the transmission depends sensitively on the H I ionization state of the IGM.

The Lyα LF is subject to the above mentioned physical effects. In particular Dayal et al. (2011) have shown that the effects of reionization and dust distribution in the ISM on LAE visibility are degenerated such that a high escape fraction of Lyα photons (f_α) can be compensated by a lower Lyα IGM transmission (T_α). To yield a more complete picture, we will extend this parameter space by the escape fraction of ionizing photons from galaxies ($f_{\rm esc}$) - directly determining the number of photons ionizing the IGM and the intrinsic number of emitted Lyα photons - and investigate the combined effects of $f_{\rm esc}$, T_α, f_α on LAE visibility.

While it is difficult to disentangle the different effects on LAE visibility (host galaxy number density, dust obscuration and interstellar gas content and kinematic properties) by pure number counts of LAEs, their spatial distribution can provide the possibility to separate effects on large (e.g. reionization) and galaxy scales (e.g. dust in ISM). Since the spatial distribution of LAEs is mainly sensitive to the distribution and extent of the ionized regions in the IGM, LAE clustering could provide stringent constraints on reionization which we investigate in Chapter 5. Observations on the LAE angular correlation function reveal a negligible clustering at $z \simeq 6.6$ (Kashikawa et al., 2006; Ouchi et al., 2010). Since LAE clustering decreases as reionization proceeds and ionized regions grow around the sources (McQuinn et al., 2007a; Dayal et al., 2009), the observations hint towards an almost ionized Universe at $z \simeq 6.6$.

A complementary approach was introduced by Stark et al. (2010) and consists of tracking the fraction of LBGs showing Lyα emission. As neutral patches considerably attenuate Lyα emissions during reionization, the fraction of star-forming galaxies showing Lyα emission is expected to decrease with increasing redshift. Indeed a number of observations found a drop in the fraction from $z \simeq 6$ to $z \simeq 7,8$ (Stark et al., 2010; Pentericci et al., 2011; Stark et al., 2011; Curtis-Lake et al., 2012; Ono et al., 2012; Schenker et al., 2012; Treu et al., 2012; Caruana et al., 2014; Treu et al., 2013; Pentericci et al., 2014) and inferred H I fractions ranging from 0.3 to 0.6 at $z \simeq 7$ (assuming only a change in the fraction of neutral hydrogen). Nevertheless it should be noted that the derivation of H I fractions depends critically on the assumed IGM reionization scenario. Using our model for high-redshift LAEs we also examine the fractions of LBGs showing Lyα emission.

1.5 Thesis outline

In order to shed light into the progress of reionization, in this thesis we study the topology of ionized regions during reionization and find constraints on reionization by comparing simulations to LAE observations. By performing a self-consistent reionization simulation we characterise the evolution of the ionized regions and their dependence on respective source properties and underlying hydrogen density. Furthermore from a set of high-redshift LAE models based on different reionization scenarios, we find those models that reproduce observed Lyα luminosity function and LAE clustering at $z \simeq 6.6$. Attempts to constrain reionization from these models reveal a degeneracy between the escape fraction of ionizing photons from the galaxies, reionization and the dust distribution in the galaxies.

Chapter 2 consists of two parts describing radiative transfer methods. The first part describes

a mapping of ionized spheres scheme that can be used to quickly generate the respective ionization fields from a given density and source distribution. Such a code opens up the opportunity to study radiative feedback effects by accounting for spatially dependent photoionization rate at given times in hydrodynamical simulations. A MPI parallelized mapping Strömgren sphere scheme developed by Adrian Partl (private communication) is extended by computing the ionization profiles of sources from the underlying density and temperature profiles (using 1D radiative transfer), and by a method to account for overlapping spheres. The developed scheme computes for each source the ionization fraction (H II , He II , He III) and temperature profiles and maps and accounts for the overlapping of the ionized spheres. Starting from Stroemgren's computation on a single ionized sphere (Strömgren, 1939), we study the photoionization rates of two overlapping spheres and develop a method of describing two merged spheres with help of the ionization profiles of the two single spheres. The second part describes the cosmological 3D radiative transfer code pCRASH (Partl et al., 2011) and the necessary changes in order to perform reionization simulations: each source can be described by its own spectrum and the clumpiness of the IGM is accounted for by a spatially dependent clumping factor.

In Chapter 3 a self-consistent reionization simulation in an 80 Mpc/h cosmological volume is performed. Using the source properties (spectra, luminosities) from the star formation in the hydrodynamical simulation and accounting for IGM clumpiness, pCRASH is used to generate the evolution of the respective H II , He II , He III and temperature fields. With help of this simulation we address the following questions: Can star-forming galaxies reionize the Universe? Do statistics of the ionized regions give hints about source properties? Does reionization proceed from high to low density regions or vice versa? Does our simulation produce self-shielded regions? We find that assuming an escape fraction of ionizing photons of $f_{\rm esc} = 0.3$, star-forming galaxies are able to ionize the IGM until $z \simeq 6$. Reionization is found to proceed inside-out, although hydrogen gas remains partially neutral in dense regions far from sources.

In Chapter 4 we investigate different physical effects on the visibility of LAEs (Santos, 2004; Verhamme et al., 2006; Dayal et al., 2008, 2011; Dijkstra et al., 2011), in particular we consider the amount of ionizing photons not being absorbed in the ISM and able to escape into the IGM, ($f_{\rm esc}$), the escape fraction of UV continuum (f_c) and Lyα (f_α) photons from galaxies being both attenuated by dust in the ISM and in the case of Lyα being scattered by H I , and the transmission of Lyα photons through the IGM depending sensitively on the H I amount ($\langle \chi_{HI} \rangle$). We build a model for high-redshift LAEs by coupling state of the art cosmological simulations (GADGET-2) with a dust model and a radiative transfer code (pCRASH) and constrain the parameter space $f_{\rm esc}$, $\langle \chi_{HI} \rangle$, f_α/f_c allowed by the observed Lyα luminosity function (Lyα LF) at $z \simeq 6.6$ (Kashikawa et al., 2011). Therefore we run 5 reionization simulations with $f_{\rm esc} = 0.05, 0.25, 0.5, 0.75, 0.95$, compute Ly$\alpha$ transmissions ($\langle T_\alpha \rangle_{LAE}$) of the respective ionization fields ($\langle \chi_{HI} \rangle$), calculate the observed Lyα luminosities and set the only-free parameter f_α/f_c to reconcile the observed Lyα LF. We find that LAE visibility cannot constrain reionization exclusively since there is a *three-dimensional* degeneracy between $f_{\rm esc}$, $\langle T_\alpha \rangle_{LAE}$ and f_α/f_c, i.e. it depends also on the escape fraction of ionizing photons and the distribution of dust within the ISM.

In Chapter 5 we use the spatial distribution of LAEs (LAE clustering) to put further constraints on the parameter space $f_{\rm esc}$, $\langle \chi_{HI} \rangle$ and f_α/f_c. Using LAE models that reproduce the Lyα LF at $z \simeq 6.6$ we compare model results with the observed angular correlation function at $z \simeq 6.6$ (Kashikawa et al., 2006). We find that reionization has the largest impact on the amplitude of the LAE angular correlation functions (ACFs), and its imprints are clearly distinguishable from those of $f_{\rm esc}$ and f_α/f_c. Furthermore we investigate, firstly, when a galaxy produces enough luminosity to be identified as a LBG and/or LAE, and secondly, which fraction of its lifetime a galaxy is identified as a LBG or/and a LAE. We find that galaxies with a critical stellar mass of $M_\star = 10^{8.5}(10^{9.5})\,{\rm M}_\odot$ produce enough luminosity to stay visible as LBGs (LAEs), and the duty cycle of LBGs with (without) Lyα emission increases with the UV magnitude (and stellar mass).

In Chapter 6 predictions of other observables as the dependence of the Lyα equivalent width (EW) on the UV luminosity (M_{UV}) and the fraction of LBGs showing Lyα emission ($X_{Ly\alpha}$) are made by using the physical model for high-redshift LAEs. Compared to observations (Kashikawa et al., 2011) model UV bright galaxies show larger Lyα equivalent widths, which leads to a declining $X_{Ly\alpha}$ towards fainter UV luminosities while observations indicate the opposite trend (Stark et al., 2010, 2011). As the simulations do not resolve the ISM our modelling of dust attenuation is approximative. Thus the LAE model is expanded such that the Lyα emissions of UV bright galaxies are more suppressed than of fainter galaxies and the observed Lyα LF and LAE ACF at $z \simeq 6.6$ are reproduced. The Lyα equivalent width of the UV bright galaxies decreases as intended and for $EW > 50$ Å as a

LAE selection criterion $X_{Ly\alpha}$ declines with increasing UV luminosity which is in accordance with the observational trend. With help of a toy model it is examined how the predictions of the EW-M_{UV} relation and M_{UV}-dependency of $X_{Ly\alpha}$ can vary as the observed LAE and LBG LFs constraining the LAE model are changed. Both, EW-M_{UV} and $X_{Ly\alpha}$-M_{UV} relations, depend sensitively on the assumed luminosity functions, while amplitude and M_{UV}-dependency of $X_{Ly\alpha}$ alter with the chosen equivalent width cut for identifying LAEs.

In Chapter 7 a summary of this thesis and its conclusions are given.

Chapter

2

Radiative Transfer Simulations

We have implemented a one-dimensional radiative transfer scheme following the ionization fronts of hydrogen (H II) and helium (He II, He III) and temperature for a given ionizing spectrum. Since the ionized regions carved by galaxies in the intergalactic medium (IGM) can be well approximated by spherical bubbles, we have developed a a mapping-sphere-scheme, similar to that presented in Thomas and Zaroubi (2008). Starting from spherically averaged temperature and density fields and using our 1D radiative transfer scheme, we compute the effect of each source on the IGM temperature and ionization profiles, which are then mapped onto a grid. Furthermore, in order to perform self-consistent reionization simulations, we have extended the three-dimensional radiative transfer code pCRASH described in Partl et al. (2011) by: the possibility of an arbitrary number of spectra, the inclusion of a local and thus spatially-dependent clumping factor and photon tracking from previous snapshots.

2.1 Introduction

In order to describe the Epoch of Reionization different approaches have been developed to derive the effect of radiation on the gas in the intergalactic medium (IGM). Methods include semianalytical models (Choudhury and Ferrara, 2005, 2006), semi-numerical models (Mesinger and Furlanetto, 2007; Zahn et al., 2007) and numerical simulations (Trac et al., 2008; Ciardi et al., 2012; Iliev et al., 2012).

Semi-analytical models describe the time evolution of radiation (photoionization rates (Γ_i)) and gas (ionization fractions (χ_i), temperature (T), density including IGM clumpiness) quantities globally. Rate equations of the ionization fractions and temperature are solved for mean/global quantities, making the model easily extendible for various physical processes and assumptions. State-of-the-art models (e.g. Choudhury and Ferrara, 2005) account for an inhomogeneous IGM distribution, different classes of ionizing sources (Population III stars, Population II stars and quasi-stellar objects), stellar evolution models, and radiative feedback inhibiting star formation in low-mass galaxies. Due to short computation times, semi-analytic models represent a powerful tool to perform parameter studies and to investigate the effects of relevant and additional physical processes. However, they do not provide any spatial information on the evolving ionized structures, making structure analysis impossible.

In contrast, semi-numerical models are not only reasonably fast methods but also provide spatial information. Using density fields, i.e. spatially dependent density distribution, from numerical DM simulations or linear methods and a prescription for the identified sources, the ioniziation fields are generated by an excursion-set approach (Mesinger and Furlanetto, 2007; Zahn et al., 2007) or by a combination of 1D radiative transfer and a mapping-of-spheres-scheme (Thomas et al., 2009). In the excursion-set approach spheres of varying radius surrounding every point in the IGM are considered: if the number of ionizing photons within the sphere exceeds the number of interior hydrogen atoms, i.e. exceeding the excursion-set barrier (fulfilling the criterion for ionization), the point is considered as ionized. Proceeding from large to small spheres (smoothing scales) ensures that cells ionized by neighbouring sources are also accounted correctly (Zahn et al., 2007). In the second approach based on the underlying density field the ionization profiles of the ionizing sources are computed by using

a one dimensional radiative transfer scheme. Assuming a homogeneous growth of the ionized region around each source, spheres containing the calculated ionization profiles are mapped on a grid (Thomas et al., 2009). Due to their approximate approach semi-numerical models are well-suited to performing reionization simulations for large cosmological volumes and large-scale structure studies, but fail to take the source spectra and the resulting heating of the IGM into account, or to properly follow the inhomogeneous density distribution.

In numerical models the temporal evolution of the ionization fields are computed self-consistently. From a DM only or hydrodynamical simulation the sources are generated either by imposing a relation between the halo mass and the number of ionizing photons, or using the information on the stellar population for a more sophisticated source model. Performing three dimensional radiative transfer the expansion of the ionized regions based on the source locations, luminosities and spectra is followed. These models are capable of tracking the ionization fronts and the heating of the IGM depending on the sources, but are computationally far more expensive than semi-numerical approaches. Within the numerical radiative transfer schemes two main types of algorithms have been developed. On the one hand there are ray-tracing schemes (Paardekooper et al., 2010; Hasegawa and Umemura, 2010; Ciardi et al., 2001; Maselli et al., 2003, 2009; Partl et al., 2011; Abel et al., 2002; Wise and Abel, 2011; Razoumov and Cardall, 2005): photons are considered to be emitted from the sources and propagate through the medium while absorption and reemission are calculated along their propagation paths; radiative transfer is solved on regular, adaptive, unstructured grids or no grids (using particles to represent the density field). On the other hand there are methods which exploit the moments of the radiative transfer equation (Gnedin and Abel, 2001; Aubert and Teyssier, 2008). The critical approximation in this method is the assumption on the Eddington tensor which basically describes the propagation of light. Using the optically thin Eddington tensor (Gnedin and Abel, 2001) radiation is assumed to propagate in straight lines, thus leading also to an unphysical propagation of ionization fronts behind an optically thick obstacle. Even an alternative formulation of the Eddington tensor, the M1 closure relation developed by Levermore (1984) to solve the radiative transfer equation in the optically thick limit but also ensuring some accuracy in the optically thin limit, suffers the same problem (Aubert and Teyssier, 2008).

In order to simulate the epoch of reionization we have firstly developed a semi-numerical radiative transfer scheme further, and secondly extended the numerical radiative transfer code pCRASH (Partl et al., 2011) to enable self-consistent reionization simulations. The semi-numerical scheme is based on a one dimensional radiative transfer code and a mapping-spheres-scheme described in Section 2.2. This scheme represents an extension of the MPI parallelized mapping-Strömgren-sphere-scheme developed by Adrian Part (private communication). pCRASH is a three dimensional ray-tracing gridbased Monte Carlo radiative transfer code suited for cosmological radiative transfer calculations; we elaborate on the necessary extensions for a complete self-consistent reionization simulation in Section 2.3.

2.2 Mapping-Spheres-Scheme

The mapping-sphere-scheme is a semi-numerical radiative transfer scheme that takes the averaged density and temperature distribution around sources and source characteristics as luminosity and spectral shape into account. Based on the method of Thomas et al. (2009), the radial ionization and temperature profiles of all sources are computed with help of one dimensional (1D) radiative transfer, adjusting for overlapping ionized spheres, and resized spheres are mapped on a grid to obtain the distribution of ionized regions. Based on the underlying density and temperature distribution, the 1D radiative transfer code computes ionization and temperature profiles for each source by taking the specified spectrum of the respective source into account. In order to solve the evolution of the ionization fractions we use a special numerical scheme for stiff systems of production-destruction equations which we describe in Section 2.2.1. Details of the 1D radiative transfer code including the rates considered for ionization, recombination, heating and cooling as well as the algorithm of the code are presented in Section 2.2.2. When spheres of individual sources are mapped on to a grid, they may overlap and the sizes of the spheres may not correspond to the interior ionizing emissivity. Hence, we analyze the problem of overlapping spheres in Section 2.2.3 and develop a model in Section 2.2.4, which resizes the spheres according to the fraction of overlap. In a last step the mapping-Strömgren-sphere-scheme developed by Adrian Partl is used and the resized ionized spheres mapped on to a grid. To speed up calculations the mapping-spheres-scheme can be run on multiple processors; the method of its parallelization is described in Section 2.2.4. Finally, in Section 2.2.5 we compare the results for

a cosmological ionization field to those obtained with the three dimensional radiative transfer code pCRASH.

2.2.1 Patankar schemes

Stiff equations are differential equations for which straightforward numerical methods, e.g. Euler methods, are numerically unstable, unless the step size is chosen to be extremely small. In order to solve such stiff systems of production-destruction equations as the differential equation for the ionization fractions, Burchard et al. (2003) presented modified Patankar-type methods of first- and second order in time that are numerically robust, unconditionally positive and conservative. The form of the production-destruction equations with N constituents, represented by the vector $\mathbf{c} = (c_1, ..., c_N)^T$, is given by

$$\begin{aligned} \partial_t c_i &= P_i(\mathbf{c}) - D_i(\mathbf{c}) && (2.1)\\ &= \sum_{j=1}^{N} p_{i,j}(\mathbf{c}) - \sum_{j=1}^{N} d_{i,j}(\mathbf{c}), && (2.2) \end{aligned}$$

where $P_i(\mathbf{c}) \geq 0$, $D_i(\mathbf{c}) \geq 0$ and each production-destruction term may depend on $\mathbf{c}$. Since $p_{i,j}(\mathbf{c})$ is the rate at which constituent j transforms into constituent i and $d_{i,j}(\mathbf{c})$ the rate at which constituent i transforms into constituent j, $p_{i,j}(\mathbf{c})$ and $d_{i,j}(\mathbf{c})$ need to satisfy $p_{i,j}(\mathbf{c}) = d_{j,i}(\mathbf{c})$ for $i \neq j$. Solving the constituents' equations the forward Euler scheme

$$c_i^{n+1} = c_i^n + \Delta t \ (P_i(\mathbf{c}^n) - D_i(\mathbf{c}^n)) \quad (2.3)$$

is a conservative method but nonpositive. To sustain a positive method equation 2.3 is modified by the Patankar-trick.

$$c_i^{n+1} = c_i^n + \Delta t \ (P_i(\mathbf{c}^n) - D_i(\mathbf{c}^n)\frac{c_i^{n+1}}{c_i^n}) \quad (2.4)$$

Rearranging this equation shows the positiveness of the Patankar method

$$c_i^{n+1} = \frac{c_i^n + \Delta t P_i(\mathbf{c}^n)}{1 + \Delta t \frac{D_i(\mathbf{c}^n)}{c_i^n}}. \quad (2.5)$$

To increase the order of accuracy of this method the Runge-Kutta scheme can be used.

Patankar-Runge-Kutta scheme

By analogy with the Patankar-Euler scheme the destruction term are weighted with the quotient of the constituents and the Patankar-Runge-Kutta scheme is given by

$$\begin{aligned} c_i^{(1)} &= c_i^n + \Delta t \left(P_i(\mathbf{c}^n) - D_i(\mathbf{c}^n)\frac{c_i^{(1)}}{c_i^n} \right) && (2.6)\\ c_i^{n+1} &= c_i^n + \frac{\Delta t}{2} \left(P_i(\mathbf{c}^n) + P_i(\mathbf{c}^{(1)}) - (D_i(\mathbf{c}^n) + D_i(\mathbf{c}^{(1)})\frac{c_i^{n+1}}{c_i^{(1)}} \right). && (2.7) \end{aligned}$$

Compared to the Patankar-Euler scheme this method is of second order and thus of higher accuracy. Nevertheless, applying the Patankar-Runge-Kutta scheme to one of the prominent examples of stiff ordinary differential equations, the chemical reaction of Robertson, Burchard et al. (2003) finds an unphysical exponential increase of two of three constituents. The Robertson test case is given by

$$\begin{aligned} \frac{\mathrm{d}c_1}{\mathrm{d}t} &= -0.04 \ c_1 + 10^4 \ c_2 \ c_3 \\ \frac{\mathrm{d}c_2}{\mathrm{d}t} &= 0.04 \ c_1 - 10^4 \ c_2 \ c_3 - 3 \times 10^7 \ c_2^2 \quad (2.8)\\ \frac{\mathrm{d}c_3}{\mathrm{d}t} &= 3 \times 10^7 \ c_2^2 \end{aligned}$$

and shows significantly different time scales for transformations of constituents.

Modified Patankar-Runge-Kutta scheme

Due to the instability of the Patankar-Runge-Kutta scheme in stiff test problems, Burchard et al. (2003) introduced a numerically stable, positive and conservative method, the so called Modified Patankar-Runge-Kutta scheme.

$$c_i^{(1)} = c_i^n + \Delta t \left(\sum_{j=1}^{N} p_{i,j}(\mathbf{c}^n) \frac{c_j^{(1)}}{c_j^n} - \sum_{j=1}^{N} d_{i,j}(\mathbf{c}^n) \frac{c_i^{(1)}}{c_i^n} \right) \tag{2.9}$$

$$c_i^{n+1} = c_i^n + \frac{\Delta t}{2} \left(\sum_{j=1}^{N} \left(p_{i,j}(\mathbf{c}^n) + p_{i,j}(\mathbf{c}^{(1)}) \right) \frac{c_j^{n+1}}{c_j^{(1)}} - \sum_{j=1}^{N} \left(d_{i,j}(\mathbf{c}^n) + d_{i,j}(\mathbf{c}^{(1)}) \right) \frac{c_i^{n+1}}{c_i^{(1)}} \right) \tag{2.10}$$

2.2.2 1D radiative transfer

Ionization fractions

The radiation of the sources is allowed to propagate radially assuming an underlying IGM density distribution which is the radially averaged density distribution from the source in the cosmological simulation box. The ionization fraction of hydrogen (H II) and helium (He II, He III) at location r and time t are obtained by solving the rate equations:

$$\frac{\mathrm{d}n_{\mathrm{HII}}}{\mathrm{d}t} = \Gamma_{\mathrm{HI}} n_{\mathrm{HI}} + \beta_{\mathrm{HI}} n_e n_{\mathrm{HI}} - \alpha_{\mathrm{HII}} n_e n_{\mathrm{HII}} \tag{2.11}$$

$$\frac{\mathrm{d}n_{\mathrm{HeII}}}{\mathrm{d}t} = \Gamma_{\mathrm{HeI}} n_{\mathrm{HeI}} + \beta_{\mathrm{HeI}} n_e n_{\mathrm{HeI}} - \alpha_{\mathrm{HeII}} n_e n_{\mathrm{HeII}} - \beta_{\mathrm{HeII}} n_e n_{\mathrm{HeII}} + \alpha_{\mathrm{HeIII}} n_e n_{\mathrm{HeIII}} \tag{2.12}$$

$$\frac{\mathrm{d}n_{\mathrm{HeIII}}}{\mathrm{d}t} = \Gamma_{\mathrm{HeII}} n_{\mathrm{HeII}} + \beta_{\mathrm{HeII}} n_e n_{\mathrm{HeII}} - \alpha_{\mathrm{HeIII}} n_e n_{\mathrm{HeIII}} \tag{2.13}$$

Here n_{HI} and n_{HII} depict the number densities for neutral and ionized hydrogen, while n_{HeI}, n_{HeII}, n_{HeIII} represent the number densities for neutral, single and double ionized helium. The driving processes determining the ionization fractions are photoionization (Γ, ionization due to absorption of ionizing photons), collisional ionization (β (Cen, 1992), ionization by collisions with electrons), and recombination (α) (Cen, 1992). The subscript of the rates notes the respective specie, e.g. Γ_{HI} is the photoionization rate for neutral hydrogen and α_{HII} is the recombination rate for ionized hydrogen. While the collisional ionization and recombination rates are dependent on the temperature, i.e. the kinetic energy of the particles, the photoionization rate is strongly determined by the intensity and spectrum of the emitted photons.

$$\begin{aligned} \Gamma_{\mathrm{HI}} &= \int_{E_{\mathrm{HI}}}^{\infty} \sigma_{\mathrm{HI}} F_\nu(E,r,t) \frac{\mathrm{d}E}{E} + f_{\mathrm{H}} \left[\int_{E_{\mathrm{HI}}}^{\infty} \sigma_{\mathrm{HI}} \left(\frac{E - E_{\mathrm{HI}}}{E_{\mathrm{HI}}} \right) F_\nu(E,r,t) \frac{\mathrm{d}E}{E} \right] \\ &+ f_{\mathrm{H}} \left[\frac{n_{\mathrm{HeI}}}{n_{\mathrm{HI}}} \int_{E_{\mathrm{HeI}}}^{\infty} \sigma_{\mathrm{HeI}} \left(\frac{E - E_{\mathrm{HeI}}}{E_{\mathrm{HI}}} \right) F_\nu(E,r,t) \frac{\mathrm{d}E}{E} \right] \end{aligned} \tag{2.14}$$

$$\begin{aligned} \Gamma_{\mathrm{HeI}} &= \int_{E_{\mathrm{HeI}}}^{\infty} \sigma_{\mathrm{HeI}} F_\nu(E,r,t) \frac{\mathrm{d}E}{E} + f_{\mathrm{He}} \left[\int_{E_{\mathrm{HeI}}}^{\infty} \sigma_{\mathrm{HeI}} \left(\frac{E - E_{\mathrm{HeI}}}{E_{\mathrm{HeI}}} \right) F_\nu(E,r,t) \frac{\mathrm{d}E}{E} \right] \\ &+ f_{\mathrm{He}} \left[\frac{n_{\mathrm{HI}}}{n_{\mathrm{HeI}}} \int_{E_{\mathrm{HeI}}}^{\infty} \sigma_{\mathrm{HI}} \left(\frac{E - E_{\mathrm{HI}}}{E_{\mathrm{HeI}}} \right) F_\nu(E,r,t) \frac{\mathrm{d}E}{E} \right] \end{aligned} \tag{2.15}$$

$$\Gamma_{\mathrm{HeII}} = \int_{E_{\mathrm{HeII}}}^{\infty} \sigma_{\mathrm{HeII}} F_\nu(E,r,t) \frac{\mathrm{d}E}{E} \tag{2.16}$$

Here σ_i (i = H I, He I, He II) are the bound-free photoionization cross-sections given by Osterbrock (1989). For all three species (H I, He I, He II) the first term is the primary ionization - ejection of electrons by absorption of ionizing photons - while the second and third terms represent the effect of secondary ionization - ejection of electrons by absorption parts of the energy of the primary ejected electrons. As given by Shull and van Steenberg (1985) the terms

$$f_{\mathrm{H}} = 0.3908 \left(1 - \left(\frac{n_{\mathrm{HII}}}{n_{\mathrm{HI}} + n_{\mathrm{HII}}} \right)^{0.4092} \right)^{1.7592} \tag{2.17}$$

and

$$f_{\rm He} = 0.0554 \left(1 - \left(\frac{n_{\rm HII}}{n_{\rm HI} + n_{\rm HII}}\right)^{0.4614}\right)^{1.6660} \tag{2.18}$$

reflect the fraction of primary electrons that cause secondary ionizations. At distance r and time t the radiation flux of a source with a total luminosity L and a spectral energy distribution I(E) [erg s^{-1} Hz^{-1}] for photons of energy E is given by

$$F_\nu(E,r,t) = e^{-\tau(E,r,t)}\ L\ \frac{I(E)}{\int_0^\infty I(E){\rm d}E}\ \frac{1}{(r/{\rm Mpc})^2}\ \ ({\rm cm}^{-2}{\rm s}^{-1}) \tag{2.19}$$

where the respective optical depth is the sum of the optical depths of all species

$$\tau(E,r,t) = \sum_i \int_r \sigma_i(E) n_i(r,t) {\rm d}r. \tag{2.20}$$

Determining photoionization any spectrum of the source can be considered. Note that any photons below 13.6 eV (threshold for ionizing hydrogen) have no effect on ionization.

Solving the rate equations Since the rate equations displayed in equation 2.13 represent a stiff system of production-destruction equations they are solved by using the Modified Patankar-Runge-Kutta scheme. To identify the constituents and their respective production and destruction rates we rewrite equation 2.13 in matrix notation:

$$\frac{\rm d}{{\rm d}t}\begin{pmatrix} n_{\rm HI} \\ n_{\rm HII} \\ n_{\rm HeI} \\ n_{\rm HeII} \\ n_{\rm HeIII} \end{pmatrix} = \begin{pmatrix} -\beta_{\rm HI} n_e - \Gamma_{\rm HI} & \alpha_{\rm HII} n_e & 0 & 0 & 0 \\ \beta_{\rm HI} n_e + \Gamma_{\rm HI} & -\alpha_{\rm HII} n_e & 0 & 0 & 0 \\ 0 & 0 & -\beta_{\rm HeI} n_e - \Gamma_{\rm HeI} & \alpha_{\rm HeII} n_e & 0 \\ 0 & 0 & \beta_{\rm HeI} n_e + \Gamma_{\rm HeI} & -\alpha_{\rm HeII} n_e - \beta_{\rm HeII} n_e - \Gamma_{\rm HeII} & \alpha_{\rm HeIII} n_e \\ 0 & 0 & 0 & \beta_{\rm HeII} n_e + \Gamma_{\rm HeII} & -\alpha_{\rm HeIII} n_e \end{pmatrix} \begin{pmatrix} n_{\rm HI} \\ n_{\rm HII} \\ n_{\rm HeI} \\ n_{\rm HeII} \\ n_{\rm HeIII} \end{pmatrix} \tag{2.21}$$

As can be seen the rate equations for hydrogen and helium are decoupled and thus can be treated as separate systems: one with two constituents, H I and H II, and another one with three constituents, He I, He II and He III. Starting with the rate equations for hydrogen we can use the Modified Patankar scheme and write the corresponding numerical scheme for a set of two constituents c_1 and c_2 with the production rates p_{12} (rate at which constituent 1 is transformed to constituent 2) and p_{21} and the destruction rates d_{12} (rate at which constituent 1 is destroyed into constituent 2) and d_{21}.

$$c_1^{n+1} = c_1^n + \Delta t \left(p_{12}\frac{c_2^{n+1}}{c_2^n} - d_{12}\frac{c_1^{n+1}}{c_1^n}\right) \tag{2.22}$$

$$c_2^{n+1} = c_2^n + \Delta t \left(p_{21}\frac{c_1^{n+1}}{c_1^n} - d_{21}\frac{c_2^{n+1}}{c_2^n}\right) \tag{2.23}$$

To obtain a matrix notation rewriting yields

$$\left(1 + \frac{d_{12}\Delta t}{c_1^n}\right) c_1^{n+1} \qquad -\frac{p_{12}\Delta t}{c_2^n} \qquad c_2^{n+1} = \qquad c_1^n \tag{2.24}$$

$$-\frac{p_{21}\Delta t}{c_1^n} c_1^{n+1} \qquad + \left(1 + \frac{d_{21}\Delta t}{c_2^n}\right) \qquad c_2^{n+1} = \qquad c_2^n \tag{2.25}$$

where $p_{12} = d_{21}$ and $p_{21} = d_{12}$ following Burchard et al. (2003). We translate the general description of constituents and production/destruction rates to the respective ones for hydrogen: $c_1 = n_{\rm HI}$, $c_2 = n_{\rm HII}$, $p_{12} = \beta_{\rm HI} n_e + \Gamma_{\rm HI}$, $p_{21} = \alpha_{\rm HII} n_e$.

Following the same analysis we apply the Modified Patankar scheme to the set of equations for helium, solving for three constituents (c_1, c_2, c_3), the respective production (p_{12}, p_{21}, p_{23}, p_{32}) and

destruction rates (d_{12}, d_{21}, d_{23}, d_{32}).

$$c_1^{n+1} = c_1^n + \Delta t \left(p_{12} \frac{c_2^{n+1}}{c_2^n} - d_{12} \frac{c_1^{n+1}}{c_1^n} \right) \tag{2.26}$$

$$c_2^{n+1} = c_2^n + \Delta t \left(p_{21} \frac{c_1^{n+1}}{c_1^n} - d_{21} \frac{c_2^{n+1}}{c_2^n} + p_{23} \frac{c_3^{n+1}}{c_3^n} - d_{23} \frac{c_2^{n+1}}{c_2^n} \right) \tag{2.27}$$

$$c_3^{n+1} = c_3^n + \Delta t \left(p_{32} \frac{c_2^{n+1}}{c_2^n} - d_{32} \frac{c_3^{n+1}}{c_3^n} \right) \tag{2.28}$$

As before we rewrite the equations for a matrix notation:

$$\left(1 + \frac{d_{12}\Delta t}{c_1^n}\right) c_1^{n+1} - \frac{p_{12}\Delta t}{c_2^n} c_2^{n+1} = c_1^n \tag{2.29}$$

$$-\frac{p_{21}\Delta t}{c_1^n} c_1^{n+1} + \left(1 + \frac{(d_{21}+d_{23})\Delta t}{c_2^n}\right) c_2^{n+1} - \frac{p_{23}\Delta t}{c_3^n} c_3^{n+1} = c_2^n \tag{2.30}$$

$$- \frac{p_{32}\Delta t}{c_2^n} c_2^{n+1} + \left(1 + \frac{d_{32}\Delta t}{c_3^n}\right) c_3^{n+1} = c_3^n \tag{2.31}$$

Here the constituents are $c_1 = n_{\mathrm{HeI}}$, $c_2 = n_{\mathrm{HeII}}$, $c_3 = n_{\mathrm{HeIII}}$, the production/destruction rates are given by $p_{12} = \beta_{\mathrm{HeI}} n_e + \Gamma_{\mathrm{HeI}}$, $p_{21} = \alpha_{\mathrm{HeII}} n_e$, $p_{23} = \beta_{\mathrm{HeII}} n_e + \Gamma_{\mathrm{HeII}}$, $p_{32} = \alpha_{\mathrm{HeIII}} n_e$.

Equations 2.25 and 2.31 depict only the numerical scheme of the Modified Patankar scheme. Since the Modified Patankar-Runge-Kutta scheme is of second order and based on the Modified Patankar scheme, the numerical step for the Modified Patankar-Runge-Kutta scheme can be written in terms of the numerical steps of the Modified Patankar scheme $\zeta\left(c_i^n, p_{ij}(\mathbf{c}^n)\right)$ from c_i^n to c_i^{n+1} (equations 2.25 and 2.31):

$$c_i^{(1)} = \zeta\left(c_i^n, p_{ij}(\mathbf{c}^n)\right) \tag{2.32}$$

$$c_i^{n+1} = \zeta\left(c_i^n, p_{ij}(\mathbf{c}^n) + p_{ij}(\mathbf{c}^{(1)})\right) \tag{2.33}$$

Temperature

As the ionization fractions are determined by the temperature dependent recombination and collisional ionization rates, it is essential to follow the temperature evolution. The IGM is heated and cooled by different processes. While heating is dominated by the excess photon energy after ionization, cooling is caused by various interactions between particles and/or photons. The respective rate equation to obtain the evolution of the temperature is given by

$$\begin{aligned} \frac{3k_B n}{2}\frac{\mathrm{d}T}{\mathrm{d}t} = {} & f_{\mathrm{Heat}} \sum_{\mathrm{i=H\,I,He\,I,He\,II}} n_i \int \sigma_i\left(E - E_i\right) F_\nu(E,r,t) \frac{\mathrm{d}E}{E} \\ & + \frac{\sigma_s n_e}{m_e c^2} \sum_{\mathrm{i=H\,I,He\,I,He\,II}} \int F_\nu(E,r,t)(E - 4k_B T)\mathrm{d}E \\ & - k_B T \frac{n}{n_e}\frac{\mathrm{d}n_e}{\mathrm{d}t} \\ & - \sum_{\mathrm{i=H\,I,He\,I,He\,II}} \zeta_i n_e n_i - \sum_{\mathrm{i=H\,I,He\,I,He\,II}} \eta_i n_e n_i - \sum_{\mathrm{i=H\,I,He\,I,He\,II}} \psi_i n_e n_i \\ & - \theta_{ff} n_e (n_{\mathrm{HII}} + n_{\mathrm{HeII}} + n_{\mathrm{HeIII}}) - \varpi n_e. \end{aligned} \tag{2.34}$$

Here n_e is the number density of free electrons, and $n = n_{\mathrm{H}} + n_{\mathrm{He}} + n_e$ is the number of free particles per unit volume. The first term on the right hand side represents the photoheating due to the ionization of the three species H I, He I and He II. σ_i and E_i describe the cross section and the threshold energy of ionization of the ith species (H I, He I or He II). The second term accounts for the Compton heating that becomes important close to the source, σ_s is the Thomson scattering cross-section of an electron of mass m_e. The variation in the number of free particles leading to adiabatic cooling is depicted in the third term. The fourth to eighth terms are collisional ionization cooling (ζ_i), recombination cooling (η_i), collisional excitation cooling (ψ_i), Bremsstrahlung cooling

(θ_{ff}) and Compton cooling/heating by the CMB background ($\overline{\omega}$), respectively. While the expressions for the photoionization and Compton heating were obtained from Thomas and Zaroubi (2008), the cooling terms are identical with those implemented in pCRASH (Maselli et al., 2009; Partl et al., 2011). The fraction of heat that is deposited by secondary electrons is given by an extrapolation of a fitting formula by Shull and van Steenberg (1985)

$$f_{\mathrm{Heat}} = \begin{cases} 0.9971 \left[1 - \left(1 - \frac{n_{\mathrm{HII}}}{n_{\mathrm{HI}}+n_{\mathrm{HII}}}{}^{0.2663}\right)^{1.3163}\right] & \text{if } \frac{n_{\mathrm{HII}}}{n_{\mathrm{HI}}+n_{\mathrm{HII}}} > 10^{-4} \\ 0.15 & \text{if } \frac{n_{\mathrm{HII}}}{n_{\mathrm{HI}}+n_{\mathrm{HII}}} \leq 10^{-4}. \end{cases} . \tag{2.35}$$

The evolution of the temperature is calculated using the Patankar-Runge-Kutta scheme. Thus c_i in equation 2.7 represents the temperature T and $P_i(\mathbf{c})$ and $D_i(\mathbf{c})$ the heating (photoionization, Compton) and cooling (collisional ionization, recombination, collisional exciation, Bremsstrahlung, Compton).

Algorithm

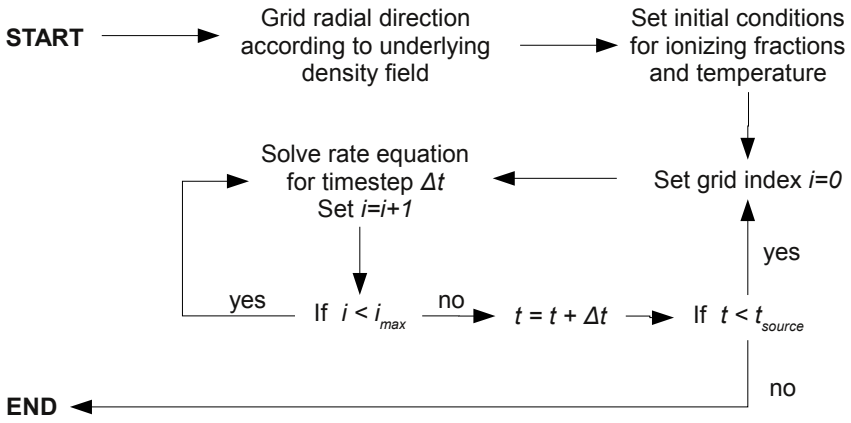

Figure 2.1: Scheme of 1D radiative transfer code for computing ionization and temperature profiles of an ionizing source. Radial distance to the source r is binned and accordingly the grid index i increases with r. Within a timestep Δt radial bins are updated along the direction of light propagation.

To solve the rate equations the radial distance is binned depending on the underlying density distribution, i.e. with increasing density the radial bin size decreases, and the initial conditions for the ionization (H II, He II, He III) and the temperature profiles are set accordingly. The default is a completely neutral medium. Starting at the source location $r = 0$ the radius of the Strömgren sphere is calculated with the density and temperature at the source location. Based on a resolution criterion and a logarithmic binning which accounts for the decreasing flux at larger distances, the width of the innermost radial bin Δr_1 is computed. The width of the next radial bin Δr_2 is likewise computed but based on the density and temperature at $r = r_1$. This procedure is continued until all N bin widths have been calculated. Starting at the source locations the ionization fractions and the temperature are updated for a timestep Δt in each bin. This timestep does not refer to the intrinsic timesteps used to solve the rate equations, they are chosen by the adaptive modified Patankar scheme, i.e. if the ionization fraction or the temperature changes by more than 1%, the timestep is reduced. Within one timestep Δt the radial cells are updated in the direction of the propagation of the radiation, i.e. the $i+1^{th}$ cell is updated after the i^{th} cell where $i = 0$ represents source location. This fact makes the code causal. Due to this scheme the propagation of the radiation is effectively higher than the speed of light c, but the speed of the growing ionization fronts is much smaller, so that the difference due to this approximation is negligible. After all radial bins have been updated, time is increased by another timestep Δt and the new ionization fractions and temperature are calculated again. As shown in Fig. 2.1 this scheme is continued until the time t reaches the initially defined evolution time t_{source}.

Testing the 1D radiative transfer code

In this section our 1D radiative transfer code is tested against analytic solutions and compared to results obtained from the 3D radiative transfer code pCRASH. The evolution of the ionization front in an uniform background including only hydrogen can be derived analytically, whereas including helium and evolving temperature requires a numerical scheme. Firstly we test our 1D radiative transfer code against the analytic solution of a Strömgren sphere (considering only hydrogen), and secondly we consider a test case which includes helium and an evolving temperature and compare results to those obtained with pCRASH. Finally we evaluate and discuss dependencies of the ionization fronts on different spectral shapes.

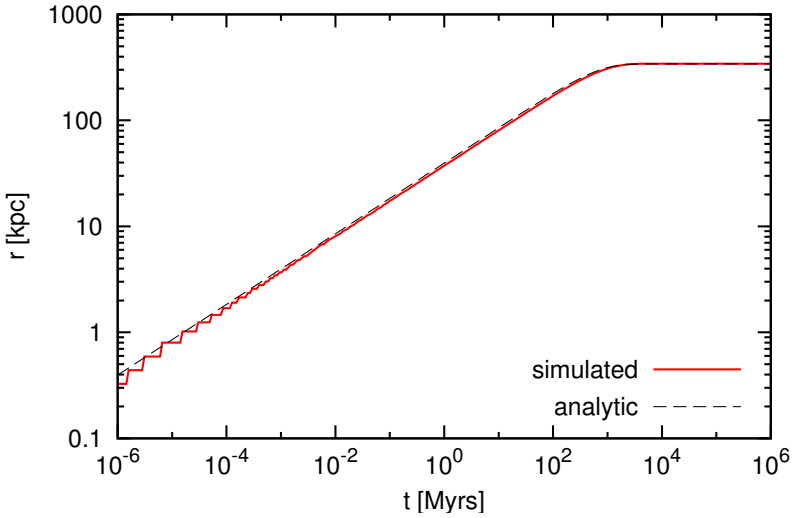

Figure 2.2: Simulated (solid, red) and theoretical (dashed, black) evolving ionization front in an uniform background with a constant hydrogen number density of $n_H = 1.9 \times 10^{-4}$ cm^{-3} and a constant temperature of $T = 10^4$ K. The source is assumed to emit only photons at $E = 13.6$ eV and has a luminosity of $L = 10^{42}$ erg s^{-1}.

Evolution of the hydrogen ionization front: In the first test case a H II sphere expands around a source that emits photons at a constant rate. The temperature and density distributions are assumed to be homogeneous and constant in time. The maximum ionized sphere of a source emitting ionizing photons of $E_{ion} = 13.6$ eV at a rate Q is given by the Strömgren sphere (Strömgren, 1939)

$$R_s = \left(\frac{3Q}{4\pi\alpha_B(T) C n_H^2} \right)^{1/3}, \tag{2.36}$$

and the evolution of the ionization front is analytically (Dopita and Sutherland, 2003) described by

$$r_I = R_s \left(1 - e^{-t/t_{rec}}\right)^{1/3} \tag{2.37}$$

$$t_{rec} = \left(C\alpha_B(T) n_H\right)^{-1}. \tag{2.38}$$

Here t_{rec} is the recombination time and depends on the recombination coefficient $\alpha_B(T) = 2.6 \times 10^{-13}(T/10^4)^{-13}$ cm^3 s^{-1}, the number density of hydrogen n_H and the respective clumping factor C. The adopted values in this test case are $n_H = 1.9 \times 10^{-4}$ cm^{-3}, $QE_{ion} = L = 10^{42}$ erg s^{-1}, $C = 1$ and $\alpha_B = 2.6 \times 10^{-13}$ cm^3 s^{-1}. Since the source ionizes first the surrounding hydrogen, subsequent photons propagate either to the ionization front or reionize the recombining hydrogen. Hence, the ionized sphere expands with time (see Figure 2.2) until the ionized volume represents the volume in which the recombination rate equals the emission rate of the ionizing photons, the so-called Strömgren sphere (Strömgren, 1939). In Figure 2.2 the dashed black line represents the analytic solution based on equation 2.37, while the red solid line shows the numerical result from the 1D radiative transfer code. The numerical solution is within 5% of the theoretical value for radii that are at least 1% of the final Strömgren radius. For even smaller distances from the source the resolution limit of the radial

binning needs to be increased as it introduces discontinuities in the numerical solution, as can be seen for distances smaller than 3 kpc in Figure 2.2.

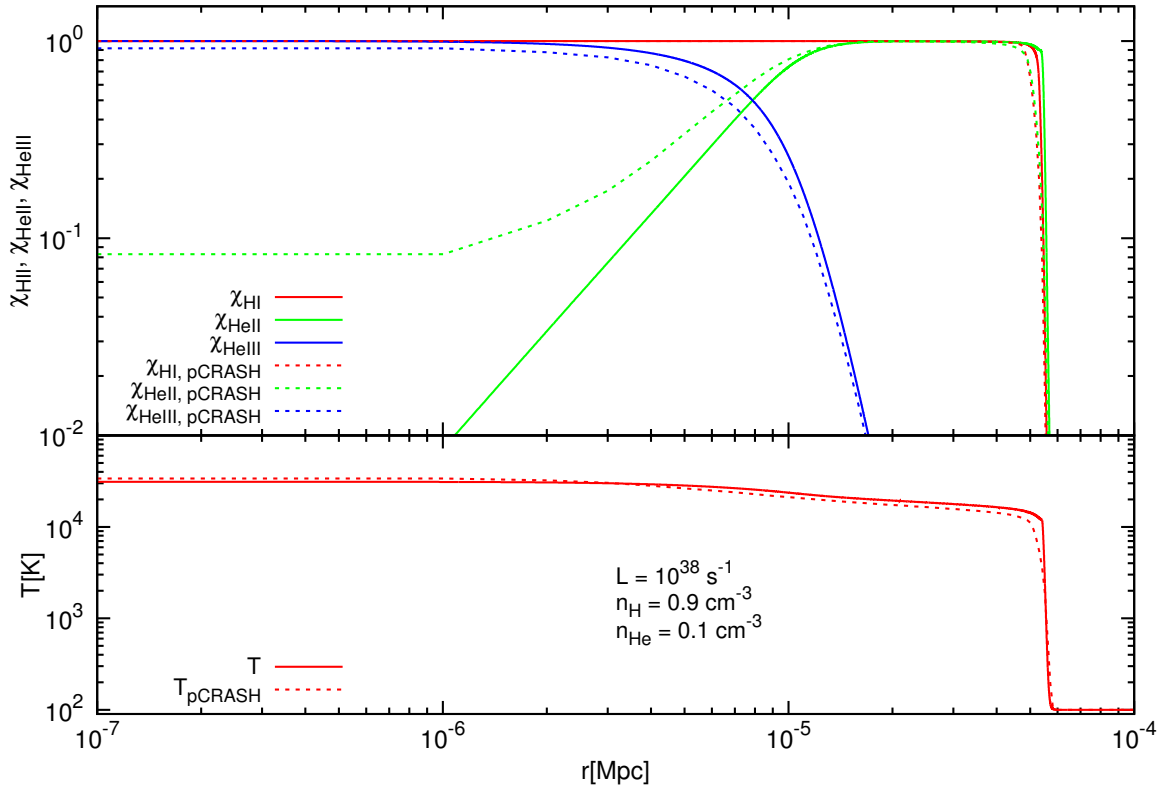

Figure 2.3: Comparison of the ionization fraction χ_{HII} (red), χ_{HeII} (blue), χ_{HeIII} (green) profiles in the upper panel and temperature profiles in the lower panel between the 1D radiative transfer scheme (solid curves) and pCRASH (dashed curves). The medium consists to 90% of hydrogen and 10% of helium with a constant number density $n = 1$ cm^{-3} and an initial temperature of 10^2 K. The source has a luminosity of $L = 10^{38}$ erg s^{-1} and emits a black body spectrum at $T = 6 \times 10^4$ K. Due to the non-adaptive spatial resolution of pCRASH, the ionization profiles obtained by the 1D radiative transfer scheme differ in the vicinity of the source.

Evolution of the hydrogen and helium ionization front including temperature: In this test we compare the ionization fronts including helium and an evolving temperature after an evolution time of 0.6 Myr to results of pCRASH. Here the medium is considered to consist of 90% hydrogen and 10% helium, with a total number density of $n = 1$ cm^{-3} and an initial temperature of $T = 10^2$ K. A source with a luminosity of 10^{38} erg s^{-1} starts to emit a spectrum of a black body of $T = 6 \cdot 10^4$ K. In Figure 2.3 we show the obtained profiles for the ionization fractions in the upper panel and the temperature in the lower panel as solid lines, while dashed lines indicate the results obtained with pCRASH. For all ionization fractions and the temperature we find that the results of our 1D radiative transfer code are in overall agreement with those of pCRASH. At small distances from the source we can see from Figure 2.3 that ionization fractions for helium differ, i.e. the 1D radiative transfer shows lower χ_{HeII} and respectively higher χ_{HeIII} fractions than pCRASH: since the radial binning in the 1D radiative transfer code is adapted to the underlying density, the resolution close to the source is higher than in pCRASH where a constant binning is adopted. Thus in the inner vicinity of the source the ionization profiles are computed more accurately and the 1D radiative transfer gives more reliable results due to its adaptive binning. Hence, limited to the adopted spatial resolution the ionization and temperature profiles can be calculated accurately with the developed 1D radiative transfer code.

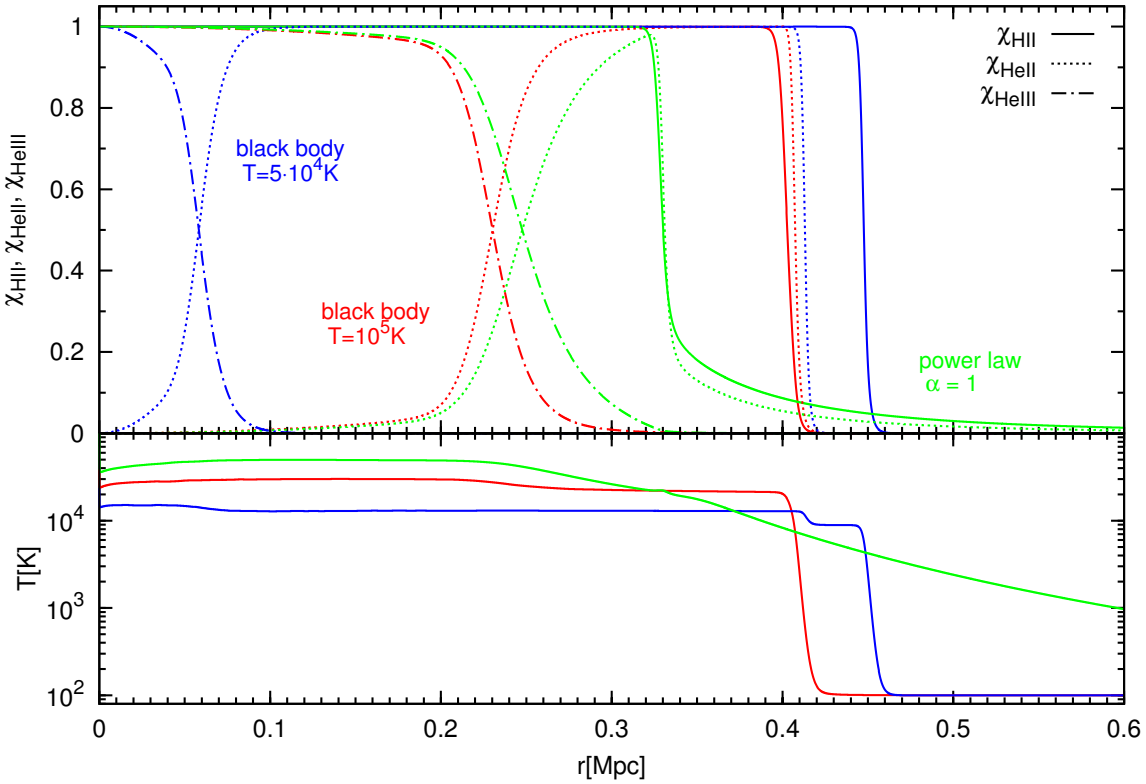

Figure 2.4: Comparison of the ionization ($\chi_{\rm HII}$, $\chi_{\rm HeII}$, $\chi_{\rm HeIII}$) and temperature profiles of different source spectra but the same luminosity ($L = 10^{43}$ erg s^{-1}) for energies $E \geq 13.6$ eV. The blue, red, green lines correspond to a black body spectrum at $T = 5 \times 10^4$ K, at $T = 10^5$ K and a power law spectrum $\propto \nu^{-1}$. The medium consists of 75% of hydrogen and 25% of helium with a constant number density $n = 10^{-4}$ cm^{-3} and an initial temperature of 10^2 K. In the upper panel the fraction of ionized hydrogen (H I, solid lines), of single ionized helium (He II, dotted lines) and double ionized helium (He III. dashed-dotted lines) are shown, while in the lower panel the respective temperature for the three spectra are presented.

Profiles of different spectra

In this section our 1D radiative transfer code is used to study the effect of different spectral shapes on the H II, He II and He III ionization profiles. Therefore, two black body spectra of $T = 5 \times 10^4$ K and $T = 10^5$ K, and a power law spectrum following $L_\nu \propto \nu^{-1}$ are analysed (see Figure 2.5). As the black body spectra decrease exponentially towards higher energies, they provide less high energy photons than power law spectra. Their spectra are softer and are representative for spectra from stars and star-forming galaxies, while quasars emit a larger fraction of high energy photons and are modelled by power law spectra.

In order to allow a direct comparison of spectral shapes we assume the ionizing luminosity of all spectra to be of the same value $L = 10^{43}$ erg s^{-1} in our study. The medium consists of 75% of hydrogen and 25% of helium. Initially it is completely neutral ($n = 10^{-4}$ cm^{-3}) and its temperature is assumed to be $T = 10^2$ K.

Since hydrogen and helium have different ionization energies (13.6 eV for H II, 24.5 eV for He II and 54.4 eV for He III), the spectral shape should be reflected in the position of the ionization fronts. Further the presence of high energy photons determines the shape and broadening of the ionization fronts. This relation between the spectral shape and the positions and shape of the ionization fronts is discussed in the following by comparing our three example spectra.

Starting with the hydrogen (H II) ionization front, we find that the front of the black body spectrum of $T = 5 \times 10^4$ K is at the largest distance (450 kpc), followed by the black body spectrum of $T = 10^5$ K (400 kpc) and the power law spectrum (330 kpc). Since black body spectra provide more hydrogen ionizing photons in the range $\nu_{\rm HI} \leq \nu < \nu_{\rm HeI}$, more photons are available for hydrogen ionization. Photons capable of helium ionization ($\nu \geq \nu_{\rm HeI}$) also contribute to the ionization of hy-

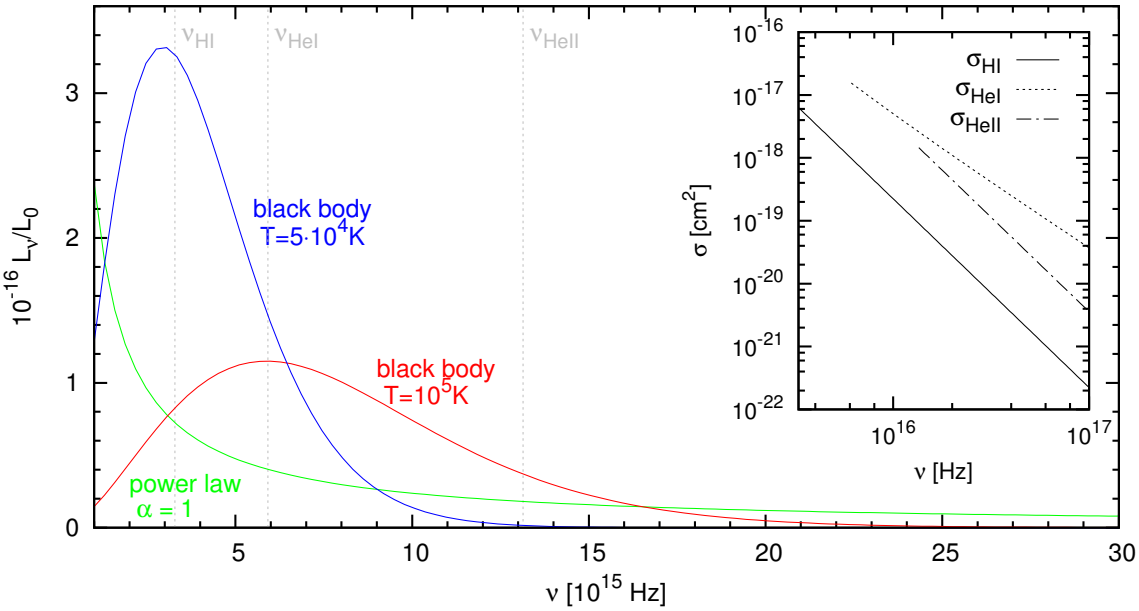

Figure 2.5: Large panel: Black body spectrum at $T = 5 \times 10^4$ K (blue), black body spectrum at $T = 10^5$ K (red) and power law spectrum (green) for the same luminosity $L = 10^{43}$ erg s^{-1}. Vertical lines show the frequencies for ionization of H I, He I and He II. Small panel: Cross-sections for the three species H I (solid), He II (dotted) and He III (dashed-dotted).

drogen, however, at those energies the cross-sections for helium are larger (see inset panel in Figure 2.5) leading to an increased probability of ionizing helium.

The ionization front of single ionized helium (He II) follows basically the ionization front of hydrogen where the number of photons able to ionize helium is comparable to the number of photons able to ionize hydrogen taking the different number densities of hydrogen and helium into account. This applies to the black body of $T = 10^5$ K and the power law spectra, while for the black body of $T = 5 \times 10^4$ K the He II front is at smaller distances than the H II front. As can be seen from Figure 2.5 the latter spectra provides by approximately a factor 3 more hydrogen than helium ionizing photons. For the other two spectra the numbers of ionizing photons for hydrogen and helium are more balanced and we find that the He II front is at slightly larger distances than the H II front: as the HeI cross section is larger than the H I cross section at energies $E \geq h\nu_{\mathrm{HeI}}$, helium is more likely to absorb an ionizing photon.

The ionization front of double ionized helium (He III) is determined by the number of photons with energies larger than 54.4 eV. Since the black body spectrum at $T = 5 \times 10^4$ K has nearly no photons at such energies, the source can only double ionize helium in small volumes, i.e. the He III ionization fronts propagates only to small distances. Since the other spectra provide more high energy photons, their He III regions are larger. Although the black body spectrum at $T = 10^5$ K provides more ionizing photons at energies close to the ionizing threshold (ν_{HeII}) than the power law spectrum, the total number of photons capable of double ionizing helium is higher for the power law spectra, thus its He III ionization front is found at larger distances.

Comparing the ionization fronts of the black body spectra with the power law spectrum, it is seen that the ionization front for black body spectra is very sharp, while it is more broadened for power law spectra. This effect is especially seen for the H II and He II fronts and can be explained by the extended tail of high energy photons which is cut off by the exponential decrease in black body spectra.

Up to now we have only discussed the shape and position of ionization fronts, however the temperature of the gas is sensitive to the spectra of the sources. This becomes relevant for the 21 cm brightness temperature which is sensitive on the spatial distribution of the kinetic gas temperature. When the gas becomes ionized the remaining energy of the absorbed photon goes into heating. Thus the more high energy photons are available for ionization, the more the gas is heated: due to the higher number of high energy photons the temperature in the ionized region of the source emitting

a power law spectrum exceeds the temperature of the black body spectra in Figure 2.4. The same applies for the temperature difference of the two black body spectra. Since the main heating process is due to ionization, the ionization fronts are also imprinted in the temperature profiles. In particular for the black body of $T = 5 \times 10^4$ K this is well seen, as at each ionization front we see a drop in temperature. The more ionized a region, the more ionization events have occured, each heating the gas by the excess energy of the ionizing photons. The same is found for the black body at $T = 10^5$ K, while there are only two drops in the temperature discernible due to the small difference in the positions of the H II and He II fronts. In the case of the power law spectrum these temperature steps are not seen due to the extended ionization fronts, but the temperature declines steadily following the decrease in the ionization fractions of He III, He II and H II respectively.

In summary the relative positions of the ionization fronts (H II, He II, He III) are determined by the spectral shape of the emitted photons: the more the spectrum is centred at higher, i.e. helium ionizing, energies, the lower is the difference in the positions of the ionization fronts. Furthermore the spectral shape of the high energetic photons ($\nu > \nu_{\rm HeII}$) characterises the shape of the ionization fronts, the more the spectrum extends to higher energies, the more the ionization front is broadened.

2.2.3 Overlapping spheres

In the previous section we presented a 1D radiative transfer scheme that computed the ionization and temperature profiles of a single source which resulted in an ionized sphere. In a realistic scenario multiple sources will emit ionizing photons and their surrounding ionized spheres may merge. Since we want to derive the ionization field of multiple sources from the ionization profiles of each single source, we need to develop an adequate mapping-spheres-scheme. Thus we address, firstly, the problem of two overlapping spheres and, secondly, three or more overlapping spheres. In the case of merging ionized spheres, photons of one sphere can propagate into the other sphere and contribute to their growth. To obtain a scheme how to account for this overlapping, firstly, we analyse the ionization fraction and the corresponding photoionization in the ionization equilibrium and, secondly, we derive an approximate scheme based on this analysis.

The medium is ionized by the ionizing photons that are emitted by the sources, thus the main quantity that determines the ionization fraction is the photoionization rate. In the case of a single source the photoionization rate and the corresponding ionization fraction can be easily computed, we wish to extend this computation of photoionization rate to two sources. Assuming the two sources are located at the same position, they can be considered also as a single source with their cumulative luminosity. However, when two spatially separated sources are considered, it is questionable whether we can add the ionization fractions obtained from the single sources to yield the resultant ionization fractions. Considering equation 2.14 and the example of two sources at the same position, this cannot be true. As we can note in equation 2.14 the resultant photoionization rate can be obtained by summation of the photoionization rates of the spheres. Hence, to account for the overlap of spheres we consider the photoionization rates of single spheres, combined single spheres and merged spheres.

Photoionization rate of a single sphere In line with equation 2.13 the radial ionization distribution is computed by solving the evolution equation for the ionization rate.

$$\frac{{\rm d}n_{\rm HII}}{{\rm d}t} = \Gamma_{\rm HI} n_{\rm HI} - \alpha_{\rm HII} n_e n_{\rm HII} \tag{2.39}$$

This equation is nearly identical to that for hydrogen in equation 2.13 but excludes the collisional ionization term. Since collisional ionization becomes important for very high temperature and becomes much smaller than the photoionization rate in our calculations, we will neglect it in the following consideration. In the next step equation 2.39 is simplified by $n_e = n_{\rm HII}$, $n_{\rm HII} = X n_{\rm H}$ and $n_{\rm HI} = (1 - X) n_{\rm H}$:

$$\frac{{\rm d}X}{{\rm d}t} = \Gamma_{\rm HI}(1 - X) - \alpha_{\rm HII} n_{\rm H} X^2 \tag{2.40}$$

In this model the sphere grows until the recombination rate balances the photoionization rate and ionization equilibrium is reached (${\rm d}X/{\rm d}t = 0$). Assuming a source emitting N_ν photons of frequency ν per second, the photoionization rate at a distance r from the source is given by

$$\Gamma_{\rm HI}(r) = \int_{\nu_{\rm HI}}^{\infty} \frac{N_\nu \sigma_{\rm HI}(\nu)}{4\pi r^2} e^{-\tau_\nu(r)} {\rm d}\nu \tag{2.41}$$

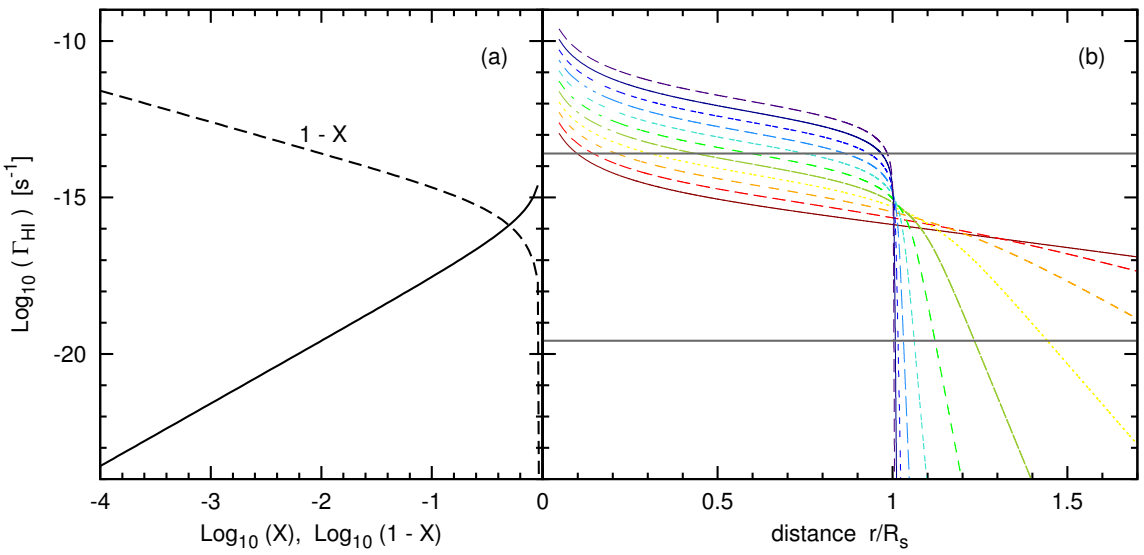

Figure 2.6: Left panel: Dependence of the neutral (dashed line) and ionization (solid line) fraction on the photoionization rate for $n_{\rm H} = 10^{-3}{\rm cm}^{-3}$ and $T = 10^4{\rm K}$. Right panel: Photoionization rate profiles for $n_H = 10^{-3}{\rm cm}^{-3}$ and $T = 10^4{\rm K}$ and $Q = 10^{44+i}$, $i = 0..10$ (red to blue). The black lines indicate $\Gamma_{\rm HI,upper}$ and $\Gamma_{\rm HI,lower}$.

and along the direction of light propagation the optical depth $e^{-\tau_\nu(r)}$ is defined by

$$\tau_\nu(r) = \int_r \sigma_{\rm HI}(\nu) n_H (1 - X(r)) {\rm d}r. \tag{2.42}$$

In the following we will consider a source that emits $N_{\nu_{\rm HI}}$ photons of hydrogen ionization energy $h\nu_{\rm HI}$ per second into a homogeneous medium of hydrogen. The number density of hydrogen in the medium will be denoted by $n_{\rm H}$ and given in ${\rm cm}^{-3}$. Substitution of $\nu = \nu_{\rm HI}$, $\sigma = \sigma_{\rm HI}(\nu_{\rm HI})$ and $\tau = \tau_{\nu_{\rm HI}}$ into equation 2.41 leads to

$$\Gamma_{\rm HI}(r) \quad = \quad \frac{N_{\nu_{\rm HI}}\sigma}{4\pi r^2} e^{-\tau(r)}. \tag{2.43}$$

Following Strömgren (1939) we introduce the optical depth $y \equiv e^{-\tau}$ and find for equations 2.40 and 2.42

$$\frac{N_{\nu_{\rm HI}}\sigma}{4\pi r^2} y(1 - X) \quad = \quad \alpha_{\rm HII} n_{\rm H} X^2 \tag{2.44}$$

$$-{\rm d}\tau \quad = \quad -\frac{{\rm d}y}{y} = (1 - X) n_{\rm H} \sigma {\rm d}r. \tag{2.45}$$

We solve equation 2.45 for $(1 - X)$ and insert into equation 2.44.

$$\frac{N_{\nu_{\rm HI}}}{4\pi\alpha_{\rm HII} n_{\rm H}^2 r^2} {\rm d}y \quad = \quad -X^2 {\rm d}r \tag{2.46}$$

Referring to Strömgren (1939) we introduce the cubed distance $z \equiv \frac{r^3}{R_s^3}$ with the Strömgren volume $R_s^3 = \frac{3N_{\nu_{\rm HI}}}{4\pi\alpha_{\rm HII} n_{\rm H}^2}$ and equation 2.46 yields

$$\frac{dy}{dz} \quad = \quad -X^2. \tag{2.47}$$

Furthermore we can rewrite equation 2.40 by

$$\frac{1 - X}{X^2} \quad = \quad a\frac{z^{2/3}}{y} \quad \text{with} \quad a = \frac{3}{n_{\rm H}\sigma R_s} \tag{2.48}$$

$$\Rightarrow X \quad = \quad \frac{y}{2az^{2/3}} \left(\sqrt{1 + \frac{4az^{2/3}}{y}} - 1 \right). \tag{2.49}$$

Solving equations 2.47 and 2.48 we gain the radial distribution of the ionization fraction $X(r)$ and the photoionization rate $\Gamma_{\rm HI}(r)$. Figure 2.6 shows the different photoionization profiles for different

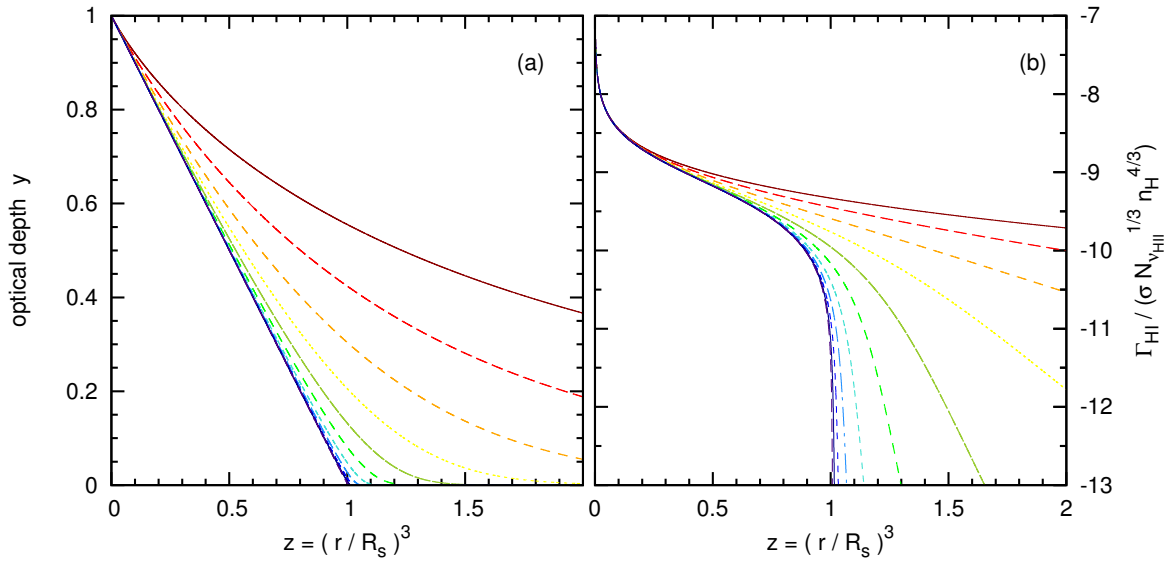

Figure 2.7: Profiles for different values of $a \propto (n_{\rm H} N_{\nu_{\rm HI}})^{-1/3}$ for $n_{\rm H} Q = 10^{41+i}$, $i = 0...10$ (red to blue). Left panel: Optical depth $y = e^{-\tau}$ versus $z = (r/R_s)^3$ Right panel: $\Gamma_{\rm HI}/(\sigma N_{\nu_{\rm HI}}^{1/3} n_{\rm H}^{4/3})$ versus $z = (r/R_s)^3$, showing the different profiles for different values of a.

ionizing photon rates $Q = N_{\nu_{\rm HI}}$, a density of $n_{\rm H} = 10^{-3}$ cm^{-3} and a temperature of $T = 10^4$ K. A change in the density causes a shift in the normalisation of the corresponding photoionization rate profiles, but not a change in their shape. In fact, based on the solutions for $n_{\rm H} = 10^{-3}$ cm^{-3} we can derive any solution for a different density. From equation 2.48 we can see that the shape of the ionization fraction X depends only on the parameter a, since y and z are dimensionless variables (see Figure 2.7). The dimensionless parameter a depends on the density, the number of ionizing photons and the temperature (when recombination rate is considered as temperature dependent).

$$a = \frac{3}{n_{\rm H}\sigma R_s} = \frac{3}{\sigma}\left(\frac{4\pi}{3}\right)^{1/3} (\alpha_{\rm HII})^{1/3} (n_{\rm H} N_{\nu_{\rm HI}})^{-1/3} \tag{2.50}$$

Since the photoionization rate is given by

$$\begin{aligned} \Gamma_{\rm HI} &= \sigma \frac{N_{\nu_{\rm HI}}}{4\pi r^2} y \\ &= \sigma \left(\frac{1}{36\pi}\right)^{1/3} (\alpha_{\rm HII})^{2/3} (N_{\nu_{\rm HI}})^{1/3} (n_{\rm H})^{4/3} y z^{-2/3} \end{aligned} \tag{2.51}$$

we can derive all possible solutions for different densities $n_{\rm H}$, recombination $\alpha_{\rm HII}$ or photon rate $N_{\nu_{\rm HI}}$ from the profile of the optical depth y. With help of this relation we can transform any photoionization rate $\Gamma_{\rm HI}(n_{{\rm H}i}, N_i)$ to any $\Gamma_{\rm HI}(n_{{\rm H}j}, N_j)$ as long as $a(n_{{\rm H}i}, N_i) = a(n_{{\rm H}j}, N_j)$.

$$\Gamma_{\rm HI}(n_{{\rm H}i}, N_i) = \Gamma_{\rm HI}(n_{{\rm H}j}, N_j) \left(\frac{\alpha_{{\rm HII}_i}}{\alpha_{{\rm HII}_j}}\right)^{2/3} \left(\frac{N_i}{N_j}\right)^{1/3} \left(\frac{n_{{\rm H}i}}{n_{{\rm H}j}}\right)^{4/3} \tag{2.52}$$

Consequently we can describe trends of the photoionization rate due to different densities or recombination rates by the number of ionizing photons $N_{\nu_{\rm HI}}$. We show those profiles of the photoionization rates for different number of ionizing photons in the right panel of Figure 2.6 assuming a density of $n_{\rm H} = 10^{-3}$ cm^{-3}. We note that with an increasing number of ionizing photons, the decrease in the photoionization rate at the Strömgren radius becomes steeper: for high $N_{\nu_{\rm HI}}$ the decrease is very steep and resembles a cutoff, while for small $N_{\nu_{\rm HI}}$ the decrease in the photoionization rate can become so shallow that a sphere larger than the Strömgren sphere is partly ionized. In the left panel of Figure

2.6 the solid black line indicates the relation between the photoionization rate and the ionized fraction of hydrogen in ionization equilibrium (see equation 2.40) for a density of $n_{\rm H} = 10^{-3}$ cm^{-3}. With help of this relation the photoionization rates in the right panel can directly be associated with the corresponding fraction of ionized hydrogen.

While the photoionization profile is fixed by the value of parameter a, its normalisation depends critically on the density $n_{\rm H}$. As can be seen from equation 2.40 the only other parameters that appear in the relation between $\Gamma_{\rm HI}$ and X are α_B and $n_{\rm H}$. As α_B varies marginally with temperature, the value of $n_{\rm HI}$ is the main driver. If the density is decreased by a factor of 10, the photoionization rate will also drop by a factor of 10, while the parameter a is reduced by a factor $10^{1/3}$. Thus the corresponding photoionization profile moves towards a more pronounced sphere, i.e. in the right panel in Figure 2.6 we move up (by a factor of $10^{1/3}$) to the next shown photoionization profile. By decreasing $n_{\rm H}$ and keeping $N_{\nu_{\rm HI}}$ constant, the parameter a has been changed. To obtain the initial value of a, $N_{\nu_{\rm HI}}$ needs to be lowered by a factor $10^{1/3}$, and we obtain the initial photoionization profile. In summary, decreasing the density shifts the curves shown in both panels of Figure 2.6 to lower photoionization rates due to equation 2.40, but does not change the relation between the photoionization profile and the photoionization rate-ionization fraction relation. For this reason we can use our example for $n_{\rm H} = 10^{-3}$ cm^{-3} to find characteristic photoionization rates as a function of the parameter a. As can be seen in Figure 2.6 the value of the ionization fraction X changes only insignificantly when the photoionization rate is decreased (increased) below (above) a certain photoionization rate $\Gamma_{\rm HI}$. Therefore we will introduce critical photoionization rates which refer to a very low ($x_{\rm c,lower}$) or high ($x_{\rm c,upper}$) ionization fraction

$$\begin{aligned} x_{c,upper} &= 0.99 \\ x_{c,lower} &= 0.01 \end{aligned} \tag{2.53}$$

and respectively

$$\begin{aligned} \Gamma_{\rm HI,c,upper} &= \alpha_{\rm HI} n_H \frac{x^2_{\rm c,upper}}{1 - x_{\rm c,upper}} \\ \Gamma_{\rm HI,c,lower} &= \alpha_{\rm HI} n_H \frac{x^2_{\rm c,lower}}{1 - x_{\rm c,lower}}. \end{aligned} \tag{2.54}$$

In order to determine the radius $z_c^{1/3}$ at which the critical photoionization rates $\Gamma_{\rm HI,c}$ occur, we

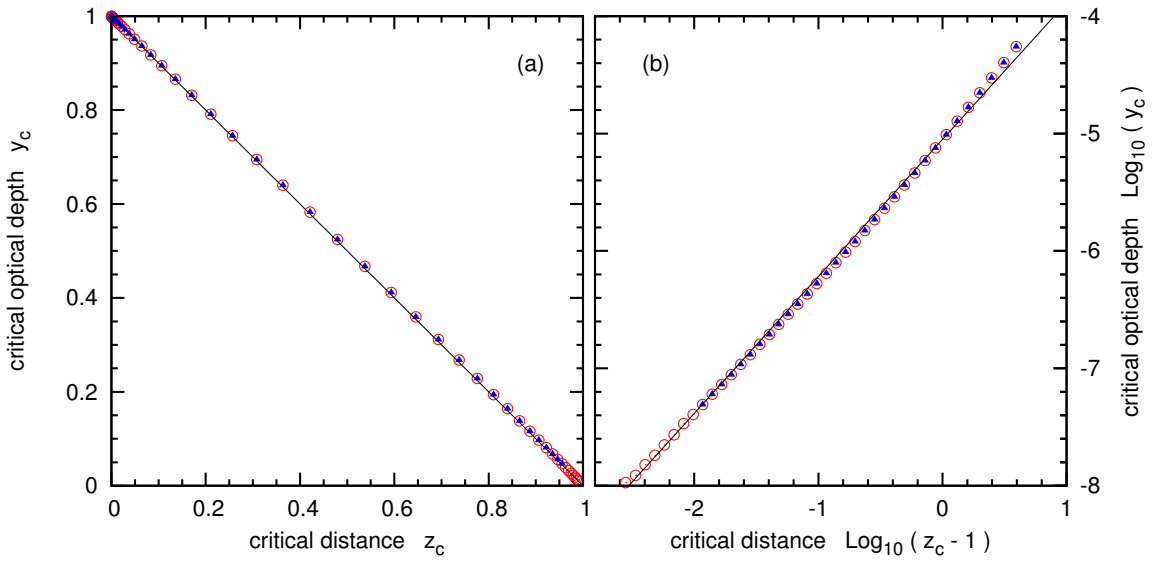

Figure 2.8: Computed points (critical optical depth y_c at critical distance z_c) for $n_{\rm H} = 10^{-3}$cm^{-3} (red circles) and $n_{\rm H} = 10^{-5}$cm^{-3} (blue triangles). y_c decreases with larger radius of the upper critical photoionization rate $\Gamma_{\rm HI,c,upper}(n_{\rm H})$ (left panel), while it increases with larger radius of the lower critical photoionization rate $\Gamma_{\rm HI,c,upper}(n_{\rm H})$ (right panel). The black lines show the fitting curves according to equations 2.56 and 2.57.

compute the radii of the critical photoionization rates for the profiles in Figure 2.6. Notice that in

Figure 2.6 the profiles are for different numbers of ionizing photons but the same density of $n_{\rm H} = 10^{-3}$ cm^{-3}. With help of equations 2.48 and 2.54 we obtain

$$\frac{\Gamma_{\rm HI,c}}{\alpha_{\rm HII} n_{\rm H}} = \frac{x_c^2}{1-x_c} = \frac{y_c}{a z_c^{2/3}} \tag{2.55}$$

and compute y_c at the radii z_c of the critical photoionization rates for different photoionization profiles, i.e. different values of $a(n_H, N_{\nu_{HI}})$. We plot y_c against z_c for the upper (left panel of Figure 2.8) and the lower case (right panel in Figure 2.8) and fit the relation with

$$y_c = 1 - z_c \tag{2.56}$$

for the former case and

$$y_c = 8.9 \cdot 10^{-6} (z_c - 1)^{7/6} \tag{2.57}$$

for the latter. Since each point refers to a different value of $a(n_H, N_{\nu_{HI}})$, the relations 2.56 and 2.57 hold for all densities and numbers of ionizing photons. To write z_c in terms of a and x_c we insert equation 2.48 and find the radius $z_c^{1/3}$ of the critical photoionization rate for the former

$$1 - z_c = z_c^{2/3} a \frac{x_c^2}{1-x_c} \tag{2.58}$$

and the latter case

$$8.9 \cdot 10^{-6} (z_c - 1)^{7/6} = z_c^{2/3} a \frac{x_c^2}{1-x_c}. \tag{2.59}$$

The resulting relations between the parameter $a(n_{\rm H}, N_{\nu_{\rm HI}})$ and the radius of the upper (left panel) and lower (right panel) critical photoionization rate are shown in Figure 2.9. As can be seen the radius

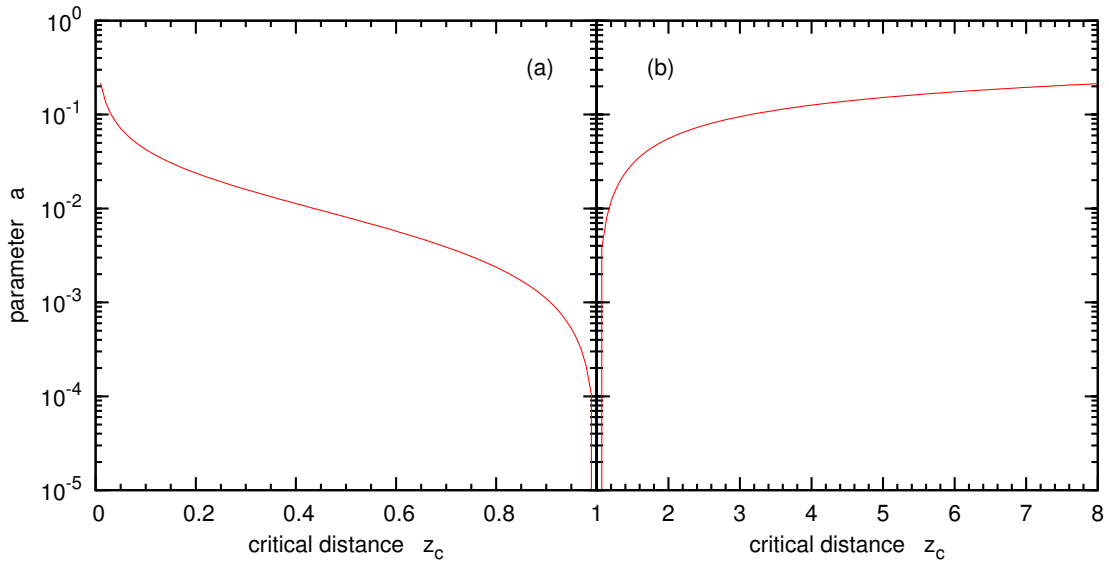

Figure 2.9: The profile of the photoionization rate depends solely on the parameter $a(n_{\rm H}, N_{\nu_{\rm HI}})$, hence the critical distance z_c where the photoionization rate causes an ionization fraction of 0.01 (lower) or 0.99 (upper) also depends on this parameter a. For the upper critical photoionization rate $\Gamma_{\rm HI,c,upper}(n_{\rm H})$ (left panel) the critical distance z_c increases with rising a as the photoionization profiles become more extended for higher values of a, while for the lower critical photoionization rate $\Gamma_{\rm HI,c,lower}(n_{\rm H})$ (right panel) z_c decreases with rising a as z_c is moved to larger distances due to the increased extension of the profiles.

of the lower critical photoionization rate exceeds the Strömgren radius for any value of parameter $a(n_{\rm H}, N_{\nu_{\rm HI}})$. For this reason our interest will be largely focused on the radius of the upper critical photoionization rate when studying two overlapping spheres. For any source where the density $n_{\rm H}$ and the number of ionizing photons $N_{\nu_{\rm HI}}$ are known, we can compute the parameter a and directly

determine the radius of the critical photoionization rate r_c from Figure 2.9. This critical radius r_c describes the distance from the source above which the ionization fraction changes dramatically with the photoionization rate. For instance, if $r_c/R_s > 0.9$, a parameter $a < 4 \times 10^{-3}$ which refers to $n_{\rm H} N_{\nu_{\rm HI}} > 2 \cdot 10^{48}$ cm^{-3} s^{-1} ($T = 10^4$ K) is required.

Photoionization rate of two spheres In this section we will consider two overlapping spheres. As has been seen in the previous section above the critical radius r_c the ionization fraction changes dramatically with the photoionization rate, while below the change is marginal. Nevertheless we note that although the ionization fraction changes only marginally, the neutral fraction is subject to considerable change. The marginal change in ionization fraction above r_c may become important when two overlapping spheres are considered.

In the following the photoionization rates of single spheres are indicated by Γ_s, and that of two overlapping merged spheres by Γ_m. If in the overlapping region the photoionization rates Γ_s of both spheres are above the critical photoionization rate, the photoionization rate Γ_m of two overlapping spheres is given by the sum of the photoionization rates Γ_s of the two single spheres. If, however, the photoionization rates of the single spheres Γ_s and their sum $\Gamma_{s_1} + \Gamma_{s_2}$ are below the critical photoionization rate, the true photoionization rate Γ_m is slightly higher than the sum of the photoionization rates of the single spheres $\Gamma_{s_1} + \Gamma_{s_2}$ and thus is underestimated. Equations 2.41 and 2.42 explain this trend. Adding the photoionization rates Γ_s of two single spheres to compute the photoionization rate of the overlapping spheres, the resulting ionization fraction will be higher in the regions of overlap. However, the photoionization rates Γ_s are computed from the ionization fractions of the single spheres. In the region of overlap the ionization fraction of a single sphere is smaller than the ionization fraction of the overlapping spheres. Hence, the sum of the photoionization rates of single spheres Γ_s will not equal the true photoionization rate Γ_m because of the underestimated ionization fractions in the region of overlap. In Figure 2.10 the photoionization rates of two spheres Γ_m with a low number of ionizing photons $Q = 10^{45}$ s^{-1} are shown in combination with the sum of the photoionization rates Γ_s of the single spheres. In the merging area where the photoionization rate lies below the critical photoionization rate the described effect can be seen. Decreasing the distance between the spheres, the photoionization rates exceeds the critical one and no difference in the true (Γ_m) and the combined photoionization rate ($\Gamma_{s_1} + \Gamma_{s_2}$) is seen (cf. Figure 2.10).

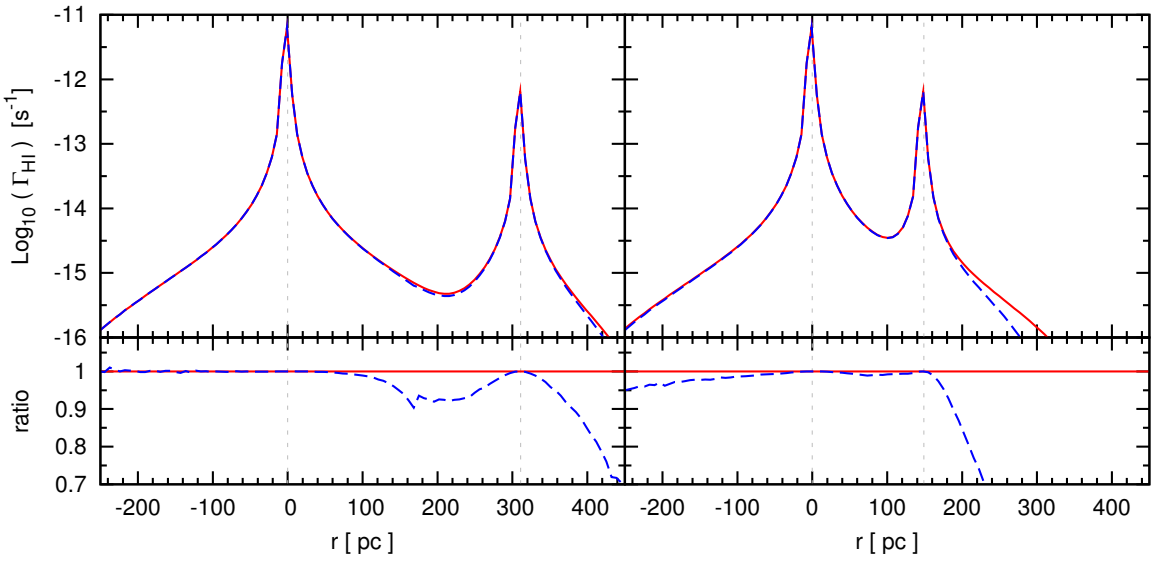

Figure 2.10: Photoionization rates of two merged spheres with $Q = 10^{45}$ s^{-1} and $Q = 10^{44}$ s^{-1}, $n_{\rm H} = 10^{-3}$ cm^{-3}, $T = 10^4$ K. The red line refers to the true photoionization rate Γ_m and the blue line shows the sum of the photoionization rates of the separated spheres Γ_s in a distance of $d = 311$ pc (left upper panel) and $d = 149$ pc (right upper panel). In the lower panels the ratio between Γ_m and Γ_s is shown. With increasing distance of the spheres the sum of the photoionization rates of the single spheres Γ_s deviate from the true photoionization rate Γ_m.

Because in reionization simulations the number of ionizing photons of the sources will exceed

10^{48} s^{-1} and the effect of underestimating the photoionization rate is comparatively small to the overall change of the photoionization rate, it is a good assumption to add up photoionization rates of single spheres to gain the photoionization rate of merged spheres.

2.2.4 Mapping model

In this section we describe our mapping-sphere-model where the ionization profiles of the sources are mapped as spheres on a grid. This model is based on the assumption that the photoionization rates of merged ionized spheres can be derived by adding photoionization rates of single spheres. As the total ionized volume of all single spheres needs to be maintained, each of the merged ionized spheres is enhanced according to the additional number of ionizing photons that are provided by the other sphere in the respective complex. Firstly, we describe our method of computing the ionized merged spheres from two single spheres and compare our results against the solution obtained by full 3D radiative transfer. Secondly, we elaborate on possibilities to extend this method towards three or more overlapping spheres and compare one approach to results of 3D radiative transfer.

Two overlapping spheres

Increasing the radii of the spheres We consider two overlapping Strömgren spheres. We start by imposing two assumptions: First the radii of the single ionized spheres are the Strömgren radii. Secondly, the ionized volume of two overlapping spheres is equal to the ionized volume of the separated spheres. This assumption is approximately justified by simulations, however, geometrical effects will cause some decrease in the ionized volumes of the merged spheres. Nevertheless simulations have shown that this decrease is less than 5% in ionized volume and we thus neglect this effect. We compute the overlapping volume ΔV numerically by integrating the ionization fraction over the whole volume for the separated and merged spheres.

$$\Delta V = \int \mathrm{d}V X_{HII}(\vec{r})|_{\text{separated spheres}} - \int \mathrm{d}V X_{HII}(\vec{r})|_{\text{overlapping spheres}} \tag{2.60}$$

In order to fulfil our second assumption we need to increase the ionized volumes of the two spheres by ΔV. So the overlapping volume ΔV needs to be redistributed to the two spheres

$$\Delta V = \Delta V_1 + \Delta V_2 \tag{2.61}$$

where ΔV_2 accounts for the additional volume of sphere 1 and ΔV_1 for the volume of sphere 2. Since the number of ionizing photons is proportional to the ionized volume, we can distribute the overlapping volume according to their luminosities L_1 and L_2. Hence, photons of sphere 2 will travel into sphere 1 and be responsible for the additional ionized volume and vice versa. Thus the additional ionized volume of sphere 1 is determined by the number of photons from sphere 2

$$\Delta V_2 = \frac{L_2}{L_1 + L_2} \Delta V \tag{2.62}$$

and the additional ionized volume of sphere 2 is given by

$$\Delta V_1 = \frac{L_1}{L_1 + L_2} \Delta V. \tag{2.63}$$

Sphere 1 needs to be increased by a volume ΔV_2 and thus the radius r_1 be stretched by a factor r_1'/r_1

$$\begin{aligned} V_1 + \Delta V_2 &= V_1' \\ \frac{4\pi}{3} r_1^3 + \Delta V_2 &= \frac{4\pi}{3} r_1'^3 \\ r_1'^3 - r_1^3 &= \frac{3}{4\pi} \Delta V_2 \\ \frac{r_1'}{r_1} &= \left(1 + \frac{3}{4\pi} \frac{\Delta V_2}{r_1^3}\right)^{1/3} = \left(1 + \frac{\Delta V_2}{V_1}\right)^{1/3}. \end{aligned} \tag{2.64}$$

and radius r_2 accordingly by

$$\frac{r_2'}{r_2} = \left(1 + \frac{\Delta V_1}{V_2}\right)^{1/3}. \tag{2.65}$$

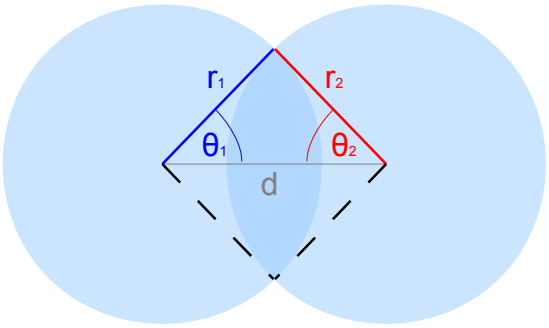

Figure 2.11: Sketch of two overlapping spheres with radii r_1 and r_2 which are separated by a distance d.

This calculation, however, does not take into account that a part of sphere 1 is overlapping with sphere 2 which is not accounted for when the sphere radius is increased. For this reason the solid angle Ω_1 of the surface area determining the amount of sphere 1 which is overlapping with sphere 2 needs to be known. We thus introduce a fraction of the solid angle corresponding to the overlapping surface area $k_1 = \frac{\Omega_1}{4\pi} = 1 + \cos\theta_1$ and reformulate equation 2.64

$$\begin{aligned} V_1 + \Delta V_2 &= V_1'(1-k_1) + k_1 V_1 \\ \Delta V_2 &= (1-k_1)(V_1' - V_1) = \frac{1}{2}(1+\cos\theta_1)(V_1' - V_1) = \frac{2\pi}{3}(1+\cos\theta_1)(r_1'^3 - r_1^3) \\ \frac{r_1'}{r_1} &= \left(\frac{2\Delta V_2}{1+\cos\theta_1}\frac{1}{\frac{4\pi}{3}r_1^3} + 1\right)^{1/3} = \left(\frac{2}{1+\cos\theta_1}\frac{\Delta V_2}{V_1} + 1\right)^{1/3} \end{aligned} \tag{2.66}$$

and equation 2.65 accordingly

$$\frac{r_2'}{r_2} = \left(\frac{2}{1+\cos\theta_2}\frac{\Delta V_1}{V_2} + 1\right)^{1/3}. \tag{2.67}$$

Computing the solid angle According to Figure 2.11 the solid angles $1+\cos\theta_1$ and $1+\cos\theta_2$ can be determined by considering the intersection line of the two spheres with radii r_1 and r_2 and a distance d. Using the law of cosine we find

$$\cos\theta_1 = \frac{r_1^2 - r_2^2 + d^2}{2r_1 d} \tag{2.68}$$

$$\cos\theta_2 = \frac{r_2^2 - r_1^2 + d^2}{2r_2 d} \tag{2.69}$$

But since these angles are derived from the spheres before being enhanced, they are too small and accordingly the stretch factor of the radius is also underestimated. To overcome this problem we compute the new radii (equations 2.66 and 2.67) from the computed intersection angles (equation 2.68 and 2.69), and from these new radii we derive new intersection angles. We repeat this computation until an equilibrium state is reached.

Computation of the ionization profile

1. Extract photoionization profile for each source
2. Determine the radius r_{min} for each source where r_{min} represents the distance between the source position and the minimum of the total photoionization rate along the line between both sources. If d represents the distance between the sources we consider two cases:
   (a) if $r_{min} \geq R_s$: map the single source photoionization rates Γ_s and add them

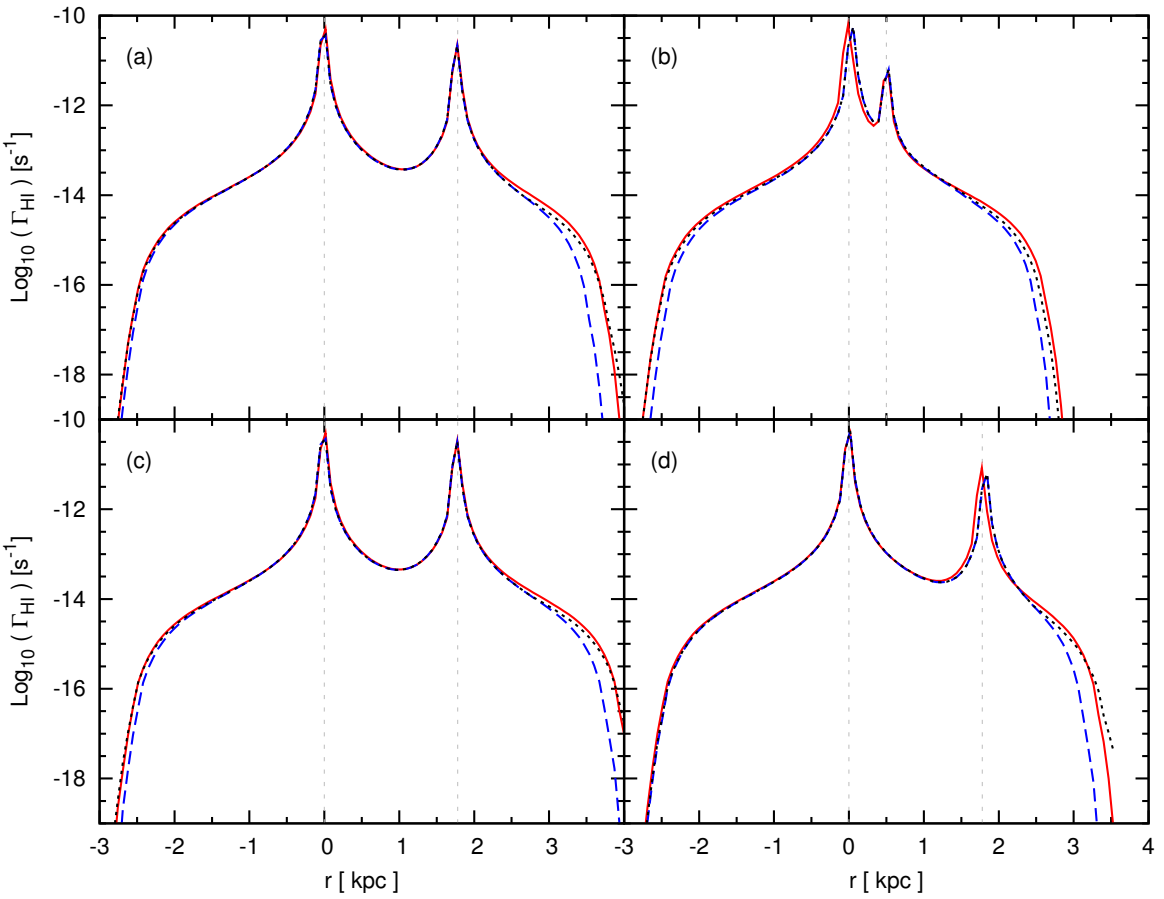

Figure 2.12: Photoionization rates of two melted spheres with various combinations of Q and distances d for $n_{\rm H} = 10^{-3}$ cm^{-3}, $T = 10^4$ K. The solid red line refers to the true photoionization rate, the blue dashed line shows the sum of the photoionization rates of the separated spheres and the black dotted line the sum of the photoionization rate of the single spheres after resizing. (a) $Q_1 = 10^{48}$ s^{-1}, $Q_2 = 0.33 \cdot 10^{48}$ s^{-1}, $d = 1.78$ kpc, (c) $Q_1 = 10^{48}$ s^{-1}, $Q_2 = 0.5 \cdot 10^{48}$ s^{-1}, $d = 1.78$ kpc , (d) $Q_1 = 10^{48}$ s^{-1}, $Q_2 = 0.125 \cdot 10^{48}$ s^{-1}, $d = 1.78$ kpc , (b) $Q_1 = 10^{48}$ s^{-1}, $Q_2 = 0.125 \cdot 10^{48}$ s^{-1}, $d = 0.50$ kpc. Q_1 refers to the source on the left and Q_2 on the right. The distance r is measured in respect to the position of source 1. Blue lines diverge from the red lines, especially at larger distances but after resizing the true photoionization rate (red) is accurately recovered (black line).

(b) if $r_{min} < d < R_s$: stretch the radius by a factor f and map single source photoionization rates. The factor is logarithmical interpolated between $f = 1$ at $r = r_{min}$ and a precomputed final factor f at $r = R_s$ (see equations 2.66 and 2.67).

3. Convert photoionization rate Γ to $X_{\rm HII}$ by

$$X_{\rm HII} = \frac{\Gamma_{\rm HI}}{2\alpha_{\rm HII} n_{\rm H} \left(\sqrt{1 + \frac{4\alpha_{\rm HII} n_{\rm H}}{\Gamma_{\rm HI}}} - 1 \right)} \tag{2.70}$$

Comparison to 3D radiative transfer For a number of combination of sphere sizes and distances we compare our mapping sphere model with the solution obtained by full 3D radiative transfer. To perform the full 3D radiative transfer we use the Monte Carlo ray tracing scheme pCRASH (Ciardi et al., 2001; Maselli et al., 2003, 2009; Partl et al., 2011) which is described more detailed in Section 2.3.

In Fig. 2.12 we show the photoionization rates along the axis that connects both source locations. We note that in the following we will refer to the photoionization rate of the merged spheres obtained by 3D radiative transfer calculations as the "true photoionization rate"; however, the 3D radiative transfer calculation might also suffer from inaccuracies but provide the best available solution. For

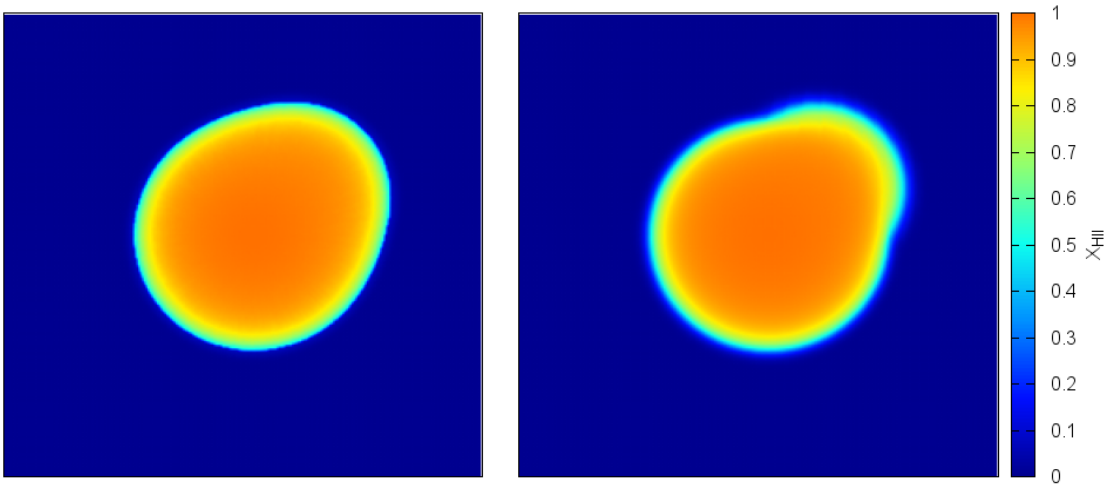

Figure 2.13: Slice through the center of a 10 kpc box containing two sources of $Q = 10^{48}$ erg s^{-1} and $Q = 0.5 \cdot 10^{48}$ erg s^{-1} that are located on space diagonal and have a distance of 1.78 kpc. In the left panel we show the ionized regions obtained from the full 3D radiative transfer. The right panel depicts the resulting map of ionization fraction for our model of obtaining the merged ionized spheres from two single spheres.

each combination of sources we show the true photoionization rate for the two merged spheres Γ_m (red solid line), the addition of the photoionization rates of the two single spheres Γ_s (blue dashed line) and the photoionization rate of the two single spheres after resizing $\Gamma_{s,r}$ (black dotted line).

While Γ_s deviates from Γ_m at larger distances from the source locations, we find that $\Gamma_{s,r}$ is in agreement with Γ_m after the spheres have been resized such that the total ionized volume of the merged spheres corresponds to that of the single separated spheres. Nevertheless we notice that at the edges of the ionized sphere of the fainter source Γ_m deviates slightly from $\Gamma_{r,s}$. Since the merging of the spheres causes an increase in the photon number in the ionized sphere of the fainter source, the sphere is enhanced such that the ionized volume of the merged spheres corresponds to the total one of the two single spheres. In the case of the fainter source the photoionization profile is more stretched than the profile of the brighter source when we apply our method. The larger the difference in the luminosities of both sources, the more the profile of the fainter source is stretched, leading to an increasing deviation between Γ_m and $\Gamma_{r,s}$. We may note these small deviations in the photoionization rates also in the ionization fronts of the fainter source. The corresponding ionization fields ($X_{\mathrm{HII}}^{(m)}$ and $X_{\mathrm{HII}}^{(s,r)}$) of Fig. 2.12c are shown in Fig. 2.13. While the highly ionized regions ($X_{\mathrm{HII}} > 0.8$) of $X_{\mathrm{HII}}^{(m)}$ (left panel) and $X_{\mathrm{HII}}^{(s,r)}$ (right panel) agree well, we note that the ionization front of the fainter source is more extended for $X_{\mathrm{HII}}^{(s,r)}$ than for the true solution $X_{\mathrm{HII}}^{(m)}$. In addition to the inaccuracies of the photoionization at these fronts the deviation also might be enhanced by the fact that the ionization fronts are not necessarily in ionization equilibrium and thus the conversion from photoionization rate to ionization fraction becomes inaccurate. However, apart from small deviations at the ionization fronts the ionization field of merged spheres are sufficiently described by our mapping scheme. The main advantage of this method is the computation of the ionization field without using computationally more expensive 3D radiative transfer calculations.

Three or more overlapping spheres

Since we will encounter more than two overlapping ionized spheres in cosmological scenarios, we address the question of how to distribute the ionizing photons of one sphere to its overlapping spheres. We will present two possible approaches and discuss their feasibility.

First approach In a first approach we aim to treat the problem of ionizing photon distribution accurately. Thus to distribute the ionizing photons of each sphere accurately to its neighbouring

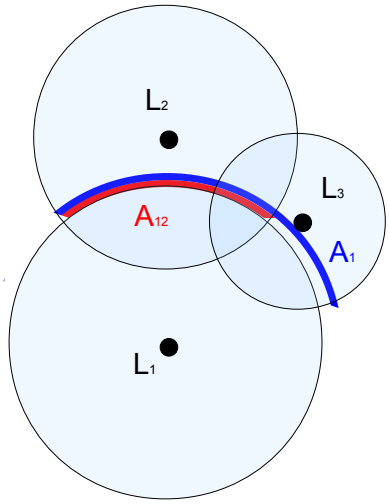

Figure 2.14: Sketch of three overlapping spheres and the surface areas A_{12} and A_1

overlapping spheres we need to compute the complete overlapping volume of the group of overlapping spheres. This can be done numerically by mapping the unresized spheres and computing their volume in addition to the sum of the volume of all separated spheres. Calculating the difference between those two volumes we derive the volume of overlap which needs to be redistributed to the spheres. The surface area A_i which is included in the overlapping spheres and the fractions A_{ij}/A_i each overlapping sphere has part in A_i are computed. Consider a sphere i of N overlapping spheres. First of all we have to find the neighbouring overlapping spheres j of sphere i. If we have determined the neighbours, we can estimate the surface area A_{ij} that sphere i has in each sphere j (see Figure 2.14). The overall overlapping volume of sphere i is thus given by

$$A_i \quad = \quad \sum_{j \neq i} A_{ij}. \tag{2.71}$$

To estimate A_{ij} for all j, sphere i is divided into surface area elements Ω_k. For each surface area element Ω_k we determine the spheres j that include the considered surface area element Ω_k of sphere i. If the surface area element Ω_k of sphere i is part of sphere j, the element A_{ij} is increased by this surface area element. If a surface area element is part of several neighbouring spheres j, the contribution by the surface area element has to be distributed. So all involved A_{ij} for $j \in$ *neighbouring overlapping spheres* are increased by surface area elements divided by the number of neighbouring overlapping spheres. The last step is to distribute the overlapping volume to each sphere i with luminosity L_i of the N spheres. If ΔV is the overlapping volume, sphere i needs to be increased by

$$x_i \, \Delta V \quad = \quad \Delta V \frac{\sum_{j \neq i} L_{ji}}{\sum_j L_j} \quad \text{with} \quad L_{ji} = \frac{A_{ji}}{A_j}. \tag{2.72}$$

So the radius r_i of sphere i is enhanced by a factor of

$$\frac{r_i'}{r_i} \quad = \quad \left(1 + \frac{1}{1 - \frac{A_i}{4\pi}} \frac{x_i \Delta V}{V_i} \right)^{1/3}. \tag{2.73}$$

Although we are able to compute the enhancing factors for each sphere theoretically, the problem of computing the overlapping volumes becomes complex and not easily solvable. For this reason we have

developed an approximate method which we will describe in the next paragraph. We note that both schemes are subject to that photons propagate only to the next neighbour sphere but not the next but one.

Second approach In our second approach we pursue an approximate approach and apply our model for two overlapping spheres to each combination of two spheres and enhance the spheres respectively. Following the comparisons between the ionization fields of the 3D radiative transfer and our mapping-spheres-scheme for two overlapping ionized spheres, we perform similar comparisons for three overlapping spheres. We compute different cases for three sources in a row (see panels (a)-(c) in Figure 2.15) and arranged in a triangle (see panels (d)-(l) Figures 2.15). From these test cases we find that our approximate approach works accurately as Γ_m and $\Gamma_{s,r}$ agree sufficiently. As this scheme seems to work at least for three overlapping spheres we generalise it and apply it to any number of overlapping spheres. Each combination of two spheres is considered and enhanced according to the respective volume of overlap. As soon as the sizes of a pair of spheres are updated, these updated sizes are used when we account for the overlap with other spheres.

2.2.5 Mapping sphere scheme for a cosmological volume

In the previous section we have developed an approximate scheme for mapping two or three overlapping ionized spheres using 1D radiative transfer. Using this model we extend the mapping Strömgren sphere scheme developed by Adrian Partl (private communication) by accounting for overlapping spheres. Furthermore the existing scheme is extended by computing the ionization profiles of all sources based on the spherically averaged, underlying density and temperature fields and 1D radiative transfer calculations. With help of this method, we are able to derive the ionization fields of a cosmological density field with sources in the collapsed regions. In this section we firstly describe this method and secondly apply it to a cosmological density field and compare the results to those from a full 3D radiative transfer calculation.

Method

In this section we describe the method to derive the ionization fields from a cosmological simulation that provides density, temperature distributions and source locations and spectra. As the scheme will scale with the number of sources, since for each source the ionization profile needs to be computed, we parallelize the code using message passing interface (MPI). To obtain the final ionization field, i.e. the mapped ionized spheres on a grid, we perform the following steps:

1. The approximate scheme for mapping two overlapping spheres using 1D radiative transfer has assumed a homogeneous distribution of density and temperature. In a cosmological simulation halos, filaments and voids form leading to very inhomogeneous density and temperature distributions. Nevertheless to compute the ionization profiles for each source in the simulation we need a radial density and initial temperature profile. For each source we find the average density and temperature profile by averaging over the profiles along a number of lines of sight. In the parallelized version the simulation box is divided in subboxes whereas each subbox is assigned to a processor. In a first step the "rays" (representing the directions of the lines of sight) are propagated until they reach the edge of their subbox. In a second step the rays are communicated to the next domain respective to their direction of propagation. If a ray encounters the edge of the box, it is communicated to the opposite side of the box, i.e. we assume periodic boundaries. Step 1 and 2 are repeated until each ray has propagated a full box length.

2. The obtained density and temperature profiles are communicated to all processors. Sources are equally distributed to processors and for each source the ionization (H II, He II, He III), temperature and photoionization profiles are computed using the 1D radiative transfer described in Section 2.2.2. When the profiles (ionization, temperature, photoionization) have been calculated they are again communicated to all processors.

3. From the position of the sources and the size of their ionized spheres, groups of overlapping sources are determined. Within each group we resize the spheres according to our mapping-sphere-model (see Section 2.2.4). This is done on each processor for all sources.

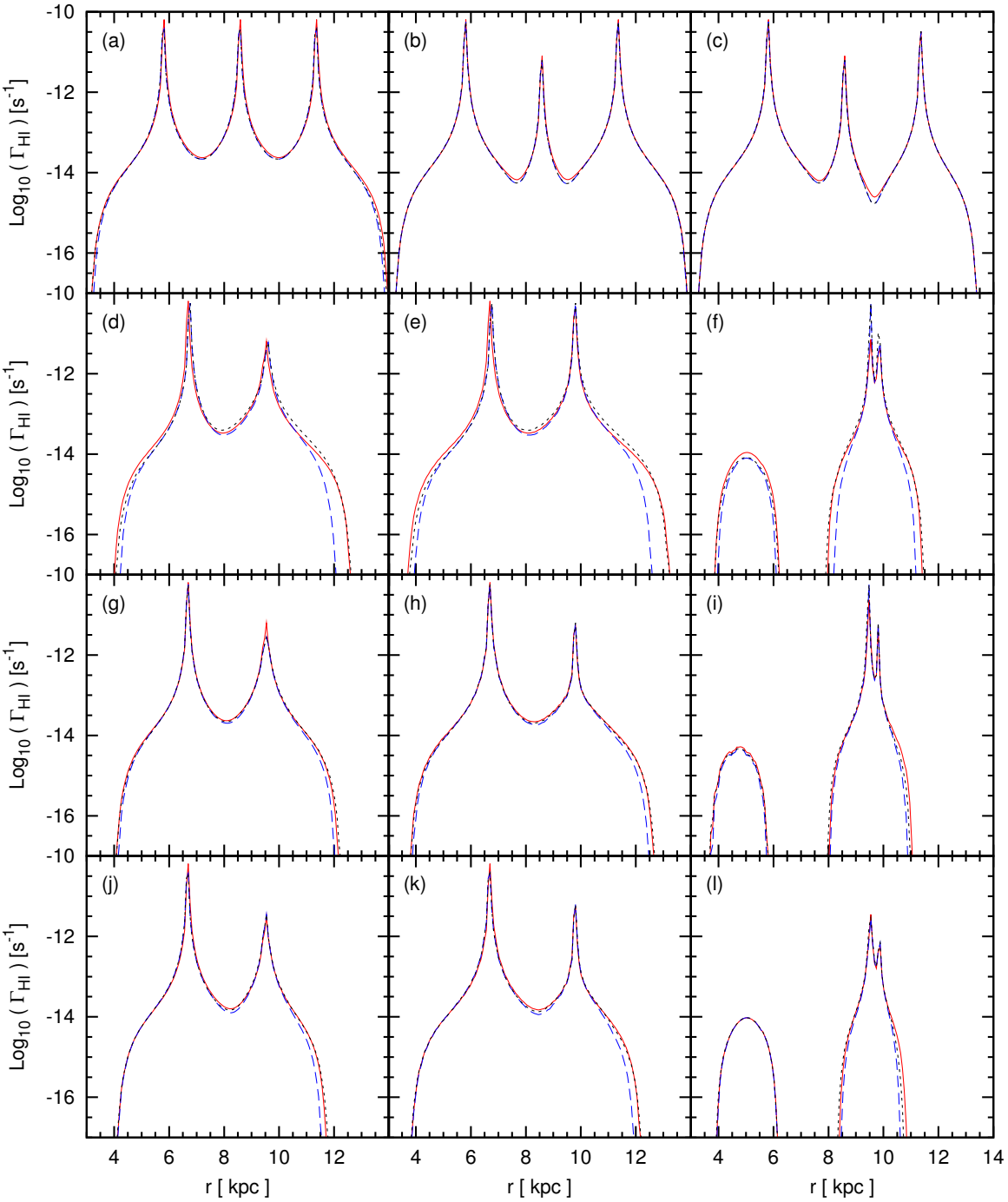

Figure 2.15: Photoionization rates of two melted spheres with various combinations of Q and distances d for $n_{\rm H} = 10^{-3}$ cm^{-3}, $T = 10^4$ K. The solid red line refers to the true photoionization rate, the blue dashed line shows the sum of the photoionization rates of the separated spheres and the black dotted line the sum of the photoionization rate of the single spheres after resizing. (a) $Q_{1,2,3} = 10^{48}$ s^{-1} in a row, $d_{12} = 2.76$ kpc, $d_{23} = 2.76$ kpc, $d_{13} = 5.52$ kpc; (b) $Q_{1,3} = 10^{48}$ s^{-1}, $Q_2 = 0.125 \cdot 10^{48}$ s^{-1} in a row, $d_{12} = 2.76$ kpc, $d_{23} = 2.76$ kpc,$d_{13} = 5.52$ kpc; (c) $Q_1 = 10^{48}$ s^{-1}, $Q_2 = 0.125 \cdot 10^{48}$ s^{-1}, $Q_3 = 0.5 \cdot 10^{48}$ s^{-1} in a row, $d_{12} = 2.76$ kpc, $d_{23} = 2.76$ kpc, $d_{13} = 5.52$ kpc; (d-f) $Q_{1,2,3} = 10^{48}$ s^{-1} in a triangle, $d_{12} = 2.76$ kpc, $d_{23} = 0.51$ kpc, $d_{13} = 2.76$ kpc, along the sightline of source 1 and 2 (d), 1 and 3 (e), 2 and 3 (f); (g-i) $Q_{1,2} = 10^{48}$ s^{-1}, $Q_3 = 0.125 \cdot 10^{48}$ s^{-1}, in a triangle, $d_{12} = 2.76$ kpc, $d_{23} = 0.51$ kpc, $d_{13} = 2.76$ kpc, along the sightline of source 1 and 2 (g), 1 and 3 (h), 2 and 3 (i); (j-l) $Q_1 = 10^{48}$ s^{-1}, $Q_2 = 0.5 \cdot 10^{48}$ s^{-1}, $Q_3 = 0.125 \cdot 10^{48}$ s^{-1}, in a triangle, $d_{12} = 2.76$ kpc, $d_{23} = 0.51$ kpc, $d_{13} = 2.76$ kpc, along the sightline of source 1 and 2 (j), 1 and 3 (k), 2 and 3 (l).

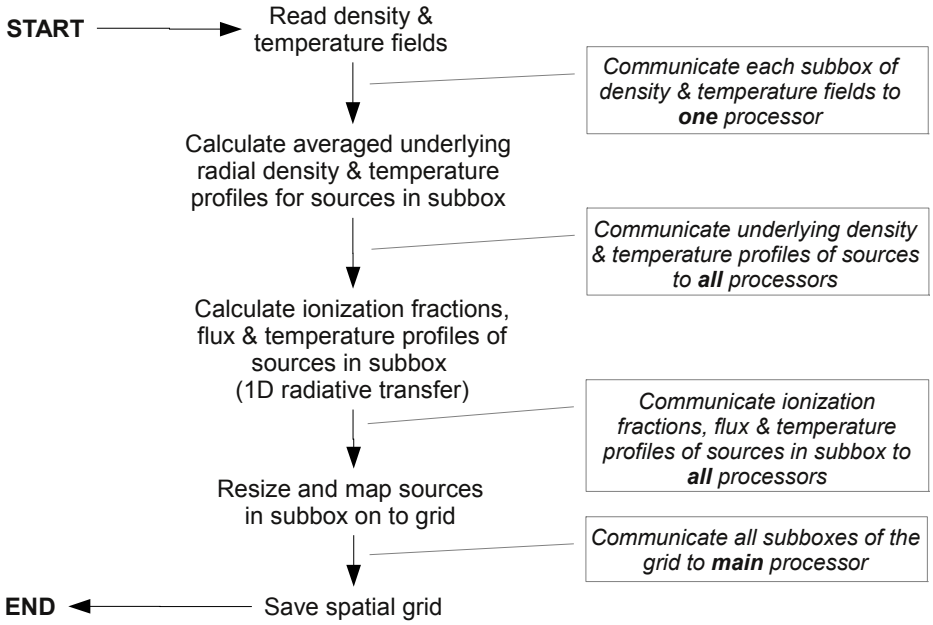

Figure 2.16: Scheme of the parallelized mapping algorithm

4. As each processor stores the final profiles of all sources but only the spatial data of a subbox, it maps each sphere on a grid that is fully or partly in its domain. The subboxes of the ionization, temperature and photoionization fields are communicated to a main processor which produces the output files.

Multiple sources in a cosmological volume

With help of the previous described algorithm we compute the ionization field at an early stage of reionization. We use the density and temperature fields of a hydrodynamical simulation at $z = 8.3$. The cosmological model adopts a ΛCDM model with $\Omega_\Lambda = 0.73$, $\Omega_m = 0.27$, $\Omega_b = 0.047$, $H_0 = 70$ km s^{-1}Mpc^{-1} and $\sigma_8 = 0.82$. The simulation box has a length of 80 Mpc/h and contains dark matter and gas particles and uses the star formation prescription by Springel and Hernquist (2003). For details about the simulation and the identification of halos and sources we refer the reader to Section 3.2 in Chapter 3. The snapshot at $z = 8.3$ contains 7940 sources which show halo masses of at least $10^9\,\mathrm{M}_\odot$/h and a circular velocities $v_{circ} > 60$ km/s. For each identified source we build the spectrum of each halo by summing up the spectra of its star particles, and applying an escape fraction of 0.14, as some papers estimate the escape fraction to be between 10% and 30% (Mitra et al., 2013; Kimm and Cen, 2014). The ionization fronts are propagated for about 100 Myr. The resultant ionization field produced by our mapping sphere scheme is shown in the right panel of Fig. 2.13. For comparison we have performed a full 3D radiative transfer run computing the evolving ionization fields until $z \simeq 7.4$ (see left panel in Fig. 2.13). From Fig. 2.13 we note that the positions and sizes of the ionized regions agree well. Nevertheless, the ionized regions of the mapping sphere scheme are more extended than those computed by the 3D radiative transfer. The reason lies in the averaging of the temperature, density and clumping factor along many lines of sights; high density regions are averaged out. Since the radius of the spheres depends on $n_H^{-2/3}$, underestimating the hydrogen density n_H leads to larger spheres. Due to the extended ionized regions the global ionization fraction is higher for the mapping sphere scheme than for the full 3D radiative transfer. This is also seen in the respective power spectra of the ionized density fluctuations in the right panel of Fig. 2.18; the power spectrum of the mapping sphere scheme shows more power and is shifted slightly more towards larger scales than the power spectrum of the full 3D radiative transfer. As expected we see the opposite trend for the neutral regions: less power on small scales for the mapping sphere scheme. Nevertheless, the

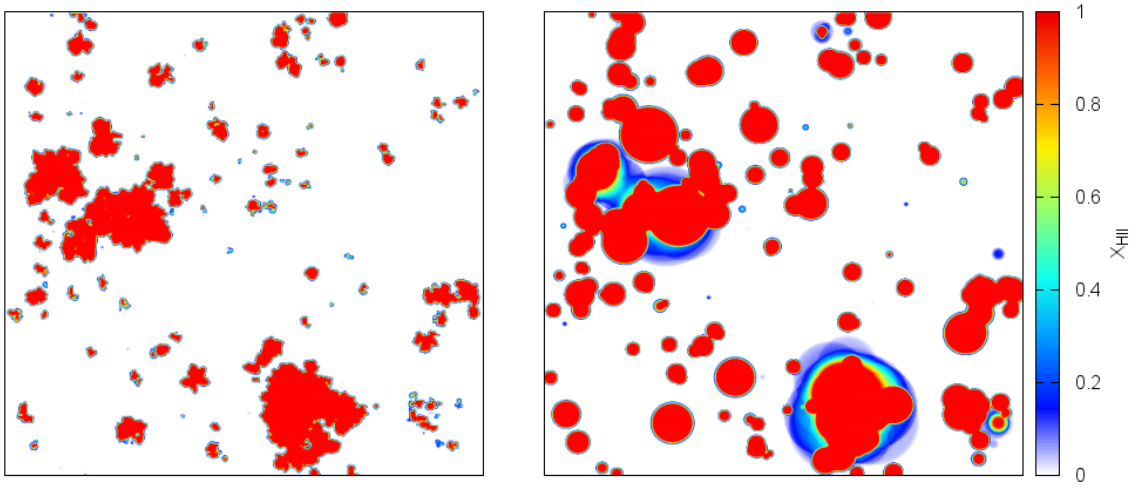

Figure 2.17: Slice of a 80 Mpc/h simulation box with 7000 sources. In the left panel the solution of the ionization field is shown for full 3D radiative transfer (pCRASH) and in the right panel for our mapping sphere scheme exploiting 1D radiative transfer. Ionized regions are larger for the mapping sphere scheme as averaging of the density profiles reduces the high density regions.

shapes of the power spectra agree and thus the distribution of the sizes of the ionized bubbles is well reflected in the mapping sphere scheme and reproduces the locations of the ionized regions.

2.3 pCRASH: a 3D radiative transfer scheme

2.3.1 Method

In this section we briefly describe the radiative transfer code pCRASH (Ciardi et al., 2001; Maselli et al., 2003, 2009; Partl et al., 2011), further details are described in Appendix A. pCRASH employs a Monte-Carlo long characteristic continuum radiative transfer scheme which uses a ray-tracing technique on a 3D grid. For a given distribution of point sources, background radiation and subsequent diffusive radiation the code follows the IGM properties solving for the time evolution of the ionization fractions ($X_{\rm HII}$, $X_{\rm HeII}$, $X_{\rm HeIII}$) and temperature (T). The matter-radiation interactions (photoionization, collisional ionization and recombination) determine the ionization fractions, while the temperature is governed by the following heating/cooling mechanisms: photoionization heating, collisional ionization cooling, recombination cooling, collisional excitation cooling, bremsstrahlung cooling, Compton cooling, adiabatic cooling. Effects like spectral filtering, shadowing and self-shielding are naturally captured by the algorithm.

Radiation is treated in pCRASH by the use of photon packets. Each source is considered as a point source with a luminosity L_s and a spectral shape $L_s(\nu_j)$. The total energy emitted the source during the simulation, E_s, is distributed into N_p photon packets, whereas the energy of each photon packet is distributed according to the respective spectral shape. Each photon packet is assigned a propagation direction (r, θ, ϕ) according to the angular emission probability distribution of the source. Starting at the cell where the source is located the photon packet is propagated along the designated direction ($x = x_E + r\sin\theta\cos\phi$, $y = y_E + r\sin\theta\sin\phi$, $z = z_E + \cos\theta$). For each cell the photon packet passes through (1) the optical depth is calculated by summing up the contribution from the different species (H I, He I, He II); (2) the number of absorbed photons in each frequency bin ν_j is determined; (3) the absorbed photons are distributed to the different species proportional to their absorption probability and the corresponding ionization fractions are increased. If the number of ionization events exceeds the number of non-ionized atoms in the cell, the remaining photons stay in the photon packet and are propagated to the next cell. In the next step the time evolution of the ionization fractions and the temperature of the cell are computed by the coupled rate equations which includes the aforementioned matter-radiation interaction and heating and cooling mechanisms. While

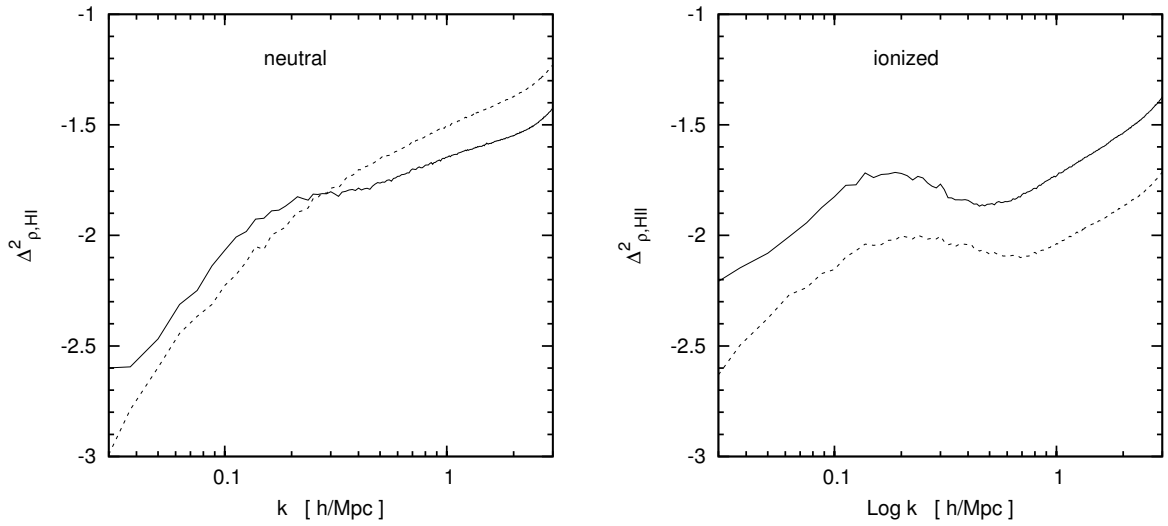

Figure 2.18: Power spectra for the neutral (left) and ionized (right) regions. Solid lines refer to the power spectra of our mapping sphere scheme, while dashed lines show the power spectra of the regions obtained with full 3D radiative transfer (pCRASH).

collisional ionization, recombination and the cooling mechanisms are treated as continuous processes, photoionization and photoheating are discrete processes in this scheme due to the discretization of the radiation field into photon packets. After the physical quantities of the cell are updated, the photon packet is propagated to the next cell. Rays are propagated instantly which is a reasonable assumption since the velocity of ionization fronts is significantly below the speed of light.

pCRASH includes different types of radiation sources: Firstly point sources including their luminosities, spectral shapes and positions can be chosen arbitrarily; secondly recombination radiation is included: if the number of recombinations in a cell exceeds a threshold, a recombination photon packet is emitted, whereas its isotropic spectral emissivity is represented by the emissivity of an arbitrary recombining atom (Mihalas, 1978; Osterbrock, 1989).

Due to the usage of a Monte-Carlo method pCRASH is subject to several numerical requirements. To ensure an accurate sampling of the frequency and time distributions each cell needs to be updated a sufficient number of times which scales with the total number of photon packets (N_p) and the gridsize ($\propto N_p/N_c^2$). Since collisional ionization and cooling mechanisms are treated as continuous processes, the time step for updating these quantities must be smaller than the time scales of those processes.

Parallelization & Run

In order to perform cosmological radiative transfer simulations a sufficient resolution in space and an accurate sampling of time and frequency are needed. Since the resolution scales directly with the number of photon packets each source emits, the code needs to process a large number of packets in a reasonable time; thus pCRASH (Partl et al., 2011) provides the parallelised version of CRASH2 (Ciardi et al., 2001; Maselli et al., 2003, 2009) using the Message Passing Interface (MPI). A detailed description of the parallelisation strategy can be found in Partl et al. (2011); here a summary is given.

The simulation box is spatially divided between the processors; each processor computes the propagation of the rays within its domain. To ensure similar work load of all processors domains are allocated depending on the overall ray density: in a first step the code calculates the ray density induced by each source according to $\propto r^{-2}$ and maps the latter on a grid; with help of a Hilbert curve the domains are distributed in such a way that the ray density in each domain is the same. Using this partitioning each processor calculates the propagation of all rays and corresponding updates of the respective cells in its domain. To enable ray propagation through the entire simulation box rays are propagated until the edges of the domain in one timestep and communicated to the corresponding next domain in the following timestep. This handling of communication ensures that processors do not end up in considerable idle time waiting for communication and the code is not heavily decelerated by communication between the processors. At given times the ionization and temperature fields are send to the main processor and written to files. With each output the code also writes checkfiles, thus

the simulation can be continued from this point at a later time. Nevertheless in the version described in Partl et al. (2011) a change of underlying fields, e.q. density or temperature, or sources is not included.

2.3.2 Updates

In order to perform realistic reionization simulations we have made necessary changes to pCRASH which we list in the following.

Spectra of sources

The original version of pCRASH described in Partl et al. (2011) allowed the assignment of a different luminosity to each source but only for one arbitrary chosen spectral shape for all sources. In our updated version an arbitrarily number of spectra is read into a list of spectra. Each source is assigned a luminosity, a spectrum and an escape fraction of ionizing photons. This enables us to perform self-consistent reionization simulations where we can exploit the full information on star formation in a hydrodynamical simulation by modelling each galaxy with a spectrum according to its stellar mass, metallicity and age. In simulations we have dealt with a list of 31000 spectra.

Clumping factor

Since pCRASH is a regular grid-based code, distinct and dense structures on smaller scales than the cell size are not resolved. In such dense regions the density in the cell is underestimated and with it the number of recombinations, ionization fronts expand faster. Since the recombination rate per volume is proportional to $\langle {n_{\rm HII}}^2 \rangle$ and not to $\langle n_{\rm HII} \rangle^2$, the respective derived recombination rate values differ considerably in clumped regions, where we expect an enhanced number of recombinations. The true number of recombinations is given by

$$\dot{N}_{rec} \;=\; \alpha \int_V {n_{\rm HII}}^2(\vec{x})\ \mathrm{d}^3x \;=\; \alpha\ C\ \langle n_{\rm HII} \rangle^2. \tag{2.74}$$

Thus to account for this enhanced number of recombinations we make use of the "clumping factor"

$$C \;\equiv\; \frac{\int n^2(\vec{x})\ \mathrm{d}^3x}{\left(\int n(\vec{x})\ \mathrm{d}^3x\right)^2} V. \tag{2.75}$$

We compute a clumping factor for each cell, a so-called local clumping factor (Raičević and Theuns, 2011), whereas we use the information of the particles in the hydrodynamical simulation from which the density field was drawn from. Following Raičević and Theuns (2011) the number density is yielded by $n = Y \varrho_g / m_p$ where ϱ_g is the gas density, m_p the proton mass and Y the respective abundance of the chosen element. Assigning a volume $V_i \approx m_i / \varrho_i$ the mean clumping factor in a volume V can be computed as

$$C \;=\; \frac{1}{N_{part}^2} \sum_i^{N_{part}} n_i \sum_j^{N_{part}} \frac{1}{n_j},\ \text{for}\ n_{i,j} \leq n_{thr} \tag{2.76}$$

where N_{part} is the number of particles in volume V and n_i the gas density at the location of particle i. Equation 2.76 assumes same mass for all particles. A complete derivation is found in the Appendix A.2. We also adopt the number density threshold in Raičević and Theuns (2011) and consider only particles below a threshold number density of $n_{thr} = \Delta_{thr} \langle n \rangle$ with $\Delta_{thr} = 100$ to exclude collapsed halos from the IGM density field. However, the masses of gas particles in GADGET simulations including a prescription for star formation are not constant as gas particles are gradually turned into star particles reducing their mass and time. These gas particles will mostly reside in halos where star formation takes place and only a negligible fraction is transported to the intergalactic medium by winds. Since the number density thresholds excludes halos, only a small fraction of gas particles will deviate from the mean particle mass and its effect on the local clumping factor will be negligible. Furthermore we derive the clumping factor from the full gas density. Since we assume an overall ratio

of hydrogen and helium as well of neutral and ionized in each cell (each particle in the cell has the same ratio), the resulting clumping factors for H II, He II and He III are the same.

$$\begin{aligned} C &= \frac{1}{N_{part}^2} \sum_i^{N_{part}} Xn_i \sum_i^{N_{part}} \frac{1}{Xn_i} \\ &= \frac{1}{N_{part}^2} \sum_i^{N_{part}} n_i \sum_i^{N_{part}} \frac{1}{n_i}. \end{aligned} \tag{2.77}$$

We use this description to compute the clumping factor in each cell of our grid and include the clumping factor in the rate equations, i.e. as a factor enhancing the recombination rates of H II, He II and He III.

Photon tracking

As mentioned earlier the original version of pCRASH (Partl et al., 2011) only allowed a simulation to be restarted with the original parameters, i.e. the underlying density field and sources (their total number, positions and spectra) could not be changed. We run reionization simulations by post-processing a series of snapshots from a hydrodynamical simulation with radiative transfer. When switching from one snapshot to the next one, the simulation needs to be stopped and set up newly: density field and sources are updated; the last outputs of the ionization fractions from the radiative transfer run are used as new input files; the temperature field is given by the maximum of the last output of the radiative transfer run and the temperature field of the new snapshot of the hydrodynamical simulation. After changing the density field and sources, the simulation could not be run further from the checkfiles in the original version of pCRASH, the photon packets of the old snapshot are removed and photons start to be emitted from the new sources. In high density regions the removal of the "old" photons can be problematic, since recombination times may become shorter than is needed for the "new" photons to propagate from the sources to those regions. Those regions recombined and method-driven oscillations are introduced. This effect is naturally enhanced by the inclusion of the clumping factor, since the latter leads to a notable enhancement of the recombination rates in high density regions.

In order to overcome this limitation, we implemented an additional option to the code which allows us to keep the old photon packets from the checkfiles but updates the density, clumping factor, temperature fields and sources: checkfiles are read, the new domain decomposition according to the new sources is calculated, existing photon packets and ionization fields are distributed to new domains, new density, temperature and clumping factor fields are read and distributed to processors. Temperature fields are not solely taken from the previous radiative transfer run, but given by the maximum temperature in each cell of the new snapshot of the hydrodynamical simulation and the previous radiative transfer run. This relies on the fact that heating by photoionization, as it is followed in the radiative transfer calculations, dominates the temperature.

2.3.3 Running a reionization simulation

In the previous sections we have briefly described the radiative transfer scheme pCRASH which we use to perform reionization simulations. Here we give a short outline how these simulations are run.

1. From the hydrodynamical simulation we map the gas density, temperature and clumping factor on a 3D grid of chosen resolution for all snapshots ($z > 5.5$).

2. We run a halo finder on the respective snapshots. With the use of a stellar synthesis model we model the spectra of the sources based on the information (stellar mass, age, metallicity) of the star particles in the halos. We assume a by input given escape fraction of ionizing photons f_{esc}.

3. We find the first snapshot that contains sources.

4. The radiative transfer simulation is set up for the first snapshot. The density, clumping factor and temperature fields are taken from the hydrodynamical output. Ionization fractions are assumed to be zero, i.e. neutral, at the start of the simulation. For the sources of the snapshot radiative transfer is calculated, whereas sources emit photons continuously; spectra are not time-dependent within one snapshot. The density $n(z)$ is evolved according to the respective redshift $n(z) = n(z_i)(1+z)^3/(1+z_i)^3$ with z_i being the redshift of the snapshot.

5. Radiative transfer calculations are performed until the redshift of the next snapshot z_{i+1} is reached.

6. From the subsequent snapshot a new radiative transfer run is set up analogue to the first snapshot (density, clumping factor, sources) but (a) the final ionization fields of the previous radiative transfer run are assumed to be the initial ones; (b) the temperature field is given by the maximum temperature of the final temperature field of the radiative transfer run and of the new snapshot of the hydrodynamical simulation; (c) propagating photon packets of the previous snapshot are conserved. With the new fields and sources radiative transfer calculations are performed until redshift of the subsequent snapshot is reached.

7. Step 6 is repeated until the global amount of neutral hydrogen fraction drops below 10^{-3}.

2.4 Conclusions

In this Chapter we have presented two methods to compute the distribution of ionized regions from a set of given sources in a cosmological volume. The first method is of approximate character and maps ionized spheres around the sources on a grid, while the second method uses a Monte-Carlo long characteristic continuum radiative transfer scheme which employs ray-tracing technique on a 3D grid extending (Partl et al., 2011).

For the approximate mapping-sphere-scheme we developed a 1D radiative transfer code which solves the evolution for H II, He II, He III and the temperature. In the case of pure hydrogen we have reproduced the analytical solution of the Strömgren sphere; in the case of hydrogen and helium we have compared it to a tested 3D radiative transfer code and found an overall agreement. For a single sphere we estimate the distances in terms of the Strömgren radius when the photoionization rate becomes critical, i.e. when the ionization fraction exceeds 0.99 or drops below 0.01. With help of this description we discuss whether the merged ionized spheres of two sources can be described by the photoionization rates of the two respective single sources. When we account for the overlapping volume of the ionized spheres and increase their sizes accordingly, we find that the addition of the photoionization rates of the enlarged spheres reproduces the photoionization rate of two merged ionized sphere sufficiently. Since this method of photoionization rate addition also works for three overlapping spheres, we extend the method to a various number of sources, whereas the increase of the ionized spheres is always done by considering pairs of spheres.

To obtain the distribution of the ionized regions we have developed a parallelised code which (1) computes the underlying density and temperature profiles for each source, (2) calculates the ionization and temperature profiles based on the spectra of the sources, (3) accounts for the overlapping of the ionized spheres, and (4) maps the spheres on to a grid. For a distribution of sources in a cosmological density field we compare the results of this mapping spheres scheme to the results from a full 3D radiative transfer simulation. Due to the method the mapping sphere scheme does not account for angular inhomogeneities in the density field; thus the ionized regions are spherical. Furthermore the ionized regions of the mapping sphere scheme are larger than those from the 3D radiative transfer calculations, since due to the averaging over all lines of sight the density profile is underestimated. Hence, for a fast computation of an ionization field at early stages of reionization our approximate scheme provides a useful tool. Nevertheless since the method scales with the number of sources, its runtime increases correspondingly making it less efficient.

We have extended the Monte-Carlo long characteristic continuum radiative transfer scheme pCRASH which employs ray-tracing technique on a 3D grid: the possibility of an arbitrary number of spectra, the inclusion of a local clumping factor and photon tracking from previous snapshots. To carry out a complete reionization simulation with pCRASH the snapshots of the hydrodynamical simulation are consecutively post-processed by (1) using density and temperature distributions of the hydrodynamical simulation as input for the radiative transfer calculations, (2) modelling identified halos as sources whose properties depend on star particle characteristics (stellar mass, age, metallicity), and (3) running pCRASH for each snapshot.

This provides us with a tool to perform self-consistent reionization simulations as the source properties described in the hydrodynamical simulation expand into the radiative transfer via the spectra of the sources. Combined with the memory of propagating photons from the respective previous snapshot, pCRASH ensures a consistent photon propagation when snapshots are updated. Unless otherwise stated, this is the 3D radiative transfer scheme used for the remainder of this thesis.

Chapter

3

Can uv radiation from star forming galaxies reionize the universe?

We perform a self-consistent simulation of reionization by post-processing a hydrodynamical simulation (GADGET-2) with 3D radiative transfer (pCRASH), where the location and spectra of the ionizing radiation is set by the stellar component of the hydrodynamical simulation. Following ionization fractions of hydrogen (H I *) and helium (He* II*, He* III*), and temperature in our simulation, we find that reionization occurs rather late, starting at $z \simeq 11$ and ending at $z \simeq 6$, and shows inside-out character, ionizing high density regions near sources earlier than low density regions far from sources. Sizes of ionized regions depend primarily on the evolution time and stellar masses of the enclosed galaxies, while stellar ages and metallicities play a negligible role. Accounting for the clumpiness of the intergalactic medium (IGM) locally, our simulation exhibits self-shielded partially neutral regions even at the end of reionization. The thermal state of the IGM follows the ionization progress and reflects the distribution of the photoionization rate. We find that the IGM temperature is lower behind ionization fronts than in the interior of ionized regions where equilibrium ionizing emissivity has been reached; in regions of ionization equilibrium the temperature-density relation is inverted ($T \propto T_0(1+\delta)^{\gamma-1}$ with $\gamma - 1 = -0.2$) as cooling in denser regions becomes more efficient due to an increasing number of recombinations.*

3.1 Introduction

The Epoch of Reionization marks the last major phase transition in the universe going from a neutral to an ionized state. Starting from a completely neutral state the first stars and galaxies provide the ionizing photons to build up ionized regions in the intergalactic medium (IGM) until the universe is completely ionized at $z \geq 6$. Since reionization changes the thermal state of the IGM and causes an ionizing background radiation, it affects subsequent structure formation by various feedback mechanisms: photoionization heating increases the gas temperature and subsequently the Jeans mass leading to a supression of low-mass halos due to the available insufficient cooling mechanisms at early times as local adiabatic expansion or Compton scattering of the CMB. Lyman-Werner photons dissociate H_2 molecules which represent a major coolant for gravitational collapse. Radiative feedback leads to a suppression of low-mass galaxies in addition to supernova feedback that can limit subsequent star formation as supernova explosions cause gas outflows from the galaxies. These feedback mechanisms do not suppress halos with masses of at least $10^9\,\mathrm{M}_\odot$, but they become effective for lower-mass halos. Hence, the contribution of low-mass halos to reionization remains an open question. Recent papers (Iliev et al., 2012; Ahn et al., 2012) agree that so-called minihalos ($M_h \simeq 10^5 - 10^8\,\mathrm{M}_\odot$) contribute in the form of the first stars at very early times, however as soon as their surroundings becomes ionized their star formation is suppressed due to radiative feedback, and then high-mass halos dominate the progress of reionization. Although low-mass halos have no impact when reionization is completed, they shift the beginning of reionization towards higher redshifts as low-mass halos are formed earlier on. In this case the free electrons that are already present at redshifts ($z > 10$) lead to a boost of the

intergalactic electron-scattering optical depth. This brings into agreement the CMB measurements of the optical depth and observational constraints from the Gunn-Peterson trough (Fan et al., 2006) and Lyα optical depth (Bolton and Haehnelt, 2007; Becker et al., 2014) suggesting that reionization ended late at $z \geq 6 - 7$.

Essential for reionization are the properties of the ionizing sources, in particular the number of ionizing photons they provide and the hardness of their spectra. Various papers (Choudhury and Ferrara, 2007; Sokasian et al., 2003, 2004; Wyithe and Loeb, 2003; Yajima and Khochfar, 2014) conclude that star forming galaxies, i.e Population II stars and earlier on the metal-free Population III stars, dominated reionization. Providing even harder ionizing spectra than the hottest stars quasars present an interesting alternative reionization source. According to observations, however their number is not high enough to provide enough UV photons for reionization (Fan et al., 2001; Dijkstra et al., 2004a; Meiksin, 2005; Bolton and Haehnelt, 2007; Srbinovsky and Wyithe, 2007; Salvaterra et al., 2005, 2007) and overall their contribution is limited by the observed X-ray background up to 10% (McQuinn, 2012). An even more poorly constrained but essential parameter is the escape fraction of ionizing photons (f_{esc}). f_{esc} represents the fraction of UV ionizing photons that are not absorbed within the galaxy and escape into the IGM. A variety of theoretical models have been used and predicted values ranging from 0.01 to 0.8 (Razoumov and Sommer-Larsen, 2010; Yajima et al., 2011; Ferrara and Loeb, 2013; Wise and Cen, 2009; Kimm and Cen, 2014; Gnedin et al., 2008; Mitra et al., 2013), as well as different dependencies on the halo mass: while Gnedin et al. (2008); Wise and Cen (2009) suggested increasing values with increasing halo masses, (Razoumov and Sommer-Larsen, 2010; Yajima et al., 2011; Ferrara and Loeb, 2013) found the opposite trend.

As upcoming 21cm measurements will reveal the size and distribution of the ionized regions during reionization, it is necessary to understand how they will be influenced by source properties (luminosities (masses), spectra) and feedback effects. In recent work McQuinn et al. (2007a) concludes the rarer the sources, the larger and more spherical the ionized regions. Hence, comparing to reionization scenarios that take only high-mass sources into account, an inclusion of low-mass sources leads to an earlier start of reionization and a more homogeneous distribution of small ionized regions (Ahn et al., 2012). While the early stages of reionization are dominated by the first stars (low-mass sources), the late history is entirely driven by the high-mass sources. As the mean ionization fraction rises, the Jeans mass filtering suppresses low-mass sources in a larger fraction of the volume, known as self-regulation, reducing the contribution of low-mass sources to reionization. This Jeans mass filtering compensates for the difference in the emissivity of halos, as low-mass halos with high emissivities achieve a given ionization fraction earlier than those with low emissivities (Iliev et al., 2007). Nevertheless, this self-regulation effect (later stages of reionization are dominated by high-mass sources) has not been seen in Kim et al. (2013) and (Sobacchi and Mesinger, 2013b) unless supernovae feedback is ineffective in high-z galaxies (Kim et al., 2013) or as modeling radiative feedback of the UV background with an instantaneous transition in the minimum halo mass overestimates the importance of the latter (Sobacchi and Mesinger, 2013b). Directly connected with the distribution of the ionized regions is the question how reionization proceeded, i.e. which regions were ionized first and which last. The formation of sources in collapsed regions would suggest that high density regions close to sources ionize earlier than low density regions far from sources; indeed this inside-out character of reionization has been found in various reionization simulations (Iliev et al., 2006; Ciardi et al., 2012; Iliev et al., 2012) and has been used in seminumerical approaches (Mesinger and Furlanetto, 2007; Zahn et al., 2007). Nevertheless the reionization scenario in Finlator et al. (2009) deviates from this picture. They find that although reionization begins in the overdense regions, it first leaks into voids and ionizes filaments last due to high recombination rates and low emissivities (referred to as 'inside-out-middle' reionization).

Although the epoch of reionization is dominated by the ionization of hydrogen, its progress is modified by the presence of helium. The inclusion of helium delays reionization as a number of ionizing photons are used for ionizing helium other than hydrogen. Furthermore at the end of reionization a higher mean gas temperature of the IGM is found due to the inclusion of He II photoionization (Ciardi et al., 2012).

In this work we aim to build a self-consistent model of reionization by exploiting the full information on the source characteristics for the computation of the ionized regions. To date only a few reionization simulations have attempted this approach (Gnedin, 2014); most of them using either a fixed spectral energy distribution (Ciardi et al., 2012; Norman et al., 2013) or inferring the number of ionizing photons solely from the halo masses in DM only simulations which do not follow the feedback processes controlled by their baryonic components (Iliev et al., 2014). By modeling the spectra and luminosities of each source in accordance with the properties that were obtained in the hydrodynamical simulation,

we study the effects of source characteristics on reionization topology and its signatures in helium.

Recent works (Gnedin, 2014) have started to perform coupled cosmological radiative transfer and hydrodynamical simulations. Since these simulations are computationally very expensive, we instead post-process our hydrodynamical simulation with radiative transfer calculations. Furthermore it has been shown by Bolton and Haehnelt (2013) that far from sources high density regions become self-shielded, i.e. remaining predominantly neutral, due to their enhanced number of recombinations. Since our radiative transfer calculations are performed on a grid, we attempt to account for the full clumpiness of the IGM that is given by the resolution of the SPH simulation. Thus we compute for each cell a local clumping factor to reflect the density variation of the gas.

The outline of this Chapter is as follows. In Section 3.2 we describe the details of the hydrodynamical and radiative transfer simulations that are used to perform our reionization simulation. We analyze the galaxy population obtained from the hydrodynamical simulation and describe our modelling of the spectra of the identified galaxies. We present our results in Section 3.3 and discuss the global ionization and thermal history, the ionization topology and the corresponding 21cm signal. Finally we conclude in Section 3.4.

3.2 Simulations

In this Section we describe firstly the hydrodynamical simulation and the selection criteria by which we identify galaxies. Secondly we elaborate on our modeling of the sources and briefly comment on their ionizing capacities. Last we shortly explicate the radiative transfer runs which post-process the hydrodynamical outputs.

3.2.1 Hydrodynamical Simulation

We analyse a hydrodynamical simulation that has been carried out using the TreePM-SPH code GADGET-2 (Springel, 2005) and a box size of $80h^{-1}$ comoving Mpc (cMpc). The simulation adopts a ΛCDM universe with dark matter (DM), dark energy and baryonic density parameter values of (Ω_Λ, Ω_m, Ω_b) = (0.73, 0.27, 0.047), a Hubble constant $H_0 = 100h = 70\mathrm{kms}^{-1}\mathrm{Mpc}^{-1}$, and a normalisation $\sigma_8 = 0.82$. These parameters are in agreement with the results from WMAP5 (Komatsu et al., 2009). 2×1024^3 DM and gas particles were followed, leading to a mass per DM or gas particle of $3.6 \times 10^7 h^{-1}\mathrm{M}_\odot$ and $6.3 \times 10^6 h^{-1}\mathrm{M}_\odot$, respectively. The softening length for the gravitational force is $3h^{-1}$ comoving kpc. The value of the smoothing length for the SPH kernel needed to compute the hydrodynamic forces can drop at most to the gravitational softening.

According to the star formation prescription of Springel and Hernquist (2003) the ISM is described as an ambient hot gas containing cold clouds. The two phases are in pressure equilibrium and provide the reservoir for star formation. The relative number of stars of different masses is computed according to the Salpeter initial mass function (IMF; Salpeter, 1955) between 0.1-100$\mathrm{M}_\odot$. The density of the cold and of the hot phase represents an average over small regions of the ISM, within which individual molecular clouds cannot be resolved by simulations sampling cosmological volumes. The simulation also includes the feedback model described in Springel and Hernquist (2003) which models several feedback processes: (a) thermal feedback: supernovae (SN) inject entropy into the ISM, heat up nearby particles and destroy molecules, (b) chemical feedback: metals produced by star formation and SN are carried by winds and pollute the ISM, and (c) mechanical feedback: galactic winds powered by SN. Finally, the run assumes a metallicity-dependent radiative cooling (Sutherland and Dopita, 1993) and a uniform redshift-dependent UV Background (UVB) produced by quasars and galaxies as given by Haardt and Madau (1996) which is switched on at redshift $z \simeq 6$.

Galaxies are identified as gravitationally-bound groups of at least 20 total (DM+gas+star) particles using the Amiga Halo Finder (AHF; Knollmann and Knebe, 2009). We use only "well-resolved" galaxies containing at least 5 star particles. Furthermore since Chiu et al. (2001) showed that an identification of low-mass halos with low-mass galaxies ($M_{gas} < 10^8 - 10^9\,\mathrm{M}_\odot$) would result in an overestimate of number of low baryonic systems by several orders of magnitude but for $v_{circ} > 40$ km/s the stellar mass function would follow the dark matter, we consider only halos with a circular velocity of at least $v_{circ} > 60$km/s. Since this hydrodynamical simulation does not include local radiative feedback this source selection is also agreement with Okamoto et al. (2008); Okamoto and Frenk (2009), the former of which found that reionization can remove most of the baryons from halos with low maximum circular velocities.

3.2.2 Source Model

Each galaxy in our hydrodynamical simulation is characterized by its constituent star particles; whereupon each star particle represents a stellar population that is described by its stellar mass, age and stellar metallicity. From these properties we derive the intrinsic spectrum for each star particle by using the stellar population synthesis code STARBURST99. To obtain the total spectrum of a galaxy, we sum over all spectra of the star particles of the galaxy.

In the following we discuss how the properties of galaxies, their spectra and number of ionizing photons evolve over cosmic time. Since the spectra of galaxies depend on their stellar masses, ages and metallicities, we start by describing the evolution of the galaxies in respect to these quantities. Due to gravity gas clouds collapse with cosmic time and subsequently start to form stars and galaxies. gas from the intergalactic medium is accreted into the potential wells of galaxies and triggers more star formation; the galaxies grow, i.e. their stellar mass increases. Consequently as galaxies grow, their stellar populations become older. Conversely new galaxies form over cosmic time possessing younger stellar populations. As star formation proceeds, the Universe is enriched with elements, the primordial elements of hydrogen, helium, deuterium and lithium are diluted as stars form and explode and the overall metallicity in particular in star-forming regions rises. Thus the first stars and galaxies exhibit very low metallicities, while subsequent galaxies show higher metallicities.

As star formation is ongoing the metallicity of new forming galaxies depends strongly on their environment: if the galaxy forms in the vicinity of other galaxies whose supernovae have enriched the medium with metals, the galaxy metallicity will be higher than for galaxies that form in a region with no prior star formation. Thus the range of metallicities of young galaxies broadens over time, while older and more massive galaxies tend to have higher metallicities. As mentioned earlier these properties of the galactic stellar populations (stellar mass, age, metallicity) determine their ionizing power and are essential for controlling the progress of reionization. We find that while age and metallicity change the hardness of the spectra, stellar mass only varies their amplitude. Hence, the more stellar mass a galaxy contains, the higher is its luminosity and number of ionizing photons. With decreasing age and metallicity the spectra become harder, i.e. generating more high energy photons. In general the

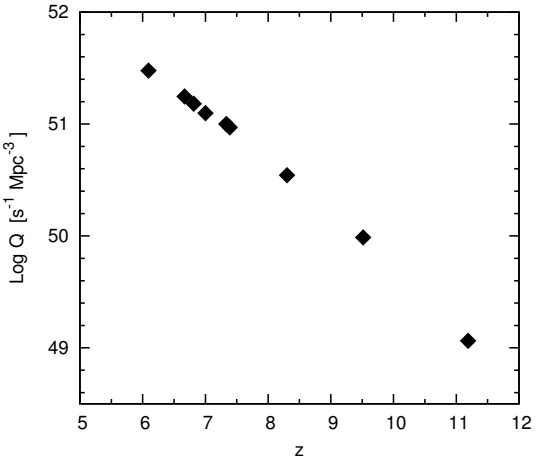

Figure 3.1: Total number of ionizing photons per volume as a function of redshift

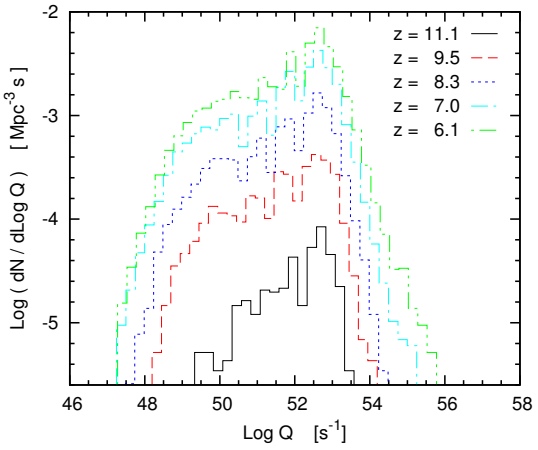

Figure 3.2: Distribution of galaxies per volume versus their number of ionizing photons at different redshifts

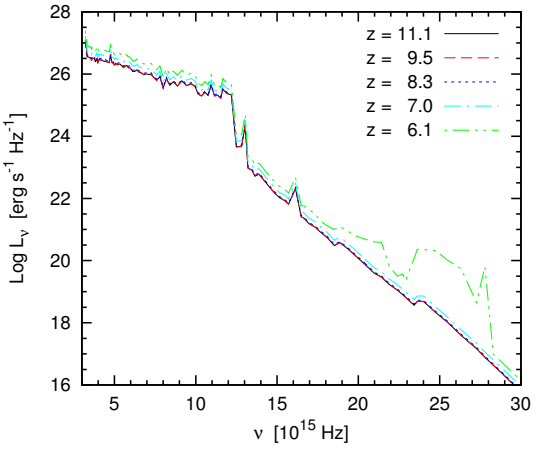

Figure 3.3: Mean spectral density of star forming regions at different redshifts

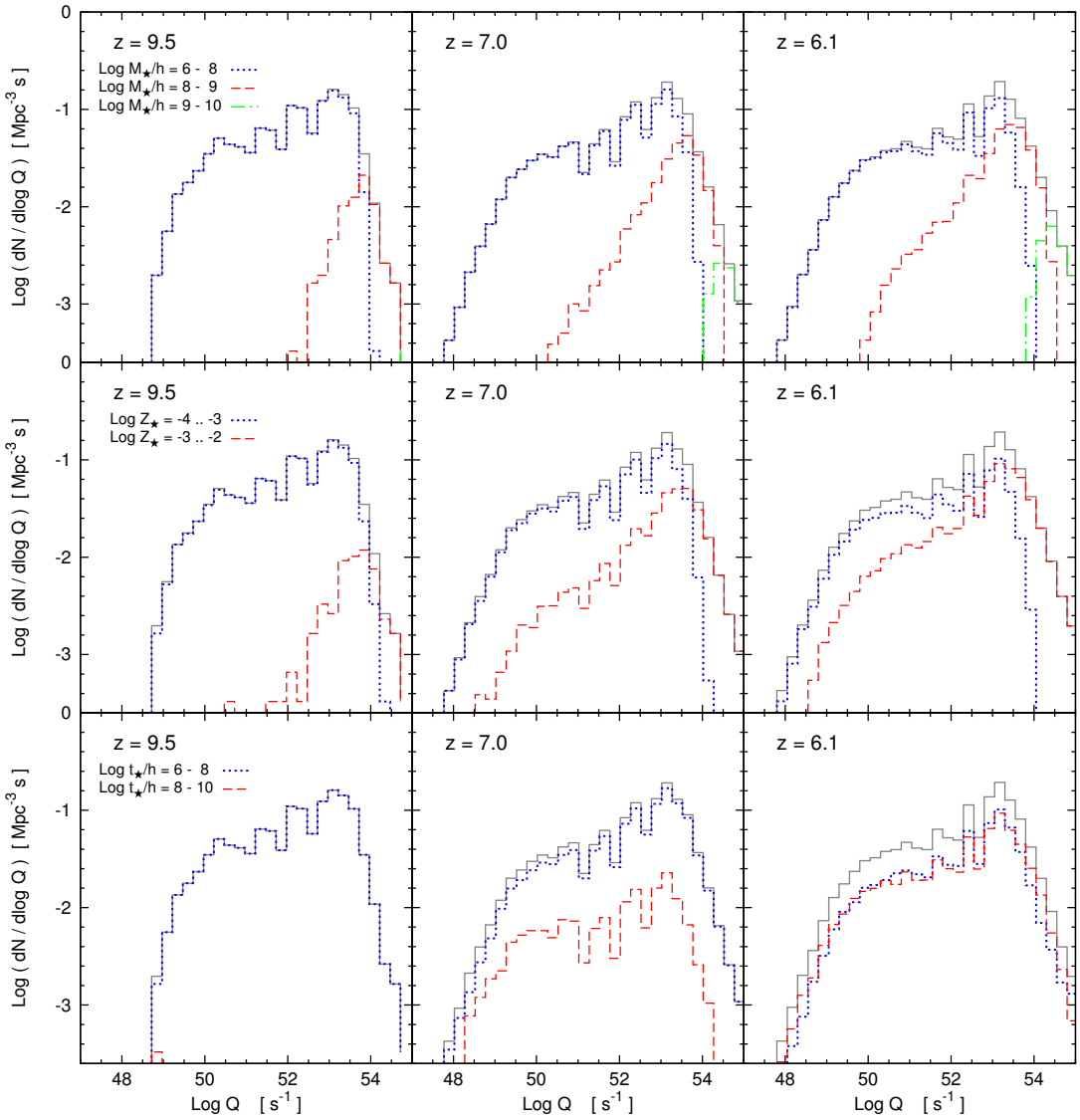

Figure 3.4: Distribution of number of ionizing photons per source at different redshifts. Black lines show the total number, while blue (red) lines show sources with small (high) mass, low (high) metallicty and low (high) age.

age has a greater effect on the hardness of the spectra than the metallicity.

By means of Figures 3.1, 3.2 and 3.3 we discuss the global evolution of the spectral shape and the number of ionizing photons of galaxies in relation to galaxy evolution. As the number of galaxies increases over cosmic time, the number of ionizing photons in our simulation volume rises accordingly (see Fig. 3.1). Due to hierarchical galaxy formation, not only does the number of galaxies increase, but also the stellar mass distribution shifts towards higher stellar masses: in Fig. 3.2 the range of ionizing photons emitted by galaxies becomes broader towards lower redshifts. Whilst the formation of more massive galaxies over cosmic time increases the amount of ionizing photons that can be emitted by a galaxy (maximum Q in Fig. 3.2 increases towards lower redshifts), the ageing of galaxies tends to decrease the number of ionizing photons (minimum q in Fig. 3.2 decreases towards lower redshifts). We find the overall shift of the stellar mass distribution towards higher stellar masses is also reflected in the mean spectrum of all galaxies in the simulation: in Fig. 3.3 the mean spectral luminosity increases with decreasing redshift, leading to higher numbers of ionizing photons and thus implying more massive galaxies.

Since ionization characteristics for hydrogen and helium depend strongly on the number of ionizing photons and the spectral hardness of the sources, we break down the contribution of the different

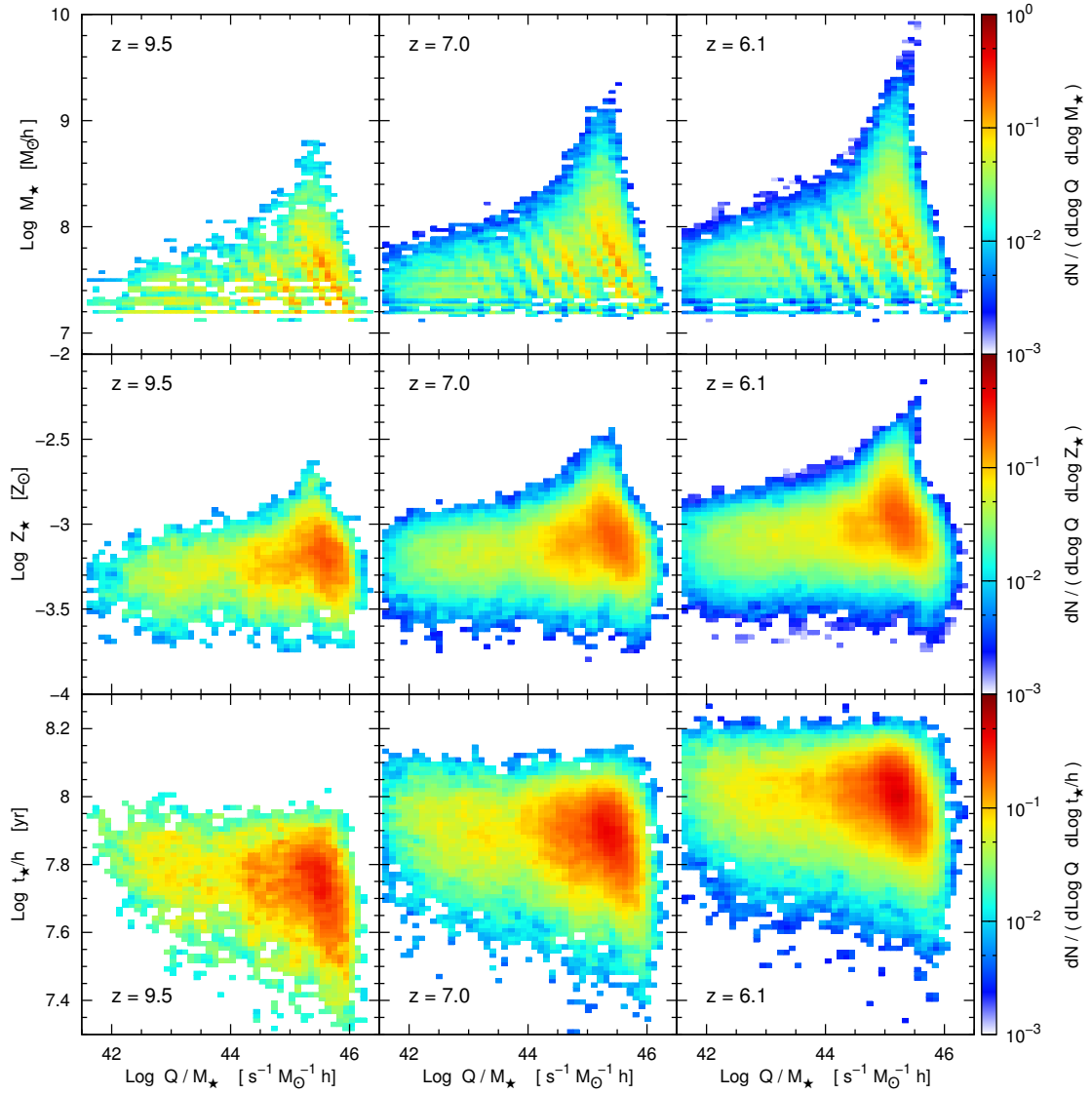

Figure 3.5: Normalised number of galaxies in bins of number of ionizing photons per stellar mass and stellar mass (top row), metallicity (middle row) and age (bottom row) for redshifts $z = 9.5$ (left column), 7.0 (center column) and 6.1 (right column). The normalised number of galaxies is colour-coded.

galaxies to the number of ionizing photons and spectra. The dominant effect for the number of ionizing photons per source is the growth of the stellar mass in the galaxies, as we can see in Fig. 3.4 it increases with rising stellar mass. From Fig. 3.4 we also find that the number of ionizing photons increases with metallicity and stellar age. To understand these trends we need to understand how spectra change with age, metallicity, and selection effects: in general the spectrum of a unit stellar mass becomes softer for higher ages and metallicities, leading to a decrease of the number of ionizing photons. The trend of the ionizing photons of our galaxies with stellar age reflects the predicted trend of a stellar spectrum. Whilst the number of ionizing photons in a stellar spectrum decreases with metallicity, for the population of galaxies it rises due to the correlation of galaxy mass with redshift.

To quantify how stellar age and metallicity influence the number of ionizing photons per stellar mass ($Q/M_\star$), we show in Fig. 3.5 the normalised number of galaxies in bins of number of ionizing photons per stellar mass and stellar mass, metallicity and age for redshifts $z = 9.5$, 7.0 and 6.1. First we note that during reionization the distribution of galaxies grows towards higher stellar masses (top row, from left to right), higher metallicities (second row), and higher ages (third row). Secondly, we find the trends of $Q/M_\star$ with stellar metallicity and age reflecting predicted trends by spectra: considering the majority of galaxies (red areas in Fig. 3.5) $Q/M_\star$ increases for decreasing stellar age

and metallicity, as spectra become harder and release more ionizing photons; furthermore the upper limit of $Q/M_\star$ increases with decreasing stellar mass, which hints towards the fact that the most massive galaxies are older and more metal-rich.

3.2.3 Reionization simulation with pCRASH

The radiative transfer is followed using the 3D grid-based MPI-parallelized code pCRASH (Ciardi et al., 2001; Maselli et al., 2003, 2009; Partl et al., 2011). pCRASH is a Monte Carlo based ray tracing scheme which tracks the time evolution of the IGM gas properties including ionization fractions (H I and He I, He II) and the temperature. The ionising radiation in the medium is represented by a number of multi-frequency photon packages that are emitted from a number of sources. The code calculates the relevant matter-radiation interactions (photoionization, recombination, collisional ionization), the heating/cooling of the IGM (collisional ionization cooling, recombination cooling, collisional excitation cooling, bremsstrahlung, Compton cooling/heating, adiabatic cooling, photoheating) and includes diffuse radiation following the recombinations of ionized atoms.

For the reionization simulation we post-process each of the 10 snapshots in the redshift range $z \simeq 6-11$ with radiative transfer; snapshots at higher redshifts do not exhibit resolved sources. From each snapshot of the hydrodynamical simulation we use the density and temperature field as an input for the radiative transfer calculations. For the corresponding sources we calculate the luminosities and spectra by summing up the spectra of all their star particles as described in Section 3.2.2. We assume an escape fraction of $f_{esc} = 0.3$ which is in agreement with Mitra et al. (2013); Yajima et al. (2011). We group the identified halos to make the radiative transfer computation feasible. Starting with the most massive halos, we add less massive accompanying galaxies, within twice the virial radius of the main galaxy but at least 0.7 Mpc/h, to the considered main halo. Each source emits about 10^7 photon packets/rays per 100 Myrs which are updated every 100 yrs and are propagated on a 512^3 grid. The spectrum of each source is binned into 125 frequency intervals ranging from 3.21×10^{15}Hz to 3.30×10^{16}Hz. Starting with the snapshot at $z \simeq 11$ showing the first resolved sources we compute the evolving ionization fields for hydrogen (H II) and helium (He II, He III) as well as the temperature field. We update the density at each timestep (redshift z) by $n(z) = n(z_{snap})(1+z)^3/(1+z_{snap})^3$ with z_{snap} being the redshift of the used snapshot. If the calculations have reached the redshift of the subsequent snapshot, density and temperature fields are replaced. For the temperature field we assume for each cell the maximum temperature considering the temperature fields of the last radiative transfer output and the new snapshot of the hydrodynamical simulation, which relies on the fact that heating by photoionization, as it is followed in the radiative transfer calculations, dominates the temperature. Furthermore we also adapt the field of the local clumping factors; the local clumping factor is computed for each cell based on the underlying density distribution of the SPH simulation and accounts for the clumpiness of the IGM (Raičević and Theuns, 2011). We run the radiative transfer until hydrogen is completely ionized at $z \simeq 6$.

3.3 Results

3.3.1 Reionization History

We start our analysis of our reionization simulation by deriving globally averaged quantities that can give us hints on the topology of reionization, and further characterise the geometry of the ionized regions using Fourier analysis.

Evolution of the ionization fractions

In our simulation the first ionizing sources form at redshift $z \simeq 11$ and hydrogen in the IGM is ionized by 99% at $z \simeq 6.1$. In Fig. 3.6 we show the evolution of the ionization fractions H II, He II and He III over the respective redshift interval. At the beginning of reionization only a few sources in the density peaks start to ionize the surrounding IGM. As structures in the universe develop with cosmic time, more galaxies form in density peaks and existing galaxies grow by accumulating gas. As such, the number of ionizing photons rises steadily and the ionized bubbles around the sources grow and merge until the universe is ionized causing the ionization fraction to rise as the redshift decreases until it finally reaches unity, as can be seen for H II in Fig. 3.6. We find that He II ionization fraction follows the H II ionization fraction until the amount of He III becomes significant at $z < 8$. To

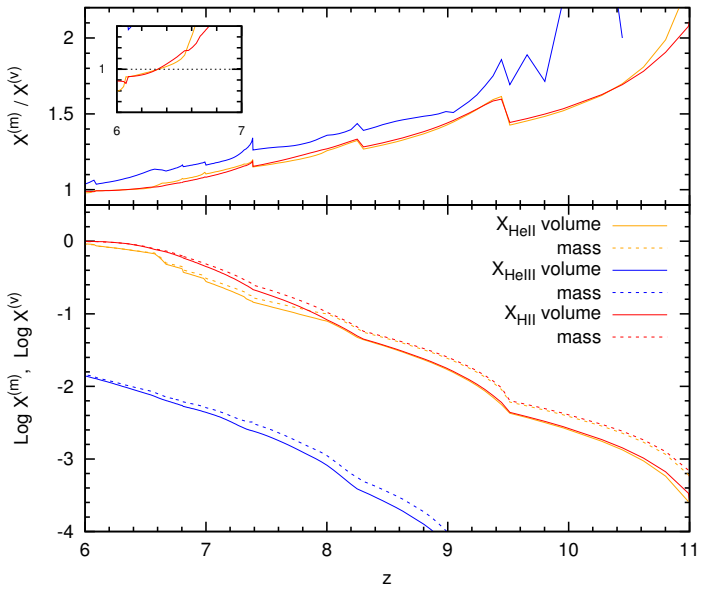

Figure 3.6: The bottom panel shows the evolution of the globally averaged ionized fractions H II (red), He II (yellow) and He III (blue): mass-weighted, $X^{(m)}$, (dashed) and volume-weighted ,$X^{(V)}$, (solid). The top panel represent their ratio.

explain this finding we need to consider the spectra of the ionizing sources and the ionizing energies of the different species. While to ionize H I and He I photons with energies of at least 13.6eV and 24.6eV respectively are needed, to obtain He III energies of at least 54.4eV are required. Within the range of the ionizing energy for H I and He I the spectra of our sources, i.e. the energy-dependent luminosity, do not change substantially for $t < 10^8$yr, however the luminosity at higher energies (i.e. for He II ionization) decreases by several orders of magnitude. Due to the limited number of He II ionizing photons, He III rises later in time when the number of galaxies has increased sufficiently.

Having described the global evolution of the ionization fraction we turn to the question of the geometry of reionization. A first hint is given by the relation between the volume-weighted ($X^{(V)}$) and mass-weighted ($X^{(m)}$) ionization fractions shown in Fig. 3.6. At high redshifts, i.e. at early times, we find that the mass-weighted fraction exceeds the volume-weighted fraction by a factor of more than 1.5. The more the universe becomes ionized, the more the mass-weighted fraction converges towards the volume-weighted fraction, until at $X_{\rm HII} \simeq 0.9$ and $X_{\rm HeII} \simeq 0.9$ the volume-weighted fraction becomes slightly larger than the mass-averaged, though it remains below for He III.

$$\frac{X^{(m)}}{X^{(V)}} = \frac{V}{M}\frac{X^{(m)}M}{X^{(V)}V} = \frac{1}{\bar{\varrho}}\frac{M_{ion}}{V_{ion}} = \frac{\varrho_{ion}}{\bar{\varrho}} \tag{3.1}$$

The ratio between $X^{(m)}$ and $X^{(V)}$ equals to the averaged density inside the ionized regions in units of the mean density of the universe. A ratio larger than unity indicates a reionization process with an inside-out character, i.e. high density regions are ionized first, as the ionization fronts expand mid- and low density regions nearby the ionizing sources become ionized subsequently and finally voids are ionized. For densities with $\mathrm{Log}(1+\delta) \leq 1$ our reionization scenario shows inside-out character. The turnover when the ratio $X^{(m)}/X^{(V)}$ becomes lower than 1 is due to some very high density regions ($\mathrm{Log}(1+\delta) > 1$) that remain partially neutral since the number of ionizing photons is not high enough to keep them ionized. These findings can be seen in Fig. 3.7 where we show the mean hydrogen ionization fraction at the respective overdensity at the different stages of reionization. Indeed we find that for overdensities of $\mathrm{Log}(1+\delta) \leq 1$ the mean ionization fraction increases with overdensity for all redshifts until the universe is fully ionized. As reionization proceeds the slope flattens indicating that the ionization fronts are expanding towards the low density regions. Both the rising slope as well as its flattening, shows the inside-out character of reionization. Nevertheless for high overdensities ($\mathrm{Log}(1+\delta) > 1$) the relation between the mean ionization fraction and overdensity changes during reionization. While we find still an inside-out character of reionization at early times, we see that the mean ionization fraction decreases with overdensity at later times.

As structures are becoming more distinct, the dense regions become so dense that the existing ionizing sources cannot keep these regions fully ionized due to the high recombination rates, i.e. very dense regions remain partially neutral. Within our simulation the recombination rate is given by a combination of the overdensity in each cell and the local clumping factor

$$C = \frac{\int n(\vec{x})^2 \, \mathrm{d}^3x}{\left(\int n(\vec{x}) \, \mathrm{d}^3x \right)^2}. \qquad (3.2)$$

This clumping factor accounts for the clumpiness of the averaged region and depicts the factor by which the number of recombinations has to be multiplied with to represent the realistic number of recombinations.

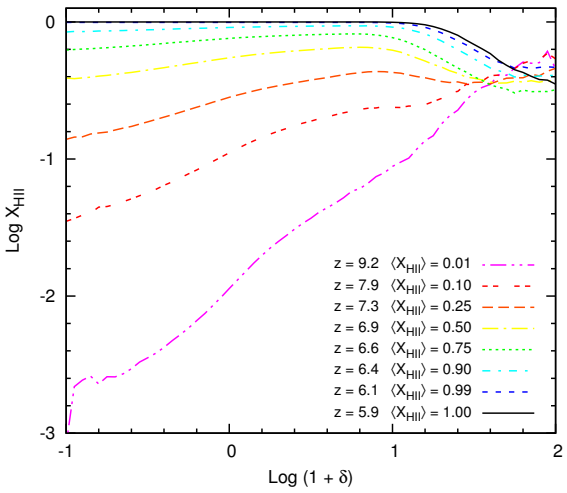

Figure 3.7: Mean hydrogen ionization fraction against overdensity at different redshifts.

In Fig. 3.8 we show the detailed neutral hydrogen fraction versus overdensity distribution at $z = 9.2 - 5.9$, corresponding to mean neutral hydrogen fractions of $\langle X_{\rm HI} \rangle = 0.99 - 3 \times 10^4$. At $z = 9.2 - 6.4$, i.e. before reionization is completed, we note a bimodality in the distribution, cells are preferentially either neutral or ionized. At the beginning of reionization ($z = 9.2$) we find a neutral patch at $\mathrm{Log}(\mathrm{X_{HI}}) = 0$ and an ionized one at $\mathrm{Log}(\mathrm{X_{HI}}) \approx -4$; for intermediate $X_{\rm HI}$ values the number of cells is much lower, since the ionization fronts are rather sharp and not extended. As reionization proceeds, the mean neutral fraction of the ionized cells decreases with declining redshift: Log $(\mathrm{X_{HI}}) \approx -4$, -4.5, -5, -5.5 at $z = 9.2$, 7.3, 6.4, 5.9 respectively. This evolution depicts the increase of the photoionization rate within the ionized regions with cosmic time, as the rising number and size of galaxies causes a rise in the number of ionizing photons.

After reionization has completed ($z = 5.9$), we find that nearly all cells of overdensities $\mathrm{Log}(1+\delta) \leq 1$ are ionized ($X_{\rm HI} < 10^{-4}$), while the neutral fraction ranges up to $X_{\rm HI} \approx 0.6$ for high overdensities ($\mathrm{Log}(1 + \delta) > 1$). Furthermore we observe a correlation between neutral hydrogen fraction and overdensity: on average the neutral hydrogen fraction rises with increasing overdensity, which is caused by the increasing recombination rate at higher densities. As the ionized hydrogen fraction is not solely determined by the density but also by the respective photoionization rate, the distinct shape of the correlation suggests for a restricted range of photoionization values. After reionization has completed, ionizing photons propagate freely in the IGM and are only absorbed to balance recombinations; thus the ionizing emissivity (and thus the photoionization rate) is nearly homogeneous and independent of the density. Hence, the larger the ionized regions in the IGM are, the more homogeneous is the

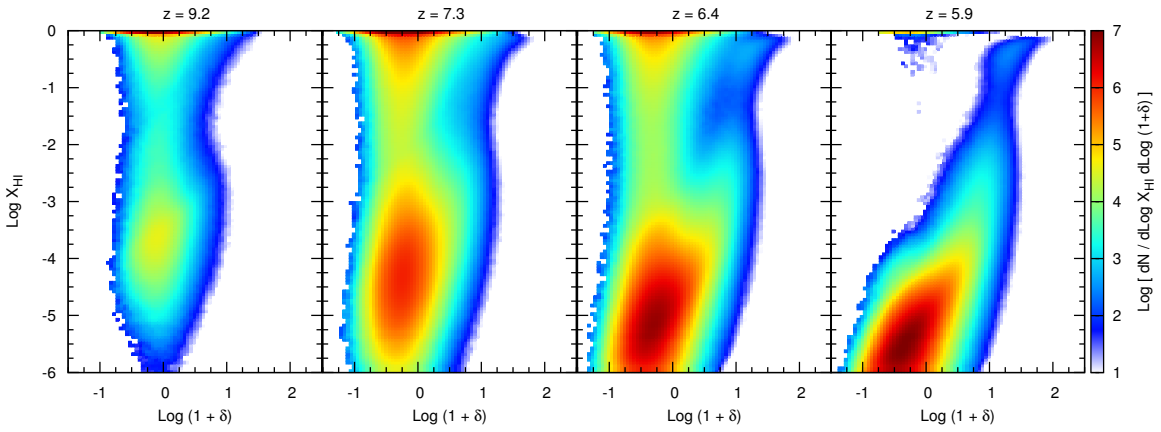

Figure 3.8: Contour plots of the distribution of neutral hydrogen fraction against overdensity at redshifts $z = 9.2$, 7.3, 6.4 and 5.9 ($\langle X_{\rm HI} \rangle = 0.99$, 0.75, 0.10 and 3×10^{-4} respectively). The color scale coresponds to the number of cells within each neutral hydrogen fraction and overdensity bin.

ionizing emissivity inside these regions, and the stronger is the correlation between neutral hydrogen fraction and overdensity. As the mean ionized hydrogen fraction decreases towards higher redshifts, ionized regions become smaller and the correlation between neutral hydrogen fraction and overdensity becomes less pronounced. We find that our results on the evolution of the neutral hydrogen fraction versus overdensity distribution are in agreement with the findings in Gnedin (2000).

Geometry of the ionized regions

In this section we discuss the geometry of reionization by means of a sequence of cuts through our simulation box and the evolution of the power spectra of the ionized and neutral regions.

In Fig. 3.9 we show the spatial distribution of the ionized (yellow) regions at four different redshifts during reionization ($z = 9.2, 7.3, 6.6, 6.1$). With the appearance of the first stars and galaxies, ionized regions grow around the sources, and start to merge in regions of strongly clustered sources (see second panel ($z = 7.3$) in Fig. 3.9). As reionization proceeds, existing ionized regions become larger, and newly formed galaxies cause the occurrence of small ionized regions in the neutral (black-cyan) patches ($z = 6.6$). At $z = 6.1$ the ionized regions have merged completely and the entire simulation box is 99% ionized.

In order to analyse the size distribution of the ionized and neutral regions we compute the power spectra of the ionized and neutral density fluctuations. The 3D power spectrum $\Delta^2(k)$ of the density field $\Delta_\varrho(\vec{x}) = 1 + \delta_\varrho(\vec{x})$ is given by

$$\Delta^2(k) \equiv \frac{k^3}{2\pi^2}\langle|\widetilde{\Delta}_\varrho(\vec{k})|^2\rangle \tag{3.3}$$

$$\widetilde{\Delta}_\varrho(\vec{k}) \equiv \frac{1}{V^{1/2}}\int \Delta_\varrho(\vec{x})\ \exp(i\vec{k}\vec{x})\ \mathrm{d}^3x \tag{3.4}$$

where $\Delta_\varrho(\vec{x})$ is given in units of the mean, $V = L^3$ is the associated volume and k the wavenumber in units of $2\pi/L$. Identifying $\Delta_\varrho(\vec{x})$ in equation 3.3 with the gas density fluctuations we obtain the respective power spectrum of the gas density field. To obtain the power spectra for the ionized and neutral gas density fluctuations, we replace $\Delta_\varrho(\vec{x})$ by $X_{\rm HII}\ \Delta_\varrho(\vec{x})$ and $(1-X_{\rm HII})\ \Delta_\varrho(\vec{x})$ respectively. We show the 3D power spectra of the total (Δ^2_ϱ), ionized ($\Delta^2_{\varrho,\rm HII}$) and neutral ($\Delta^2_{\varrho,\rm HI}$) density fluctuations at different redshifts to demonstrate the progress of reionization.

At the beginning of reionization ($z \simeq 9.2$) the ionized regions around the first sources are small extending up to a size of 5 Mpc/h (see Fig. 3.9). In Fig. 3.10 we see that the power spectrum of the ionized density fluctuations ($\Delta^2_{\varrho,\rm HII}$) is dominated by fluctuations on scales smaller than the maximum size of the ionized bubbles, $k > 1.3$ h/Mpc, and the power towards larger scales drops rapidly, since there are no larger ionized regions. The power spectrum of the neutral density fluctuations ($\Delta^2_{\varrho,\rm HI}$) agrees to a high degree with the power spectrum of density fluctuations (Δ^2_ϱ) as most of the IGM is neutral.

As reionization proceeds ($9.2 > z > 6.9$) the ionized regions grow in size; with decreasing redshift $\Delta^2_{\varrho,\rm HII}$ flattens for scales smaller than the largest ionized regions of about 10 Mpc/h ($k = 0.6$ h/Mpc)

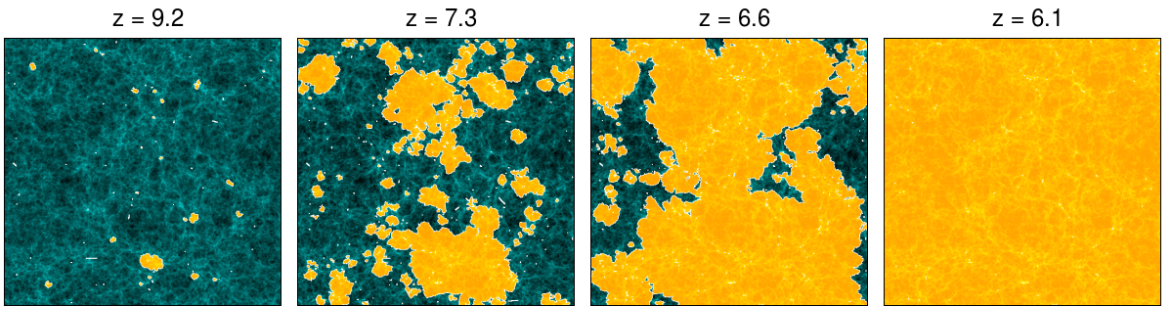

Figure 3.9: Slices through the 80 Mpc/h box at redshifts $z = 9.2, 7.3, 6.6, 6.1$ corresponding to $\langle X_{\rm HII}\rangle = 0.01$, 0.25, 0.75, 0.99 respectively. The density field is shown for neutral regions in black-cyan and for H II regions in yellow.

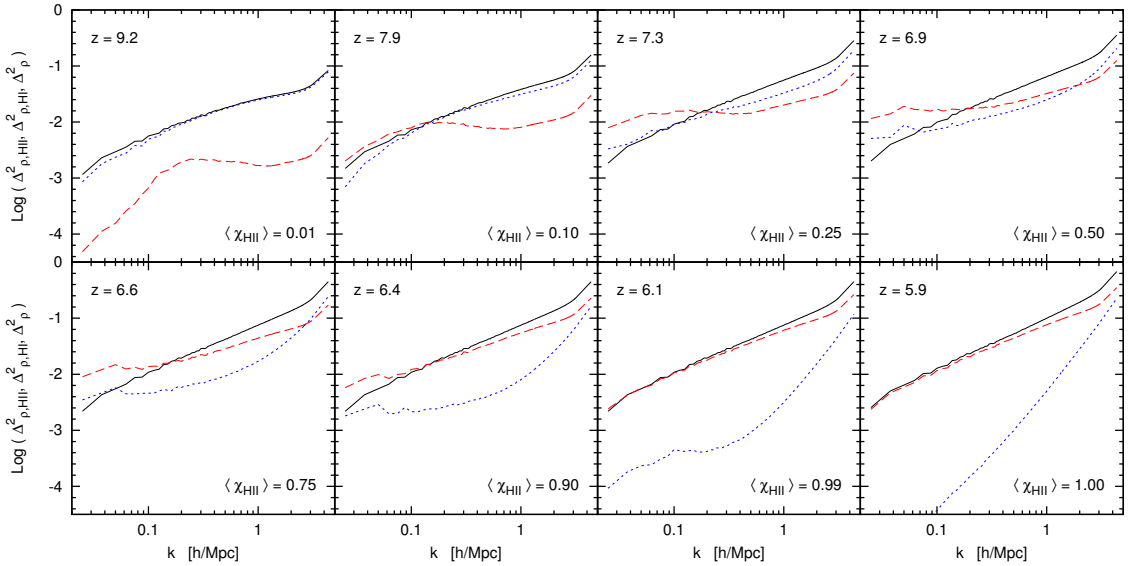

Figure 3.10: 3D power spectra Δ^2 of the total density (solid, black), the neutral gas density (dotted, blue) and the ionized gas density (dashed, red) at different redshifts, as labelled.

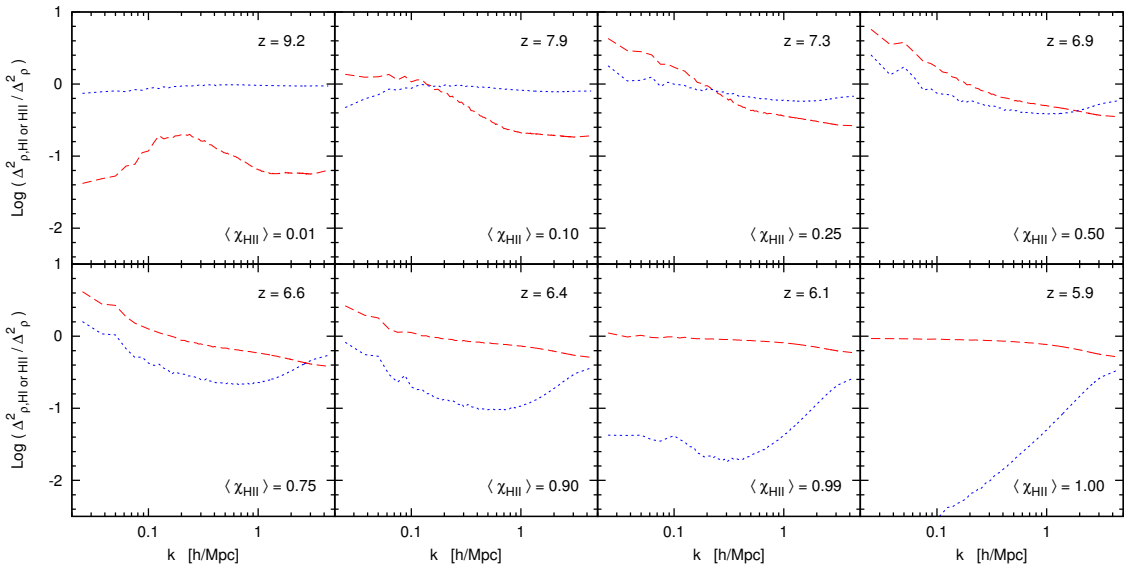

Figure 3.11: Ratios of the power spectra Δ^2 of the neutral gas density to the total density (dotted, blue), $\Delta^2_{\varrho,\mathrm{HI}}/\Delta^2_{\varrho}$, and the ionized gas density to the total density (dashed, red), $\Delta^2_{\varrho,\mathrm{HII}}/\Delta^2_{\varrho}$, at different redshifts, as labelled.

at $z = 7.9$, 20 Mpc/h ($k = 0.3$ h/Mpc) at $z = 7.3$ and about $30-40$ Mpc/h ($k = 0.2-0.15$ h/Mpc) at $z = 6.9$). As sources are strongly clustered, ionized regions start to merge and their sizes reach scales that are half of the boxlength at $z = 6.9$ when the IGM is on average 50% ionized. Nevertheless as new galaxies form, small ionized regions appear in the neutral patches (see Fig. 3.9 at $z = 7.3$ and 6.6), leading to an increase of the power in $\Delta^2_{\varrho,\mathrm{HII}}$ at small scales (< 2 Mpc/h) with a corresponding decrease in $\Delta^2_{\varrho,\mathrm{HI}}$ decreases accordingly.

As the ionized regions merge and grow ($6.9 < z < 6.1$), $\Delta^2_{\varrho,\mathrm{HII}}$ converges to Δ^2_{ϱ} (see Fig. 3.11 for $\Delta^2_{\varrho,\mathrm{HII}}/\Delta^2_{\varrho}$ converging to 1), while the amplitude of $\Delta^2_{\varrho,HI}$ decreases with the disappearance of neutral regions. At large scales $\Delta^2_{\varrho,\mathrm{HII}}$ remains flat until the entire simulation box is ionized. When the universe is fully ionized at $z = 5.9$ we find that $\Delta^2_{\varrho,\mathrm{HII}}$ has converged to Δ^2_{ϱ}. Nevertheless it still shows slightly less power on small scales which is also reflected in $\Delta^2_{\varrho,\mathrm{HI}}$ where power on intermediate

to large scales has decreased considerably but increases noticeably towards small scales. The reason for the small scale power in $\Delta^2_{\varrho,\mathrm{HI}}$ are the small partially neutral patches in high density peaks that were not ionized due to the insufficient number of ionizing photons from the sources.

3.3.2 The correlation between reionization redshift and density

In the previous Section we used the mass-weighted and volume-weighted ionization fractions as well as the power spectra of the ionized gas density fluctuations to conclude that reionization proceeds with an inside-out character. If this is the case, we should find a correlation between the reionization redshift and the density, i.e. with increasing density the redshift rises at which the respective volume became ionized.

In order to test this we record the redshift of ionization for each cell in our simulation; a region is considered to be reionized when its ionization fraction exceeds 90%. Since ionization fronts are sharp, i.e. the transition between onset of ionization and completion is fast, the threshold when a cell is assumed to be ionized does not play a major role. We show the density field at $z \simeq 6$ in the left and the corresponding redshift field in the right panel of Fig. 3.12. From this Figure we can see that the reionization redshift is associated with the corresponding density on large scales: galaxies form in high density regions and thus first ionize their surrounding until the ionizing radiation can penetrate to intermediate and lower density regions far from the sources. To quantify this correlation we compute the cross correlation between reionization redshift and density field. First we define the dimensionles fluctuations fields of the gas density

$$\Delta_\varrho \;=\; 1+\delta_\varrho(\vec{x}) \;=\; \frac{\varrho(\vec{x})}{\bar{\varrho}} \tag{3.5}$$

and of the reionization redshift

$$\Delta_z \;=\; 1+\delta_z(\vec{x}) \;=\; \frac{1+z_{ion}(\vec{x})}{1+\bar{z}}, \tag{3.6}$$

where $\bar{\varrho}$ is the mean gas density of the universe and the $\bar{z}$ is the mean value of the reionization redshift field $z_{ion}(\vec{x})$. Secondly we construct the two point statistics of the inverse Fourier transforms of the respective fluctuation fields $\Delta_i(\vec{x})$ and $\Delta_j(\vec{x})$ and derive the corresponding 3D cross or auto power

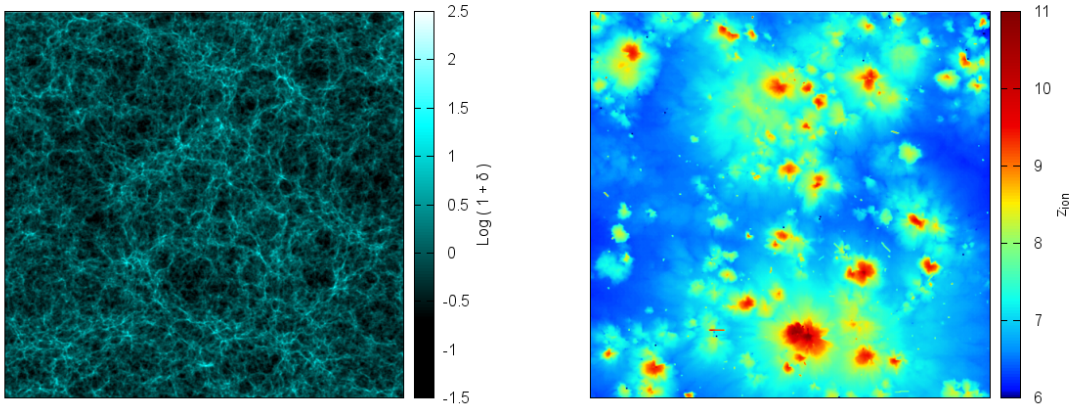

Figure 3.12: Slices from our 80 Mpc/h simulation box. Left: density field $1+\delta_\varrho$. Right: reionization redshift field z_{ion}. Large-scale overdense regions near sources are generally ionized earlier than large-scale underdense regions far from sources.

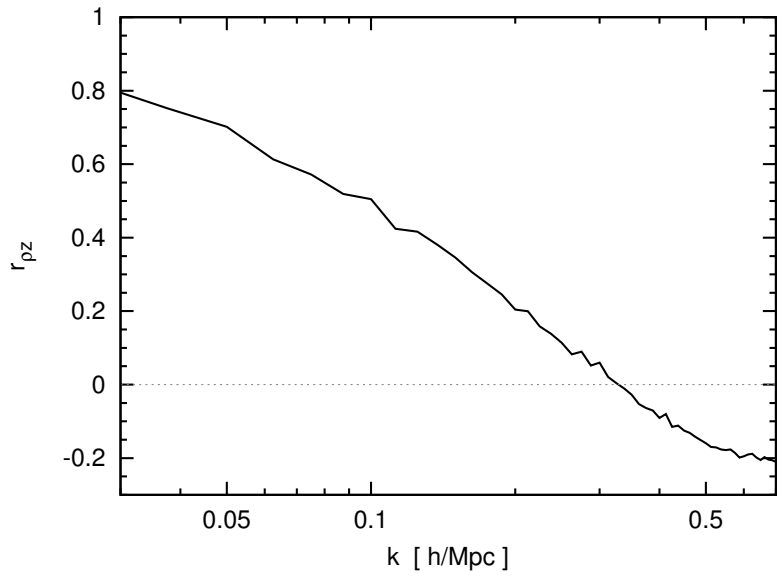

Figure 3.13: Cross correlation $r_{\varrho z}$ between overdensity $(1+\delta)$ and redshift of ionization z_{ion} at $\bar{z} \simeq 7$ as a function of wavenumber k (black solid line). The grey dotted line marks the line of no correlation or anticorrelation.

spectra $P_{ij}(k)$.

$$P_{ij}(k) = \langle \Delta_i^{\vec{k}} \Delta_j^{-\vec{k}} \rangle \tag{3.7}$$

$$\Delta^{\vec{k}} = \frac{1}{(2\pi)^{3/2}\ V^{1/2}} \int \Delta(\vec{x})\ \exp(i\vec{k}\vec{x})\ \mathrm{d}^3x \tag{3.8}$$

The cross correlation between the redshift (Δ_z) and density (Δ_ϱ) fluctuation fields is given by

$$r_{\varrho z}(k) = \frac{P_{\varrho z}(k)}{\sqrt{P_{zz}(k)\ P_{\varrho\varrho}(k)}}. \tag{3.9}$$

In Fig. 3.13 we show the cross correlation $r_{\varrho z}$ that we obtained for our reionization simulation. Indeed we find on scales larger than ~ 3 Mpc/h a correlation between the density and reionization redshift fluctuations. This correlation increases towards larger scales since large-scale overdense regions near sources are generally ionized earlier than large-scale underdense regions far from sources. Nevertheless for smaller scales than 3 Mpc/h density and reionization redshift fluctuations become anticorrelated, i.e. higher density regions ionize later than low density regions. With increasing density the number of recombinations becomes important and eventually high enough to prevent full ionization, leading to an anticorrelation between ϱ and z_{ion}. This hint to partially neutral high density regions agrees with our previous results from the power spectrum of the ionized density fluctuations and the ionization fraction-density relation. At scales smaller than ~ 1.4 Mpc/h we reach the minimum distance between sources as we have grouped sources within a minimal radius of 0.7 Mpc/h.

3.3.3 Is there a statistical difference in the ionization profiles for different source properties?

In this section we investigate the imprint of source characteristics in the ionization structure. As we have shown in Chapter 2 the ionization profiles depend on the spectral shapes of the sources which may differ more or less for different source characteristics. Hence, we compute the mean ionization profiles for different groups of sources. We classify into young ($t_\star/h < 10^8$ yr) and old ($t_\star/h > 10^8$ yr), low ($Z_\star < 10^{-3}$ $Z_\odot$) and high ($Z_\star > 10^3$ $Z_\odot$) metallicities and different stellar mass ($M_\star$) ranges ($10^6 - 10^8$ $M_\odot$/h, $10^8 - 10^9$ $M_\odot$/h, $10^9 - 10^{10}$ $M_\odot$/h). In Figures 3.14 - 3.16 the average ionization profiles of hydrogen (H II) and helium (He II, He III) are shown for different redshifts during reionization as noted. Based on our classified groups of sources we discuss the influence of stellar mass, stellar metallicity and stellar age respectively:

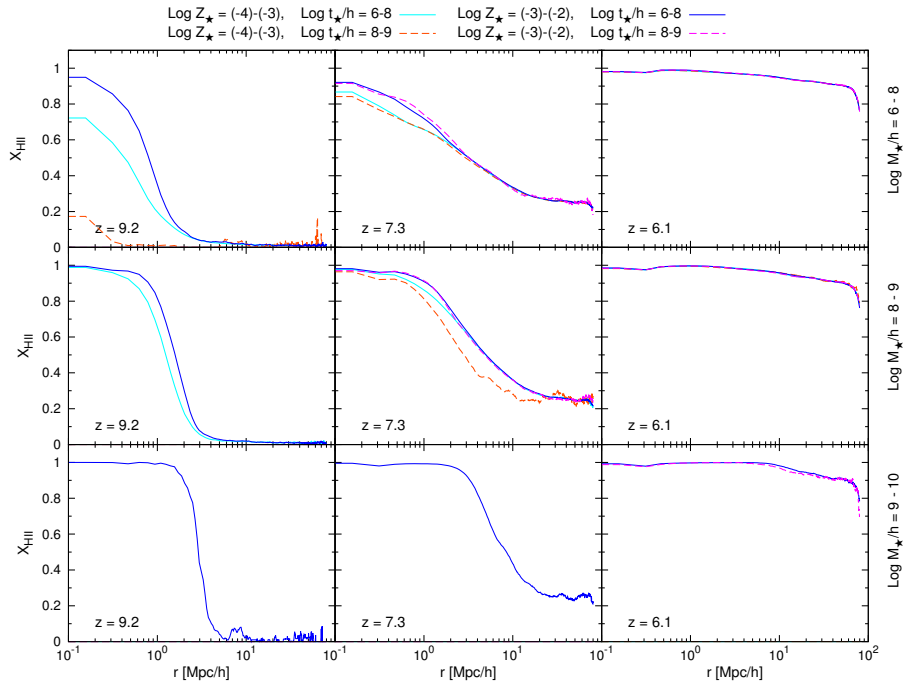

Figure 3.14: Evolution of the mean $X_{\rm HII}$ ionization profiles from $z = 9.2$ (left column) to $z = 6.1$ (right column). For the computation of the mean all sources within the respective stellar mass, age and metallicity bin are taken into account. The first row shows the profiles for $10^6 \leq M_\star/h \leq 10^8$, the second for $10^8 \leq M_\star/h \leq 10^9$ and the third for $10^9 \leq M_\star/h \leq 10^{10}$. In each panel profiles are shown for old (magenta/orange) and young (blue/light blue), low (orange,light blue) and high (red, blue) metallicity galaxies.

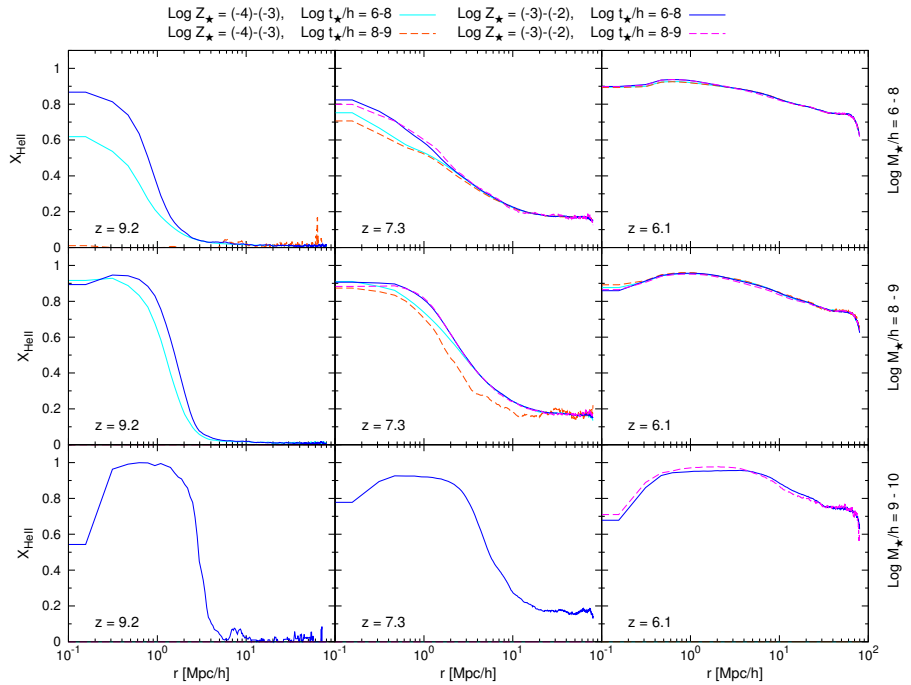

Figure 3.15: Evolution of the mean $X_{\rm HeII}$ ionization profiles from $z = 9.2$ (left column) to $z = 6.1$ (right column). For the computation of the mean all sources within the respective stellar mass, age and metallicity bin are taken into account. The first row shows the profiles for $10^6 \leq M_\star/h \leq 10^8$, the second for $10^8 \leq M_\star/h \leq 10^9$ and the third for $10^9 \leq M_\star/h \leq 10^{10}$. In each panel profiles are shown for old (magenta/orange) and young (blue/light blue), low (orange,light blue) and high (red, blue) metallicity galaxies.

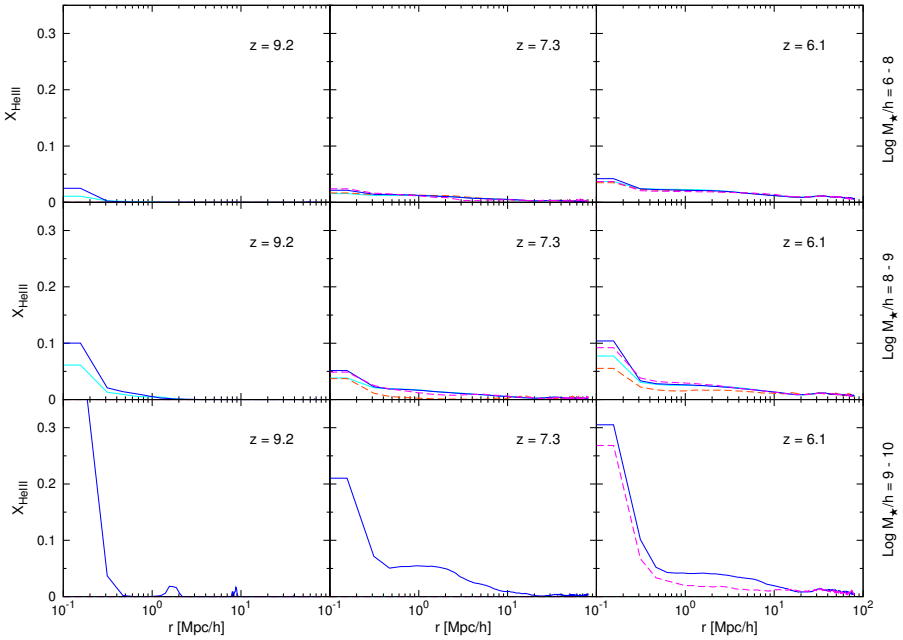

Figure 3.16: Evolution of the mean X_{HeIII} ionization profiles from $z = 9.2$ (left column) to $z = 6.1$ (right column). For the computation of the mean all sources within the respective stellar mass, age and metallicity bin are taken into account. The first row shows the profiles for $10^6 \leq M_\star/h \leq 10^8$, the second for $10^8 \leq M_\star/h \leq 10^9$ and the third for $10^9 \leq M_\star/h \leq 10^{10}$. In each panel profiles are shown for old (magenta/orange) and young (blue/light blue), low (orange,light blue) and high (red, blue) metallicity galaxies.

- **Mass:** Comparing the hydrogen and helium ionization profiles, we find that with increasing stellar mass the size of the ionized H II and He III spheres around the galaxies rises. This is expected since the number of ionizing photons is proportional to the stellar mass, leading to larger ionized regions for higher stellar mass galaxies. The effect can also be seen for He II, although with rising stellar mass the amount of He III increases in the inner core leading to a decrease in He II.

- **Metallicity:** From our ionization profiles we find that sources with higher metallicity exhibit larger ionized spheres. Considering the spectra for a fixed stellar mass sources with low metallicity should show higher number of ionizing photons and hence should produce larger ionized spheres. In Section 3.2.2, however we found a general trend in our galaxy population: the larger the stellar masses of the galaxies, the higher are their metallicities and ages. The observed trend origins from the correlation of the metallicities with stellar masses: on average galaxies with high metallicities are more massive, leading to a higher number of ionizing photons and increasing the size of the ionized regions.

- **Age:** The differences due to different ages are not strong but we comment on the slight differences we observe. For hydrogen the ionized spheres of the younger galaxies exceed those of the older ones, since the spectra of young stellar populations exhibit more ionizing photons per stellar mass. For He III we see this trend even more pronounced than for hydrogen: as the ionization energy of helium exceeds the one of hydrogen, helium is even more sensitive to the number of high energy photons in the spectra, leading to the better distinction between old and young populations. Naturally we find for He II the opposite trend, i.e. the ionized spheres of old galaxies exceed the ionized spheres of young galaxies, since for young galaxies a greater fraction of He II was ionized to He III than for old galaxies.

To conclude, the ionization profiles are mainly determined by the stellar masses of the sources. Since spectra are only weakly affected by stellar metallicities, the ionization profiles are dominated by the stellar masses of the sources and not the stellar metallicities. Stellar ages change the spectral shape

to a greater extent and thus while reionization is ongoing younger sources show slightly larger ionized regions than older sources.

3.3.4 Thomson optical depth

The optical depth along the mean line of sight between redshift z and the observer at redshift $z = 0$ is given by the Thomson scattering events of the free electrons.

$$\tau_e = c\sigma_T \int_0^z \mathrm{d}z' \; n_e(z') \frac{\mathrm{d}t}{\mathrm{d}z'} \qquad (3.10)$$

Here $\sigma_T = 6.65 \times 10^{-25}$ cm^2 is the Thomson scattering cross section, c the speed of light and $n_e(z)$ the mean number density of free electrons at redshift z

$$n_e(z) = n_{\mathrm{H}} X_{\mathrm{HII}}(z) \; (1+z)^3 \qquad (3.11)$$

where n_H is the mean hydrogen density today and $X_{\mathrm{HII}}(z)$ the hydrogen ionization fraction at redshift z. We compute the optical depth from the simulation outputs which provide us with the ionization fractions of hydrogen and helium for $z > 5.9$. For $5.9 \leq z < 3$, i.e. before helium is completely ionized, we assume $X_{\mathrm{HII}} = 1$, $X_{\mathrm{HeII}} = 0.95$ and $X_{\mathrm{HeIII}} = 0.02$ adopting the values from the last output of our simulation at $z \simeq 5.9$. For redshifts $z \leq 3$ we assume that helium is fully ionized, $X_{\mathrm{HeII}} = 0$ and $X_{\mathrm{HeIII}} = 1$.

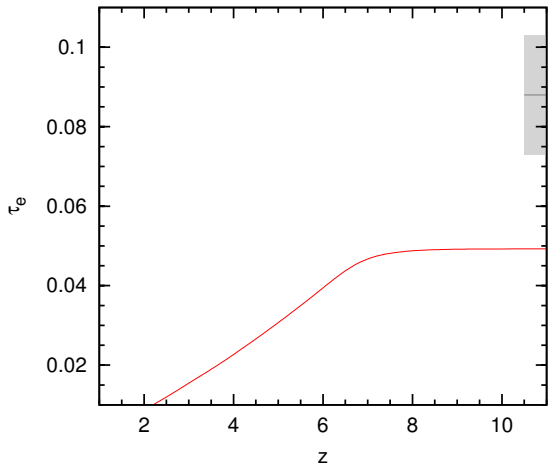

Figure 3.17: Evolution of the Thomson scattering optical depth of our reionization simulation (red, solid line). The dark grey line and the grey shaded area represent the 7-yr WMAP results value of 0.088±0.015.

In Fig. 3.17 we show the integrated optical depth obtained from our simulation and the measurements of the polarization of the CMB inferring the optical depth between us and the surface of last scattering (recombination). We find that our value for τ_e is lower than the WMAP7 value and its corresponding 1σ range. This deviation is due to the late reionization of hydrogen in our simulation and hints to two possible scenarios: either reionization occurred at higher redshifts or low mass sources which we do not resolve in our simulation partly ionize the IGM at very high redshifts leading to an extended reionization history such as in Ahn et al. (2012).

3.3.5 Thermal history

In this section we discuss the evolution of the gas temperature in the IGM during reionization: as the number of galaxies and their stellar mass rises with cosmic time (decreasing redshift), the amount of ionizing radiation and the number of ionization events increases. With each ionization event the IGM is heated by the remaining energy of the photon that is not used for ionization; this photoionization heating causes the mean gas temperature to rise during reionization as can be seen in Fig. 3.18. Analyzing the relation between temperature and density we can understand how reionization affects the heating of overdense regions around sources and of underdense regions far from sources. To extract the effects of photoionization heating by reionization we first analyze the temperature-density relation of the pure hydrodynamical simulation.

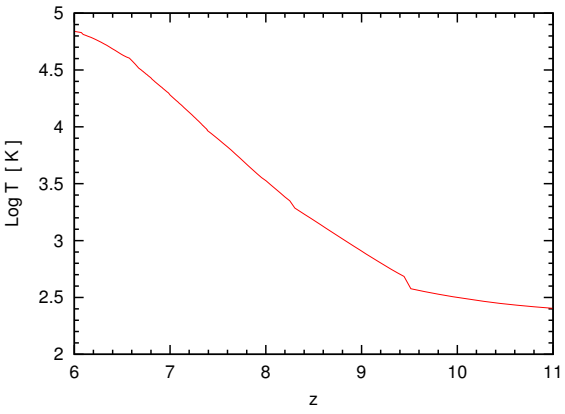

Figure 3.18: Evolution of the globally averaged temperature.

In the upper panel of Fig. 3.19 we show the mean temperature versus the overdensity at different redshifts. We find that with increasing density the IGM temperature rises. As gas particles falling into

deeper potentials gain more thermal energy, dense regions gain higher temperatures than less dense regions. With cosmic time the universe expands and its mean density decreases, the global temperature cools adiabatically. Nevertheless as structures form gas falls into gravitationally generated potential wells and is shock heated raising the mean gas temperature with decreasing redshift (see upper panel in 3.19).

Including the effect of photoionization heating by reionization, i.e. considering the results of the radiative transfer post-processed simulation, the temperature-density relation changes substantially (see middle panel in Fig. 3.19). As reionization proceeds, first overdense (Log$(1+\delta) < 1$) regions are heated followed by the underdense regions. While at the beginning of reionization the mean temperature rises with overdensity reflecting the trend in the hydrodynamical simulation, the relation is inverted towards the end of reionization, i.e. underdense regions exhibit a higher temperature than overdense regions. For very overdense regions (Log$(1+\delta) > 1$) we find an inverted relation during the whole progress of reionization.

To understand this thermal evolution we analyze the temperature-density relations in Fig. 3.20 at the different redshifts $z = 9.2$, 7.3, 6.4, 5.9 (corresponding to $\langle X_{\rm HII}\rangle = 0.01$, 0.25, 0.75, 1.00). From this Figure we find that the temperature evolution follows the ionization history, i.e. within ionized or partly ionized regions the temperature is increased. At the beginning of reionization (see $z = 9.2$ case in Fig. 3.20) only small regions around the sources are ionized and their temperature rises up to several 10^4 K due to photoionization heating.

As reionization proceeds the ionized regions grow and heat their interior above 10^4 K. From Fig. 3.20 we find for intermediate redshifts ($9 > z > 6.1$) two and at later times ($z < 7$) three preferred temperatures in these ionized regions to which we denote by $T_{eq} \approx 6 \times 10^4$ K, $T_{\rm HII} \approx 1.5 \times 10^4$ K and $T_{\rm HeII} \approx 3.5 \times 10^4$ K. The cells that have been heated to T_{eq} have reached their final ionization equilibrium where photoionization heating is balanced by recombination cooling; the photoionization rate is not increased noticeably by radiation of additional sources that are added with the growth of the ionized region. Since the recombination rate scales inversely with the density, cooling becomes more efficient for high density regions leading to an inverted temperature-density relation, i.e. temperature rising for decreasing density $T = T_0(1+\delta)^{\gamma-1}$ with $\gamma - 1 = -0.2$. Regions where final ionization equilibrium has been reached are located around the ionizing sources while regions where cells have been heated up to $T_{\rm HII}$ or $T_{\rm HeII}$ are farther from sources beyond the final ionization equilibrium front. Consequently the regions of $T_{\rm HII}$ and $T_{\rm HeII}$ are those where the IGM has been ionized but not reached the final ionization equilibrium. Located farther from the ionizing sources the high energy photons from the galaxies have been used up to ionize hydrogen and helium within the final ionization equilibrium regions. Thus only photons with lower energies are available to ionize the

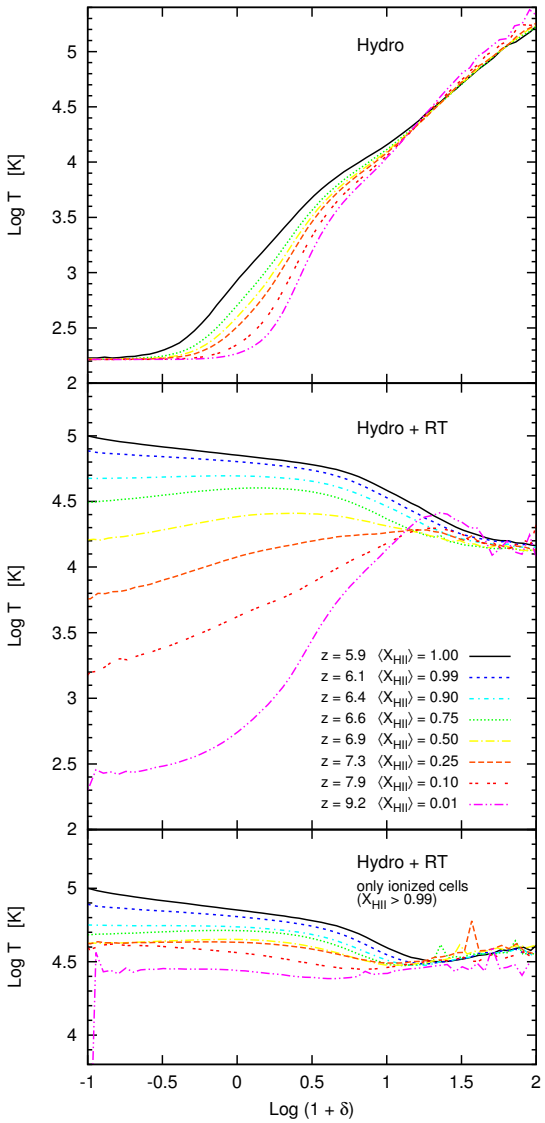

Figure 3.19: Mean temperature versus overdensity at different redshifts: The top panel shows the mean temperatures from the hydrodynamic simulation; the middle panel depicts the mean temperatures from the full reionization simulation, i.e. including radiative transfer; the bottom panel shows the mean temperature from the full reionization simulation but taking only cells ($X_{HII} > 0.99$) into account.

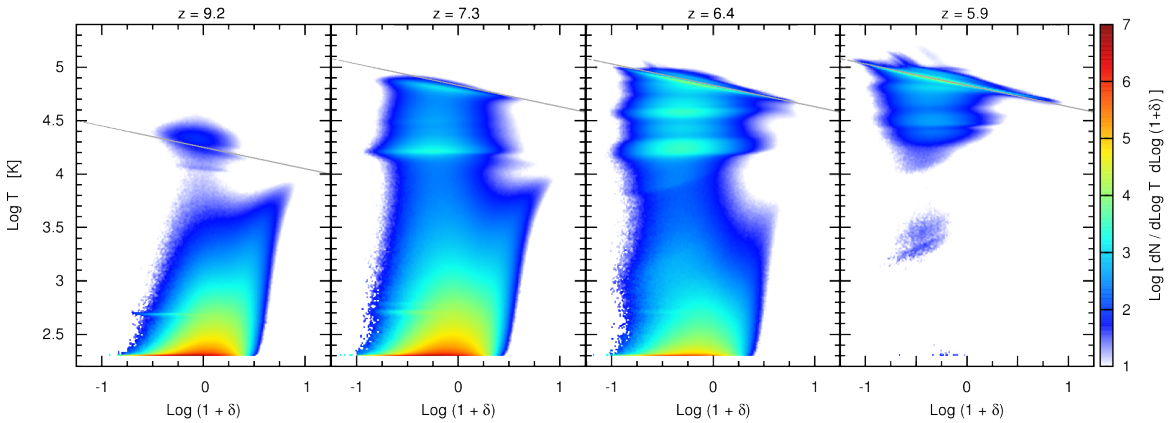

Figure 3.20: Contour plots of the distribution of gas temperature against the overdensity at redshifts $z = 9.2$, 7.3, 6.4 and 5.9. The color scale corresponds to the number of cells within each temperature and overdensity bin. The grey lines show the inverted temperature relation $T = T_0(1+\delta)^{\gamma-1}$ with $\gamma - 1 = -0.2$.

medium but do not provide sufficient energy for heating. Hence, the regions of $T_{\rm HII}$ correspond to regions of completely ionized hydrogen but not helium, while regions that have been heated up to $T_{\rm HeII}$ correspond to ionized regions where helium is completely single ionized. As photons with higher energies are required for ionizing helium, regions heated up to $T_{\rm HeII}$ are surrounded by the cooler $T_{\rm HII}$ regions and occur later in the reionization process when the spectra of the sources are harder due to the increased stellar metallicity. Furthermore we find the corresponding temperature-density relations to be isothermal indicating that the increasing trend of the temperature with rising density in the hydrodynamics is compensated by the photoionization heating.

As the universe becomes more and more ionized the final ionization equilibrium fronts expand until the IGM is in ionization equilibrium; the $T_{\rm HII}$ and $T_{\rm HeII}$ regions vanish (see $z \simeq 6$ case in Fig. 3.20) as their cells are also heated up to T_{eq}.

With this detailed analysis we can understand the evolution of the mean temperature-density relation. Starting from a neutral medium the mean temperature increases towards higher densities due to the deeper potential wells for collapsed structures. As the ionized regions grow, the volume fraction being in the final ionization equilibrium increases and explains the gradual inversion of the temperature-density relation. The final temperature-density relation satisfies $T = T_0(1+\delta)^{\gamma-1}$ with $\gamma - 1 = -0.2$, in agreement with Trac et al. (2008). Trac et al. (2008) found this relation after reionization was completed and interpreted it as a result that voids are ionized last and thus have less time to cool compared to halos and filaments. We find that this inverted temperature-density relation is due to the density dependency of the final ionization equilibrium and becomes more pronounced as more cells reach this equilibrium state. In very overdense regions the mean temperature decreases also due to the partial neutral patches that show a lower ionization fraction and thus the photon energy is primarily used to keep the region partially ionized. If we consider only cells that are completely ionized ($X_{\rm HII} > 0.99$), we find that the temperature-density relation in very overdense regions is not inverted, suggesting that only cells close to or at source locations which exhibit a very high ionizing emissivity are taken into account.

3.3.6 The 21 cm signal

One of the promising observables to detect reionization is the 21cm line representing the energy difference between the singlet and triplet state of neutral hydrogen. However, the intensity of the 21cm in emission or absorption depends on the difference between the spin temperature T_s and the CMB temperature T_{CMB}; thus the differential brightness temperature of the 21cm radiation is given

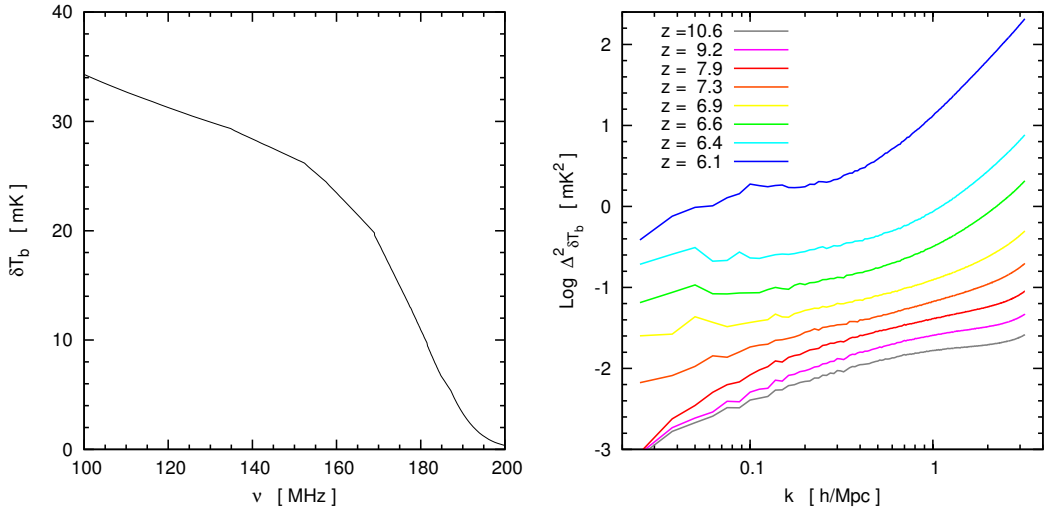

Figure 3.21: Left: globally averaged 21cm differential brightness temperature of reionization in the respective frequency interval ($\nu = hc/\lambda_{21cm}(1+z)$). Right: Dimensionless power spectra of the differential brightness temperature at different redshifts. Redshifts $z = 10.6$, 9.2, 7.9, 7.3, 6.9, 6.6, 6.4, 6.1 correspond to $\langle X_{\rm HII}\rangle \simeq 10^{-3}$, 10^{-2}, 0.1, 0.25, 0.5, 0.75, 0.9, 0.99, respectively.

by

$$\begin{aligned}\delta T_b &= \frac{T_s - T_{CMB}(z)}{1+z}\,(1-\exp(-\tau)) \\ &\approx \frac{T_s - T_{CMB}(s)}{1+z}\,\frac{3\lambda_{21cm}^3 A_{10} T_{21cm} n_{HI}(z)}{32\pi T_s H(z)} \\ &= 28.5\text{mK}\left(\frac{1+z}{10}\right)^{1/2}(1+\delta)\frac{\Omega_b}{0.042}\frac{h}{0.073}\left(\frac{0.24}{\Omega_m}\right)^{1/2}. \end{aligned} \tag{3.12}$$

Here τ is the 21 cm optical depth along the line of sight, $\lambda_{21cm} = 21.16$ cm the restframe wavelength, T_{21cm} the corresponding energy difference between the singlet and triplet state and A_{10} the Einstein emission coefficient, $1+\delta = n_{\rm HI}/\langle n_{\rm HI}\rangle$ the mean number density of neutral hydrogen in units of the mean $\langle n_{\rm HI}\rangle \propto (1+z)^3$ and $H(z)$ the Hubble constant which we approximate for $z >> 1$ by $H_0\Omega_m^{1/2}(1+z)^{3/2}$. In this work we assume $T_s \ll T_{CMB}$, since the UV background from early sources heats the neutral IGM gas above the CMB temperature via the Wouthuysen-Field effect (Lyα pumping). This assumption is mostly true during reionization and only fails at very early times of reionization when the first sources turn on.

For each output of our reionization simulation we compute the corresponding brightness temperature fields $\delta T_b(\vec{x})$ from which we derive the global average brightness temperature $\langle\delta T_b\rangle(z)$ and the respective power spectra. In the left panel of Fig. 3.21 we show $\langle\delta T_b\rangle(\nu)$ where lower frequencies correspond to higher redshifts, $\nu(z) = hc/(\lambda_{21cm}(1+z))$. The 21 cm line is seen in emission and decreases towards lower redshifts (higher frequencies). While the universe is predominantly neutral and $\langle\delta T_b\rangle$ shows values of several 10 mK at early times, the ionized regions around the sources grow leading to a shrinking of the neutral regions as reionization proceeds, $(1+\delta)$ and correspondingly $\langle\delta T_b\rangle$ decreases until the universe is completely ionized ($1+\delta \approx 0$).

The evolution of the differential brightness temperature on different scales can be analyzed with help of the power spectra of the 21cm signal at various redshifts (see right panel in Fig. 3.21). From the brightness temperature fields $\delta T_b(\vec{x})$ we compute the dimensionless power spectrum $\Delta^2_{\delta T_b}$ of the density contrast $\delta T_b(\vec{x})/\langle\delta T_b\rangle$ is given by

$$\Delta^2_{\delta T_b} = \frac{k^3}{2\pi^3}P(k) = \frac{k^3}{2\pi^3}\,\langle|\Delta_{\delta T_b}(\vec{k})|^2\rangle. \tag{3.13}$$

Due to the growth (shrinking) of the ionized (neutral) regions during reionization the power spectrum first rises as the density contrast increases and secondly power is transferred from small to large scales.

At the beginning of reionization the 21cm power spectrum coincides with the power spectrum of the neutral density fluctuations (cf. Fig. 3.10) as the universe is predominantly neutral. As small ionized bubbles grow around the sources ($9 \leq z \leq 7.5$) the 21cm power spectrum steepens exhibiting more power on smaller scales (corresponding to the size of the inoized bubbles). As the small ionized regions and ionized clusters merge ($7.5 \leq z \leq 6.9$) the 21cm power spectrum flattens; ionized regions extend to larger scales whereat their sizes become more comparable (their size distribution sharpens). Having built up sufficient large ionized regions and clusters ($6.9 \leq z \leq 6.6$), the photons can propagate within these regions and increase the size of the ionized regions continuously leading to a speedup of ionization and an continuous increase on all scales of the 21cm power spectrum. As the average size of the neutral regions start to decrease and the small neutral patches have been already ionized ($6.6 \leq z \leq 6.4$), ionization slows down; the 21cm power spectrum increases uniformly due to the enhanced density contrast of δT_b. At late stages of reionization the large ionized regions start to merge causing the neutral regions to split and become smaller ($6.4 \leq z \leq 6$); the 21cm power spectrum firstly steepens again due to the lack of neutral regions on larger scales, and secondly its amplitude rises as the decreasing neutral fraction enhances the contrast between ionized and neutral regions. Furthermore we find an enhanced power on small scales: in high density regions, i.e. on small scales, the number of recombination outweighs the photoionization events leaving the regions partly neutral.

In summary, as the universe becomes more ionized, the brightness temperature decreases, the 21cm signal vanishes in the ionized regions and leads to an increased density contrast on the scales of the ionized regions which determines the shape of the power spectrum. Hence, the 21cm signal and its power spectrum tracks not only the distribution of the neutral patches (shape of the power spectrum) but also the average neutral fraction (amplitude of the power spectrum and mean brightness temperature).

3.4 Conclusions

In order to simulate self-consistently the Epoch of Reionization we have post-processed a hydrodynamical simulation of an 80Mpc/h box with 3D radiative transfer where the sources of ionizing radiation are modeled using the stellar masses, ages and metallicities provided by the star particles in the hydrodynamical simulation. Reionization starts rather late with the appearance of the first resolved halos $M_h > 10^9\,\mathrm{M}_\odot$ at $z \simeq 11$ and finishes at $z \simeq 6$. While He II follows the evolution of H II from early times on, the first He III regions appear considerably later at $z \simeq 7-8$; at $z \simeq 6$ X_{HeIII} has just reached a value of 0.015, reflecting the stellar spectral shape of the sources. Starting at the source locations the ionized bubbles grow, cluster and merge with cosmic time; the increase in their spatial extension is seen in the power spectrum of the ionized density fluctuations. Analyzing the relation between the mass-weighed and volume-weighed ionization fraction as well as the cross correlation between density and redshift of ionization, we find that our reionization scenario shows inside-out character: high density regions around sources are ionized first while low density regions far from sources are ionized last. We find a correlation between density and the reionization redshift on scales larger than 3 Mpc/h; on smaller scales dense or clumpy regions farther from sources remain partially neutral due to a high number of recombinations; the power spectrum of the neutral density fluctuations increases on smaller scales even after reionization finished. Analogously we find the same features of power on small scales in the 21cm power spectrum at the end of reionization. In the 21cm power spectrum are not only the neutral density fluctuations encoded, but its amplitude reflects also the global ionization fraction of hydrogen.

The global as well as the local thermal evolution follows the global or local ionization history. Within fully ionized regions where ionizing photons propagate unattenuated the temperature-density relation is inverted according to $T \propto T_0(1+\delta)^{\gamma-1}$ with $\gamma - 1 = -0.2$; cooling in denser regions is more efficient due to the increasing number of recombinations. Interestingly, during reionization the value of the temperature behind the ionization fronts (within the ionized regions) is considerably lower than in regions where the photons can propagate freely.

Analysing the sizes of the ionized spheres for different stellar metallicities, ages and stellar masses, we find that predominantly stellar mass and slightly stellar age determine the size of the ionized bubble, while stellar metallicity has no noticeable effect. Nevertheless it turns out to be rather difficult to differentiate the properties of star-forming galaxies during the epoch of reionization by means of the ionization bubbles.

We have simulated the epoch of reionization self-consistently by modeling each source with their individual luminosity and spectrum and accounting for the clumpiness of the IGM individually in each cell by the use of a local clumping factor. Without imposing another model for self-shielded regions (as has been done in Bolton and Haehnelt (2013); Mesinger et al. (2015)) we obtain partial neutral patches in high density regions. These neutral regions are located not too far from ionizing sources but the enhanced number of recombinations keeps the medium partially neutral making them likely to be candidates for Lyman limit systems.

Nevertheless our simulation suffers from multiple caveats: Firstly we only account for sources showing halo masses of at least $10^9\,\mathrm{M}_\odot$. Although the contribution of low-mass halos during reionization is certainly limited by radiative feedback, they dominate the beginning of reionization and shift its start towards higher redshifts. A partially ionized universe at high redshifts ($z > 10$) due to the presence of low-mass halos might explain the rather high observed value of the optical depth which cannot be obtained for late high-mass reionization scenarios as ours. Due to self-regulation reionization is dominated by high-mass halos at later times (Ahn et al., 2012) when radiative feedback becomes efficient in suppressing low-mass halos. Thus our reionization scenario is a fair approximation as soon as high-mass halos dominate the ionization history at an ionization fraction of about 20% for late overlap (Ahn et al., 2012).

Secondly we do not perform a radiation hydrodynamical simulation; coupled simulations of radiative transfer and hydrodynamics are computationally very expensive making simulations of large volumes that are needed to trace reionization feasible only at low resolutions. Although our simulation does not include effects of radiative feedback on galaxy formation, we aim to account for this process by considering only sources with halo masses of at least $10^9\,\mathrm{M}_\odot$, i.e. galaxies that are not destroyed by radiative feedback.

Thirdly we assume an arbitrary constant value for the escape fraction of ionizing photons for all galaxies. This might be a rough assumption, as the escape fraction might vary with halo mass (Ferrara and Loeb, 2013) and/or redshift (Kim et al., 2013; Dijkstra et al., 2014). A decreasing escape fraction with halo mass leads to a more homogeneous size distribution of the ionized regions, whilst an increasing escape fraction results in larger ionized regions around the most massive sources. A variation of the escape fraction with redshift affects the duration of reionization as well as the size distribution of the ionized regions. If the escape fraction decreases with redshift, the ionization of the IGM starts slowly but is accelerated with cosmic time, whilst an increasing escape fraction with redshift softens the increase in the number of ionizing photons with time and results in a more extended reionization scenario with a more homogeneous size distribution of the ionized regions.

Our results highlight the importance of resolving small scale high density peaks leading to first stars at the beginning of reionization or self-shielded regions farther from sources at later times. Having reionization modelled self-consistently our results on the ionization topology are in agreement with other works but allows a more detailed analysis of the link between ionization characteristics and source properties. Nevertheless the source properties might be altered due radiative feedback, especially at early times. Since the inclusion of radiative feedback demands a radiation-hydrodynamical code we leave this for future work.

Chapter

4

The visibility of Lyman Alpha Emitters: constraining reionization, escape fraction of ionizing photons and dust [1]

We couple state of the art cosmological simulations (GADGET-2) with a dust model and a radiative transfer code (pCRASH) to build a complete model for high-redshift Lyman Alpha emitters (LAEs). Due to the poor constraints available on the escape fraction of H I ionizing photons ($f_{\rm esc}$) from galaxies, we study five different reionization scenarios using $f_{\rm esc} = 0.05, 0.25, 0.5, 0.75, 0.95$. For a given $f_{\rm esc}$ and $\langle\chi_{HI}\rangle$ combination, the only free-parameter left to match model results to observed Lyα and UV luminosity functions of LAEs at $z \simeq 6.6$ is the relative escape of Lyman Alpha (Lyα) and continuum photons from the galactic environment (f_α/f_c). Allowing for clumped dust, we find a three-dimensional degeneracy between $f_{\rm esc}$, $\langle\chi_{HI}\rangle$ and f_α/f_c such that a decrease in the intrinsic Lyα luminosity can be compensated by an increase in the Lyα transmission through the intergalactic medium and/or an increasing Lyα escape out of the galactic environment. The observations can be reconciled with the theoretical model for a much larger parameter space $\langle\chi_{HI}\rangle \simeq 0.5 - 10^{-4}$ or $\langle T_\alpha\rangle_{LAE} \simeq 0.4 - 0.5$, $f_{\rm esc} \simeq 0.05 - 0.50$ and $f_\alpha/f_c = 0.6 - 1.8$, i.e., if dust is indeed clumped in the interstellar medium of high-redshift galaxies, we can not differentiate between a Universe which is either completely ionized or half neutral, or where 40% or 50% of Lyα radiation of the LAEs is transmitted, or has an $f_{\rm esc}$ ranging between 5-50%.

4.1 Introduction

The Epoch of Reionization (EoR) begins when the first stars start producing neutral hydrogen (H I) ionizing photons, carving out an ionized Strömgren region in the neutral intergalactic medium (IGM) around themselves, and ends when all the H I in the IGM is ionized. Understanding the process of cosmic reionization is extremely important because in addition to marking the last major change in the ionization state of the Universe, it affected all subsequent structure formation through a number of radiative feedback effects (see e.g. Barkana and Loeb, 2001; Ciardi and Ferrara, 2005; Maio et al., 2011; Sobacchi and Mesinger, 2013a; Wyithe and Loeb, 2013, and references therein). A broad picture that has emerged (Choudhury and Ferrara, 2007) is one wherein hydrogen reionization is an extended process that starts at $z \approx 15$ and is about 90% complete by $z \simeq 8$; while it is initially driven by metal-free Population III stars in low-mass halos ($\leq 10^8 M_\odot$), the conditions for star formation in these halos are soon erased by a combination of chemical and radiative feedback by $z \simeq 10$. However, any attempt at modelling reionization necessarily requires a number of important assumptions regarding the number of H I ionizing photons produced by the source galaxy population depending on their physical properties, the fraction of these photons ($f_{\rm esc}$) that can escape out of the galactic environment and contribute to reionization, and the clumping factor of the IGM at high-redshifts, to name a

[1] This chapter contains work which is published in Hutter, A.; Dayal, P.; Partl, A.M.; Müller, V; MNRAS 441 2861-2877, 2014; doi: 10.1093/mnras/stu791

few (Salvaterra et al., 2011). Given these assumptions, reionization scenarios need to be constantly updated as new data sets are acquired.

By virtue of their continually growing numbers, a valuable new data set is provided by high-redshift Lyman Alpha Emitters (LAEs); this is a class of galaxies identified by means of their Lyman Alpha (Lyα) emission line at 1216 Å in the galaxy rest-frame. Indeed, hundreds of LAEs have now been confirmed in the epoch of reionization: $z \simeq 5.7$ (Malhotra et al., 2005; Shimasaku et al., 2006; Hu et al., 2010; Curtis-Lake et al., 2012), $z \simeq 6.6$ (Taniguchi et al., 2005; Kashikawa et al., 2006; Hu et al., 2010; Ouchi et al., 2010; Kashikawa et al., 2011) and $z \simeq 7$ (Iye et al., 2006; Ouchi et al., 2009; Stark et al., 2010; Pentericci et al., 2011). In addition to their number statistics, LAEs have been rapidly gaining popularity as probes of reionization and high-redshift galaxy evolution for two reasons: (a) the strength, width and continuum break bluewards of the Lyα line makes their detection unambiguous, and (b) Lyα photons are extremely sensitive to attenuation by H I; the observed Lyα luminosity can then be used to infer the ionization state of the IGM at redshifts close to those of the emitter and hence to reconstruct, at least piecewise, the cosmic reionization history.

However, interpreting LAE data is complicated by a number of physical effects. First, the intrinsic Lyα luminosity depends on the total number of H I ionizing photons that are produced by a galaxy, depending on the star formation rate (SFR), age and metallicity of its stellar population (e.g. Santos, 2004). Second, depending on the H I and dust contents in the interstellar medium (ISM), only a fraction $(1 - f_{\rm esc})$ of these H I ionizing photons are able to contribute to the intrinsic Lyα luminosity by ionizing the ISM H I; the rest contribute to building the ionized H II region around the galaxy. We briefly digress to note that the dependence of $f_{\rm esc}$ on galaxy properties has been the subject of much recent debate: while some authors find $f_{\rm esc}$ to decrease with an increase in the halo mass (Razoumov and Sommer-Larsen, 2010; Yajima et al., 2011; Ferrara and Loeb, 2013), other works find the opposite trend (Gnedin et al., 2008; Wise and Cen, 2009). The value of $f_{\rm esc}$ also remains poorly constrained with findings ranging from a few percent (e.g. Gnedin et al., 2008) up to $20 - 30\%$ (e.g. Mitra et al., 2013) or even higher (e.g. Wise and Cen, 2009). Third, only a fraction (f_α) of the Lyα photons produced inside a galaxy can escape out of it unattenuated by dust (Dayal et al., 2008; Finkelstein et al., 2009; Nagamine et al., 2010; Forero-Romero et al., 2011; Dayal and Ferrara, 2012). Fourth, only a fraction (T_α) of the Lyα photons that emerge out of a galaxy are transmitted through the IGM and reach the observer. As expected, this transmission sensitively depends on the IGM H I ionization state and it has been shown that only galaxies residing in over-lapping H II regions would be observed as LAEs in the initial stages of reionization, i.e. reionization increases the observed clustering of LAEs (McQuinn et al., 2007b; Dayal et al., 2009). Fifth, the Lyα IGM transmission calculation is complicated by the presence of peculiar velocities. Inflows (outflows) of gas into (from) the emitter blue-shift (red-shift) the Lyα line, leading to a decrease (increase) in the value of T_α along different lines of sight, strongly affecting the visibility of galaxies as LAEs (Verhamme et al., 2006; Iliev et al., 2008; Zheng et al., 2010; Dijkstra et al., 2011). Indeed, Santos (2004) has shown that the IGM ionization state can not be constrained in the presence of peculiar velocities. However, Dayal et al. (2011) have shown that the interpretation of LAE data is much more involved; a decrease in the Lyα transmission due to peculiar velocities and/or a highly neutral IGM can be compensated by an increase in f_α due to dust being clumped in the ISM of LAEs, as per the 'Neufeld-model' (Neufeld, 1991).

A number of past theoretical works have used one or more of the above ingredients to use LAEs as tracers of reionization. With semi-analytic modelling, a number of authors (e.g. Dijkstra et al., 2007; Dayal et al., 2008; Samui et al., 2009) have shown that the LAE Lyα luminosity functions (LFs) are consistent with a fully ionized IGM and can be explained solely by an evolution of the underlying dark matter halo mass functions. However, when considered in combination with the non-evolving observed ultraviolet (UV) LFs of LAEs between $z \simeq 5.7$ and 6.6 (Kashikawa et al., 2006), some of these works (Dijkstra et al., 2007; Ouchi et al., 2010) argue for an additional dimming of the Lyα line by about 30%. A number of studies have used large pure dark matter simulations to study the clustering of LAEs (McQuinn et al., 2007a; Iliev et al., 2008; Orsi et al., 2008). Finally, a number of studies have been undertaken using cosmological hydrodynamic simulations with dust (Dayal et al., 2008, 2009; Nagamine et al., 2010; Forero-Romero et al., 2011), with radiative transfer without dust (Zheng et al., 2010) and radiative transfer with dust (Dayal et al., 2011; Forero-Romero et al., 2011; Duval et al., 2014).

This work is quite close in spirit to the calculations presented in Dayal et al. (2011) wherein the authors used (a) cosmological hydrodynamic simulations run with GADGET-2 to obtain the physical properties of $z \simeq 5.7$ galaxies, (b) a dust model that took into account the entire star formation history of each galaxy to calculate its dust enrichment and, (c) a RT code (CRASH) to obtain the ionization

fields to calculate the IGM Lyα transmission for each galaxy, in order to identify the simulated galaxies that would be observationally classified as LAEs. Using this model, the authors showed that the effects of dust and IGM are degenerate in affecting the visibility of LAEs such that a large f_α can be compensated by a small T_α and vice versa to yield a given value of the observed Lyα luminosity. However, the main caveat in that work was that the authors used a constant value of $f_{\rm esc} = 0.02$ (Gnedin et al., 2008) for all galaxies in their calculations, and started their RT runs assuming the IGM gas to be in photoionization equilibrium with a uniform ultraviolet background (UVB) produced by unresolved sources corresponding to an average neutral hydrogen fraction, $\langle \chi_{\rm HI} \rangle = 0.3$.

In this work, we substiantially enhance the model presented in Dayal et al. (2011) to build a self-consistent model that couples cosmological SPH simulations, dust modelling and a fast RT code (pCRASH) to identify LAEs without making any prior assumptions on the IGM ionization state, $f_{\rm esc}$ and the ISM dust distribution. Starting from a uniform neutral IGM, consistent with the Haardt and Madau (1996) background imposed in simulations, we use 5 different values of $f_{\rm esc} = 0.05, 0.25, 0.5, 0.75, 0.95$ in order to study how varying $f_{\rm esc}$ affects the visibility of LAEs through: (a) the direct impact on the intrinsic Lyα luminosity, and (b) the IGM Lyα transmission that depends on the topology and extent of H II regions as determined by $f_{\rm esc}$. Comparing the statistics of the simulated LAEs to observations, our aim is to jointly constrain three fundamental parameters that determine the visibility of LAEs - $f_{\rm esc}$, χ_{HI} (or T_α) and the relative escape of Lyα photons with respect to continuum photons from the dusty ISM of galaxies (f_α/f_c).

We begin by describing the hydrodynamical simulation, the dust model and the identification of galaxies as Lyman Break Galaxies (LBG) through the UV continuum in Sec. 4.2. We follow this approach since UV photons are only attenuated by dust but unaffected by the IGM ionization state, simplifying their identification. In order to validate the simulations, we compare the simulated LBG UV LFs to observations in Sec. 4.3; a comparison of the simulated LBG stellar mass functions, stellar mass densities and specific star formation rates with the observations are also shown in Sec. 4.3 for completeness. Once the physical properties of the simulated galaxies have been validated, we choose a simulation snapshot at the edge of the epoch of reonization ($z \simeq 6.7$) and post-process it with a fast RT code (pCRASH) with the 5 values of $f_{\rm esc}$ mentioned above, as explained in Sec. 4.4. We then compare the simulated LAE UV and Lyα LFs with observations (Kashikawa et al., 2011) in Sec. 4.5 in order to jointly constrain $f_{\rm esc}$, χ_{HI} and f_α/f_c. Due to the model dependent relation between χ_{HI} and the Lyα IGM transmission (T_α) we show our constraints also in terms of $f_{\rm esc}$, T_α and f_α/f_c, before concluding in Sec. 4.6.

4.2 Cosmological hydrodynamic simulations

In this section we describe the cosmological simulation used to obtain the physical properties of high-redshift galaxies and the semi-analytic model used to obtain their dust enrichment, in order to calculate their observed visibility in the UV.

4.2.1 The simulation

The hydrodynamical simulation analyzed in this work has been carried out using the TreePM-SPH code GADGET-2 (Springel, 2005). The adopted cosmological model corresponds to the ΛCDM universe with dark matter (DM), dark energy and baryonic density parameter values of (Ω_Λ, Ω_m, Ω_b) = (0.73, 0.27, 0.047), a Hubble constant $H_0 = 100h = 70 {\rm kms}^{-1}{\rm Mpc}^{-1}$, and a normalisation $\sigma_8 = 0.82$, consistent with the results from WMAP5 (Komatsu et al., 2009). The simulation box has a size of $80h^{-1}$ comoving Mpc (cMpc), and contains 1024^3 DM particles, and initially the same number of gas particles; the mass of a DM and gas particle is $3.6 \times 10^7 h^{-1}{\rm M}_\odot$ and $6.3 \times 10^6 h^{-1}{\rm M}_\odot$, respectively. The softening length for the gravitational force is taken to be $3h^{-1}$ comoving kpc and the value of the smoothing length for the SPH kernel for the computation of hydrodynamic forces is allowed to drop at most to the gravitational softening.

The runs include the star formation prescriptions of Springel and Hernquist (2003) such that the ISM is described as an ambient hot gas containing cold clouds, which provide the reservoir for star formation, with the two phases being in pressure equilibrium; the relative number of stars of different masses is computed using the Salpeter initial mass function (IMF; Salpeter, 1955) between 0.1-100${\rm M}_\odot$. The density of the cold and of the hot phase represents an average over small regions of the ISM, within which individual molecular clouds cannot be resolved by simulations sampling cosmological

volumes. The runs also include the feedback model described in Springel and Hernquist (2003) which includes (a) thermal feedback: supernovae (SN) inject entropy into the ISM, heat up nearby particles and destroy molecules, (b) chemical feedback: metals produced by star formation and SN are carried by winds and pollute the ISM, and (c) mechanical feedback: galactic winds powered by SN. In the case of mechanical feedback, the momentum and energy carried away by the winds are calculated assuming that the galactic winds have a fixed velocity of $500\,\mathrm{km\,s^{-1}}$ with a mass upload rate equal to twice the local star formation rate, and carry away a fixed fraction (50%) of the SN energy (for which the canonical value of 10^{51} ergs is adopted). Finally, the run assumes a metallicity-dependent radiative cooling (Sutherland and Dopita, 1993) and a uniform redshift-dependent UV Background (UVB) produced by quasars and galaxies as given by Haardt and Madau (1996).

Galaxies are recognized as gravitationally-bound groups of at least 20 total (DM+gas+star) particles using the Amiga Halo Finder (AHF; Knollmann and Knebe, 2009). When compared to the standard Sheth-Tormen mass function (Sheth and Tormen, 1999), the simulated mass function is complete for halo masses $M_h \geq 10^{9.2}\,\mathrm{M_\odot}$ for $z \simeq 6-8$; galaxies above this mass cut-off are referred to as the "complete sample". Of this complete sample, we identify all the "resolved" galaxies that contain a minimum of $4N$ gas particles, where $N = 40$ is the number of nearest neighbours used in the SPH computations; this is twice the standard value of $2N$ gas particles needed to obtain reasonable and converging results (e.g. Bate and Burkert, 1997). We impose an additional constraint and only use those resolved galaxies that contain at least 10 star particles so as to get a statistical estimate of the composite spectral energy distribution (SED). For each resolved galaxy used in our calculations (with $M_h \geq 10^{9.2}\,\mathrm{M_\odot}$, more than $4N$ gas particles and a minimum of 10 star particles) we obtain the properties of all its star particles, including the redshift of, and mass/metallicity at formation; we also compute global properties including the total stellar mass (M_*), gas mass (M_g), DM mass (M_h), mass-weighted stellar metallicity (Z_*) and the mass weighted stellar age (t_*).

4.2.2 Dust Model

The evidence for dust at high-redshifts comes from observations of damped Lyα systems (Pettini et al., 1994; Ledoux et al., 2002) and from the thermal dust emission from SDSS QSOs (Omont et al., 2001; Bertoldi and Cox, 2002). Although dust is produced both by SN and evolved stars, several works (Todini and Ferrara, 2001; Dwek et al., 2007) have shown that the contribution of AGBs to the total dust content is negligible at $z \gtrsim 6$, since the age of the Universe is shorter than the typical evolutionary timescales of AGBs above this redshift. We therefore make the hypothesis that Type II SN (SNII) are the primary dust factories and compute the total dust mass, M_d in each of our simulated galaxies following Dayal et al. (2010).

The dust mass of each simulated galaxy is yielded from its age and mean star formation rate over its entire star formation history. Assuming dust is produced by SNII and destroyed by star formation, SN blast waves and galactic outflows, we yield the total dust mass M_d by solving the respective production-destruction equation.

$$\frac{\mathrm{d}M_{dust}(t)}{\mathrm{d}t} = y_d \gamma \left\langle \dot{M}_\star \right\rangle - \frac{M_{dust}(t)}{\tau_{dest}(t)} - \frac{M_{dust}(t)}{M_{gas}(t)} \left[\left\langle \dot{M}_\star \right\rangle + \dot{M}_{outflow} \right] \tag{4.1}$$

The first term on the right hand side of equation 4.1 describes the dust production by SNII with an average dust mass of $y_d = 0.4\mathrm{M_\odot}$ per SN. $\left\langle \dot{M}_\star \right\rangle$ is the averaged star formation rate and $\gamma = [134.35\mathrm{M_\odot}]^{-1}$ represents the fraction of SN that are produced assuming a Salpeter IMF ranging from $0.1\mathrm{M_\odot}$ to $100\mathrm{M_\odot}$. The second term accounts for the dust destruction by SN blast waves and is defined by the corresponding destruction time scale, $\tau_{dest}(t) = M_{gas}(t) / \left[\gamma \left\langle \dot{M}_\star \right\rangle \epsilon M_s (100\mathrm{km/s}) \right]$. Here $\epsilon = 0.2$ is the efficiency of dust destruction in a SN-shocked ISM and $M_s = 6.8 \cdot 10^3 \mathrm{M_\odot}$ describes the mass that is accelerated to 100km/s by SN blast waves. The third term in equation 4.1 characterises the loss of dust due to star formation, while the fourth term specifies the loss by galactic outflows. We derive the dust mass lost in outflows of each galaxy by considering the difference between the initial assumed ($M_h \Omega_b / \Omega_m$) and the final simulated gas mass (M_{gas}).

$$\dot{M}_{outflow} = \frac{M_h \frac{\Omega_b}{\Omega_m} - M_{gas} - \left\langle \dot{M}_\star \right\rangle t_\star}{t_\star} \tag{4.2}$$

Initial and final gas masses differ mostly for high mass galaxies, while they are negligible for low mass galaxies and the dust loss in outflows could be neglected. Stars form from gas in halos and produce

dust at the end of their lifetime when they explode as SN. As stars form and the dust mass of a galaxy increases, its gas mass is reduced by a rate which is proportional to the star formation rate, $\mathrm{d}M_{gas}(t)/\mathrm{d}t = -\left\langle \dot{M}_\star \right\rangle$. For each galaxy we compute the final dust mass $M_{dust}(t_\star)$ for its current mass rated age $t_\star$.

In a next step we use the dust mass to obtain the total optical depth, τ_c, to continuum photons as

$$\tau_c = \frac{3\Sigma_d}{4as}, \tag{4.3}$$

where $\Sigma_d = M_d[\pi r_d^2]^{-1}$ is the dust surface mass density, r_d is the dust distribution radius, $a = 0.05\mu m$ and $s = 2.25\,\mathrm{g\,cm^{-3}}$ are the radius and material density of graphite/carbonaceous grains, respectively (Todini and Ferrara, 2001). Since in our model dust and gas are assumed to be perfectly mixed, the dust distribution radius is taken to be equal to the gas distribution radius $r_g = 4.5\lambda r_{vir}$ where the spin parameter (λ) has a value of about 0.04 averaged across the galaxy population studied (Barnes and Efstathiou, 1987; Steinmetz and Bartelmann, 1995; Ferrara et al., 2000) and r_{vir} is the virial radius, calculated assuming the collapsed region has an overdensity of 200 times the critical density. This dust optical depth can then be used to obtain the escape fraction of UV photons (f_c) assuming a screen-like dust distribution such that $f_c = e^{-\tau_c}$.

4.2.3 Identifying Lyman Break Galaxies

To identify the simulated galaxies that could be observed as LBGs at $z \simeq 6-8$, we start by computing their UV luminosities. We consider each star particle to form in a burst, after which it evolves passively. The total SED, including both the stellar and nebular continuum, is computed for each star particle via the population synthesis code `STARBURST99` (Leitherer et al., 1999), using its mass, stellar metallicity and age. The total intrinsic UV luminosity, L_c^{int} (at 1500 Å in the galaxy rest frame) is then calculated for each progenitor by summing the SEDs of all its star particles.

Continuum photons can be absorbed by dust within the ISM and only a fraction, f_c, escape out of any galaxy unattenuated by dust. However, these photons are unaffected by the ionization state of the IGM, and all the continuum photons that escape out of a galaxy can then reach the observer, so that the observed continuum luminosity can be expressed as $L_c^{obs} = L_c^{int} \times f_c$; this can be translated into an absolute magnitude, M_{UV}. In accordance with current observational criterion, at each redshift $z \simeq 6-8$, resolved simulated galaxies with $M_{UV} \leq -17$ are identified as LBGs.

4.3 Comparing the simulations with LBG observations

Once we have identified the simulated galaxies that would be detected as LBGs in the snapshots at $z \simeq 6-8$, we compare their UV LFs, stellar mass functions, stellar mass densities (SMD) and specific SFR (sSFR) to the observed values in order to validate the simulations used in this work.

4.3.1 UV luminosity functions

We calculate the intrinsic UV LFs by binning simulated LBGs on the basis of their intrinsic (i.e. dust-unattenuated) UV magnitudes and dividing this by the width of the UV bin (0.5 dex), and the volume of the box. We find that the intrinsic UV LF shifts towards brighter luminosities and higher number densities with decreasing redshift from $z \simeq 8$ to 6, as expected from the hierarchical structure formation scenario where successively larger systems build up with time from the merger of smaller systems. As seen in Fig. 4.1, we find that the simulated intrinsic LBG UV LFs are over-estimated with respect to the data, with the over-estimation increasing with decreasing redshift, hinting at the increasing dust enrichment of these galaxies; we note that the intrinsic UV LF at $z \simeq 8$ is already in agreement with the observations, requiring no dust correction at this redshift.

We then use the observed (i.e. dust attenuated) UV luminosity obtained for each galaxy at $z \simeq 6-8$ (see Secs. 4.2.2 and 4.2.3) to build the observed UV LF. It is encouraging to note that both the slope and the amplitude of the dust attenuated simulated LFs are in agreement with the observations for $z \simeq 6$ and 7 as seen from Fig. 4.1; as mentioned before, the simulated UV LF at $z \simeq 8$ requires no dust to match the observations. As can be seen from the same figure, the effects of dust on continuum photons at $z \simeq 6, 7$ are most severe for the most massive/luminous galaxies; indeed while $f_c \simeq 0.8$ for galaxies in halo masses of $M_h \leq 10^{10}\mathrm{M}_\odot$, the value drops steadily thereafter such that $f_c \simeq 0.01$

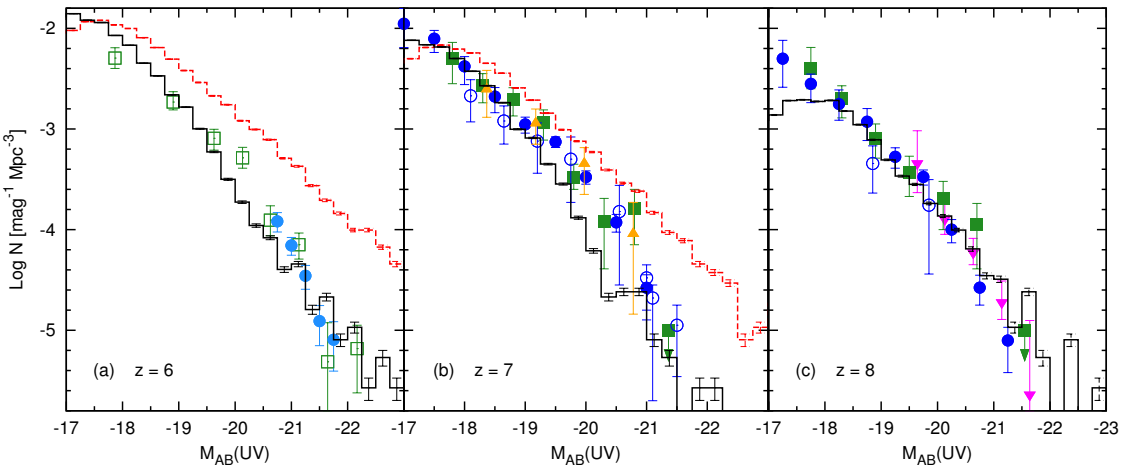

Figure 4.1: UV luminosity functions at $z \simeq 6, 7$ and 8, from left to right, as marked in each panel. In all panels, the solid black (dashed red) histograms show the dust corrected (intrinsic) simulated UV LFs with error bars showing the Poissonians error and symbols showing the observed data. The observed UV LFs have been taken from (a) $z \simeq 6$: Bouwens et al. (2007, empty squares), McLure et al. (2009, filled circles); (b) $z \simeq 7$: Bouwens et al. (2011, filled squares), McLure et al. (2010, empty circles), McLure et al. (2013, filled circles), Oesch et al. (2010, filled triangles) and (c) $z \simeq 8$: Bradley et al. (2012, filled triangles), Bouwens et al. (2011, filled squares), McLure et al. (2010, empty circles) and McLure et al. (2013, filled circles).

for the largest galaxies at both $z \simeq 6, 7$. Further, as a result of galaxies typically being less massive, younger, and hence less dust enriched with increasing redshift, averaged over all LBGs f_c drops from $\simeq 1$ at $z \simeq 8$ to 0.6 at $z \simeq 7$ and 0.5 at $z \simeq 6$. We briefly digress to note that these average f_c values are about a factor of two higher than the values inferred in Dayal et al. (2010). This is due to the different feedback models implemented in these two simulations: while only 25% of the SN energy was used to power outflows in the simulation used in Dayal et al. (2010), 50% of the SN energy has been used to power outflows in the simulation used in this work. As a result of the much larger energy inputs that power SN winds in driving out gas from the galaxy, the typical stellar masses and SFRs obtained from the simulation used in this work are about a factor two lower than those presented in Dayal et al. (2010).

Returning to our discussion regarding the observed LBG UV LFs, we notice that these also shift to progressively higher luminosities and/or higher number densities with decreasing redshift. Dayal et al. (2013) have shown that this evolution depends on the luminosity range probed: the steady brightening of the bright end of the LF is driven by genuine physical luminosity evolution due to a fairly steady increase in the UV luminosity (and hence star-formation rates) in the most massive LBGs; the evolution at the faint end arises due to a mixture of both positive and negative luminosity and density evolution as these putative systems brighten and fade, and continuously form and merge into larger systems.

Finally, we find that the best fit Schechter parameters to the dust attenuated simulated UV LFs are: faint end slope $\alpha = (-1.9 \pm 0.2, -2.0 \pm 0.2, -1.8 \pm 0.2)$ and the knee of the luminosity function $M_{UV,*} = (-19.8 \pm 0.3, -19.7 \pm 0.2, -19.9 \pm 0.3)$ at $z \simeq (6, 7, 8)$. These values are in agreement with the values $\alpha = (-1.71 \pm 0.11, -1.90 \pm 0.14, -2.02 \pm 0.22)$, $M_{UV,*} = (-20.04 \pm 0.12, -19.9 \pm 0.2, -20.12 \pm 0.37)$ and $\alpha = (-1.74 \pm 0.16, -2.01 \pm 0.21, -1.91 \pm 0.32)$, $M_{UV,*} = (-20.24 \pm 0.19, -20.14 \pm 0.26, -20.1 \pm 0.52)$ inferred observationally by McLure et al. (2009, 2013) and Bouwens et al. (2011) at $z \simeq (6, 7, 8)$, respectively.

4.3.2 Stellar mass functions and stellar mass density

We build simulated LBG mass functions by summing up LBGs on the basis of their stellar mass, and dividing this by the width of the bin and the simulated volume; for consistency with observations, this calculation is carried out for all LBGs with $M_{UV} \leq -18$. As expected from the hierarchical model, small mass systems are the most numerous, with the number density decreasing with increasing mass. Further, the mass function shifts to progressively lower masses with increasing redshifts, as fewer

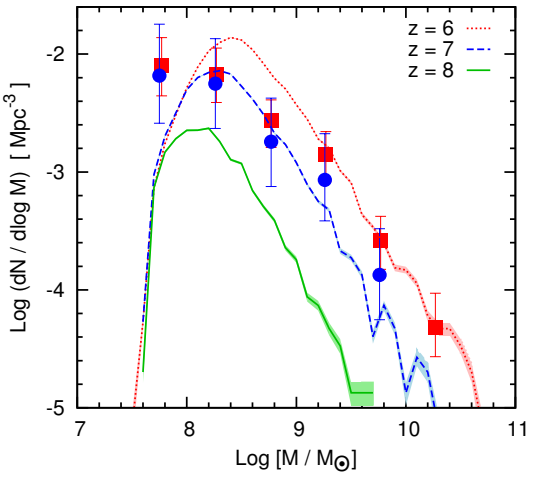

Figure 4.2: Stellar mass function for LBGs with $M_{UV} \leq -18$ at $z \simeq 6-8$. The dotted (red), dashed (blue) and solid (green) lines represent the simulated stellar mass functions for $z \simeq 6, 7$ and 8, respectively. The shaded areas denote the respective Poisson errors. Squares (circles) represent the observational stellar mass functions at $z \simeq 6$ (7) inferred by González et al. (2011), corrected for completeness but not for dust.

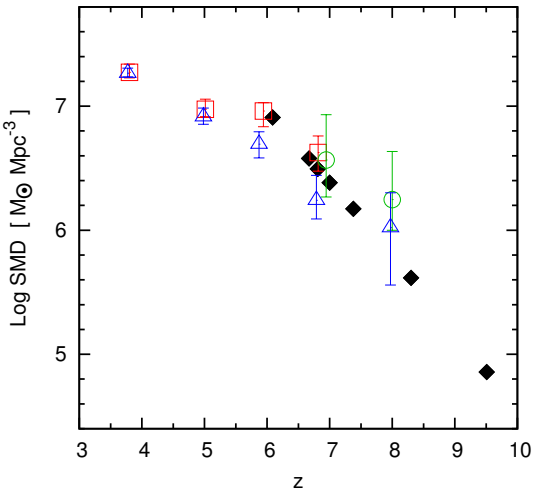

Figure 4.3: Total stellar mass density for LBGs with $M_{UV} \leq -18$. Filled black points represent the simulated SMDs; Poissonian errors are too small to be visible on the plot. The other symbols show the observed SMD values inferred by González et al. (2011, empty red squares), Labbé et al. (2010a, empty green circles), Labbé et al. (2010b, empty green circles), Stark et al. (2013, empty blue triangles).

massive systems have had the time to assemble. Both trends can be seen clearly from Fig. 4.2: at $z \simeq 6$, galaxies with $M_* \simeq 10^{8.5}\mathrm{M}_\odot$ are two orders of magnitude more numerous as compared to more massive galaxies with $M_* \simeq 10^{10.5}\mathrm{M}_\odot$. Secondly, while there are systems as massive as $10^{10.7}\mathrm{M}_\odot$ in the simulated volume at $z \simeq 6$, such systems had not the time to evolve by $z \simeq 8$ where the most massive systems have $M_* \simeq 10^{9.4}\mathrm{M}_\odot$. From the same figure, we see that the slope and amplitude of the simulated stellar mass functions are in agreement with the observations for $M_* \geq 10^{7.5}\mathrm{M}_\odot$; this number marks the limit of our simulation resolution for galaxies containing at least 4N gas particles and 10 star particles, as a result of which, the number density drops below it.

As a result of the stellar mass functions shifting to progressively lower masses and number densities with increasing redshift (see Fig. 4.2), the total SMD in the simulated volume decreases with increasing redshift, as shown in Fig. 4.3, falling by a factor of about 40 from $10^7\mathrm{M}_\odot\,\mathrm{Mpc}^{-3}$ at $z \simeq 6$ to $10^{5.4}\mathrm{M}_\odot\,\mathrm{Mpc}^{-3}$ at $z \simeq 9.5$. As expected from the agreement between the simulated stellar mass functions and those inferred observationally by González et al. (2011), the simulated SMD values are also in agreement with the observations. However, as pointed out by Schaerer and de Barros (2010) and Stark et al. (2013), including the effects of nebular emission can lead to a decrease in the observationally inferred stellar mass values; this effect causes a slight discrepancy between the SMD values obtained from our model, and those inferred by Stark et al. (2013) at $z \simeq 6$, as shown in Fig. 4.3.

4.3.3 Specific star formation rates

The specific star formation rate (sSFR) is an excellent indicator of the current SFR compared to the entire past star formation history of the galaxy. This quantity also has the advantage that it is relatively independent of assumptions regarding the IMF, metallicity, age and dust content since both the SFR and stellar mass are affected similarly by these parameters. Recently, a number of observational groups have suggested that the sSFR settles to a value consistent with $2-3\,\mathrm{Gyr}^{-1}$ at $z \simeq 3-8$ (Stark et al., 2009; González et al., 2010; McLure et al., 2011; Labbé et al., 2013; Stark et al., 2013). This result is quite surprising given that theoretically, the sSFR is expected to trace the baryonic infall rate that scales as $(1+z)^{2.25}$ (Neistein and Dekel, 2008). However, Labbé et al. (2013) and Stark et al. (2013) have shown that at least a part of this discrepancy can be accounted for by the addition of nebular emission lines; indeed, the sSFR can rise by a factor of about 5 between $z \simeq 2$

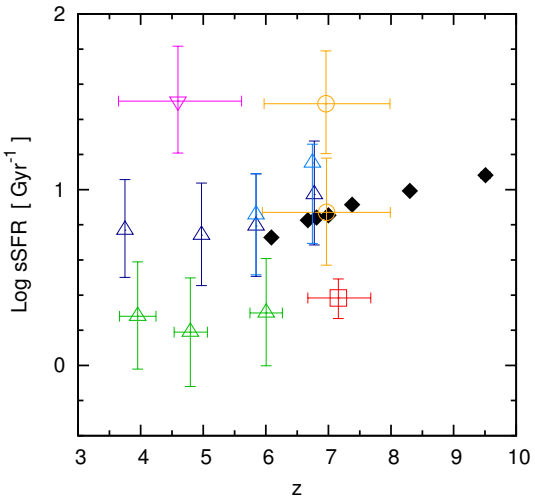

Figure 4.4: Specific star formation rate for LBGs with $M_{UV} \leq -18$. Filled black points represent the simulated sSFRs; Poissonian errors are too small to be visible on the plot. Observed sSFR values plotted have been taken from: González et al. (2010, empty red squares), Stark et al. (2009, empty green triangles), Yabe et al. (2009, empty magenta triangles), Schaerer and de Barros (2010, empty orange circles), Stark et al. (2013, empty blue triangles).

and $z \simeq 7$ when nebular emission is taken into account.

Physically, the least massive galaxies tend to have the highest sSFR: as a result of their low M_* values, even a small amount of SF can boost their sSFR compared to that of more massive systems (see also Dayal and Ferrara, 2012; Dayal et al., 2013). Since the mass function progressively shifts to lower masses with increasing redshifts, and smaller mass galaxies have larger sSFR values, the sSFR rises with increasing redshift, from $sSFR \simeq 5\,\mathrm{Gyr}^{-1}$ at $z \simeq 6$ to $sSFR \simeq 12\,\mathrm{Gyr}^{-1}$ at $z \simeq 9.5$, in accordance with other theoretical results (Dayal et al., 2013; Biffi and Maio, 2013; Salvaterra et al., 2013). We note that in the redshift range of overlap ($z \simeq 6-7$), the theoretically inferred sSFR values are in agreement with observations.

4.4 Simulating LAEs

In the previous section (and Appendix A), we have validated that the simulated galaxy population at $z \simeq 6-8$ is in agreement with a number of high-z LBG observations. We now use these galaxy populations to identify the simulated galaxies that could be detected as LAEs. We start by describing the radiative transfer code (pCRASH) used to obtain reionization topologies for $f_{\rm esc} = 0.05, 0.25, 0.5, 0.75, 0.95$, which are utilized to calculate the IGM Lyα transmission. We then describe how these transmission values, and the effects of dust on Lyα photons are taken into account, so as to obtain the observed Lyα luminosity from the intrinsic value for each galaxy. We note that all the radiative transfer and Lyα calculations are carried out using a single snapshot of the hydrodynamical simulation at the edge of the reionization epoch, at $z \simeq 6.7$.

4.4.1 Reionizing the universe with pCRASH

As mentioned in the introduction of this chapter, the progress of reionization critically depends on the total number of H I ionizing photons that can escape a galaxy and ionize the IGM around it. As expected, this depends both on the total number of H I ionizing photons produced by a galaxy, as well as the fraction that can escape the galactic environment ($f_{\rm esc}$). While the simulated star formation rates are in reasonable agreement with observations (see Appendix A), giving us a handle on the H I ionizing photon production rate, the value of $f_{\rm esc}$ remains only poorly understood: using a variety of theoretical models, the value of $f_{\rm esc}$ has been found to range between $0.01 - 0.8$ (see e.g. Ricotti and Shull, 2000; Fujita et al., 2003; Razoumov and Sommer-Larsen, 2006; Wise and Cen, 2009).

Due to the poor theoretical constraints available on the value of $f_{\rm esc}$, we do not make any prior assumptions on its value. We instead post-process the hydrodynamical simulation snapshot at $z \simeq 6.7$

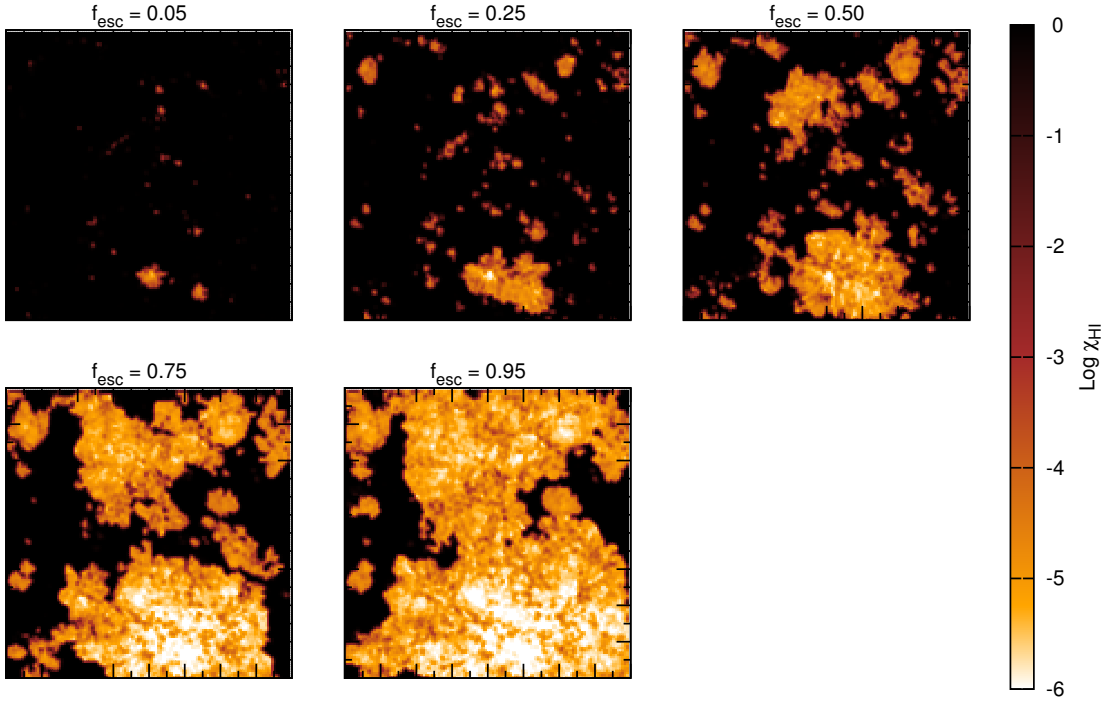

Figure 4.5: Maps ($80h^{-1}$ Mpc on a side) of the spatial distribution of H I in a 2D cut through the center of the simulated box at $z \simeq 6.7$ obtained by running pCRASH for 50 Myrs using the $f_{\rm esc}$ value marked above the panel. The colorbar shows the values (in log scale) of the H I fraction. As can be seen, reionization proceeds faster with increasing $f_{\rm esc}$ values.

with the radiative transfer code pCRASH using five different values of $f_{\rm esc} = 0.05$, 0.25, 0.50, 0.75 and 0.95 to study how varying $f_{\rm esc}$ affects the progress of reionization.

We now briefly describe pCRASH and interested readers are referred to Ciardi et al. (2001), Maselli et al. (2003, 2009) and Partl et al. (2011) for more details. pCRASH is a 3D grid-based MPI-parallelized radiative transfer code that utilizes a combination of ray tracing and Monte Carlo schemes. It follows the time evolution of the IGM gas properties including ionization fractions (H I and He I, He II) and the temperature. A large number of point sources with different spectra emit photon packages into the medium. The relevant matter-radiation interactions (photoionization, recombination, collisional ionization) as well as the heating/cooling of the IGM (collisional ionization cooling, recombination cooling, collisional excitation cooling, bremsstrahlung, Compton cooling/heating, adiabatic cooling, photoheating) are calculated. In addition, the code includes diffuse radiation following recombinations of ionized atoms. For the radiative transfer runs, we use the density and temperature fields obtained from the $z \simeq 6.7$ snapshot of the hydrodynamical simulation as the inputs for pCRASH. For each resolved source in the SPH simulation, the luminosity and spectrum were calculated by summing up the spectra of all their star particles, as described in section 4.2.3; we processed 31855 resolved sources from the snapshot at $z \simeq 6.7$. The spectrum of each source was binned into 125 frequency intervals ranging from 3.21×10^{15}Hz to 3.30×10^{16}Hz. Each source emitted 10^7 rays and we used 10^6 timesteps per 500 Myrs on a 128^3 grid; we used the mean local clumping factor of each cell obtained from the underlying density distribution from the SPH simulation to account for the clumpiness of the IGM (Raičević and Theuns, 2011). Depending on the escape fraction the runs were carried out on 64 or 128 processors on AIP clusters. Each simulation was run until the IGM global hydrogen fraction dropped to $\langle \chi_{HI} \rangle \lesssim 10^{-4}$, so that the entire progress of reionization could be mapped.

We now discuss the ionization fields obtained by running pCRASH on the SPH simulation snapshot at $z \simeq 6.7$ for the five different $f_{\rm esc}$ values mentioned above. Firstly, the volume of the ionized region (V_I) carved out by any source depends on its total ionizing photon output such that

$$V_I \quad \propto \quad \frac{Q f_{\rm esc}}{\chi_{HI} n_H}, \tag{4.4}$$

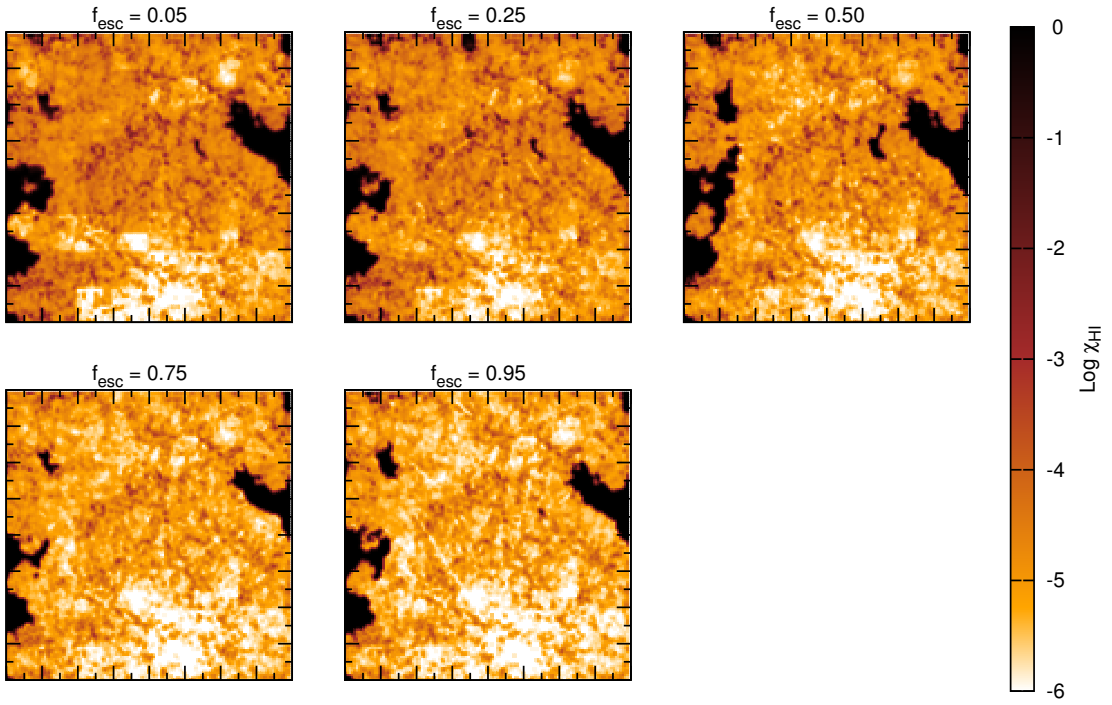

Figure 4.6: Maps ($80h^{-1}$ Mpc on a side) of the spatial distribution of H I in a 2D cut through the simulated box at $z \simeq 6.7$ obtained by running pCRASH using the $f_{\rm esc}$ value marked above the panel, until the average neutral hydrogen fraction drops to $\langle \chi_{HI} \rangle \simeq 0.1$. The colorbar shows the values (in log scale) of the H I fraction. As seen, while the topology of reionization looks very similar for the same average H I values, the degree of ionization close to any source increases with increasing $f_{\rm esc}$.

where Q is the total number of H I ionizing photons produced by the source, χ_{HI} is the H I fraction and n_H represents the number density of hydrogen atoms. From this expression, it is clear that for a given source surrounded by an IGM of a given H I density, V_I increases with $f_{\rm esc}$. In other words, given a galaxy population, at any given time, the IGM is more ionized (i.e. reionization proceeds faster) for larger $f_{\rm esc}$ values.

Secondly, the photoionization rate (Γ) at a distance r from a source depends on the source H I photon emissivity ($L_\lambda f_{\rm esc}$) such that

$$\Gamma(r) = \int_0^{\lambda_L} \frac{L_\lambda \, f_{\rm esc}}{4\pi r^2} \sigma_L \left(\frac{\lambda}{\lambda_L} \right)^3 \frac{\lambda}{hc} d\lambda, \tag{4.5}$$

where L_λ is the total specific ionizing luminosity of the emitter, λ_L is the Lyman limit wavelength (912 Å), σ_L is the hydrogen photoionization cross-section at $\lambda = \lambda_L$, h is the Planck constant and c represents the speed of light. Assuming ionization-recombination balance, it is this photoionization rate that determines the level of ionization, χ_{HI}, around an emitter. Hence, for a given emitter, χ_{HI} is expected to decrease for increasing values of $f_{\rm esc}$ (see also Sec. 2.4, Dayal et al., 2008).

These two effects can be clearly seen in Figs. 4.5 and 4.6: the former and latter show the ionization fields obtained for different $f_{\rm esc}$ by running pCRASH for a given time (50 Myrs) and until the IGM is ionized to a level of $\langle \chi_{HI} \rangle \simeq 0.1$, respectively. From Fig. 4.5, it can be clearly seen that reionization proceeds faster for increasing $f_{\rm esc}$ values: after 50 Myrs of running pCRASH, while the largest ionized region built has a size of about 15 cMpc for $f_{\rm esc} = 0.05$, the entire box is almost reionized for $f_{\rm esc} = 0.95$. Indeed, the average value of χ_{HI} drops steadily with increasing $f_{\rm esc}$ such that $\langle \chi_{HI} \rangle = (0.97, 0.82, 0.62, 0.37, 0.20)$ for $f_{\rm esc} = (0.05, 0.25, 0.5, 0.75, 0.95)$ respectively. Increasing $f_{\rm esc}$ by a factor of 19, from 0.05 to 0.95 has the effect of decreasing the neutral hydrogen fraction; while the IGM is essentially neutral for $f_{\rm esc} = 0.05$, it is almost ionized for $f_{\rm esc} = 0.95$.

From Fig. 4.6, we find that the topology of reionization looks similar for all the five $f_{\rm esc}$ values by the time the average H I fraction has dropped to $\langle \chi_{HI} \rangle = 0.1$. However, the time taken to reach this

average ionization state is very different for the five runs; while the run with $f_{\rm esc} = 0.95$ took 80 Myrs to reach this ionization level, the runs with $f_{\rm esc} = 0.05$ took about ten times longer ($\simeq$ 800 Myrs) to build up these ionized regions. We also note that although the spatial distribution of the ionization fields looks very similar for the varying $f_{\rm esc}$ values, the level of ionization in any given cell increases with increasing $f_{\rm esc}$ as seen from the same figure (see also Eqn. 4.5).

To summarize, we find that increasing $f_{\rm esc}$ both accelerates the progress of reionization and leads to higher ionization fractions in the ionized regions. A combination of both these factors leads to a larger IGM Lyα transmission T_α with increasing $f_{\rm esc}$, as explained in the following.

4.4.2 Identifying LAEs

In this section, we start by explaining how we calculate the intrinsic Lyα luminosity produced by each simulated galaxy at $z \simeq 6.7$. We then show how we calculate the Lyα attenuation by ISM dust and IGM H I to determine the fraction of this intrinsic luminosity that is finally observed.

Intrinsic Lyα luminosity

As mentioned above, star formation in galaxies produces photons more energetic than 1 Ryd, with a certain fraction ($f_{\rm esc}$) escaping into, and ionizing the IGM. The rest of these photons ($1 - f_{\rm esc}$) ionize the H I in the ISM. Due to the high density of the ISM, these electrons and protons recombine on very short timescales giving rise to a Lyα emission line of luminosity

$$L_\alpha^{int} = \frac{2}{3} Q (1 - f_{\rm esc}) h \nu_\alpha, \tag{4.6}$$

where the factor two-thirds arises due to our assumption of case-B recombinations for optically thick H I in the ISM (Osterbrock, 1989), and ν_α represents the Lyα frequency in the galaxy rest frame.

However, this line is Doppler broadened by the rotation of the galaxy so that the complete line profile can be expressed as

$$L_\alpha^{int}(\nu) = \frac{2}{3} Q (1 - f_{\rm esc}) h \nu_\alpha \frac{1}{\sqrt{\pi} \Delta\nu_d} \exp\left[-\frac{(\nu - \nu_\alpha)^2}{\Delta\nu_d^2} \right], \tag{4.7}$$

where $\Delta\nu_d = (v_c/c)\nu_\alpha$. For realistic halo and disk properties, the rotation velocity of the galaxy (v_c) can range between v_h and $2v_h$, where v_h is the halo rotation velocity (Mo et al., 1998; Cole et al., 2000). We use the central value of $v_c = 1.5 v_h$ in all the calculations presented in this paper.

Effects of dust

The intrinsic Lyα luminosity produced by a galaxy has to penetrate through dust in the ISM, with only a fraction f_α emerging out of the galactic environment. In Sec. 4.2.2, we have shown calculations for the total dust enrichment of each simulated galaxy and the resulting value of f_c. The relation between f_α and f_c depends on the adopted extinction curve if dust is homogeneously distributed; it also depends on the differential effects of radiative transfer on Lyα and UV photons if dust is inhomogeneously distributed/clumped (Neufeld, 1991; Hansen and Oh, 2006). While some pieces of evidence exist that the SN extinction curve (Bianchi and Schneider, 2007) can successfully be used to interpret the observed properties of the most distant quasars (Maiolino et al., 2006) and gamma-ray bursts (Stratta et al., 2007), the effect of dust inhomogeneities in enhancing the escape fraction of Lyα photons with respect to continuum photons through the Neufeld effect (Neufeld, 1991) remains controversial. On the one hand, Finkelstein et al. (2009) have found tentative observational evidence of $f_\alpha/f_c > 1$ for $z \simeq 4.5$ LAEs and Dayal et al. (2009, 2011) have shown that models require $f_\alpha/f_c > 1$ to reproduce LAE data at $z \lesssim 6$. On the other hand, Laursen et al. (2013) have shown that a value of $f_\alpha > f_c$ requires very special circumstances (no bulk outflows, very high metallicity, very high density of the warm neutral medium and a low density and highly ionized medium) that are unlikely to exist in any realistic ISM; moreover, they show that a value of $f_\alpha/f_c > 1$ results in very narrow Lyα lines that are sensitive to infalling gas, resulting in low T_α values. Due to its poor understanding, the relative escape fraction f_α/f_c is left as a free parameter in our model and its value is fixed by matching the theoretical LAE Lyα and UV LFs to the observations, as shown in Sec. 4.5 that follows.

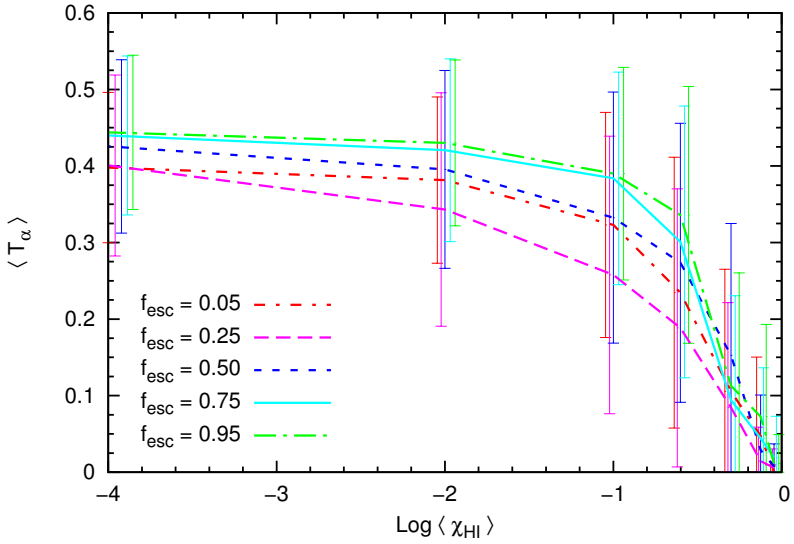

Figure 4.7: Mean transmission of all galaxies (averaged over 48 LOS) in the simulation snapshot at $z \simeq 6.7$ as a function of the mean IGM hydrogen neutral fraction. Red (dash-dotted), magenta (long dashed), dark blue (short dashed), light blue (dotted) and green (long dashed-dotted) lines show the relation for $f_{\rm esc} = 0.05$, 0.25, 0.5, 0.75 and 0.95 and error bars indicate the 1σ dispersion.

Effects of the IGM

The Lyα photons that escape out of a galaxy unabsorbed by dust are attenuated by the H I they encounter along the line of sight (LOS) between the emitter and the observer, with a fraction $T_\alpha = e^{-\tau_\alpha}$ being transmitted through the IGM. This optical depth to H I (τ_α) can be calculated as

$$\tau_\alpha(v) \quad = \quad \int_{r_{em}}^{r_{obs}} \sigma_0 \; \Phi\left(v + v_P\left(r\right)\right) \; n_{HI}(r) \; {\rm d}r, \tag{4.8}$$

where $v = (\lambda - \lambda_\alpha)\lambda_\alpha^{-1} c$ is the rest-frame velocity of a photon with frequency λ relative to the Lyα line center at $\lambda_\alpha = 1216$Å. Further, v_P accounts for the IGM peculiar velocity, $n_{HI}(r)$ the H I density at a physical distance r from the emitter, $\sigma_0 = \pi e^2 f / m_e c$ is the absorption cross section, f is the oscillator strength, e is the electron charge, m_e is the electron mass, and $\Phi(v)$ is the Voigt profile; this profile consists of a Gaussian core and Lorentzian damping wings. For regions of low H I density, pressure line broadening becomes unimportant and the line profile can be approximated by the Gaussian core. However, the Lorentzian damping wings become important in regions of high H I density and the complete profile must then be used. Although it is computationally quite expensive, we use the complete Voigt profile for all our calculations. We note that we include the effects of peculiar velocities (v_P) in determining τ_α: inflows (outflows) of gas towards (from) a galaxy will blueshift (redshift) the Lyα photons, increasing (decreasing) τ_α, which leads to a corresponding decrease (increase) in T_α. We compute τ_α by stepping through our simulation box which is divided into a grid of 128^3 cells, with each cell having a size of 117 physical kpc; this is the same grid that is used to run pCRASH, as described in Sec. 4.4.1. For any galaxy, we start calculating τ_α at the galaxy position $r_{em} = 0$, until the edge of the box is reached r_{obs}. The value of $v_P(r)$ and $n_{HI}(r)$ in each cell are then obtained from GADGET-2 and pCRASH runs, respectively. A single GADGET-2 snapshot at $z \simeq 6.7$ suffices for our work because the Lyα line redshifts out of resonance with H I extremely quickly; to a first approximation, the spatial scale imposed by the Gunn-Peterson damping wing on the size of the H II region corresponds to a separation of about 280 kpc (physical) at $z = 6$ (Miralda-Escude, 1998). Interested readers are referred to Dayal et al. (2011) for complete details of this calculation.

We use the ionization fields obtained by running pCRASH (see Sec. 4.4.1) with the five different $f_{\rm esc}$ values to calculate the average T_α for each galaxy along 48 lines of sight (LOS). For a given ionization state, the final T_α value of each galaxy is taken to be the average along all 48 LOS. For each galaxy we compute the observed Lyα luminosity (L_α^{obs}) by using the individual values for f_α and

T_α of the respective galaxy.

$$L_\alpha^{obs} = f_\alpha T_\alpha L_\alpha^{int}. \tag{4.9}$$

In consistency with current observational criteria, galaxies with $L_\alpha^{obs} \geq 10^{42}$erg s^{-1} and an equivalent width ($EW = L_\alpha^{obs}/L_c^{obs} \geq 20$Å) are then identified as LAEs and used to build the LAE UV and Lyα LFs. We note that the Lyα LFs along different LOS are subject to cosmic variance as shown in Appendix B.1.

We also remind the reader that T_α is fixed from the ionization state of the IGM as explained above. Then, the only free parameter that we are left with to identify LAEs is the relative escape fraction of Lyα and continuum photons i.e. f_α/f_c. This final free parameter is fixed by matching the simulated LFs to the observed ones, as explained in Sec. 4.5.

Before proceeding to a comparison between the theoretical results and observational data, we briefly digress to show the relation between T_α and $\langle\chi_{HI}\rangle$ for our 5 $f_{\rm esc}$ values. As can be seen from Fig. 4.7 (see also Sec. 4.4.1), the mean IGM transmission ($\langle T_\alpha\rangle$) averaged over all galaxies increases with decreasing $\langle\chi_{HI}\rangle$ values: as ionized regions grow larger, they allow all galaxies to transmit more of their Lyα flux through the IGM. The inhomogeneity of the ionized regions also leads to a huge variation in T_α as seen from the 1σ dispersions in the same figure. Finally, our mean IGM transmission values are consistent with the results obtained by Jensen et al. (2013b), Iliev et al. (2008) and Dijkstra et al. (2007) for $f_{\rm esc} = 0.05$; we note that Lyα transmission calculations have not been performed for escape fractions higher than this value.

4.5 Joint constraints on reionization topology and dust using LAE luminosity functions

From Secs. 4.4.1 and 4.4.2, it is clear that $f_{\rm esc}$ affects the observed Lyα luminosity both through its effect on the intrinsic Lyα luminosity and through its effect on the ionization state of the IGM. Further, for a given $f_{\rm esc}$ and ionization state, the only free parameter left in our model is the escape fraction of Lyα photons compared to UV-continuum photons, f_α/f_c. In this section we use the LAE data accumulated by Kashikawa et al. (2011) to simultaneously constrain and find best fits to our 3 parameters, $f_{\rm esc}$, $\langle\chi_{HI}\rangle$ and f_α/f_c. We use pCRASH outputs for $\langle\chi_{HI}\rangle \simeq 0.9, 0.75, 0.5, 0.25, 0.1, 0.01$ and 10^{-4} for each of the five $f_{\rm esc} = 0.05, 0.25, 0.5, 0.75, 0.95$ at $z \simeq 6.7$. For each such combination, we start from the special case of assuming $f_\alpha/f_c = 0.68$ which corresponds to dust being homogeneously distributed in the ISM in Sec. 4.5.1, and progress to the more general scenario of varying f_α/f_c to best fit the observations, in Sec. 4.5.2.

4.5.1 Homogeneous dust

As shown in Eqn. 4.6, the intrinsic Lyα luminosity produced by a galaxy depends on the fraction of H I ionizing photons that ionize the H I in the ISM. It is thus naturally expected that L_α^{int} decreases with increasing $f_{\rm esc}$ since this leads to fewer photons being available for ionization in the ISM. This behaviour can be seen from panel (a) of Fig. 4.8 where we find that the amplitude of the Lyα LF drops by a factor of about 40 as $f_{\rm esc}$ increases from 0.05 to 0.95. This drop seems surprising at the first glance: as $f_{\rm esc}$ increases by a factor of about 19, the intrinsic Lyα LF would be expected to drop by the same amount. However, this result can be easily explained by the fact that we identify galaxies as LAEs based on the Lyα luminosity being larger than 10^{42}erg s^{-1} and an $EW \geq 20$Å. As $f_{\rm esc}$ increases, fewer and fewer galaxies are able to fulfil these selection criteria, leading to an enhanced drop in the amplitude of the Lyα LF.

The ratio f_α/f_c depends on many physical effects (see e.g. Laursen et al., 2013), including the distribution of the Lyα sources in the dusty ISM (Scarlata et al., 2009), the ISM H I column densities and velocities. However, a natural consequence of simulating cosmological volumes is that we are unable to resolve the ISM of individual galaxies. We therefore start with the special scenario wherein dust is homogeneously distributed in the ISM and Lyα photons are not scattered by dust and H I within the ISM. Since SNII are assumed to be the main sources of dust in our model, we deduce the ratio $f_\alpha/f_c = 0.68$ purely from the corresponding SN extinction curve (Bianchi and Schneider, 2007). This fixed ratio is then applied uniformly to all galaxies in the simulation snapshot at $z \simeq 6.7$. Once f_α has been fixed using this ratio, the only two parameters that can affect the slope and amplitude of the Lyα LFs are $f_{\rm esc}$ and χ_{HI}.

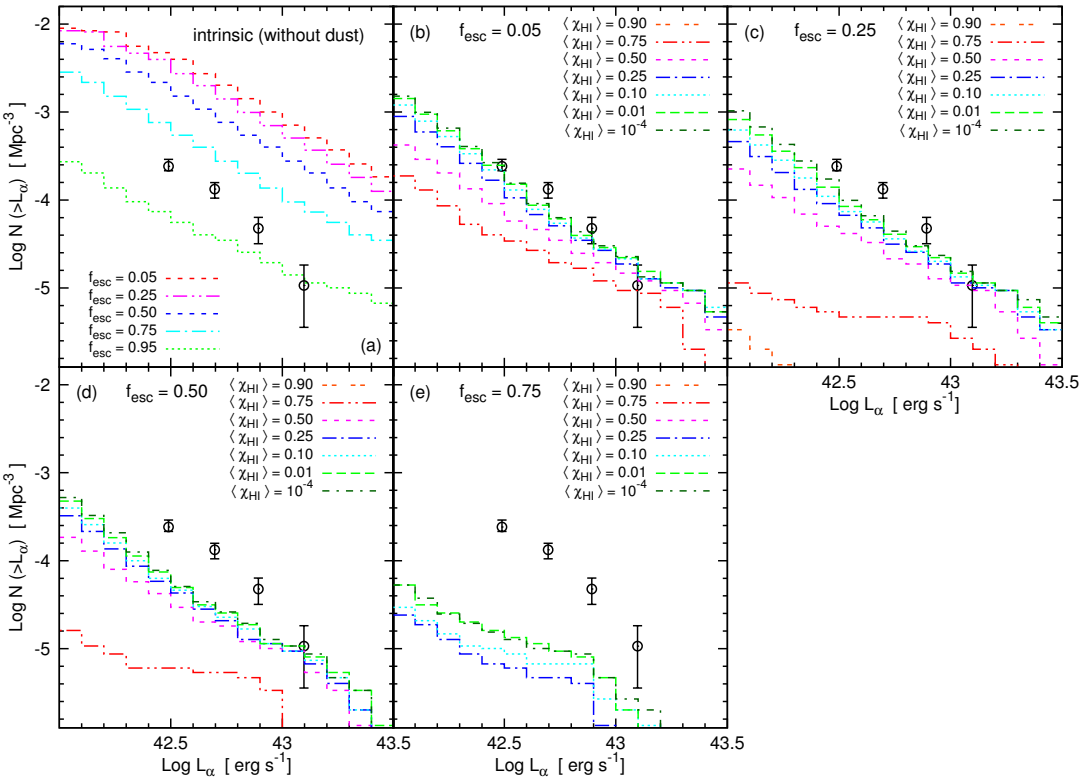

Figure 4.8: The cumulative Lyα LFs. Panel (a) shows the intrinsic Lyα LFs for escape fractions $f_{\rm esc} = 0.05$, 0.25, 0.50, 0.75, as marked. The lines in the other panels show the results for homogeneously distributed SNII dust ($f_\alpha/f_c = 0.68$) for different $\langle\chi_{HI}\rangle$ states ($\langle\chi_{HI}\rangle \simeq 0.90$, 0.75, 0.50, 0.25, 0.10, 0.01, 10^{-4}) obtained using the fixed $f_{\rm esc}$ value marked above the panel. In each panel, black open circles show the Lyα LFs at $z \simeq 6.5$ inferred observationally by Kashikawa et al. (2011). Due to the EW selection criterion no LAEs are identified for $f_{\rm esc} = 0.95$.

We start by discussing the Lyα LF evolution as a function of $\langle\chi_{HI}\rangle$. As expected from Eqn. 4.8, for a given $f_{\rm esc}$, τ_α decreases with decreasing $\langle\chi_{HI}\rangle$, leading to an increase in the IGM Lyα transmission. This naturally results in an increase in the amplitude of the Lyα LF by making galaxies more luminous in the observed Lyα luminosity, L_α^{obs}, as can be seen from panels (b)-(e) of Fig. 4.8. However, the effect of decreasing χ_{HI} is the strongest on the visibility of the faintest galaxies and decreases with increasing luminosity. This is because the spatial scale imposed by the Gunn-Peterson damping wing on the size of the H II region corresponds to a separation of about 280 kpc (physical) at $z \simeq 7$ (Miralda-Escude, 1998). The most massive galaxies are easily able to carve out H II regions of this size as a result of their relatively large H I ionizing photon output. However, in the initial stages of reionization, only those faint galaxies that are clustered are able to build H II regions of this size and become visible as LAEs (McQuinn et al., 2007a; Dayal et al., 2009). Hence, for a given $f_{\rm esc}$, the faint-end slope of the Lyα LF becomes steeper with decreasing $\langle\chi_{HI}\rangle$ values as seen from panels (b)-(e) of Fig. 4.8. We also see that the slope and amplitude of the Lyα LFs start converging for $\langle\chi_{HI}\rangle \simeq 10^{-2}$; this corresponds to the average H I fraction at which galaxies typically inhabit H II regions such that the red part of the Lyα line escapes unattenuated by H I.

We now discuss the evolution of the Lyα LFs with $f_{\rm esc}$. As we have already noted in Fig. 4.6, although the spatial distribution of the ionization fields looks very similar for the varying $f_{\rm esc}$ values for a given $\langle\chi_{HI}\rangle$, the χ_{HI} value in any given cell decreases with increasing $f_{\rm esc}$. This leads to an increase in T_α with $f_{\rm esc}$ such that for $\langle\chi_{HI}\rangle \simeq 0.1$, averaged over all LAEs, $\langle T_\alpha\rangle = (0.43, 0.45, 0.48, 0.59)$ for $f_{\rm esc} = (0.05, 0.25, 0.50, 0.75)$. However, this slight increase in T_α is compensated by the decrease in the intrinsic Lyα luminosity with increasing $f_{\rm esc}$ as shown in panel (a) of Fig. 4.8. As a result, the amplitude of the resulting Lyα LFs decreases slightly as $f_{\rm esc}$ increases from 0.05 to 0.5 for a given $\langle\chi_{HI}\rangle$; however, the slopes are very similar since $f_{\rm esc}$ affects the intrinsic luminosity of all simulated

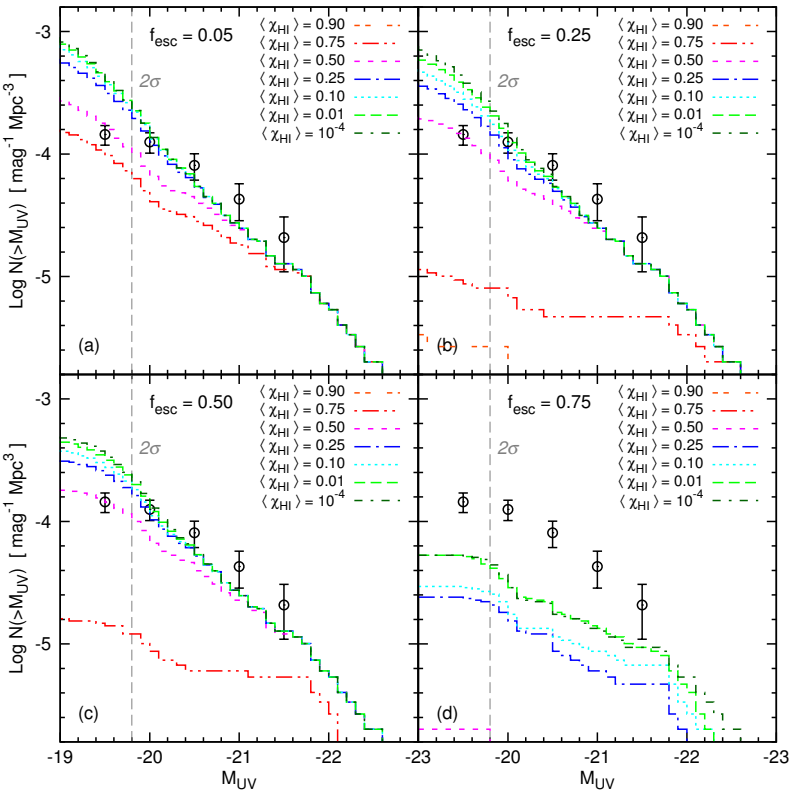

Figure 4.9: The cumulative UV LFs for simulated LAEs using a homogeneous dust case ($f_\alpha/f_c = 0.68$). The lines in the panels show the UV LFs for different $\langle\chi_{HI}\rangle$ states ($\langle\chi_{HI}\rangle \simeq 0.90, 0.75, 0.50, 0.25, 0.10, 0.01, 10^{-4}$) obtained using the fixed $f_{\rm esc}$ value marked above the panel. In each panel, black open circles show the LAE UV LFs at $z \simeq 6.5$ inferred observationally by Kashikawa et al. (2011). The vertical grey dotted lines indicate the limiting 2σ magnitude in the z' band (see Kashikawa et al., 2011); measurements for fainter magnitudes may be uncertain because the corresponding z'-band magnitudes are no longer reliable. Due to the EW selection criterion no LAEs are identified for $f_{\rm esc} = 0.95$.

galaxies by the same factor. The Lyα LF drops steeply between $f_{\rm esc} = 0.5$ and 0.75 and there are no simulated galaxies that would be identified as LAEs for $f_{\rm esc} = 0.95$. This steep drop for $f_{\rm esc} > 0.5$ arises due to our imposed criterion of the observed Lyα EW being larger than 20Å. For a continually star-forming galaxy with an age of about 200Myr, a stellar metallicity of $Z_* = 0.02 Z_\odot$ and $f_{\rm esc} = 0$, the intrinsic Lyα EW has a value of about 114Å; we note that this intrinsic EW would decrease for increasing values of Z_* and $f_{\rm esc}$. For a value of $f_{\rm esc} = (0.75,\ 0.95)$, this intrinsic EW then reduces to about (28.5, 5.7)Å . Then, taking into account the effect of the IGM transmission very few (none) of our simulated galaxies fulfil the EW selection criterion for $f_{\rm esc} = 0.75$ (0.95) leading to a steep drop in the number density of LAEs; the total number density of LAEs drops to zero for $f_{\rm esc} = 0.95$.

Finally, we note that both the slope and amplitude of the simulated Lyα LFs are in agreement with observations for $f_{\rm esc} = 0.05$ and $\langle\chi_{HI}\rangle \leq 0.1$; for $f_{\rm esc} \geq 0.25$, the simulated Lyα LFs are underestimated with respect to the data, even for a fully ionized IGM.

The UV LFs are not directly dependent on the IGM ionization state. However, both their slope and amplitude are affected by $\langle\chi_{HI}\rangle$ since these are the UV LFs for the simulated galaxies that would be identified as LAEs on the basis of L_α^{obs} and the EW. It is interesting to note that with our deeper Lyα luminosity limit of $L_\alpha^{obs} \geq 10^{42}$erg s^{-1}compared to the observational limit of $10^{42.4}$ erg s^{-1}, we find that the cumulative UV LFs keep rising until $M_{UV} \leq -19$ for $f_{\rm esc} \leq 0.5$ as seen from panels (a)-(c) of Fig. 4.9. From these same panels, we find that the bright-end slope of the UV LF ($M_{UV} \leq -21.5$) matches the observed UV LFs for all values of $\langle\chi_{HI}\rangle$ and $f_{\rm esc} \leq 0.5$. Further, the UV LFs start converging at much higher values of $\langle\chi_{HI}\rangle \simeq 0.25$, compared to the value of 0.1 required for the Lyα LFs to settle. Similar to the behaviour seen for the Lyα LF, for a given $f_{\rm esc} \leq 0.5$, the faint end of the UV LF steepens with decreasing $\langle\chi_{HI}\rangle$ as more and more of these galaxies are able

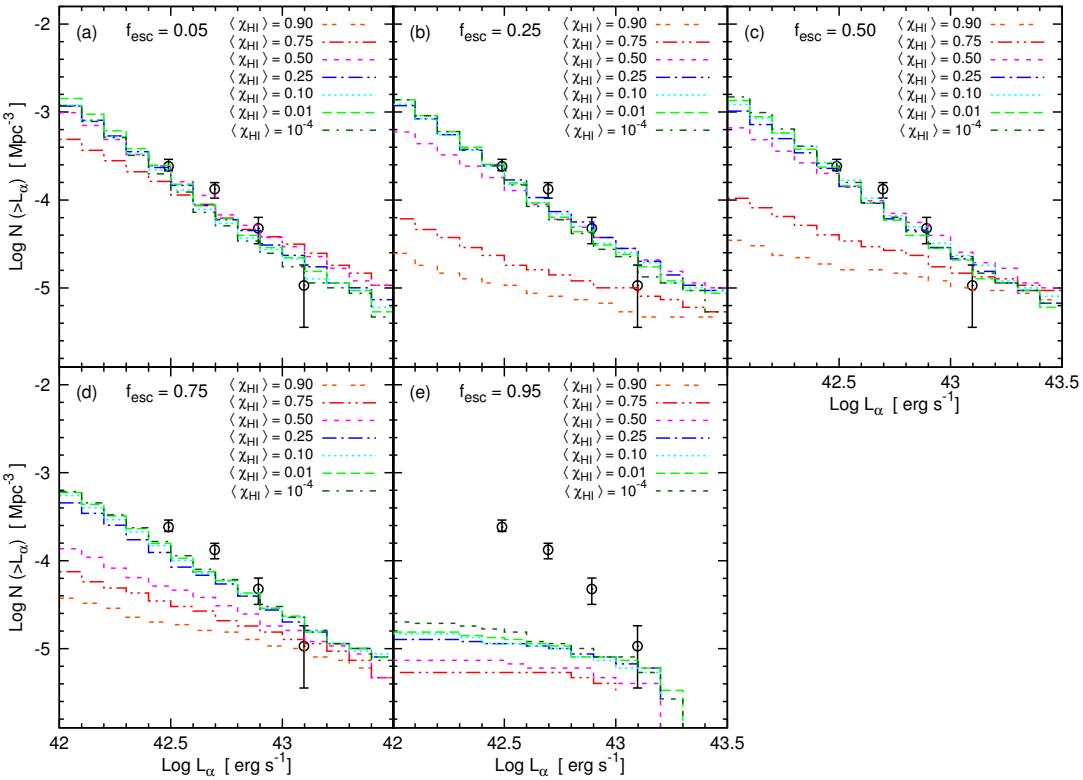

Figure 4.10: The cumulative Lyα LFs. The panels show the best-fit simulated results for the f_α/f_c values shown in Table 4.1. The panels show the results for different $\langle\chi_{HI}\rangle$ states ($\langle\chi_{HI}\rangle \simeq 0.90$, 0.75, 0.50, 0.25, 0.10, 0.01, 10^{-4}) obtained using the fixed $f_{\rm esc}$ value marked above the panel. In each panel, black open circles show the Lyα LFs at $z \simeq 6.5$ inferred observationally by Kashikawa et al. (2011).

to transmit enough of their Lyα flux to be visible as LAEs. Again, for a given $\langle\chi_{HI}\rangle$, while the amplitude of the UV LFs decreases slightly between $f_{\rm esc} = 0.05$ and 0.5, the slope remains the same. The steep drop in the number of LAEs for $f_{\rm esc} \simeq 0.75$ naturally leads to a drop in the UV LF shown in panel (d) of the same figure; as for the Lyα LF, the UV LF amplitude is zero for $f_{\rm esc} = 0.95$ due to no simulated galaxies being classified as LAEs.

Finally, we note that by jointly reproducing the observed Lyα and UV LFs, we can constrain for $f_{\rm esc} = 0.05$ one of the most important parameters for reionization: $\langle\chi_{HI}\rangle \leq 0.1$ or $\langle T_\alpha\rangle_{LAE} \geq 0.43$.

However, we caution the reader that this result is only valid in case the ISM dust is homogeneously distributed. Since using only the UV LFs allows a much larger parameter range of $\langle\chi_{HI}\rangle \leq 0.25$, a question that arises is whether this larger parameter space could also be reconciled with the Lyα LFs given clumped dust that could increase L_α^{obs} by increasing f_α. We carry out these calculations in Sec. 4.5.2 that follows.

4.5.2 Clumped dust

A number of works have shown that inhomogeneously distributed (clumped) dust in the ISM can enhance the escape fraction of Lyα photons compared to UV photons which are not resonantly scattered by H I (Neufeld, 1991; Hansen and Oh, 2006). However, the amount by which the ratio f_α/f_c can be enhanced by clumped dust sensitively depends on the amount of dust that is bound in cold neutral gas clouds, and the number of these encountered by Lyα photons within the galaxy. Since such sub-grid parameters can not be resolved by our cosmological simulation, we use f_α/f_c as a free parameter and explore the range required to reproduce the data for the different $f_{\rm esc}$ and $\langle\chi_{HI}\rangle$ combinations discussed in Sec. 4.5.1.

As shown in Section 4.5.1, an increasing $f_{\rm esc}$ reduces the intrinsic Lyα luminosity for all galaxies, leading to a drop in the amplitude of the Lyα LF. However, since $L_\alpha^{obs} \propto (1 - f_{\rm esc}) f_\alpha T_\alpha$, a decrease in

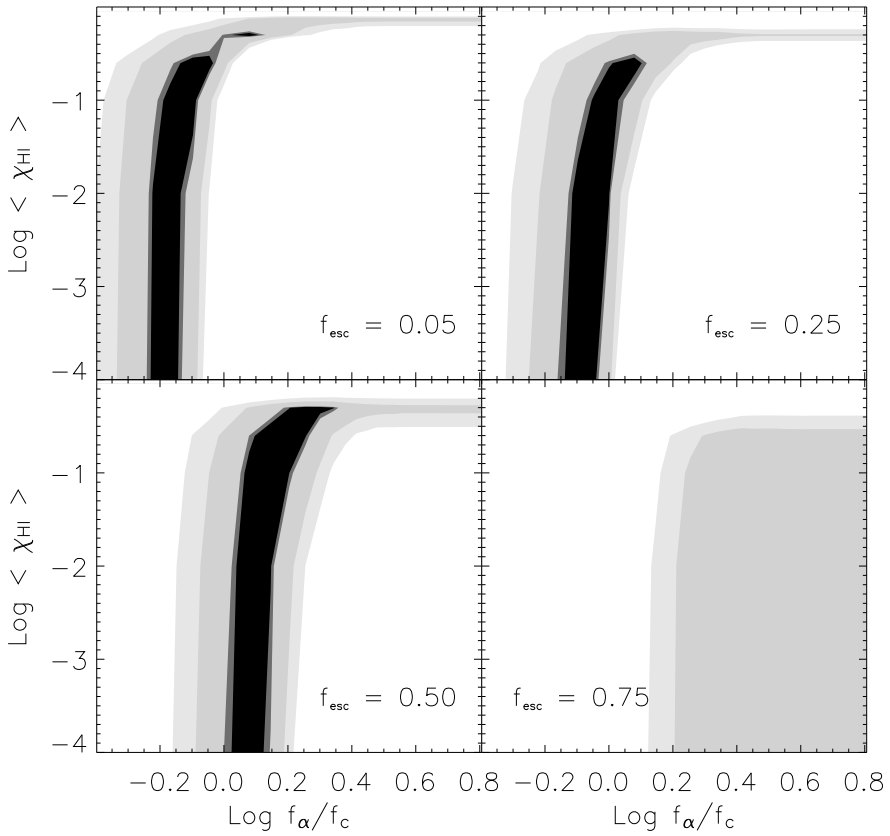

Figure 4.11: $1-5\sigma$ probability contours (black to light gray respectively) for the combinations of $\langle\chi_{HI}\rangle$, $f_{\rm esc}$ and f_α/f_c shown in Table. 4.1 that best fit the observed Lyα LF data at $z \simeq 6.5$ Kashikawa et al. (2011). Within a 1σ error, we can not distinguish between $\langle\chi_{HI}\rangle \simeq 10^{-4}$ to 0.5, f_α/f_c from 0.6 to 1.8 and $f_{\rm esc}$ ranging between 0.05 and 0.5. There exists a *degeneracy* between the IGM ionization state, escape fraction of H I ionizing photons and the dust clumping inside high-redshift galaxies such that a decrease in the IGM Lyα transmission can be compensated by an increase in the intrinsic Lyα luminosity produced, and the fraction of this luminosity that can escape the galaxy.

the intrinsic Lyα luminosity (due to an increasing $f_{\rm esc}$) can be compensated by a larger fraction of Lyα photons escaping out of the galaxy (i.e. a higher f_α) and/or a larger amount being transmitted through the IGM (i.e. a larger T_α). Hence, for a given $\langle\chi_{HI}\rangle$ (i.e. T_α) by allowing values of $f_\alpha/f_c > 0.68$, the amplitude of the Lyα LF can be boosted. However, it is important to note that since we use a constant value of f_α/f_c for all galaxies, it only changes the amplitude of the Lyα LF at the bright end; raising this ratio makes the faint-end slope slightly steeper since a number of galaxies which are at our detection limit ($L_\alpha \geq 10^{42}$erg s^{-1}and $EW \geq 20$Å) become visible as LAEs with increasing f_α/f_c.

It is interesting to note that even using f_α/f_c ratios such that f_α saturates to 1, the simulated Lyα LFs are well below the observations for $\langle\chi_{HI}\rangle \simeq 0.75$, for all $f_{\rm esc} = 0.05$ to 0.95, as seen from panels (a)-(e) of Fig. 4.10. This is because the H II regions built by faint galaxies are too small to allow a large IGM Lyα transmission, even for $f_{\rm esc} = 0.95$. We now discuss the results for varying $f_{\rm esc}$: as mentioned in Sec. 4.5.1, the Lyα and UV LFs can be well reproduced using the homogeneous dust case for $f_{\rm esc} = 0.05$ for $\langle\chi_{HI}\rangle \leq 0.1$. In the case of clumped dust, the simulated LFs match the observations for $f_{\rm esc} = 0.05$ for $\langle\chi_{HI}\rangle$ as high as 0.5, provided that the decrease in T_α is compensated by f_α/f_c increasing to 1.2 (see table 4.1). For $f_{\rm esc} = 0.25, 0.5$, within a 1σ error the simulated LFs can be reconciled with the observations for $\langle\chi_{HI}\rangle \leq 0.5$, given that f_α/f_c increases to 1.6, 1.8, respectively as shown in table 1; however, due to a decrease in the intrinsic Lyα luminosity and EW, the faint-end slope of the simulated LFs is always under-estimated with respect to the data for $\langle\chi_{HI}\rangle \geq 0.5$. As $f_{\rm esc}$ increases to 0.75 and above, the amplitude of the Lyα LFs can not be boosted up to the observed value, even for $f_\alpha = 1$; although the H II regions built by these galaxies are very large as a result of the

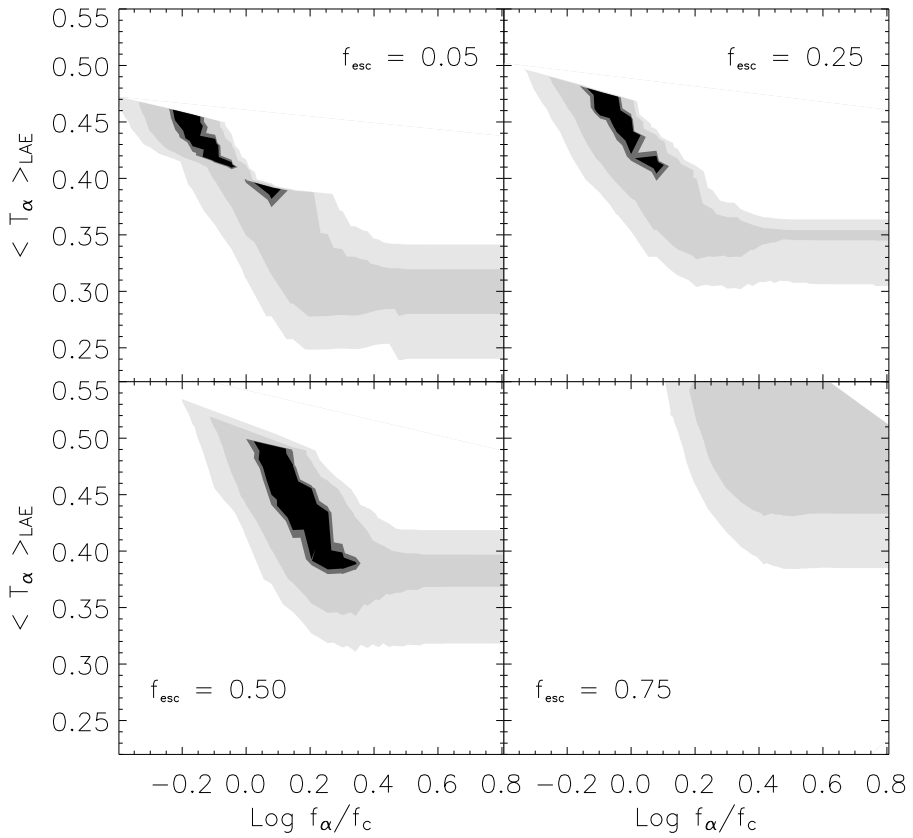

Figure 4.12: $1-5\sigma$ probability contours (black to light gray respectively) for the combinations of $\langle\chi_{HI}\rangle$, $f_{\rm esc}$ and f_α/f_c shown in Table. 4.1 that best fit the observed Lyα LF data at $z\simeq 6.5$ Kashikawa et al. (2011). Within a 1σ error, we can not distinguish between $\langle T_\alpha\rangle_{LAE}\simeq 0.38$ to 0.5, f_α/f_c from 0.6 to 1.8 and $f_{\rm esc}$ ranging between 0.05 and 0.5. There exists a *degeneracy* between the IGM Lyα transmission, escape fraction of H I ionizing photons and the dust clumping inside high-redshift galaxies such that a decrease in the IGM Lyα transmission can be compensated by an increase in the intrinsic Lyα luminosity produced, and the fraction of this luminosity that can escape the galaxy.

large H I ionizing photon escape fraction leading to large T_α values, the EW of the Lyα line prevents most of these galaxies from being classified as LAEs (see also Sec. 4.5.1 above).

We therefore find a *three-dimensional degeneracy* between the IGM ionization state $\langle\chi_{HI}\rangle$, the escape fraction of H I ionizing photons ($f_{\rm esc}$) and the clumped/inhomogeneous distribution of dust in the ISM of galaxies (governing f_α/f_c) such that a decrease in L_α^{int} with increasing $f_{\rm esc}$ can be compensated by a larger T_α and f_α/f_c. However, we find that the $\langle\chi_{HI}\rangle$ values which reproduce the observations decrease with increasing $f_{\rm esc}$ because an increasing f_α can not compensate for the decrease in the intrinsic Lyα luminosity. This degeneracy can be seen from Fig. 4.11 where we show contours of $1-5\sigma$ deviations from the observations (Kashikawa et al., 2011), obtained by computing the χ^2 values for all the combinations of $f_{\rm esc}=(0.05,..,0.95)$, $\langle\chi_{HI}\rangle=(10^{-4},..,0.90)$ and $f_\alpha/f_c=(0.60,..,1.8)$, as shown in Table. 4.1.

The relation between $\langle\chi_{HI}\rangle$ and $\langle T_\alpha\rangle$ is complex due to the dependency upon the reionization topology as shown in Dijkstra et al. (2011) (see also Fig. 4.7 and Jensen et al., 2013b) and the assumed line shape (e.g. Gaussian, double-peaked, Jensen et al., 2013b; Laursen et al., 2011; Duval et al., 2014). For this reason we also show the three-dimensional degeneracy in terms of the mean transmission across all LAEs ($\langle T_\alpha\rangle_{LAE}$) for a given combination of $f_{\rm esc}$ and f_α/f_c in Fig. 4.12.

We note that for a given $\langle\chi_{HI}\rangle$ the mean transmission of all LAEs $\langle T_\alpha\rangle_{LAE}$ decreases for increasing f_α/f_c: with rising f_α/f_c more galaxies, with lower values of T_α, are identified as LAEs, leading to a decline in $\langle T_\alpha\rangle_{LAE}$. This effect can be seen for the maximum $\langle T_\alpha\rangle_{LAE}$ values, within a 4σ error, in each panel of Figure 4.12 and it demonstrates the dependency of $\langle T_\alpha\rangle_{LAE}$ on f_α/f_c.

From Figure 4.11 and 4.12, we see that within a 1σ error, the observed Lyα and UV LFs can be

Table 4.1: For the $\langle \chi_{HI} \rangle$ value shown in column 1, for the $f_{\rm esc}$ value shown as a subscript in each of the columns 2-4, we show the f_α/f_c ratio required to fit the simulated LAE Lyα and UV LFs to those observed by Kashikawa et al. (2011) within a $1-\sigma$ error. Dashes indicate that the simulated LFs could not be matched to the observations within a $1-\sigma$ error, even for the maximum possible value of $f_\alpha = 1$.

$\langle \chi_{HI} \rangle$	$(f_\alpha/f_c)_{0.05}$	$(f_\alpha/f_c)_{0.25}$	$(f_\alpha/f_c)_{0.5}$
0.50	1.2	1.6	1.8
0.25	0.8	1.2	1.4
0.10	0.68	1.0	1.4
0.01	0.68	0.9	1.2
10^{-4}	0.60	0.8	1.2

reproduced for $f_{\rm esc}$ values ranging between $0.05-0.5$ and $\langle \chi_{HI} \rangle \simeq 10^{-4}-0.5$ or $\langle T_\alpha \rangle \simeq 0.38-0.5$, provided that the decreasing intrinsic Lyα luminosity (with increasing $f_{\rm esc}$) and decreasing IGM transmission (with increasing $\langle \chi_{HI} \rangle$) is compensated by an increasing $f_\alpha/f_c = 0.6$ to 1.8. This implies that if dust is indeed clumped in the ISM of high-redshift galaxies such that the relative Lyα escape fraction can be as high as 1.8 times the UV escape fraction, we can not differentiate between a universe which is either completely ionized or half neutral (or where $38-50\%$ of LAE Lyα radiation is transmitted through the IGM) or an $f_{\rm esc}$ ranging between 5-50%. This parameter space is much larger than that allowed for a homogeneous dust distribution, where matching to the observations requires $f_{\rm esc} = 0.05$ and $\langle \chi_{HI} \rangle \leq 0.1$ ($\langle T_\alpha \rangle_{LAE} \geq 0.43$).

4.6 Conclusions

In this work we couple state of the art cosmological simulations run using GADGET-2 with a dust model and a radiative transfer code (pCRASH) to build a physical model of $z \simeq 6.7$ LAEs to simultaneously constrain the IGM reionization state, the escape fraction of H I ionizing photons and ISM dust distribution (homogeneous/clumped).

We start by validating the properties of the simulated galaxy population against observations of high-redshift ($z \simeq 6-8$) LBGs. Identifying bound structures using the Amiga Halo Finder, simulated galaxies which are complete in the halo mass function ($M_h \geq 10^{9.2} M_\odot$), contain a minimum of $4N$ gas particles ($N = 40$) and a minimum of 10 star particles are identified as the "resolved" population". For each such resolved galaxy, we use the mass, age and metallicity of each of its star particles to build the composite spectra. We use a dust model (Dayal et al., 2010) that calculates the SNII dust-enrichment depending on the entire star formation history of a given galaxy, to obtain the associated escape fraction of UV photons. Once these calculations are carried out, galaxies with a dust-attenuated UV magnitude $M_{UV} \leq -17$ are identified as LBGs at $z \simeq 6-8$. Comparing the predictions by the simulation against LBG observations, we find that the slope and amplitude of the dust-attenuated UV LFs are in good agreement with the data at $z \simeq 6, 7$ while the UV LF at $z \simeq 8$ requires no dust to match to the observations, such that $f_c \simeq (0.5, 0.6, 1.0)$ at $z \simeq (6, 7, 8)$, averaged over all LBGs. The theoretical Schechter parameters are found to be $\alpha = (-1.9 \pm 0.2, -2.0 \pm 0.2, -1.8 \pm 0.2)$ and $M_{UV,*} = (-19.8 \pm 0.3, -19.7 \pm 0.2, -19.9 \pm 0.3)$ at $z \simeq (6, 7, 8)$, and are consistent with those inferred observationally (McLure et al., 2009, 2013; Bouwens et al., 2011). We also find that the theoretical LBG stellar mass functions, SMDs and sSFRs are in excellent agreement with the data at $z \simeq 6-8$ (see Sec. 4.3).

Once that the physical properties and dust enrichment of the simulated galaxy population have been validated against the mentioned observational data sets, we proceed to modelling LAEs. This requires further information on (a) the fraction of the H I ionizing photons produced by a galaxy that are absorbed by ISM H I ($1-f_{\rm esc}$) and contribute to the Lyα emission line; the rest ($f_{\rm esc}$) emerge out and contribute to reionization, (b) the relative effect of ISM dust on Lyα and UV photons (f_α/f_c), and (c) the level to which the IGM is ionized by the galaxy population ($\langle \chi_{HI} \rangle$), in order to calculate the IGM Lyα transmission. Since $f_{\rm esc}$ remains poorly constrained with proposed values ranging between 1-100% (e.g. Ricotti and Shull, 2000; Gnedin et al., 2008; Ferrara and Loeb, 2013), we use five different values of $f_{\rm esc} = 0.05, 0.25, 0.5, 0.75, 0.95$ to run the radiative transfer code (pCRASH) in order to obtain various "reionization" states of the simulated volume as it evolves from being fully

neutral ($\langle\chi_{HI}\rangle \simeq 1$) to completely ionized ($\langle\chi_{HI}\rangle \simeq 10^{-4}$); pCRASH follows the time evolution of the ionization fraction (H I) and temperature given the spectra of the source galaxy population. Once these calculations are carried out, galaxies with $L_\alpha^{obs} \geq 10^{42}$erg s^{-1} and $EW \geq 20$Å are identified as LAEs; the only free parameter of the model (f_α/f_c) is then fixed by matching the simulated LFs to the observations.

We start from the simplest case of considering the SNII produced dust to be *homogeneously distributed* in the ISM. The SNII extinction curve yields $f_\alpha/f_c = 0.68$. Using this model, we find that for a given $f_{\rm esc}$, the IGM Lyα transmission increases with decreasing $\langle\chi_{HI}\rangle$, with this increase being most important for the smallest galaxies; as $\langle\chi_{HI}\rangle$ decreases, even small galaxies are able to ionize a large enough H II region around themselves to be visible as LAEs. Hence, the Lyα LF becomes *steeper* with decreasing $\langle\chi_{HI}\rangle$ for any given $f_{\rm esc}$ value. Further, for a given $\langle\chi_{HI}\rangle$, although the ionization fields look very similar for different $f_{\rm esc}$ values, the degree of ionization (χ_{HI}) in any cell increases with $f_{\rm esc}$ due to an increase in the H I ionizing photon emissivity. This leads to a slight increase in T_α with $f_{\rm esc}$ for a given $\langle\chi_{HI}\rangle$. However, this increase is more than compensated by the decrease in the intrinsic Lyα luminosity with increasing $f_{\rm esc}$ (as less photons are available for ionizations in the ISM), as a result of which the Lyα LF decreases slightly in amplitude with $f_{\rm esc}$ for a given $\langle\chi_{HI}\rangle$. Finally, comparing simulated Lyα and UV LFs with observations, we find that for a homogeneous ISM dust distribution and $f_{\rm esc} = 0.05$, we can *constrain* $\langle\chi_{HI}\rangle \leq 0.1$ *or* $\langle T_\alpha\rangle_{LAE} \geq 0.43$.

We also explore the scenario of dust being inhomogeneously distributed/clumped in the ISM of high-redshift galaxies, boosting up the ratio of f_α/f_c. For a given $\langle\chi_{HI}\rangle$ value, an increase in $f_{\rm esc}$ leads to a drop in the amplitude of the Lyα LF due to a decrease in L_α^{int}, as mentioned above. In the clumped dust scenario, this decrease can be compensated by an increase in f_α. For $\langle\chi_{HI}\rangle \simeq 0.5$, $f_{\rm esc}$ values as high as 0.5 can be reconciled with the data, given that f_α/f_c increases from $\simeq 0.6$ to 1.8 as $f_{\rm esc}$ increases from 0.05 to 0.5. We thus find a *three-dimensional degeneracy* between $\langle\chi_{HI}\rangle$, $f_{\rm esc}$ and f_α/f_c such that a decrease in L_α^{int} with increasing $f_{\rm esc}$ can be compensated by a larger T_α and f_α/f_c. Due to the model dependency (e.g. Lyα line profile, reionization topology) of the $\langle\chi_{HI}\rangle$ -$\langle T_\alpha\rangle$ relation we also rephrase our result by converting the $\langle\chi_{HI}\rangle$ values to the corresponding mean transmission values for LAEs ($\langle T_\alpha\rangle_{LAE}$). Within an 1σ error, we find that allowing for clumped dust, the data can be reproduced for a wide parameter space of $\langle T_\alpha\rangle_{LAE} \simeq 0.38 - 0.50$ or $\langle\chi_{HI}\rangle \simeq 0.5 - 10^{-4}$, $f_{\rm esc} \simeq 0.05 - 0.5$ and $f_\alpha/f_c \simeq 0.6 - 1.8$, i.e., if dust is indeed clumped in the ISM of high-redshift galaxies such that the relative Lyα escape fraction can be as high as 1.8 times the UV escape fraction, we can not differentiate between a universe which is either completely ionized or half neutral or where on average $38 - 50\%$ of the Lyα radiation is transmitted, or has an $f_{\rm esc}$ ranging between 5-50%. We caution the reader that although the constraints in terms of $\langle T_\alpha\rangle_{LAE}$ account for the model dependent relation between $\langle\chi_{HI}\rangle$ and $\langle T_\alpha\rangle$, the value of $\langle T_\alpha\rangle_{LAE}$ sensitively depends on the galaxies that are classified as LAEs for a given combination of $f_{\rm esc}$, $\langle\chi_{HI}\rangle$ and f_α/f_c.

We now discuss some of the caveats involved in this work. Firstly, an enhancement of the escape fraction of Lyα photons with respect to continuum photons via the Neufeld effect (Neufeld, 1991) in a clumpy ISM remains controversial: on the one hand Hansen and Oh (2006) showed that such enhancement was possible if the Lyα photons encountered a certain number of "clumps". On the other hand, Laursen et al. (2013) have shown that enhancing the ISM Lyα escape fraction requires very specific conditions (no bulk outflows, very high metallicity, very high density of the warm neutral medium and a low density and highly ionized medium) that are unlikely to exist in any real ISM.

Secondly, as a consequence of simulating cosmological volumes we are unable to resolve the ISM of the individual galaxies to be able to model the Lyα line profile that emerges out of any galaxy. We have therefore assumed the emergent Lyα line to have a Gaussian profile with the width being set by the rotation velocity of the galaxy. However, several observational (Tapken et al., 2007; Yamada et al., 2012) and theoretical works (Verhamme et al., 2008; Jensen et al., 2013b) have found the emerging Lyα line profile to be double-peaked; this profile results in higher IGM Lyα transmission values compared to a Gaussian profile (Jensen et al., 2013b). An increase in T_α due to such a double-peaked profile allows our theoretical LFs to fit the observations with slightly lower f_α/f_c values.

Thirdly, we assume a constant escape fraction $f_{\rm esc}$ for all galaxies. Although the value of $f_{\rm esc}$ and its dependence on galaxy properties (such as the stellar mass) are only poorly known, recent work hints at an $f_{\rm esc}$ that decreases with increasing mass (Ferrara and Loeb, 2013; Paardekooper et al., 2011). If $f_{\rm esc}$ is indeed higher for low-mass galaxies, the ionization topology would become more homogeneous with the H II regions being built by low-mass (high-mass) galaxies being larger (smaller) than the constant $f_{\rm esc}$ case. This would have two effects: on the one hand the IGM Lyα transmission would be enhanced (decrease) for low-mass (high-mass) galaxies, leading to a steeper Lyα LF. On the other

hand, due to its direct dependence on $f_{\rm esc}$, the intrinsic Lyα luminosity would decrease (increase) for low-mass (high-mass) galaxies, leading to a flattening of the Lyα LF. The relative importance of these two effects is the subject of a work currently in preparation.

Fourthly, we assume that dust in high-redshift galaxies is solely produced by type II supernovae. However, as shown by Valiante et al. (2009), AGB stars can start contributing to significantly, and even dominate, the dust budget in regions of very high star formation (e.g. QSO/quasars) after $150 - 500$ Myrs. However, a significant part of this extra dust could be destroyed by forward SN shocks (Bianchi and Schneider, 2007) that have also not been considered in this work.

In ongoing calculations, our aim is to see whether the parameter space allowed by "clumped" dust can be narrowed with a combination of LAE clustering and through 21cm brightness maps that will be directly testable with upcoming observations with the Subaru Hyper-Suprime Camera and LoFAR.

Chapter

5

Large scale clustering and duty cycle of LAEs[1]

We calculate Lyman Alpha Emitter (LAE) angular correlation functions (ACFs) at $z \simeq 6.6$ and the duty cycle of Lyman Break Galaxies (LBGs) with/without Lyman Alpha (Lyα) emission using a model that combines SPH cosmological simulations (GADGET-2), dust attenuation and a radiative transfer code (pCRASH). The ACFs are a powerful tool that significantly narrows the 3D parameter space allowed by LAE Lyα and UV luminosity functions (LFs) alone. With this work, we simultaneously constrain the escape fraction of ionizing photons $f_{esc} = 0.05-0.5$, the mean fraction of neutral hydrogen in the intergalactic medium (IGM) $\langle \chi_{HI} \rangle \lesssim 0.01$ and the dust-dependent ratio of the escape fractions of Lyα and UV continuum photons $f_\alpha/f_c = 0.6 - 1.2$. Our results show that reionization has the largest impact on the amplitude of the ACFs, and its imprints are clearly distinguishable from those of f_{esc} and f_α/f_c. We also show that galaxies with a critical stellar mass of $M_* = 10^{8.5}(10^{9.5})\mathrm{M}_\odot$ produce enough luminosity to stay visible as LBGs (LAEs). Finally, the duty cycle of LBGs with (without) Lyα emission increases with the UV magnitude (and M_*): considering observed (dust and IGM attenuated) luminosities, the fraction of its lifetime a galaxy spends as a LBG (LAE) increases from 35% to 80% ($\simeq 0 - 70\%$) as M_{UV} decreases from $M_{UV} = -18.5$ to -23.5 (M_* increases from $10^8 - 10^{10.5}\mathrm{M}_\odot$). Thus in our model the brightest (most massive) LBGs most often show Lyα emission.

5.1 Introduction

The Epoch of Reionization (EoR) marks a major phase change in the ionization state of the Universe. While the intergalactic medium (IGM) is predominantly composed of neutral Hydrogen (H I) at the beginning of this epoch, it is completely ionized by the end, as a result of H I ionizing photons produced by both stars and quasars. However, the progress of reionization has been hard to pin down since it has a number of feedback effects on structure formation. In particular, the ultraviolet background (UVB) built up during reionization leads to photo-heating of gas, quenching star formation (at least temporarily) in the very galaxies that drive this process (see e.g. Barkana and Loeb, 2001; Ciardi and Ferrara, 2005; Maio et al., 2011; Sobacchi and Mesinger, 2013a; Wyithe and Loeb, 2013, and references therein).

Lyman Alpha (Lyα) photons are a powerful tool in understanding the ionization state of the IGM given their high optical depth (τ) to H I (e.g. Madau and Rees, 2000)

$$\tau = 1.5 \times 10^5 h^{-1} \Omega_m^{-1} \frac{\Omega_b h^2}{0.019} \left(\frac{1+z}{8} \right)^{3/2} (1 + \delta_H) \ \chi_{HI}, \tag{5.1}$$

where h is the Hubble parameter, Ω_b and Ω_m represent the cosmic baryon and matter density respectively, $(1 + \delta_H)$ is the hydrogen over-density and χ_{HI} is the fraction of neutral hydrogen. As seen from this equation, even a neutral hydrogen fraction as low as 10^{-5} can lead to a significant attenuation of Lyα photons at high-z, making them extremely sensitive probes of H I in the IGM. As

[1] This chapter contains a preprint version which was submitted to MNRAS as Hutter, A.; Dayal, P; Müller, V.; doi: 10.1093/mnras/stv929

a result, a class of high-z galaxies called Lyman Alpha Emitters (LAEs), detected by means of their Lyα line (at 1216 Å in the rest frame), have become extremely popular probes of reionization, with statistically significant samples available in the reionization epoch, at $z \simeq 5.7$ and 6.6 (Malhotra et al., 2005; Taniguchi et al., 2005; Shimasaku et al., 2006; Hu et al., 2010; Kashikawa et al., 2006; Ouchi et al., 2010; Kashikawa et al., 2011). Indeed, a number of theoretical papers have used semi-analytic (e.g. Dijkstra et al., 2007; Dayal et al., 2008; Samui et al., 2009) or numerical (e.g. McQuinn et al., 2007a; Iliev et al., 2008; Dayal et al., 2011; Forero-Romero et al., 2011; Duval et al., 2014; Hutter et al., 2014) models to reproduce the observed number counts of LAEs (the Lyα luminosity function; LF) at various redshifts in the reionization epoch. However interpreting a change in the Lyα LF is rendered challenging by the fact that the observed Lyα luminosity depends on: (a) the fraction of H I ionizing photons (1-$f_{\rm esc}$) produced by a galaxy that are able to ionize the interstellar H I resulting in the Lyα recombination line, with the rest ($f_{\rm esc}$) escaping to ionize the IGM, (b) the fraction of the intrinsic Lyα photons that can emerge out of the galactic environment unattenuated by dust (f_α) and H I and (c) the fraction of these emergent Lyα photons that are transmitted (T_α) through the IGM (depending on $\langle \chi_{HI} \rangle$) and reach the observer.

Given these uncertainties, we require an alternative measurement to constrain the ionization state using LAEs. One such strong measure is provided by the two-point angular correlation function (ACF) of LAEs that describes their spatial clustering. Indeed, McQuinn et al. (2007a) have shown that the spatial clustering can hardly be attributed to anything other than the large scale ($\sim$ Mpc scale) ionization regions created during reionization. However, Iliev et al. (2008) caution that the LAE clustering might not be a good indicator for reionization patchiness since the density, neutral fraction and velocity fields are highly anisotropic, leading to a large variation in the IGM transmission and LAE visibility along different lines of sight (LOS). Building on this, Zheng et al. (2010) have shown that Lyα radiative transfer modifies the ratio of observed and intrinsic Lyα luminosities depending on the density and velocity structure of the environment, i.e. LOS (transverse) density fluctuations are suppressed (enhanced), leading to a change in the amplitude of the two-point correlation function compared to the case without the environmental selection effect. However, while Behrens and Niemeyer (2013) have confirmed a correlation between the observed Lyα luminosity and the underlying density and velocity field, they do not find a significant deformation of the two-point correlation function by post-processing hydrodynamical simulations with a Lyα radiative transfer code.

A second probe is presented by the fraction of Lyman Break Galaxies (LBGs) that show Lyα emission: given that the physical properties of LBGs do not evolve in the 150 Myr between $z \simeq 6$ and 7, a sudden change in the fraction of LBGs showing Lyα emission could be attributed to reionization (e.g. Stark et al., 2010, 2011; Pentericci et al., 2011). However, this interpretation is complicated by caveats including the redshift dependence of the relative effects of dust on Lyα and ultraviolet (UV) continuum photons (Dayal and Ferrara, 2012) and the fact that simple cuts in EW and UV luminosity may lead to uncertainties in the LAE number densities (Dijkstra and Wyithe, 2012).

Coupling a cosmological SPH simulation snapshot at $z \simeq 6.6$ with a radiative transfer (RT) code (pCRASH) and a dust model, Hutter et al. (2014) have shown that the effects of $f_{\rm esc}$, f_α and T_α are degenerate on the LAE visibility: reproducing the observed Lyα LFs can not differentiate between a Universe which is either completely ionized or half neutral ($\langle \chi_{HI} \rangle \simeq 0.5 - 10^{-4}$), or has an $f_{\rm esc}$ ranging between 5-50%, or has dust that it either clumped or homogeneously distributed in the interstellar medium (ISM) with $f_\alpha/f_c = 0.6 - 1.8$; here f_c represents the fraction of UV photons that emerge out of the ISM unattenuated by dust. In this work, we extend our calculations to use the two-point LAE ACF to narrow down the 3-dimensional parameter space of $\langle \chi_{HI} \rangle$, $f_{\rm esc}$ and f_α/f_c. Further, we study the time evolution of both the Lyα and UV luminosities to show the *fraction* of its lifetime that a galaxy is visible as a LAE or LBG, both considering the *intrinsic* and (observed) *dust and IGM-attenuated* luminosities.

The cosmological model corresponds to the ΛCDM Universe with dark matter (DM), dark energy and baryonic density parameter values of (Ω_Λ, Ω_m, Ω_b) = (0.73, 0.27, 0.047), a Hubble constant $H_0 = 100h = 70 {\rm kms}^{-1}{\rm Mpc}^{-1}$, and a normalisation $\sigma_8 = 0.82$, consistent with the results from WMAP5 (Komatsu et al., 2009).

5.2 The model

In this section we briefly describe our physical model for high-redshift LAEs that couples cosmological SPH simulations run using GADGET-2 with a RT code (pCRASH) and a dust model, and interested

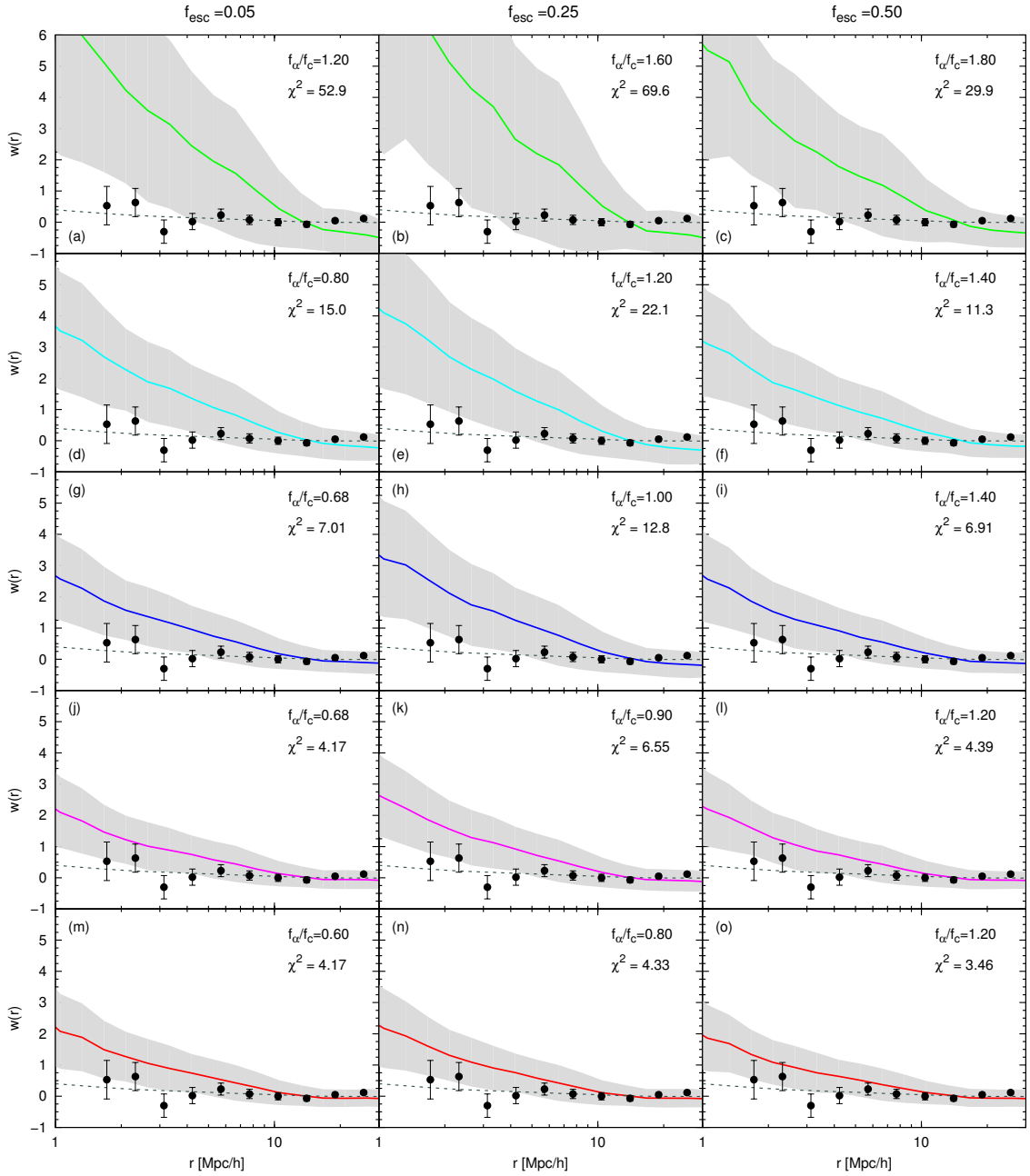

Figure 5.1: Angular correlation function for simulated LAEs. The mean ACF is calculated from 36 mock catalogues (12 along each of x, y, z directions) assuming volumes with a depth of $30h^{-1}$ Mpc and a FoV of $\sim 3{\times}10^3 h^{-2}$ Mpc^2. In each panel, the solid line shows the ACF of the best fit (f_α/f_c, $f_{\rm esc}$, $\langle\chi_{HI}\rangle$) combinations for which the simulated LAE Lyα LFs are within the 1σ limit of the observations by Kashikawa et al. (2011) with shaded regions showing the variance across the mock catalogues. In each panel, the grey dashed line shows the ACF for LBGs from the whole box, corresponding errors on the ACF for LBGs are comparable with the line width, and black points represent the observational results by Kashikawa et al. (2006). Columns show the results for $f_{esc} = 0.05, 0.25$ and 0.5, as marked. The values of $\langle\chi_{HI}\rangle$ are marked at the end of each row, with the f_α/f_c value marked in each panel, along with the χ^2 error.

readers are referred to Hutter et al. (2014) for a detailed description.

The hydrodynamical simulation analysed in this work was carried out with the TreePM-SPH code GADGET-2 and has a box size of $80h^{-1}$ comoving Mpc (cMpc) and contains 1024^3 DM particles, and initially the same number of gas particles; the mass of a DM and gas particle is $3.6 \times 10^7 h^{-1}{\rm M}_\odot$ and $6.3 \times 10^6 h^{-1}{\rm M}_\odot$, respectively. The simulation includes all the standard processes of star formation

Table 5.1: For the $\langle\chi_{HI}\rangle$ value shown in Column 1, we summarise the f_α/f_c ratio required to best fit the simulated Lyα LF to observations (Kashikawa et al., 2011) within 1σ limits in columns 2-4 with subscripts showing the $f_{\rm esc}$ value used (Hutter et al., 2014).

$\langle\chi_{HI}\rangle$	$\langle f_\alpha/f_c\rangle_{0.05}$	$\langle f_\alpha/f_c\rangle_{0.25}$	$\langle f_\alpha/f_c\rangle_{0.5}$
0.50	1.2	1.6	1.8
0.25	0.8	1.2	1.4
0.10	0.68	1.0	1.4
0.01	0.68	0.9	1.2
10^{-4}	0.60	0.8	1.2

and its associated metal production and feedback using the prescription of Springel and Hernquist (2003), using a Salpeter Salpeter (1955) initial mass function (IMF) between $0.1-100{\rm M}_\odot$. Bound structures of more than 20 total (Dark Matter, gas and star) particles are recognised as galaxies using the Amiga Halo Finder (AHF; Knollmann and Knebe, 2009). Of all these galaxies, we only use "resolved" galaxies that are complete in the halo mass function in all our calculations - these consist of at least 160 (10) gas (star) particles and have a halo mass $M_h \gtrsim 10^{9.2}{\rm M}_\odot$. Assuming each star particle to have formed in a burst, we calculate its spectra, and rest-frame intrinsic Lyα (L_α^{int}) and UV continuum (L_c^{int}; 1505Å) luminosities depending on the stellar mass, age and metallicity using the population synthesis code STARBURST99 (Leitherer et al., 1999). For each galaxy, the dust mass and its corresponding UV attenuation are calculated using the dust model described in Dayal et al. (2011). The observed UV luminosity is then calculated as $L_c^{obs} = f_c \times L_c^{int}$ where f_c is the fraction of UV photons that emerge out of the ISM unattenuated by dust which is fixed by matching to the observed evolving UV LF at $z \simeq 6-8$; galaxies with an absolute UV magnitude $M_{UV} \lesssim -17$ are then identified as LBGs. The observed Lyα luminosity (L_α^{obs}) is then calculated as $L_\alpha^{obs} = f_\alpha T_\alpha L_\alpha^{int}$ where f_α and T_α account for dust attenuation in the ISM and by H I in the IGM, respectively. Galaxies with $L_\alpha^{obs} \geq 10^{42}$ erg s^{-1} and $EW = L_\alpha^{obs}/L_c^{obs} \geq 20\,$Å are identified as LAEs.

Given that both L_α^{int} and $\langle\chi_{HI}\rangle$ depend on the fraction of H I ionizing photons that can escape out of the ISM ($f_{\rm esc}$), we use five values of $f_{\rm esc}$=0.05, 0.25, 0.5, 0.75, 0.95 to post-process the $z \simeq 6.6$ snapshot of the hydrodynamical simulation with the 3D radiative transfer (pCRASH). To explore the full range of $\langle\chi_{HI}\rangle$ (that determines T_α) we run pCRASH starting from a completely neutral to a completely ionized state and obtain ionization fields for different values of the mean fraction of neutral hydrogen $\langle\chi_{HI}\rangle$; for each galaxy we assume the initial line profile to be Gaussian and compute the average Lyα transmissions along 48 different lines of sight (LOS). For each combination of f_{esc} and $\langle\chi_{HI}\rangle$ the transmission T_α is then fixed and the only free parameter that can be adjusted to match Lyα luminosities to observations (Kashikawa et al., 2011) is the relative escape fraction of Lyα and UV photons from the ISM, $p = f_\alpha/f_c$.

From the Lyα LFs we find the following trends: the amplitude of the LAE Lyα LF decreases with increasing f_{esc} due to a decrease in L_α^{int}. However, this decline can be compensated by an increase in either f_α/f_c or T_α (in an increasingly ionized IGM). Comparing our model Lyα LFs to observations (Kashikawa et al., 2011) we found that allowing for clumped dust ($p \gtrsim 0.6$), the observations can be reproduced for $\langle\chi_{HI}\rangle \simeq 0.5-10^{-4}$, $f_{esc} \simeq 0.05-0.5$ and $f_\alpha/f_c = 0.6-1.8$ within a 1σ error.

5.3 Constraints from LAE clustering

Given the sensitivity of Lyα photons to H I, the ionization field should be imprinted in the spatial distribution of the LAEs which can be quantified by the two point correlation functions (ACF). In this section, we use the ACF of theoretical LAEs for each of these best-fit combinations (that match the Lyα LF to within a 1-σ error as summarised in Table 5.1) to narrow the joint constraints on $\langle\chi_{HI}\rangle$, $f_{\rm esc}$ and f_α/f_c. We start by describing our procedure for obtaining LAE ACFs, which depends both on the depth along the LOS (Peebles, 1980) since all galaxies are projected to a plane perpendicular to the LOS, as well as the chosen field of view (FoV), which should be comparable to that observed (Kashikawa et al., 2006). Indeed, while the measured ACF should be independent of the FoV if large enough areas are sampled, the restricted observational FoV leads to an ACF that is not independent of cosmic variance (cf. Appendix C.1). To get an estimate of the average ACF and its variance, we

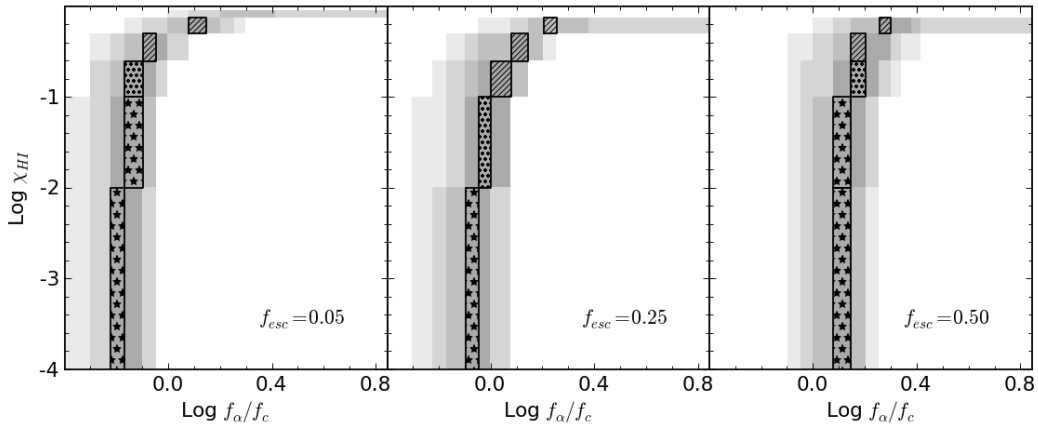

Figure 5.2: The grey shaded regions show the 1-5σ (dark grey to white respectively) regions for the combinations of f_{esc}, $\langle\chi_{HI}\rangle$ and f_α/f_c that best fit the observed Lyα LF data from Hutter et al. (2014). We over-plot black contours for 3σ (stars), 5σ (dots), $> 5\sigma$ (hatching) by comparing model results to observed ACF data Kashikawa et al. (2006). As shown, LAE clustering observations $(3-\sigma)$ require an IGM that has $\chi_{HI} \lesssim 0.01$, $f_\alpha/f_c \leq 1.2$ and $f_{esc} \leq 0.5$. See Sec. 5.3 for details.

generate 36 mock catalogues (12 along each of x, y, z directions) for over-lapping volumes comparable to that observed by Kashikawa et al. (2006), corresponding to a redshift distance $\Delta z \sim 0.1$ at $z \simeq 6.5$ and a field of view (FoV) of $\sim 3 \times 10^3 h^{-2}$Mpc^2. Using the Landy-Szalay estimator we compute the ACF in each mock survey region denoted by $w_i(r)$ with respect to the mean LAE number density $\overline{n}$ of the complete simulation box and estimate the mean value of $w(r)$ as well as its variance from our mock catalogues as

$$\overline{n}(1+w(r)) \quad = \quad \frac{1}{N}\sum_{i=1}^{N} n_i(1+w_i(r)) \tag{5.2}$$

We start by calculating the LBG ACF (over the entire box) to get an estimate of the underlying galaxy population. As seen from Fig. 5.1, LBGs are almost homogeneously distributed and the ACF is consistent with essentially no clustering on scales $\lesssim 30h^{-1}$ Mpc (q.v. Appendix C.2). On the other hand, the LAE ACF is affected both by ISM dust, as well as the large scale topology of reionization. It might be expected that in the early stages of reionization, only those galaxies that are clustered and hence capable of building large H II regions would be visible as LAEs (leading to a large amplitude of the ACF), with the amplitude of the ACF decreasing as reionization progresses and faint objects are able to transmit enough flux through the IGM to be visible as LAEs. Indeed, as shown in Fig. 5.1, LAEs exhibit precisely this behaviour. For a given f_{esc} value (we remind the reader this corresponds to a fixed L_α^{int}), as the IGM becomes more ionized (going down the vertical columns in the Fig. 5.1), smaller galaxies are able to transmit more of their flux through the IGM, requiring lowering f_α/f_c values to fit the Lyα LF. While for a half neutral IGM (panel a), only strongly clustered galaxies are visible as LAEs ($w(r) \simeq 4.5$) at scales of $\simeq 2h^{-1}$Mpc, T_α increases for a completely ionized IGM at the same scale, leading to a more homogeneous LAE distribution resulting in a lower amplitude of the ACF (panel m; $w(r) \simeq 1.5$).

At a given value of $\langle\chi_{HI}\rangle$, L_α^{int} decreases with increasing f_{esc} (horizontal rows in the same figure) which must be compensated by an increase in f_α/f_c (q.v. Appendix C.3). However, this compensation results in very similar ACFs at a given $\langle\chi_{HI}\rangle$ value. Our results therefore show that the ACF is driven by the reionization topology (as determined by $\langle\chi_{HI}\rangle$), with f_{esc} and the local f_α/f_c having a marginal effect (a factor of about 1.5) on its amplitude.

We then calculate the χ^2 errors between our simulated ACFs and observations, and find that observations constrain $\langle\chi_{HI}\rangle \lesssim 0.01$ for $f_{esc} = 0.05,\ 0.5$ and $\langle\chi_{HI}\rangle \lesssim 10^{-4}$ for $f_{esc} = 0.25$ (to within a $3-\sigma$ error). Further, while the f_α/f_c ratio is compatible with homogeneously distributed dust for $f_{esc} = 0.05$, the decrease in L_α^{int} requires clumped dust ($f_\alpha/f_c \geq 0.7$) for $f_{esc} = 0.25$ and 0.5.

To highlight the importance of the spatial clustering of LAEs, we show the $1-5\sigma$ constraints allowed by matching the Lyα LFs to observations in Fig. 5.2. As seen, these encompass a region such

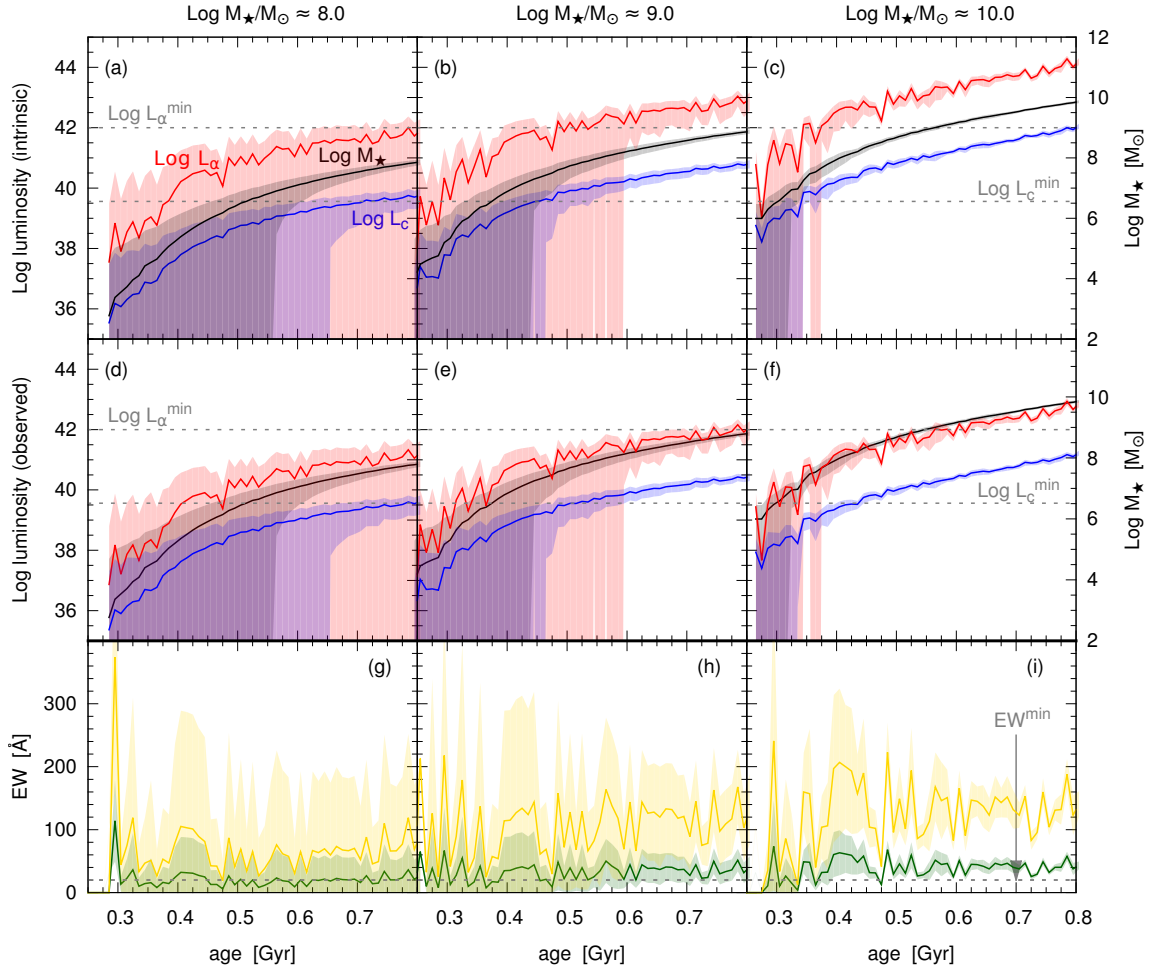

Figure 5.3: Time evolution of M_*, Lyα and UV luminosities and EWs across three M_* bins of $10^8, 10^9$ and 10^{10}M$_\odot$ as marked above each column. The upper 3 panels show the intrinsic quantities (M_* in black; L_α^{int} in red (upper line); L_c^{int} in blue (lower line)); we use $f_{esc} = 0$ for the Lyα luminosity. The middle three panels show the observed quantities (M_* in black; L_α^{obs} in red (upper line); L_c^{obs} in blue (lower line)) where we assume $T_\alpha = 0.45$, $f_\alpha = 0.68 f_c$ and a individual f_c depending on the dust mass of each galaxy. The dashed lines in the top two panels show the current observational limits corresponding to the Lyα (10^{42}erg s^{-1}) and UV ($10^{39.6}$erg s^{-1}/Å) luminosities. The lower 3 panels show the intrinsic (yellow, upper line) and observed (green, lower line) Lyα EWs with the dashed line showing the minimum limit of 20Å. In each panel shaded regions show the variance in the given M_* bin.

that $\langle \chi_{HI} \rangle \simeq 10^{-4} - 0.5$, $f_{esc} = 0.05 - 0.5$ and $f_\alpha / f_c = 0.6 - 1.8$. However, building ACFs for each of these allowed combinations, we find that theory and observations yield much tighter constraints of $\langle \chi_{HI} \rangle \simeq 0.01 - 10^{-4}$, $f_{esc} = 0.05 - 0.5$ and $f_\alpha / f_c = 0.6 - 1.2$ to within a $3 - \sigma$ error. Finally, our results show that it is the reionization topology (as parameterised by $\langle \chi_{HI} \rangle$) that drives the ACF, supporting the results obtained by McQuinn et al. (2007a).

5.4 Duty cycle of LBGs with and without Lyα emission

In this section we show how simulated $z \simeq 6.6$ galaxies build up their stellar mass (M_*), and the time evolution of their UV and Lyα luminosities, and Lyα equivalent widths (EW). We then present the fraction of their lifetime for which galaxies of different UV magnitudes are visible as LBGs with or without detectable Lyα emission, both considering intrinsic and observed luminosities for each combination of f_{esc}, $\langle \chi_{HI} \rangle$ and f_α / f_c which reproduce the Lyα LF and LAE ACF within 1σ and 3σ respectively.

5.4.1 Time evolution of stellar mass, Lyα and UV luminosities

We use the ages of each star particle to trace the growth of M_*, and the metallicity and time dependent values of the intrinsic UV and Lyα luminosities (L_c^{int} and L_α^{int}, respectively) and the intrinsic Lyα EW ($= L_{\alpha^{int}}/L_c^{int}$) for galaxies in three bins of $M_* \simeq 10^{8,9,10}$M$_\odot$. We assume that all ionizing photons emitted within galaxies are absorbed in the ISM and produce Lyα radiation, i.e. $f_{esc} = 0$, to investigate the most extreme case.

As seen from the upper three panels of Fig. 5.3, both L_c^{int} and L_α^{int} (averaged over the galaxies in the given M_* bin) rise as galaxies steadily build up in (stellar) mass, albeit with a large scatter reflecting the assembly history of different galaxies. As expected from normal star forming galaxies, the average intrinsic Lyα EW for all the three M_* bins considered here has a value between $30 - 300$Å (lower 3 panels of the same figure) that is larger than the minimum value of 20Å used to identify LAEs. Indeed, we find that once a galaxy exceeds a critical mass of roughly $10^{8.5}(10^{7.5})$M$_\odot$, it can produce enough luminosity to intrinsically be a LAE (LBG), it has also met the LBG criterion.

As for observed luminosities, we remind the reader that we compute L_α^{obs} using the fraction of UV photons that escape out of the galaxy (f_c); L_α^{obs} is computed assuming homogeneously distributed dust ($f_\alpha/f_c = 0.68$) and an IGM transmission value of $T_\alpha = 0.45$ (Hutter et al., 2014). As expected, including the effects of dust and the IGM reduces both the Lyα and UV luminosities, as shown in the middle panels of the same figure so that the critical M_* at which a galaxy has the minimum luminosity to be a LAE (LBG) increases to $10^{9.5}(10^{8.5})$M$_\odot$, although in most cases the observed EW is still larger than the minimum required value of 20Å (bottom most panels).

Taking the total age as the time between the formation of the first star and $z = 6.6$, we then calculate the fraction of its lifetime (the duty cycle) that galaxies in these 3 M_* bins spend as a LBG with and without Lyα emission ($f_{LBG\alpha}$ and f_{LBG}, respectively), considering intrinsic luminosities. As expected from our discussion above, both $f_{LBG\alpha}$ and f_{LBG} increase with increasing M_*. However, $f_{LBG\alpha} < f_{LBG}$ because of the more stringent (luminosity + EW) constraints imposed on identifying a galaxy as a LAE, as expected from the critical M_* values quoted above. To quantify, while galaxies with stellar masses of $\sim 10^8$ M$_\odot$ are visible as LBGs for roughly 15% of their lifetime ($f_{LBG} = 0.15$), they do not meet the selection criterion to be visible as LAEs ($f_{LBG\alpha} = 0$): although their intrinsic EW are larger than the minimum value of 20 Å required by observations (bottom panel of same figure), L_α^{int} does not meet the required Lyα luminosity of 10^{42} erg s^{-1}. Galaxies with $M_* \gtrsim 10^9$M$_\odot$ are massive enough to sustain star formation and maintain L_c^{int} and L_α^{int} values above the required limits: galaxies with $M_* = 10^9(10^{10})$M$_\odot$ show $f_{LBG\alpha} = 45\%$ and $f_{LBG} = 55\%$ ($f_{LAE} = 80\%$ and $f_{LBG} = 85\%$), respectively. Again, the lifetime spent as a LAE is driven by L_α^{int}, with the intrinsic EW always exceeding 20 Å(bottom panel of Fig. 5.3).

Considering observed luminosities decreases the fractional lifetime any galaxy is visible as a LBG; the decrease is more pronounced for LAEs that are additionally affected by IGM transmission. From panels (d)-(f) of Fig. 5.3, we see that in addition to galaxies with 10^8M$_\odot$, galaxies with $M_* \simeq 10^9$M$_\odot$ are also no longer visible as LAEs as a result of the Lyα luminosity dropping below visible limits; f_{LAE} drops to 40% (compared to the intrinsic value of 80%) for $M_* \simeq 10^{10}$M$_\odot$. As for LBGs, we find that f_{LBG} drops to 45% (65%) from 55% (85%) for galaxies with $M_* \leq 10^9(10^{10})$M$_\odot$.

5.4.2 The duty cycle of LBGs with and without Lyα emission

We now discuss the duty cycle for which galaxies of varying UV magnitudes $M_{UV} = -18$ to -25 are visible as LBGs with ($f_{LBG\alpha}$) or without a Lyα line (f_{LBG}) in more detail. We start with intrinsic UV luminosities as shown in Fig. 5.4: firstly, as galaxies becomes more massive, they are able to sustain large rates of star formation, leading to M_{UV} values that scale with M_*. Secondly, we find that both f_{LBG} and $f_{LBG\alpha}$ increase with an increase in the UV magnitude (or M_*), as explained in Sec. 5.4.1 above: f_{LBG} increases from 45% to 95% as M_* increases from $10^8 - 10^{10.5}$M$_\odot$. As a result of the stricter luminosity and EW criterion imposed to identify galaxies as LAEs, $f_{LBG\alpha} < f_{LBG}$ and declines more rapidly than f_{LBG} towards fainter UV luminosities, decreasing from 85% to 20% as M_* decreases from $10^{10.5} - 10^8$M$_\odot$. Further, the decrease in L_α^{int} with increasing $f_{\rm esc}$ results in a (linear) decrease in f_{LAE} as shown from panels (a)-(c) of the same figure: while f_{LAE} is comparable for $f_{esc} = 0.05, 0.25$, it decreases by about 0.07 for $f_{esc} = 0.5$, where half of the ionizing photons do not contribute to the Lyα luminosity thereby reducing the fraction of time it shows Lyα emission.

We then calculate f_{LBG} and $f_{LBG\alpha}$ including the effects of dust and IGM attenuation for each of the best-fit parameter combinations that match both the observed Lyα LF and ACF as shown

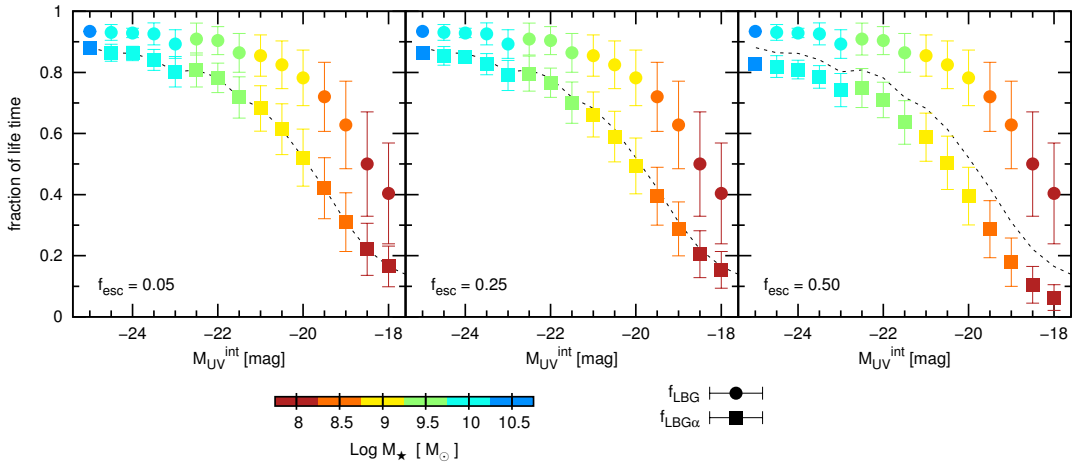

Figure 5.4: Fraction of life time that galaxies spend as LBGs with ($f_{LBG\alpha}$, squares) and without (f_{LBG}, circles) a Lyα line, as a function of the intrinsic UV luminosity for intrinsic values of Lyα and UV luminosities. The panels show the fractions for the indicated values of $f_{esc} = 0.05, 0.25, 0.5$. The mean stellar mass in each M_{UV} bin is encoded in the shown colour scale. The fractions are computed as the mean of the galaxies within M_{UV} bins k ranging from $k - 0.25$ to $k + 0.25$ for $k = -25$ .. -18 in steps of 0.5. Error bars show the standard deviations of the mean values. The dotted black line in each panel represents $f_{LBG\alpha}$ for $f_{esc} = 0.05$; as clearly seen, increasing f_{esc} to 0.5, leads to a decrease in $f_{LBG\alpha}$.

in Sec. 5.3. We use the f_c value for each galaxy according to its final dust mass at $z \simeq 6.6$ and the Lyα transmission T_α of each galaxy was obtained from the ionization field and the ratio of the escape fractions of Lyα and UV continuum photons (f_α/f_c) was set according to Table 5.1. As can be seen from Fig. 5.5 the additional attenuation by dust in the ISM and neutral hydrogen in the IGM leads to lower values for both f_{LBG} and $f_{LBG\alpha}$ (compared to the intrinsic case), as well as a rise of the mean stellar mass in each M_{UV} bin. Nevertheless we find the same trends as when considering intrinsic luminosities: f_{LBG} always exceeds $f_{LBG\alpha}$, and f_{LBG} and $f_{LBG\alpha}$ decrease towards fainter UV luminosities with $f_{LBG\alpha}$ declining more rapidly. However the relative difference between f_{LBG} and $f_{LBG\alpha}$ is larger and the decline of $f_{LBG\alpha}$ is more rapid: while f_{LBG} decreases from 80% to 35% as M_{UV} increases from -23.5 to -18.5, $f_{LBG\alpha}$ drops from 70% to essentially 0 for the same magnitude range. The stronger decline in $f_{LBG\alpha}$ is not only due to the additional dust- and IGM attenuation of the Lyα luminosities, but also due to the additional selection criterion in Lyα equivalent width which becomes more important towards UV fainter galaxies.

We also find that the decrease in f_{esc} is compensated by the increase in f_α/f_c, leading to very similar $f_{LBG,\alpha}$ ratios for all the models shown in Fig. 5.5; note that the IGM is almost ionized in most cases, leading to similar T_α values. This clearly shows that $\langle \chi_{HI} \rangle$, f_{esc} and f_α/f_c compensate each other (as shown in Hutter et al., 2014), as a result of which $f_{LBG\alpha}$ only depends on the combination of the parameters but not on their individual values.

Thus in our model, the most luminous (massive) LBGs most often show Lyα emission, irrespective of whether intrinsic or observed luminosities are considered.

5.5 Conclusions

We build a model that couples a cosmological hydrodynamical simulation run (GADGET-2) with a dust model and a radiative transfer code (pCRASH) to model high-z LAEs. Starting from a neutral IGM, we run pCRASH until the IGM is completely ionized, for f_{esc} values ranging from 0.05 to 0.95. In Hutter et al. (2014), we showed that comparing model results to Lyα LF observations simultaneously constrains the escape fraction of ionizing photons f_{esc}, the mean amount of neutral hydrogen $\langle \chi_{HI} \rangle$ and the ratio of the escape fractions of Lyα photons and UV continuum photons f_α/f_c to $\langle \chi_{HI} \rangle \simeq 10^{-4} - 0.5$, $f_{esc} = 0.05 - 0.5$ and $f_\alpha/f_c = 0.6 - 1.8$. In this paper, we calculate the ACFs for these different combinations and find that comparing these to observations significantly narrows the allowed 3D parameter space (within a $3 - \sigma$ error) to $\langle \chi_{HI} \rangle \simeq 0.01 - 10^{-4}$, $f_{esc} = 0.05 - 0.5$ and

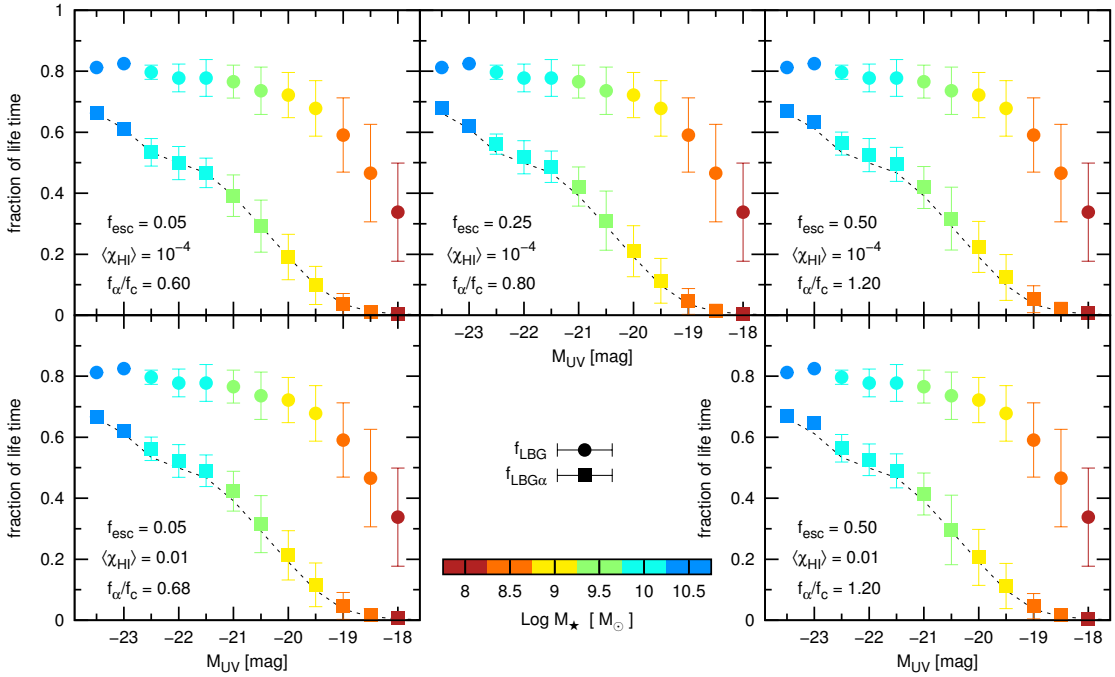

Figure 5.5: Fraction of life time that galaxies spend as LBGs (f_{LBG}, circles) or as LBGs and LAEs ($f_{LBG\alpha}$, squares) as a function of the UV luminosity for our best fit models. The mean stellar mass in each M_{UV} bin is encoded in the shown colour scale. Each panel shows one of the best fit cases with the corresponding parameters written. For each best fit model we assume individual f_c values for each galaxy according to its final dust mass at $z \simeq 6.6$; the Lyα transmission T_α of each galaxy was obtained from the respective ionization field and the ratio of the escape fractions of Lyα and UV continuum photons was set according to Table 5.1. The fractions are computed as the mean of the galaxies within M_{UV} bins k ranging from $k-0.25$ to $k+0.25$ for $k = -25$ .. -18 in steps of 0.5. Error bars show the standard deviations of the mean values. The dotted black line in each panel represents $f_{LBG\alpha}$ for $f_{esc} = 0.05$, $\langle\chi_{HI}\rangle = 10^{-4}$ and $f_\alpha/f_c = 0.60$. This plot clearly shows that the effects of these three parameters are degenerate on $f_{LBG\alpha}$.

$f_\alpha/f_c = 0.6-1.2$. While the effects of these three parameters are degenerate on the Lyα LFs, the ACF is most sensitive to large-scale ionization topologies and reionization leaves clearly distinguishable ACF imprints (boosting up the strength of the ACF) that can not be compensated by varying f_{esc} or f_α/f_c. Further, the ACF allows us to constrain $\langle\chi_{HI}\rangle \leq 0.01$, independent of the other two parameters, and we also constrain $f_{esc} \leq 0.5$ and $f_\alpha/f_c \leq 1.2$.

We then analyse the average time evolution of UV and Lyα luminosities and the duty cycle (fraction of total lifetime) of simulated galaxies at $z \simeq 6.6$ in three bins of $M_* = 10^{8,9,10}$M$_\odot$, finding the following: as soon as a galaxy exceeds a critical stellar mass of $M_* \simeq 10^{8.5}(10^{7.5})M_\odot$, its intrinsic Ly$\alpha$ (UV) luminosity is large enough for it to be identified as a LAE (LBG). Including the effects of dust and IGM attenuation naturally results in an increase in this critical mass (to $10^{9.5}$ and $10^{8.5}$M$_\odot$ for LAEs and LBGs respectively). Defining the duty cycle as the fraction of its lifetime a galaxy spends as a LBG with ($f_{LBG\alpha}$) or without Lyα emission (f_{LBG}), we find that the former is always smaller due to the more stringent luminosity and EW constraints imposed on identifying galaxies as LAEs. We find that both the intrinsic and dust-attenuated $f_{LBG\alpha}$ and f_{LBG} rise with increasing UV luminosity (and hence M_*): intrinsically, f_{LBG} ($f_{LBG\alpha}$) increases from 45% to 95% (20% to 85%) as M_* increases from $10^8 - 10^{10.5}$M$_\odot$. As expected, including the effects of dust and IGM transmission reduce these values such that f_{LBG} decreases from 80% to 35% as M_* decreases from $10^{10.5} - 10^8$M$_\odot$, $f_{LBG\alpha}$ drops from 70% to essentially 0 for the same mass range. Finally, we find that the duty cycles of all our models that reproduce the observed Lyα LF and LAE ACFs are independent of the chosen set of parameters: a larger f_α/f_c compensates a decrease in T_α, or an increase in f_{esc}. As a result, $f_{LBG\alpha}$ only depends on the combination of these 3 parameters but not on their individual values.

Thus, it is most often the most luminous LBGs that are visible in the Lyα .

Finally, we summarise the major caveats involved in this study. Firstly, we assume dust attenuation and IGM transmission to be equal to the values at $z \simeq 6.6$ in order to calculate both $f_{LBG\alpha}$ and f_{LBG}. While the dust mass (and hence attenuation) would be expected to be lower at earlier times, tracing this buildup would require tracking the dust growth in the progenitors of our simulated galaxies. This is much beyond the scope of our present paper and we defer to this analysis to a work that is in preparation. Secondly, $f_{LBG\alpha}$ would be expected to decrease with increasing z as a result of an increase in $\langle \chi_{HI} \rangle$ (leading to a decrease in T_α). However, properly accounting for the latter effect requires modelling the entire history of reionization.

While we have explored the full range of possible values for f_{esc}, its mass and z-dependence remain poorly understood, which is also one of the main caveats involved in modelling the time-evolution of reionization. An increase in f_{esc} with decreasing mass (Ferrara and Loeb, 2013, e.g.) would suppress the visibility of low-mass objects, and strongly impact the reionization fields we generate, emphasising the strong clustering of high-mass halos (Kaiser, 1984; Bardeen et al., 1986; Mo and White, 1996), whilst depressing the LF at the faint end. Bringing these values into agreement with observations would then require an f_α/f_c ratio that decreases with increasing mass. With its observations of the ionization topology, instruments such as LoFAR will be invaluable in answering some of these outstanding questions.

Chapter

6

LAE EQUIVALENT WIDTH DISTRIBUTIONS AND FRACTION OF LBGS SHOWING LYα EMISSION

We have used our model for high-redshift LAEs to predict Lyα equivalent distributions and fractions of LBGs showing Lyα emission at $z \simeq 6.6$. Using models that have reconciled the observed Lyα LF and LAE ACF at $z \simeq 6.6$ within a 1σ and 4σ limit respectively, we have reproduced the observational trend of the Lyα equivalent widths (EW) of LAEs which are rising towards fainter UV luminosities. LAEs with lower stellar masses are younger leading to an enhanced ratio between emitted Lyα and UV continuum photons. Nevertheless, while a lack of high EW values is caused by the averaging of the transmission across 48 lines of sight in an inhomogeneous ionization field, the EW values of UV bright galaxies are higher than observational found (Kashikawa et al., 2011). Due to the latter issue we have found the M_{UV} trend of the fraction of LBG showing Lyα emission ($X_{Ly\alpha}$) - decreasing towards fainter UV luminosities - to be in opposition to the observations (Stark et al., 2010, 2011). Although, as $X_{Ly\alpha}$ depends sensitively on the EW criterion for LAE selection, a higher value for the EW selection criterion has been found to invert the found trend of $X_{Ly\alpha}$ with UV luminosity (M_{UV}), and $X_{Ly\alpha}$ approaches the observational trend. We have attemped to improve our LAE model and have altered the ratio f_α/f_c from being constant to decreasing exponentially with halo mass. Observed Lyα LF and LAE ACF at $z \simeq 6.6$ are found to be still reproducible. Previous constraints on f_{esc} and $\langle \chi_{HI} \rangle$ from the ACF are not altered, but Lyα luminosities and EW values of UV bright galaxies are decreased. We have found that not only the EW-M_{UV} relation of the modified model is in a better agreement with the observation, but also $X_{Ly\alpha}$ reproduces the observations by (Stark et al., 2010) for an EW selection criterion of $> 55\AA$.

6.1 Introduction

With the appearance of the first stars and galaxies the Epoch of Reionization started. The hydrogen in the intergalactic medium (IGM) gradually turned from a neutral to an ionized state until it was fully ionized. While quasar absorption lines hint on patches of neutral hydrogen at $z > 6$ (Fan et al., 2006), the electron optical depth gained from the Cosmic Microwave background (CMB) implies that reionization occurred at $z \sim 10 - 11$ (Komatsu et al., 2011; Hinshaw et al., 2013; Planck Collaboration et al., 2014a). Since neutral patches of hydrogen can significantly attenuate the intrinsic Lyα line of galaxies, Lyα emitters (LAEs) at high redshifts are excellent tracers of reionization, a fact that certainly will be exploited by forthcoming larger and deeper surveys such as the ultra-deep Subaru/Suprime-Cam imaging surveys and the forthcoming James Webb telescope. While the Lyα luminosity function (Lyα LF) seems to remain rather constant at $z \simeq 3 - 5.7$ (Ouchi et al., 2008), high-redshift observations indicate a drop in the Lyα LF from $z = 5.7$ to $z = 6.5$ (Ouchi et al., 2010; Kashikawa et al., 2011) and even further to $z = 7.3$ (Konno et al., 2014). An even sharper drop is found in the so-called Lyα fraction, i.e. the fraction of Lyman Break galaxies (LBGs) showing Lyα emission (Stark et al., 2010; Pentericci et al., 2011; Ono et al., 2012; Schenker et al., 2012). Neutral patches from incomplete reionization are often considered as a cause for this drop. However, according

to recent works (Jensen et al., 2013b; Mesinger et al., 2015) the amount of neutral hydrogen needs to increase by a considerable amount of $\Delta\langle\chi_{HI}\rangle \sim 0.5$ from $z \sim 6$ to $z \sim 7$ to reproduce the observed drop in LAEs. Since such reionization scenarios are in tension with the constraints from the CMB, the decrease in LAEs also can be caused by an increasing abundance of self-shielded systems in the IGM (Bolton and Haehnelt, 2013) or the intrinsic galaxy properties, such as the escape fraction of ionizing photons from galaxies (Dijkstra et al., 2014).

In this regard the nature of LAEs, i.e. their stellar mass, their age, the distribution of H I and dust in the ISM, the velocity fields (outflows and inflows), is of particular interest as these properties determine the production of Lyα photons and their escape fraction from the galaxies. Observations indicate that LAEs are a younger, less-dusty subsample of LBGs (Yuma et al., 2010; Wiklind et al., 2013). Galaxies with strong Lyα emission and luminous LBGs showing Lyα emission reveal bluer UV continuum slopes than LBGs with Lyα absorption (Shapley et al., 2003; Vanzella et al., 2009; Pentericci et al., 2009; Kornei et al., 2010; Stark et al., 2010), indicating a lower dust extinction (Meurer et al., 1999; Stark et al., 2010; McLure et al., 2011; Bouwens et al., 2012; Wilkins et al., 2013). Within the LAE samples there are hints to a connection between the Lyα emission and the UV luminosity: the mean equivalent width (EW) distribution increases towards fainter UV luminosities and a deficit in large EWs is found in most luminous sources (Shapley et al., 2003; Ando et al., 2006; Ouchi et al., 2008; Pentericci et al., 2009; Vanzella et al., 2009; Stark et al., 2010). It remains an open question whether this deficiency is due to dust extinction, the amount and velocity structure of HI gas in/around the galaxy, the age dependency of the stellar populations, or a combination of those (Ando et al., 2006). Another possibility is that these trends are of statistical nature given that luminous UV galaxies lie in the low probability end of the Lyα luminosity and the EW distribution (Nilsson et al., 2009; Zheng et al., 2014). For narrowband selected LAEs the UV faint ones show younger ages and higher specific star formation rates (sSFR) than more luminous LBGs (Ono et al., 2010), but Kornei et al. (2010) found for spectroscopically confirmed LBGs that sources with Lyα emission tend to be older than those without at similar UV luminosities. The latter implies that Lyα can escape more easily once large-scale outflows have had time to reduce the dust covering fraction sufficiently. Furthermore Schenker et al. (2014) states that the UV luminosity is a coarse predictor of the Lyα EW but the physical properties are better encoded in the UV continuum slope. Indeed they find that for $7 < z < 8$ galaxies the mean EW increases towards bluer UV continuum slopes, hinting at stronger Lyα emission for less-dust obscured, or lower metallicity and hotter, or younger sources. Theoretical models (e.g. Kobayashi et al., 2010) have been successfully employed to model this dependency of the Lyα EW on the UV luminosities, finding that mainly the effects of clumpy dust and partly the dependency of the UV luminosity on the age of the stellar populations are responsible.

To trace reionization, recent works have aimed to construct an independent measure of the redshift evolution of Lyα emitting galaxies by investigating the fraction of LBGs showing Lyα emission ($X_{Ly\alpha}$) (Stark et al., 2010; Pentericci et al., 2011; Stark et al., 2011; Curtis-Lake et al., 2012; Ono et al., 2012; Schenker et al., 2012; Treu et al., 2012; Caruana et al., 2014; Treu et al., 2013; Pentericci et al., 2014). As neutral patches considerably attenuate Lyα emissions during reionization, the fraction of star-forming galaxies showing Lyα emission decreases (Stark et al., 2010; Pentericci et al., 2011; Stark et al., 2011; Curtis-Lake et al., 2012; Ono et al., 2012; Schenker et al., 2012; Treu et al., 2012; Caruana et al., 2014; Treu et al., 2013; Pentericci et al., 2014). Besides the dependency of $X_{Ly\alpha}$ on the redshift, $X_{Ly\alpha}$ decreases towards higher UV luminosities. Whilst LAEs arise predominantly in galaxies with similar blue continuum slopes across all measured UV luminosities, LBGs show redder UV slopes, i.e. softer spectra, towards higher UV luminosities. Consequently, the fraction of LBGs showing blue continuum slopes that lead to sufficient Lyα emission for LAE detection rises towards fainter UV luminosities. As the cut in EW is a major selection criterion for LAEs, this dependency is closely related to the observed dependency of the EW on the UV luminosity or the UV continuum slope and might be a hint for lower dust obscuration, age or H I column densities in UV faint galaxies. Theoretical attempts to model the dependency of $X_{Ly\alpha}$ on the UV luminosity require an escape fraction of the Lyα photons from the galaxy that decreases sufficiently for UV luminous sources (Forero-Romero et al., 2012).

In order to understand the nature of LAEs and thus the underlying mechanisms shaping the EW distribution and the UV luminosity dependency of $X_{Ly\alpha}$, e.g. dust obscuration, stellar ages, H I density and velocity distribution in the ISM, we use our LAE model (see Section 4.4.2) to predict these quantities and investigate which physical properties of LAEs and observational limits are responsible for the observed trends. As mentioned in the previous Chapters 4 and 5 our LAE model has three free parameters: the escape fraction of ionizing photons ($f_{\rm esc}$), the mean fraction of neutral hydrogen in

the IGM ($\langle\chi_{HI}\rangle$) or the mean transmission (T_α) and the ratio between the escape fraction of Lyα (f_α) and UV continuum photons (f_c), where only those combinations are considered which reproduce the observed Lyα LF (Kashikawa et al., 2011) and LAE angular correlation functions (ACF) (Kashikawa et al., 2006) at $z \simeq 6.6$. The star formation history, thus the ages and metallicities of the galaxies, is given by the hydrodynamical simulation and the dust extinction is deduced from a semi-analytical dust model (Dayal et al., 2011). Thus our model provides us with the properties of each galaxy in the simulation which enables us to analyse their impact on the observed quantities, i.e. the EW distribution and $X_{Ly\alpha}$, and gain information on the nature of LAEs. For that purpose we derive the EW distributions and fractions of LBGs showing Lyα emission for the allowed combinations of $f_{\rm esc}$, $\langle\chi_{HI}\rangle$ and f_α/f_c.

This chapter is organized as follows. In Section 6.2 the results for the EW distributions and the fraction of LBGs showing Lyα emission are shown for our original simple LAE model and we discuss emerging issues. We alter our LAE model in Section 6.3, improve the reproduction of the Lyα LF and LAE ACF and discuss the changes to the EW distribution and $X_{Ly\alpha}$. Finally we elaborate on the limits of our model to different observations in Section 6.5 and conclude in Section 6.6.

6.2 Predictions using the LAE model

In this section we use our LAE model to derive the EW distributions, the dependencies of the EW values on the corresponding UV luminosities, and the fractions of LBGs showing Lyα emission for different UV luminosities. We consider these quantities for each combination of $f_{\rm esc}$, $\langle\chi_{HI}\rangle$ and f_α/f_c that reproduce the observed Lyα LF (within 1σ limit) and LAE ACF (within 5σ limit) at $z \simeq 6.6$ (see Sections 4.5 and 5.3 respectively).

6.2.1 Equivalent widths

The Lyα EW depends on its observed Lyα (L_α^{obs}) and UV luminosity (L_c^{obs})

$$EW = \frac{L_\alpha^{obs}}{L_c^{obs}} = \frac{2}{3} h\nu_\alpha Q(1-f_{\rm esc}) f_\alpha T_\alpha \left(f_c L_c^{int}\right)^{-1} \tag{6.1}$$

where L_α^{obs} increases with declining escape fraction of ionizing photons ($f_{\rm esc}$), rising transmission of Lyα photons through the IGM (T_α), increasing escape fraction of Lyα photons (f_α), and a larger number of ionizing photons (Q). The term $h\nu_\alpha$ denotes the energy of an Lyα photon. The observed UV luminosity L_c^{obs} is given by the dust obscured intrinsic UV luminosity L_c^{int}, whereas a higher dust amount in the galaxies leads to a lower escape fraction of the UV photons f_c, lowering L_c^{obs} and subsequently enhancing the EW value.

In Figures 6.1 and 6.2 we show the cumulative EW distribution functions and the EW-UV luminosity relations for all possible ($f_{\rm esc}, \langle\chi_{HI}\rangle, f_\alpha/f_c$) combinations that are allowed by the Lyα LF and LAE ACF at $z \simeq 6.6$ (ranging from $f_\alpha/f_c = 0.6-1.2$, $f_{\rm esc} = 0.05-0.5$ and $\langle\chi_{HI}\rangle = 10^{-4}-0.1$). We note that they all show similar trends. We start by discussing the trends seen in the EW-$M_{\rm UV}$ relation in Figure 6.2. For the LAEs we find the same trend as has been observed (Ando et al., 2006; Kashikawa et al., 2011; Zheng et al., 2014): the EW values increases with lower UV luminosities. The EW value does not depend individually on f_α or f_c but it depends on the assumed ratio f_α/f_c. Although the observed UV luminosity depends on f_c, the increasing trend of the EW values with fainter UV luminosities can already be seen in the intrinsic EW-$M_{\rm UV}$ relation. Thus, intrinsic galaxy properties, i.e. Q and L_c^{int}, seem to be mainly responsible for this trend in our model. Within the hydrodynamical simulation we find that larger (brighter) galaxies are older and exhibit higher metallicities; adopting starburst spectra this causes softer spectrum and consequently a lower number of ionizing photons per stellar mass compared to smaller (fainter) galaxies. Although the number of ionizing photons per stellar mass $Q/M_\star$ differs strongly, the intrinsic UV luminosity at 1505Å per stellar mass $L_c^{int}/M_\star$ remains rather constant. As the UV luminosity decreases, the fraction Q/L_c^{int} increases, causing the observed increase of the EW values in Fig. 6.2.

When plotting each LAE in our model as a point in the EW-$M_{\rm UV}$ plane, we note a sharp lower limit of the EW values that declines towards higher UV luminosities. For $M_{UV} \geq -20$ this lower limit is due to the threshold Lyα luminosity for LAE selection, $L_\alpha^{obs} > 10^{42}$erg s^{-1}, while for higher UV luminosities it is either due to the threshold EW or the properties (age, stellar mass) of our UV luminous galaxies.

From Figure 6.2 we see that our model does not reproduce such low EW values at higher UV luminosities ($M_{UV} \lesssim -21$) as are observed. The observed Lyα luminosity of the UV bright galaxies might be not enough attenuated due to our assumed constant relation between f_α and f_c. To reproduce the small EW values at the UV bright end, the f_α values for the UV brighter galaxies need to be lower than currently assumed. This is either obtained by assuming a decreasing ratio of f_α/f_c values towards higher UV luminosities, or a stronger mass dependency of f_c such that f_c declines for higher galaxy masses. We also note that our simulations do not reproduce the very high EW values that were found in observations by Kashikawa et al. (2011) (see Fig. 6.1). This may be due to the averaging of the transmissions along 48 line-of-sights. Especially for fainter galaxies the transmissions depend strongly on the line-of-sight as their surrounding ionized regions are substantially determined by the neighbouring sources, leading to a large range of transmission and thus EW values along different lines of sight (see discussion in the next paragraph of this Section). However, since we assume all our galaxies to be PopII-dominated, the lack of high EW values might also be caused by the absence of PopIII-galaxies. PopIII-galaxies exhibit extreme low metallicities and a top-heavy initial mass function. Their high effective temperatures cause a hard spectrum and thus a strong ionizing flux that is responsible for the high EW values. Nevertheless Kashikawa et al. (2011) points out that such an extended tail towards larger EW values can be artificially produced by uncertainties in the measured UV broadband flux.

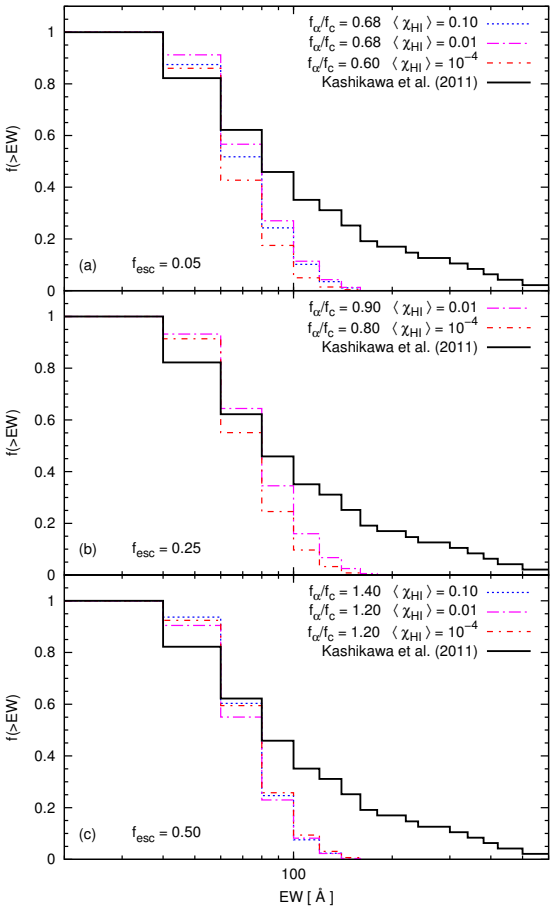

Figure 6.1: The cumulative EW distribution of the LAE samples at $z \simeq 6.6$. The black line shows the distribution obtained from observations by Kashikawa et al. (2011). The panels show the EW distributions for different $f_{\rm esc} = 0.05, 0.25, 0.5$. In each panel we show the possible $(f_\alpha/f_c, \langle\chi_{HI}\rangle)$ combinations for which the simulated LAE Lyα LFs are within the 1σ limit of the observations by Kashikawa et al. (2011). Dotted, long-dashed-dotted, short dashed-dotted lines show the best fit cumulative EW distribution for $\langle\chi_{HI}\rangle \simeq 0.1$, 0.01, 10^{-4}.

Comparing the EW-$M_{\rm UV}$ relations for the different possible parameter combinations, we discuss the trends with our three parameters $f_{\rm esc}$, $\langle\chi_{HI}\rangle$ and f_α/f_c by starting with the transmission through the IGM, T_α.

Although its effect is hardly seen in Fig. 6.2, we note in Fig. 6.1 that for the same f_α/f_c values the EW distribution shifts slightly towards higher EW values as the global neutral hydrogen fraction $\langle\chi_{HI}\rangle$ decreases. This is due to an increasing transmission T_α, which rises the observed Lyα luminosities. This effect can be seen for $f_{\rm esc} = 0.05$, $f_\alpha/f_c = 0.68$, $\langle\chi_{HI}\rangle = 0.01$ and 0.10 as well as for $f_{\rm esc} = 0.50$, $f_\alpha/f_c = 1.20$, $\langle\chi_{HI}\rangle = 10^{-4}$ and 0.01.

A more important effect is produced by a rising f_α/f_c which leads to an increase of the EW values. This leads not only to a shift towards higher EW values of the already identified LAEs, but also more galaxies that are initially below the threshold Lyα luminosity pass the LAE selection criterion, populating the lower limit of the EW values in the EW-$M_{\rm UV}$ plane. Combining these two effects causes an increased scatter in the EW-$M_{\rm UV}$ relation. As brighter galaxies contain more dust, thus exhibiting smaller f_c values, their EW values can be enhanced more by raising f_α/f_c than for fainter galaxies. Consequently, the EW values of the UV fainter sources saturate due to the saturation limit $f_\alpha \leq 1$ at lower f_α/f_c values more than those of the UV brighter sources. The different saturation limits for UV bright and faint galaxies can be seen for higher amounts of neutral hydrogen ($\langle\chi_{HI}\rangle = 0.5$) across the range of $f_{\rm esc}$ values: with rising f_α/f_c value (and thus with rising $f_{\rm esc}$ value) more UV faint galaxies reach the saturation limit, i.e. their EW values cannot be enhanced further, while

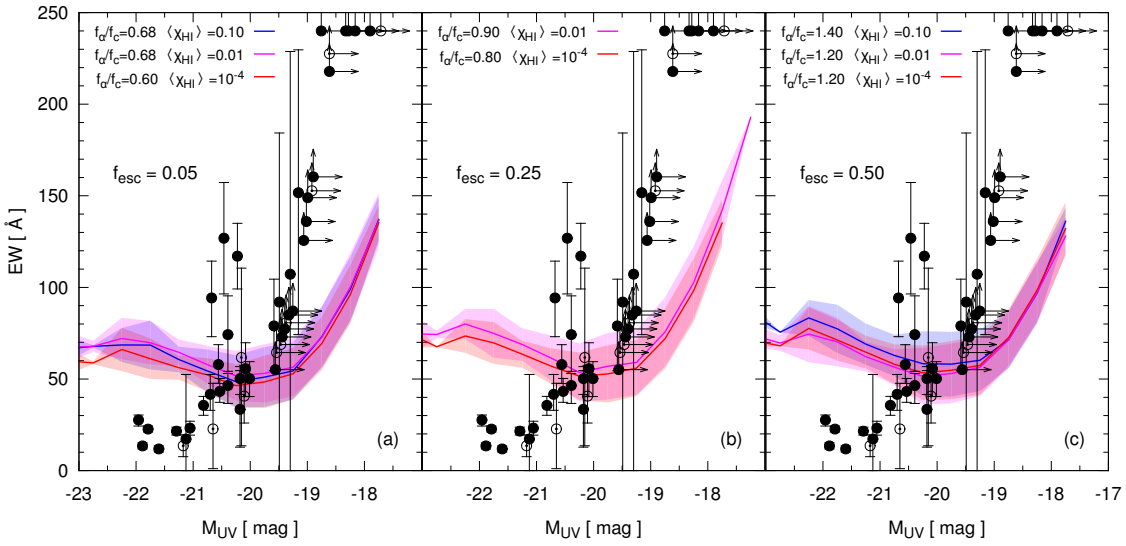

Figure 6.2: The UV luminosity-EW relation at $z \simeq 6.6$ for the best fit $(f_\alpha/f_c, f_{\rm esc}, \langle\chi_{HI}\rangle)$ combinations for which the simulated LAE Lyα LFs are within the 1σ limit of the observations by Kashikawa et al. (2011). The panels show the EW-$M_{\rm UV}$ relation for different $f_{\rm esc} = 0.05$ (left panel), 0.25 (middle panel), 0.5 (right panel) and $\langle\chi_{HI}\rangle \simeq 0.1$ (blue), 0.01 (magenta), 10^{-4} (red). Black filled circles show the spectroscopic and black open circles the photometric sample of the observations by Kashikawa et al. (2011) (Objects with EW$>$ 240Å are plotted at EW$=$ 240Å).

the EW values of UV bright galaxies still rise.

The case of $\langle\chi_{HI}\rangle = 0.5$ demonstrates the dependency of the EW-$M_{\rm UV}$ relation on $f_{\rm esc}$. As the intrinsic Lyα luminosity decreases with rising $f_{\rm esc}$, fewer faint galaxies are identified as LAEs. Since no more Lyα radiation can escape than is produced in the galaxy, i.e. $f_\alpha \leq 1$, the Lyα luminosity cannot be enhanced arbitrarily by increasing f_α/f_c and reaches a limit of $f_\alpha = 1$. Thus for rising values of $f_{\rm esc}$ the maximum EW values of the "saturated" galaxies decreases. Furthermore the UV magnitude, below which galaxies exhibit $f_\alpha = 1$, shifts towards higher UV luminosities.

Summarising, the value for $f_{\rm esc}$ needs to be sufficiently low, so that the intrinsic Lyα luminosities are high enough to generate LAEs with high EW values. Higher values of $\langle\chi_{HI}\rangle$ are compensated by a high f_α/f_c value which is also necessary to reproduce high EW values. To quantify the agreement of the simulated EW distribution (Fig. 6.1) with the observations by Kashikawa et al. (2011), we have performed the two-sample Kolmogorov-Smirnov test for each set of parameters $(f_{\rm esc}, \langle\chi_{HI}\rangle, f_\alpha/f_c)$. In accordance with our findings from Fig. 6.2, all parameter combinations suffer from a lack of high EW values, which is reflected in the KS statistics: the EW distribution deviates between $2-3\sigma$ from the observations by Kashikawa et al. (2011).

For all best fit cases which reproduce the Lyα LF and the LAE ACF at $z \simeq 6.6$, the relations between the EW values and UV luminosities of our simulated galaxies are very similar: a lack of very low EW values for UV bright galaxies and a lack of very high EW values for fainter UV galaxies. These deficiencies could be caused by the averaging of the transmission of each LAE along 48 random lines of sight instead of taking the transmission along one line of sight, as is the case for observations.

Line of sight dependency

Taking only one line of sight into account instead of averaging over 48 lines of sight, the range of transmissions and thus of the EW values increases as can be seen in Fig. 6.3. This spreading is due to the inhomogeneity of the ionization fields, leading to a high variation of the transmission of a galaxy along different lines of sights. Especially for fainter galaxies this effect is very strong, since firstly they are not able to build up sufficient ionized regions, and secondly their surrounding ionization field depends on other sources in the neighbourhood. Thus the transmission of their emitted Lyα radiation depends strongly on their neighbourhood, while for brighter galaxies a larger fraction of Lyα radiation is transmitted due to the larger surrounding ionized regions, which leads to less line of sight variance. In Fig. 6.3 variance along different lines of sight is found for all UV luminosities, but for brighter

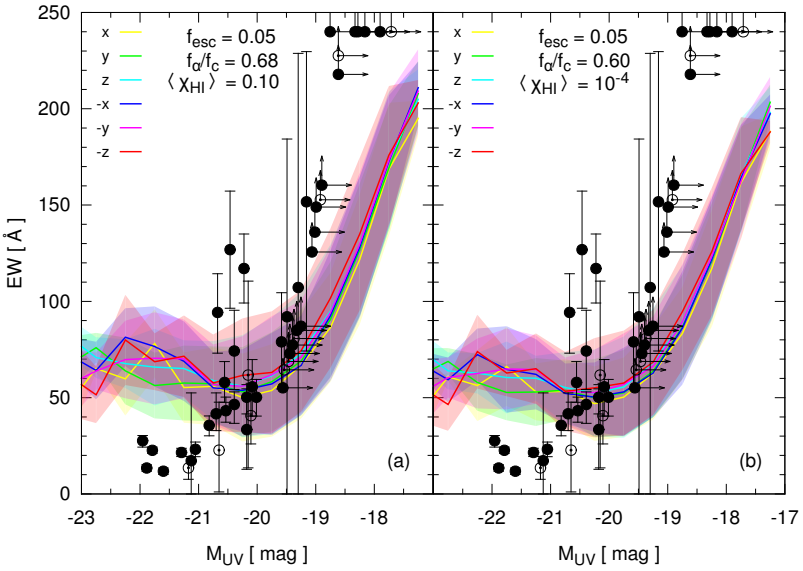

Figure 6.3: The UV luminosity-EW relation at $z \simeq 6.6$ for $f_{\rm esc} = 0.05$ $\langle \chi_{HI} \rangle = 0.10$ (left), 10^{-4} (right) and $f_\alpha/f_c = 0.68$ (left), 0.60 (right). In each panel the lines and shaded regions show the EW-$M_{\rm UV}$ relation for different lines of sight. Black filled circles show the spectroscopic and black open circles the photometric sample of the observations by Kashikawa et al. (2011) (Objects with EW> 240Åare plotted at EW= 240Å).

galaxies the variance is smaller (by up to a factor of 2-3) than for the fainter galaxies (by up to a factor of 4-5). Indeed we find that the occurrence of larger EW values can be reproduced, when we consider the observational conditions, i.e. the transmission along one line of sight. Although we find that some bright galaxies have lower EW values than before, there are also some which have higher EW values, such that the mean remains the same. However, even the lowest EW values of the brightest galaxies are insufficiently low to reconcile with observations.

6.2.2 Lyα fraction

In this section we present the resulting fractions of LAEs in the LBG population of the best fit cases and discuss their implications. In Figure 6.4 this LAE fraction is shown for two EW selection criteria (25Å (filled circles, diamonds, pentagons) and 55Å (filled squares, triangles)) and luminosity ranges ($-20.25 < M_{UV} < -18.75$ and $-21.75 < M_{UV} < -20.25$). We note that we adopt our selection criterion for LAEs to the observations by Stark et al. (2010, 2011), i.e. a galaxy is identified as a LAE, if its EW value exceeds the EW selection threshold (no selection criterion in Lyα luminosity).

From Fig. 6.4 we find that the LAE fraction ($X_{Ly\alpha}$) depends strongly upon the EW selection criterion. As the luminosities and EW values of the LAEs are fixed by a given combination of f_α/f_c, $f_{\rm esc}$ and $\langle \chi_{HI} \rangle$, the crucial parameter for $X_{Ly\alpha}$ is the EW selection criterion. We find that $X_{Ly\alpha}$ decreases with a rising EW cut. But can we distinguish between the different possible parameter combinations by the LAE fraction? Indeed we find that the different models ($f_{\rm esc}$, $\langle \chi_{HI} \rangle$, f_α/f_c) produce different LAE fractions and that different EW selection criteria cause different trends of $X_{Ly\alpha}$ with $f_{\rm esc}$, $\langle \chi_{HI} \rangle$ and f_α/f_c. On the one hand, for low EW cuts ($EW > 25$Å) $X_{Ly\alpha}$ is mainly driven by the neutral hydrogen fraction $\langle \chi_{HI} \rangle$: as $\langle \chi_{HI} \rangle$ decreases, the number of identified LAEs rises, while the number of LBGs remains constant, and $X_{Ly\alpha}$ increases. On the other hand, we have checked that for high EW cuts ($EW > 75$Å) $X_{Ly\alpha}$ depends primarily on f_α/f_c: since the declining effect on the number of LAEs with rising $\langle \chi_{HI} \rangle$ is compensated by increasing f_α/f_c values, the EW values tend towards higher values as $\langle \chi_{HI} \rangle$ increases. This leads to a higher fraction of high EW values and higher $X_{Ly\alpha}$ values. For intermediate EW cuts ($EW > 55$Å) these two effects on $X_{Ly\alpha}$, the increasing trend for decreasing $\langle \chi_{HI} \rangle$ or increasing f_α/f_c, compete with each other. Therefore no real trend in $X_{Ly\alpha}$ is noticeable in Figure 6.4 for $EW > 55$Å.

Comparing our results to the observations, we find that for faint galaxies ($M_{UV} > -20.25$) our models reproduce the observed $X_{Ly\alpha}$ values. For UV brighter galaxies ($-21.75 < M_{UV} < -20.25$) we

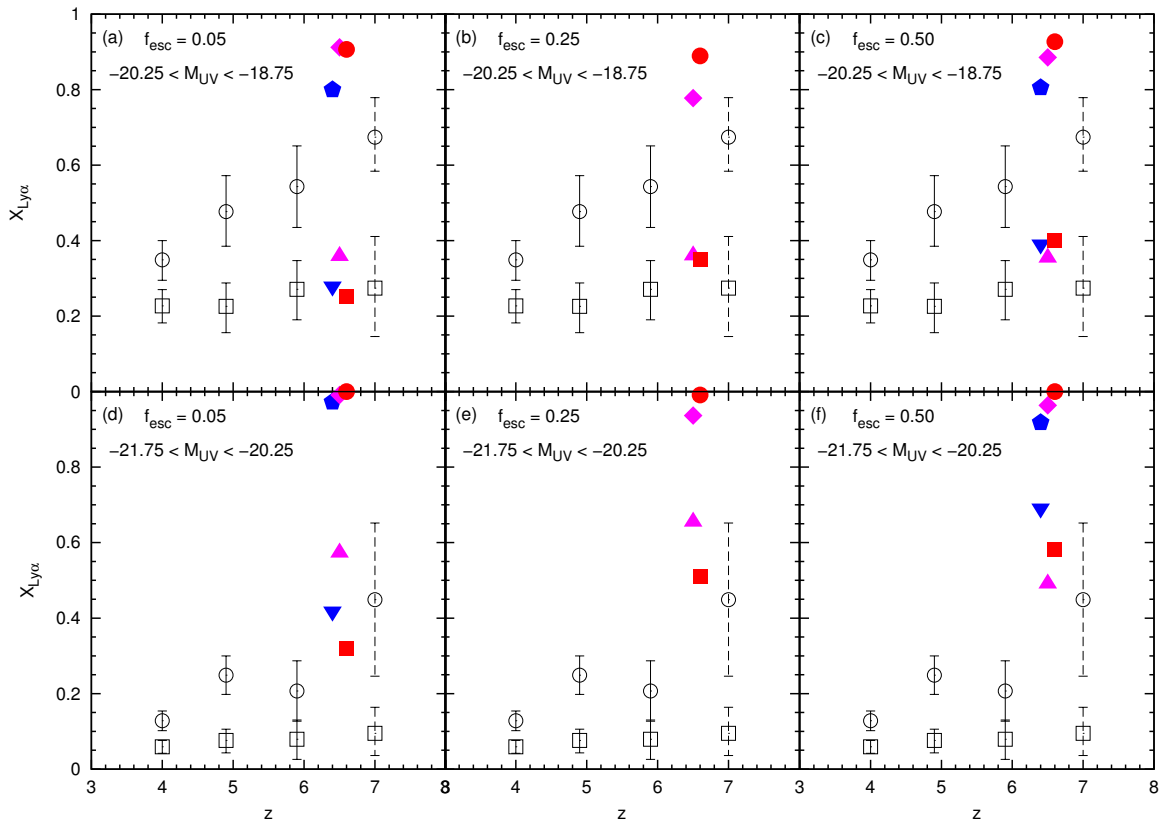

Figure 6.4: Evolution in the fraction of Lyα Emitters ($X_{Ly\alpha}$) in the LBG population over $4 < z < 6$ by Stark et al. (2011) (black empty squares and circles); points at $z \simeq 7$ are extrapolated values by Stark et al. (2011). The Lyα fraction of LBGs with EW larger than 25Å (black empty circles) and 55Å (black empty squares) are shown for two luminosity intervals ($-21.75 < M_{UV} < -20.25$ and $-20.25 < M_{UV} < -18.75$). The coloured points represent the values for the best fit ($f_\alpha/f_c, f_{\rm esc}, \langle\chi_{HI}\rangle$) combinations for which the simulated LAE Lyα LFs are within the 1σ limit and the simulated LAE ACFs within the 5σ limit of the $z \simeq 6.6$ observations (Kashikawa et al., 2006, 2011). In each panel $X_{Ly\alpha}$ of the best fit for $\langle\chi_{HI}\rangle \simeq 0.1, 0.01, 10^{-4}$ are represented by a filled pentagon, diamond, circle (upward triangle, downward triangle, square) for EW$>$ 25Å (EW$>$ 55Å) respectively. For readability the coloured points are displaced along the z-axis.

find that the dependency of $X_{Ly\alpha}$ on M_{UV} in our model is opposite to observations (the UV brighter a galaxy, the lower $X_{Ly\alpha}$) as can be seen in Figures 6.4 and 6.5. This inversion of the observed trend is caused by the EW values of the UV bright galaxies that are higher than seen in observations. This is due to our modelling of the escape fraction of the Lyα radiation f_α, where we assumed a constant f_α/f_c. As described and shown in Forero-Romero et al. (2012), Yajima et al. (2014) and (Dayal and Ferrara, 2012), the dependence of the Lyα escape fraction on galaxy luminosity is a key factor to reproduce the observations by Stark et al. (2010). Forero-Romero et al. (2012) explicitly shows that the observations cannot be reconciled using a constant value for f_α. To reproduce the observational trend of $X_{Ly\alpha}$ on M_{UV}, a f_α value is required that increases for faint galaxies. Comparing our relation of f_α with f_c to those in Yajima et al. (2014), we find that our f_α values are higher for low f_c values. Hence, in our model the Lyα luminosity is not reduced enough, leading to higher EW values and a higher fraction of LAEs than observed.

6.3 Modifying the f_α/f_c relation

In the previous section we have compared observations of the LAE clustering, the EW-M_{UV} relation and the fraction of LBGs showing Lyα emission with the results of our model. The model exhibits a lack of low EW values for UV bright galaxies, so that each UV bright LBG is also a LAE. Although the trend of the EW-M_{UV} relation is recovered, we find that our fraction of LBGs showing Lyα emission exceeds the observations for UV bright galaxies. This is directly linked to the excess EW values of

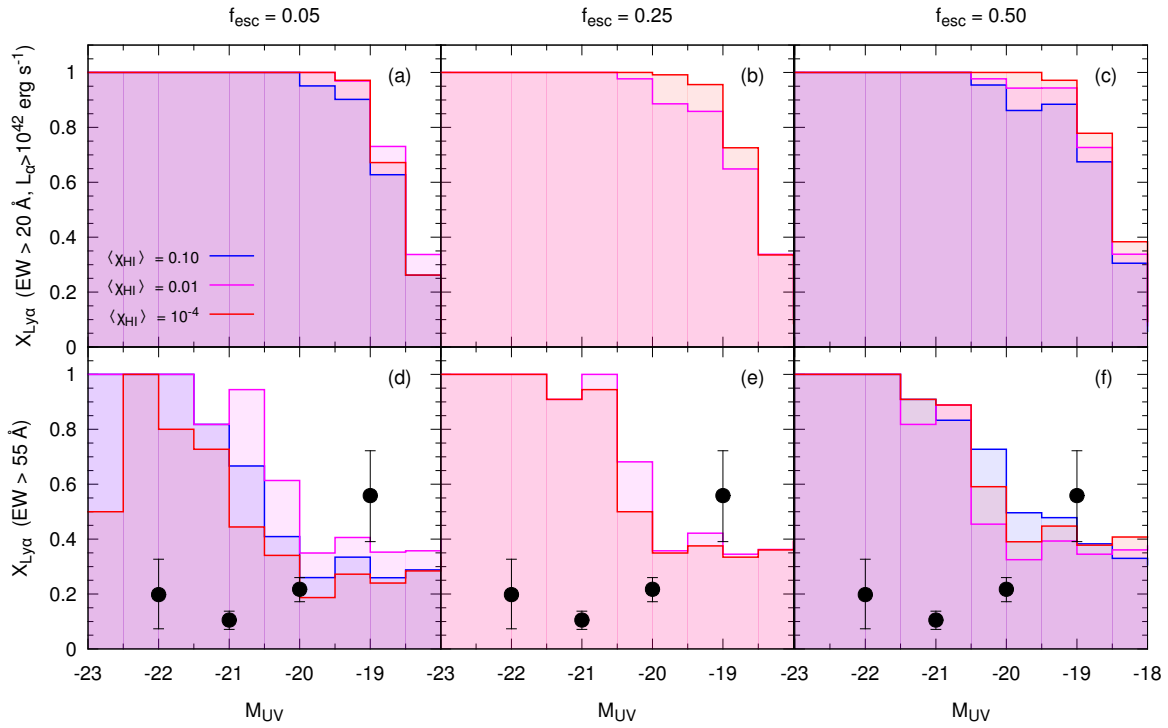

Figure 6.5: Fraction of Lyα Emitters ($X_{Ly\alpha}$) in the LBG population as a function of the observed UV luminosity at $z \simeq 6.6$. The upper and lower row refer to the fraction of LBGs showing Lyα emission with EW$>$ 20Å and $L_\alpha^{obs} > 10^{42}$erg s^{-1}, and EW$>$ 55Å, respectively. The histograms show the model results for $f_{\rm esc} = 0.05$ (left column), 0.25 (middle column), 0.50 (right column) and in each panel $\langle \chi_{HI} \rangle = 0.10$ (blue), 0.01 (magenta), 10^{-4} (red). Black points show the observations by (Stark et al., 2010) in the range of $4.5 < z < 6$ for EW$>$ 55Å. For EW$>$ 20Å observational data is not available.

UV bright galaxies, which cause each UV bright LBG to be identified as a LAE. Furthermore our mean simulated LAE ACFs exceed the observations on smaller scales, i.e. the clustering of the LAEs is stronger than observed. To address these problems, we modify our model by adapting our relation between the escape fraction of the Lyα photons (f_α) and the UV continuum photons (f_c). To suppress the Lyα luminosity of UV bright (more massive) galaxies to a greater extent, we assume an exponential cutoff at higher masses. Such a modification is plausible, as firstly self-shielded systems that attenuate the Lyα flux are more likely in the surrounding of massive sources, and secondly an inhomogeneous dust distribution that shows higher concentration towards star forming regions (in contrast to the assumption of a homogeneous distribution in our dust model) can increase the attenuation by dust, especially for more extended and massive galaxies. The relation between f_α and f_c is given by

$$f_\alpha / f_c \quad = \quad p \, \exp\left(-M_h / 3 \cdot 10^{11} \mathrm{M}_\odot\right), \tag{6.2}$$

where M_h is the halo mass of the respective galaxy and p a global parameter, which can be chosen to reproduce the observed Lyα LF. Using this modified model we recompute the LAE clustering, the EW-M$_{\rm UV}$ relation and the fraction of LBGs showing Lyα emission.

6.3.1 LAE clustering

First we discuss the effect of the stronger suppression/enhancement of transmitted Lyα emission for more/less massive galaxies on the LAE clustering. In Fig. 6.6 we show the ACFs of the identified LAEs for the modified f_α/f_c model. We note that firstly the LAEs in the modified f_α/f_c model are less clustered on shorter scales ($r < 10$Mpc/h) than those in the simple model, and secondly that the ACFs of the modified f_α/f_c converge to the ACFs of the simple model as $f_{\rm esc}$ increases (for $f_{\rm esc} = 0.5$ the two models produce nearly the same ACFs).

Although the modified f_α/f_c model was introduced to decrease the number and Lyα luminosities of UV bright LAEs, the decrease of the ACFs in the modified f_α/f_c model is not due to the decrease in

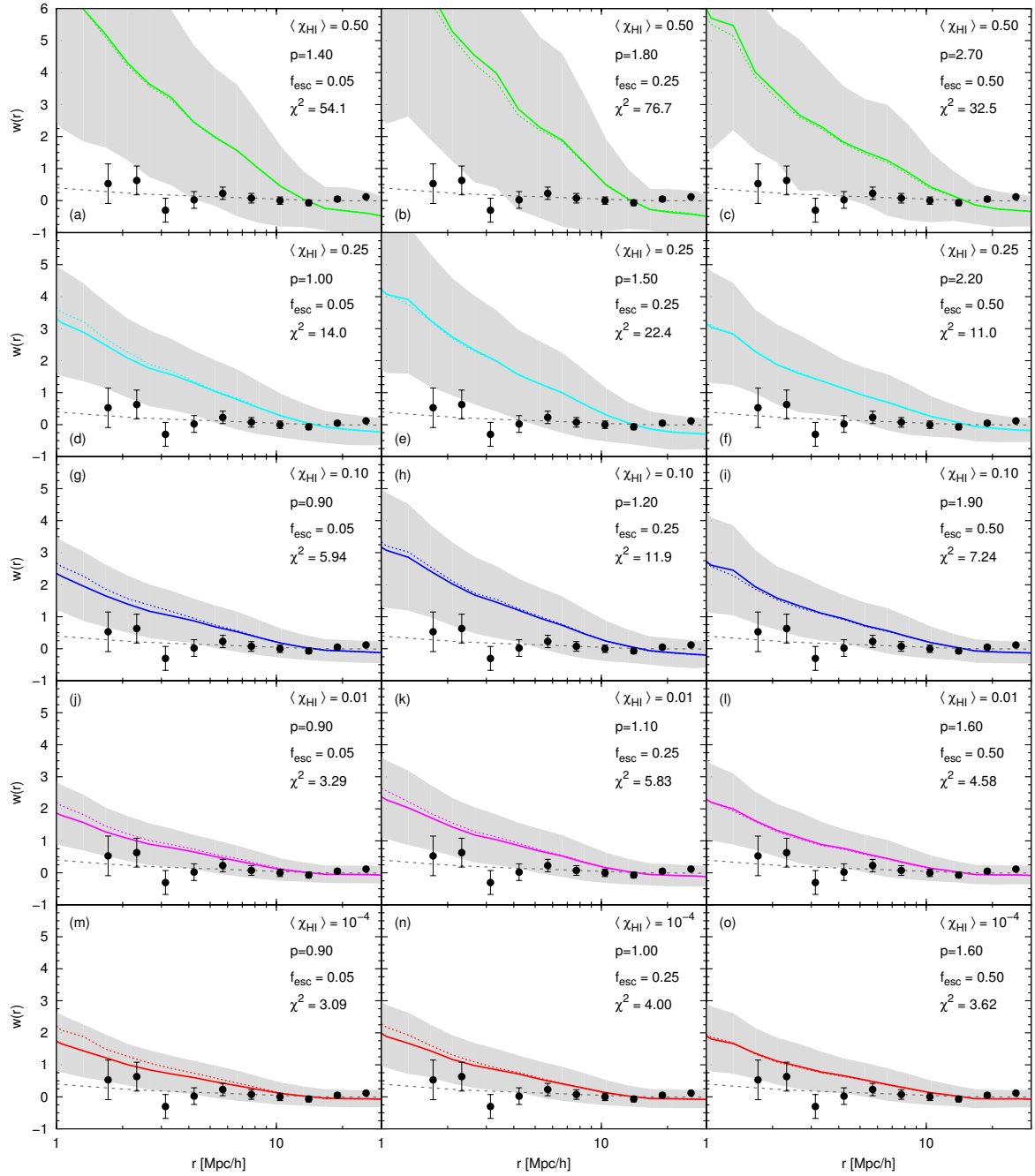

Figure 6.6: Angular correlation function of the LAEs at $z \simeq 6.6$ for the f_α/f_c model. The mean ACF is calculated from 36 mock catalogues (12 along each of x, y, z directions) assuming volumes with a depth of $30h^{-1}$Mpc and a FoV of $\sim 3 \times 10^4 h^{-2}$Mpc^2. In each panel, the solid coloured line shows the ACF of the best fit $(f_\alpha/f_c, f_{\rm esc}, \langle\chi_{HI}\rangle)$ combinations, ranging from $f_{\rm esc} = 0.05$ to 0.5 (columns) and from $\langle\chi_{HI}\rangle = 10^{-4}$ to $\langle\chi_{HI}\rangle = 0.5$ (rows) and assuming the modified f_α/f_c model. The grey shaded areas show the variance across the mock catalogues. In each panel the dotted coloured line represents the ACF of the simple model for comparison. The grey short dashed line shows the ACF for LBGs from the whole box, corresponding errors on the ACF for LBGs are comparable with the line width, and black points represent the observational results by (Kashikawa et al., 2006). The χ^2 error of the simulated LAE ACF in respect to observations is marked in each panel.

massive LAEs that show the strongest clustering (Kaiser, 1984; Bardeen et al., 1986; Mo and White, 1996, The UV brightest galaxies correspond to the most massive galaxies and thus show the strongest clustering. Considering less massive galaxies as LAEs should result in a weaker clustering.), but to the increase in the number of UV faint galaxies. If it was due to a cutback of massive LAEs, the

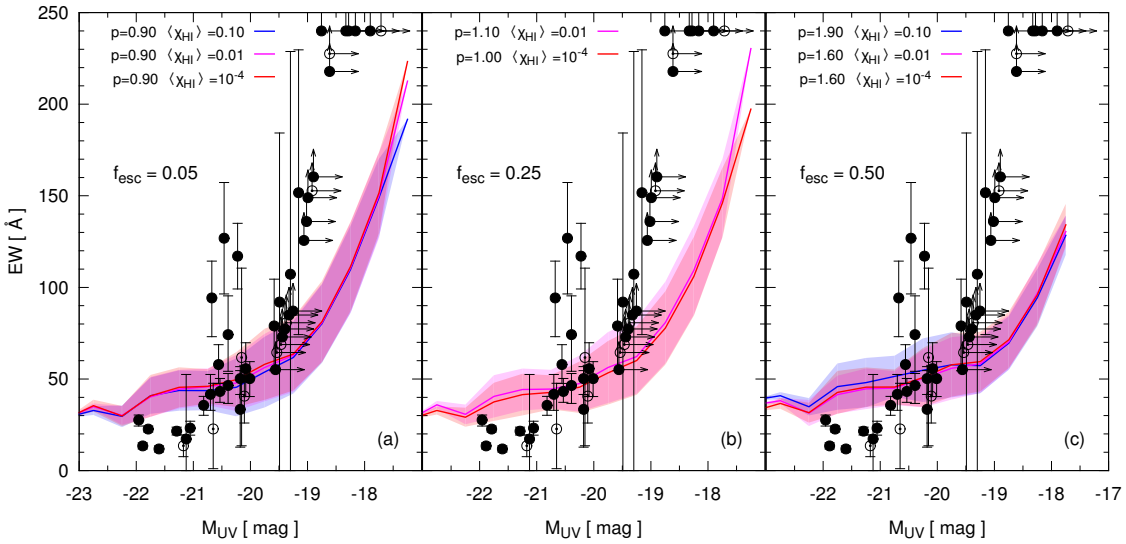

Figure 6.7: The UV luminosity-EW relation at $z \simeq 6.6$ for the best fit $(f_{\rm esc}, \langle\chi_{HI}\rangle)$ combinations for which the simulated LAE Lyα LFs are within the 1σ limit of the observations by Kashikawa et al. (2011) and $f_\alpha/f_c = pe^{-M_h/3\cdot10^{11}{\rm M}_\odot}$. The panels show the EW-$M_{\rm UV}$ relation for different $f_{\rm esc} = 0.05$ (left panel), 0.25 (middle panel), 0.5 (right panel) and $\langle\chi_{HI}\rangle \simeq 0.1$ (blue), 0.01 (magenta), 10^{-4} (red). Black filled circles show the spectroscopic and black open circles the photometric sample of the observations by Kashikawa et al. (2011) (Objects with EW> 240Å are plotted at EW= 240Å).

ACFs should decrease by a similar amount for all $f_{\rm esc}$ values. However, we find that the decrease in the ACFs declines with rising $f_{\rm esc}$ values. Due to the exponential cut in f_α for the most massive galaxies, the factor p needs to be higher than in the simple model to reproduce the observed Lyα LF (Kashikawa et al., 2011). Therefore more UV faint galaxies (LBGs) are identified as LAEs as their Lyα flux exceeds the limit for LAE identification. The increased number of LAEs leads to an overall more homogeneous distribution of the LAEs which results in a decrease of the ACFs.

To explain the second trend, the convergence of the ACFs towards higher $f_{\rm esc}$, we need to consider the intrinsic Lyα luminosities. As $f_{\rm esc}$ increases, the intrinsic Lyα luminosity decreases ($L_\alpha^{int} \propto (1-f_{\rm esc})$); thus for higher $f_{\rm esc}$ values the UV fainter galaxies exhibit such low intrinsic Lyα luminosities, that all their Lyα radiation needs to escape from the galaxies to identify them as LAEs ($f_\alpha = 1$). To reproduce the Lyα LF, an increasing value of $f_{\rm esc}$ can be compensated by a rising value of f_α/f_c (see Chapter 4). Considering rising $f_{\rm esc}$ values, more galaxies reach the $f_\alpha = 1$ limit. In the case of $f_{\rm esc} = 0.5$, where the simple and the modified f_α/f_c model produce the same ACFs, faint galaxies have already reached an f_α value of unity in the simple model. Thus, even though a higher f_α/f_c ratio is allowed for faint galaxies in the modified f_α/f_c model, no more faint galaxies can be identified as LAEs, since all their Lyα luminosity already escapes from the galactic environment.

Summarising we find that for decreasing $f_{\rm esc}$ values the modified f_α/f_c model leads to smaller clustering on scales $r < 10$ Mpc/h, which is in better agreement with the observations. We find the same quantitative estimates of the quality of the model for the Lyα LF best cases (see Table 4.1) when comparing the χ^2 values with respect to the observations. Hence, the modified f_α/f_c model does not alter the constraints on $\langle\chi_{HI}\rangle$ which we have already obtained from the ACFs of our simple model.

6.3.2 Equivalent widths

Applying the modified f_α/f_c model changes the EW-$M_{\rm UV}$ relation, in particular for UV bright galaxies. Since the escape fraction of Lyα radiation is suppressed more for high-mass galaxies, while it is enhanced for low-mass galaxies, the EW values of the transmitted (observed) Lyα line decrease for high-mass and increases for low-mass galaxies. In Fig. 6.7 we show the EW-$M_{\rm UV}$ relation for all best fit Lyα LFs and LAE ACFs cases. Comparing to the EW-$M_{\rm UV}$ relation of the simple model, we note two differences: Firstly, the average EW value of UV bright LAEs has decreased due to a stronger Lyα suppression of high-mass galaxies, and we also find UV bright LBGs that are not identified as LAEs.

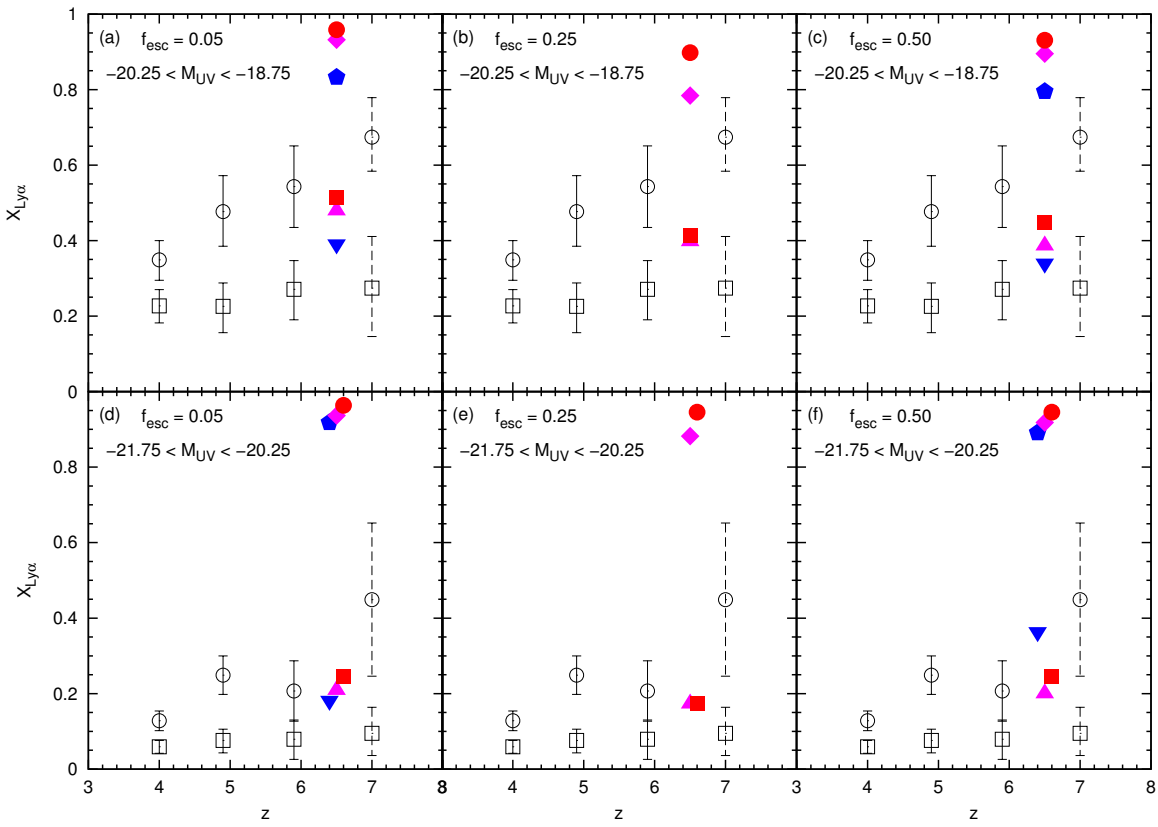

Figure 6.8: Evolution in the fraction of Lyα Emitters ($X_{Ly\alpha}$) in the LBG population over $4 < z < 6$ by Stark et al. (2011) (black empty squares and circles); points at $z \simeq 7$ are extrapolated values by Stark et al. (2011). The Lyα fraction of LBGs with EW larger than 25Å (black empty circles) and 55Å (black empty squares) are shown for two luminosity intervals ($-21.75 < M_{UV} < -20.25$ and $-20.25 < M_{UV} < -18.75$) at $z \simeq 6.6$. The coloured points represent the values for the best fit ($f_\alpha/f_c, f_{\rm esc}, \langle\chi_{HI}\rangle$) combinations for which the simulated LAE Lyα LFs are within the 1σ limit and the simulated LAE ACFs within the 5σ limit of the $z \simeq 6.5$ observations (Kashikawa et al., 2006, 2011) for the modified f_α/f_c model ($f_\alpha/f_c = p\ e^{-M_h/3\cdot10^{11}{\rm M}_\odot}$). In each panel $X_{Ly\alpha}$ of the best fit for $\langle\chi_{HI}\rangle \simeq 0.1,\ 0.01,\ 10^{-4}$ are represented by a filled pentagon, diamond, circle (upward triangle, downward triangle, square) for EW> 25Å (EW> 55Å) respectively. For readability the coloured points are displaced along the z-axis.

Secondly, higher EW values are reached for UV fainter LAEs, as their f_α/f_c value exceeds the value in the simple model. Due to the saturation limit $f_\alpha = 1$, the range of the EW values for $f_{\rm esc} = 0.5$ does not reach such high values as for $f_{\rm esc} = 0.05$ and 0.25: since the intrinsic Lyα luminosities for $f_{\rm esc} = 0.5$ are smaller than for $f_{\rm esc} = 0.05$ and 0.25, a higher f_α/f_c value is needed to identify the same galaxy as a LAE. Thus, in the case of $f_{\rm esc} = 0.5$ the ratio f_α/f_c is so high, that some galaxies have already reached the limit of $f_\alpha = 1$ and their Lyα luminosities and EW values cannot be boosted further.

6.3.3 Lyα fraction

As the f_α/f_c model changes the EW-$M_{\rm UV}$ relation for high UV luminosities, we expect the fraction of LBGs showing Lyα emission ($X_{Ly\alpha}$) to be altered. For $EW > 55$Å the trend of $X_{Ly\alpha}$ with UV luminosity has been inverted. While $X_{Ly\alpha}$ decreases with declining UV luminosities in the simple model as can be seen in Figures 6.4 ($X_{Ly\alpha} \simeq 0.35$ for $-20.25 < M_{UV} < -18.75$ and $X_{Ly\alpha} \simeq 0.5$ for $-21.75 < M_{UV} < 20.25$) and 6.5, it increases in the modified f_α/f_c model which is shown in Figures 6.8 ($X_{Ly\alpha} \simeq 0.4$ for $-20.25 < M_{UV} < -18.75$ and $X_{Ly\alpha} \simeq 0.2$ for $-21.75 < M_{UV} < 20.25$) and 6.9. As we have already seen in Sec. 6.3.2, the modified f_α/f_c model changes the EW distribution at higher UV luminosities ($M_{UV} < -20$) towards lower EW values, as f_α decreases exponentially with halo mass. Due to the more declining f_α values with rising UV luminosities, fewer LBGs exhibit large enough EW values to be identified as LAEs. This inversion of the trend of $X_{Ly\alpha}$ with $M_{\rm UV}$ is not

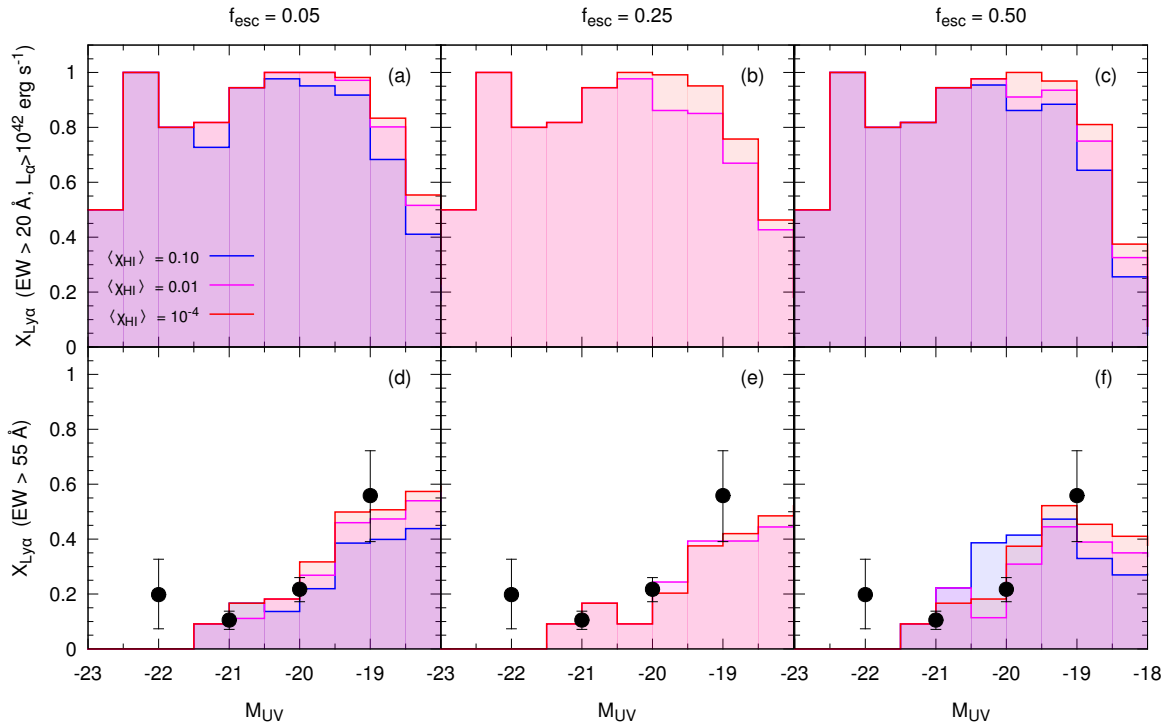

Figure 6.9: Fraction of Lyα Emitters ($X_{Ly\alpha}$) in the LBG population as a function of the observed UV luminosity for the modified f_α/f_c model. The upper and lower row refer to the fraction of LBGs showing Lyα emission with EW> 20Å and $L_\alpha^{obs} > 10^{42}$erg s^{-1}, and EW> 55Å, respectively. The histograms show in the model results for $f_{\rm esc} = 0.05$ (left column), 0.25 (middle column), 0.50 (right column) and in each panel $\langle\chi_{HI}\rangle = 0.10$ (blue), 0.01 (magenta), 10^{-4} (red). Black points show the observations by (Stark et al., 2010) in the range of $4.5 < z < 6$ for EW> 55Å. For EW> 20Å observational data is not available.

seen for an EW cut of $EW > 25$Å in Fig. 6.4. But in Fig. 6.9 we find that for $M_{UV} < -20$ $X_{Ly\alpha}$ shows a trend to decrease towards higher UV luminosities. Hence, to reproduce the trend of $X_{Ly\alpha}$ with M_{UV} not only for an EW threshold of 55Å but also of 25Å , the EW values for UV bright LBGs needed to be decreased further. Even in our modified f_α/f_c model this is not possible as the observed Lyα LF cannot be reproduced with higher Lyα luminosities.

Comparing the result for $X_{Ly\alpha}$ of the modified f_α/f_c model, we find that for an EW selection criterion of $EW > 55$Å the modified model reproduces the observations by Stark et al. (2010, 2011) well, while for an EW selection criterion of $EW > 25$Å the fraction $X_{Ly\alpha}$ is higher than the observed value and does not reproduce the observed trend with the UV luminosity. The modified f_α/f_c model leads to a decline of the EW values of UV bright galaxies. Nevertheless, this decrease is not sufficient to reproduce the observed low EW (see Sec. 6.3.2). Consequently for an EW selection criterion of $EW > 25$Å, too many LBGs are identified as LAEs, causing an increase in $X_{Ly\alpha}$.

6.4 Limits on fitting the EW-M_{UV} relation and $X_{Ly\alpha}$ to observations

In the previous sections we compared our model results to different observables such as the LAE ACFs, the EW-M_{UV} relation and LAE fraction. In section 6.2 we assumed a simple model with a fixed ratio of f_α/f_c and found that the UV bright galaxies with low Lyα EW values are not reproduced sufficiently. Since $f_{\rm esc}$ and $\langle\chi_{HI}\rangle$ (or the corresponding Lyα transmission T_α) are fixed by the radiative transfer simulations, we modified the only free parameter, f_α/f_c (by assuming a decreasing value with rising halo mass), to obtain lower EW values for UV bright galaxies and an increasing $X_{Ly\alpha}$ towards decreasing UV luminosities (Section 6.3). Nevertheless, we do not entirely recover the observed trends. In this section we discuss possible reasons.

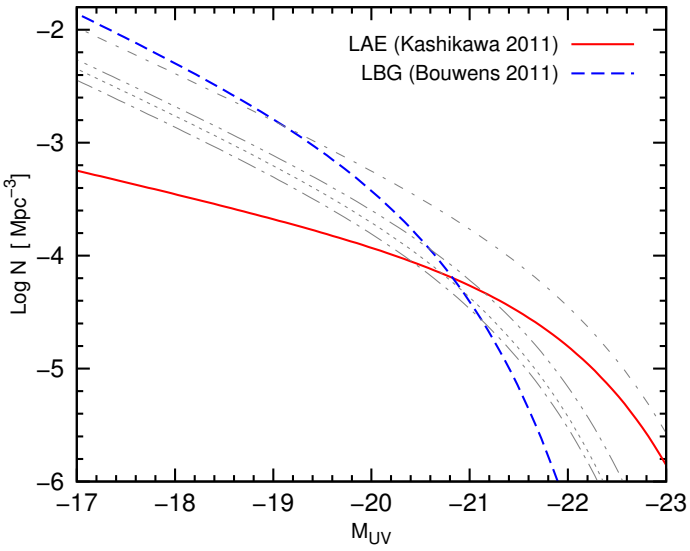

Figure 6.10: Schechter fits of the observed UV LFs for LAEs (Kashikawa et al., 2011, red solid line) and LBGs (Bouwens et al., 2011, blue dotted line). The grey dotted, long dash-dotted, dash-dottend, dash-dott-dotted lines represent the Schechter functions for the Schechter parameters $\phi^* = (-3.9, -4.0, -3.9, -3.9)$, $M^* = (-21.00, -21.00, -21.90, -21.20)$, $\alpha = -2.0$ respectively.

6.4.1 Relation between Lyα and UV luminosities

In order to explain why our model does not reproduce the low EW values for UV bright galaxies, we need to consider two facts: Firstly, the most massive galaxies exhibit the highest Lyα luminosities in our model. This is not entirely obvious, since massive galaxies have older stellar populations than less massive galaxies, and the relation between the emitted Lyα and UV luminosities depends to a large extent on the age of their stellar population (see Sec. 6.2.1), i.e. older stars produce less ionzing photons and thus Lyα photons than young stars. Since the EW value is given by the ratio of the Lyα and UV luminosity, our model implies a dependency between the Lyα luminosity and the EW value, which is in contrast to observational claims (Stanway et al., 2007; Nilsson et al., 2009; Zheng et al., 2014). Secondly, since we need to recover the bright end of the observed Lyα LF and the corresponding LAE UV LF by Kashikawa et al. (2011), the UV bright galaxies need to coincide with the most luminous LAEs. This tight connection causes higher EW values for UV bright sources, which is in contradiction with the observations (Ando et al., 2006; Shimasaku et al., 2006; Iwata et al., 2007; Ouchi et al., 2008; Vanzella et al., 2009; Shioya et al., 2009; Kashikawa et al., 2011). Observations revealed a deficiency of large EW values for UV bright LAEs, which might be due to selection effects (Stanway et al., 2007; Nilsson et al., 2009; Zheng et al., 2014) or caused by the nature of LAEs (Ando et al., 2006). Despite their lower f_c and f_α values, our UV brightest galaxies also show the highest Lyα fluxes and their minimum Lyα luminosities are limited by the bright end of the observed Lyα LF. For this reason we cannot adjust our f_α/f_c model to the extent that it entirely reproduces the observed EW-M$_{\rm UV}$ relation, i.e. reducing the EW values for UV bright galaxies sufficiently.

6.5 $X_{Ly\alpha}$ observations

As we have seen in Section 6.3 the deficiency of low EW values for UV bright sources is in tension with the observations, and consequently also the dependency of $X_{Ly\alpha}$ on the UV luminosities does not show the correct trend for low EW cuts ($EW > 25$Å). To quantify the possible trends of $X_{Ly\alpha}$ on UV luminosities within the observed LAE and LBG UV LFs, we derive $X_{Ly\alpha}$ for different EW cuts entirely from the observed LAE and LBG UV LFs.

Before we derive the dependencies of $X_{Ly\alpha}$ on the UV luminosities for different EW cuts, we estimate $X_{Ly\alpha}(M_{UV})$ roughly from the observed UV LFs of LBGs and LAEs. For the latter we employ the fitted Schechter luminosity functions

$$\Phi(M)dM = 0.1 \ln 10 \phi^* [10^{-0.4(M-M^*)}]^{\alpha+1} \exp(-10^{-0.4(M-M^*)})dM \tag{6.3}$$

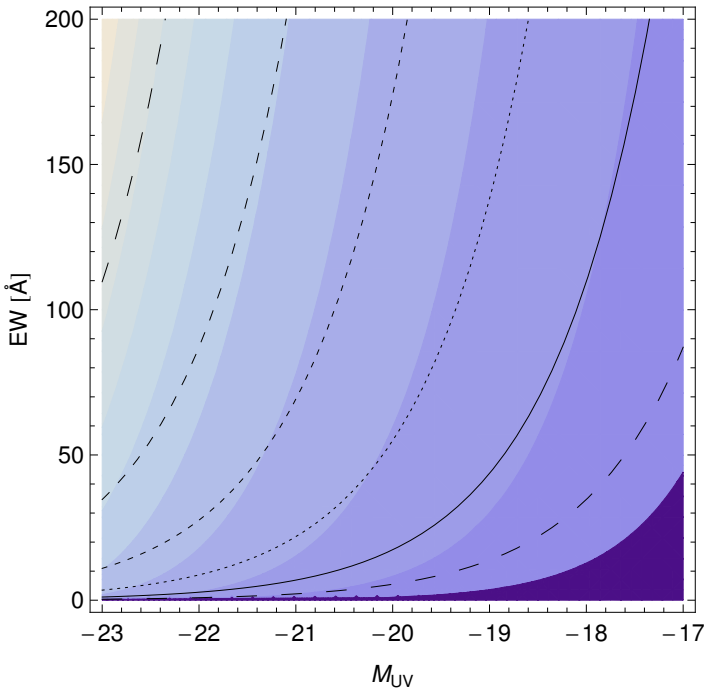

Figure 6.11: Probability distribution of the M_{UV}-EW plane. The colours show the contours of intervals bounded at constant probability density; the probability increases with lower UV luminosity and lower EW, indicated by the increase in blue. The black lines represent the lines of constant Lyα luminosity. From top to bottom the lines are for $\mathrm{Log}_{10}\left[\mathrm{L}_\alpha/\mathrm{erg\ s}^{-1}\right] = 44$ (long dashed), 43.5 (dashed), 43 (small dashed), 42.5 (dotted), 42 (solid) and 41.5 (long dashed).

of the observed LAE UV LF and Lyα LF by Kashikawa et al. (2011) and the LBG UV LF by Bouwens et al. (2011). The fitting parameters are $M^* = -20.14$, $\phi^* = 0.86 \cdot 10^{-3}$, $\alpha = -2.01$ for LBGs and $M^* = -21.72$, $\mathrm{Log}\phi^* = -4.15$, $\alpha = -1.5$ for LAEs. From Figure 6.10 we see that the LAE UV LF exceeds the LBG UV LF at higher UV luminosities, while it falls below the LBG UV LF for fainter UV luminosities. Deriving $X_{Ly\alpha}$ from these UV LFs, we obtain $X_{Ly\alpha} > 1$ for $\mathrm{M}_{UV} < -20.8$ and $X_{Ly\alpha} < 1$ for $\mathrm{M}_{UV} > -20.8$, which is in contradiction of the observations by Stark et al. (2010, 2011). Nevertheless, this consideration is approximative and does not take the actual observational selection criteria, e.g. EW cuts, into account.

In the following we analyze the $\mathrm{M_{UV}}$-dependency of $X_{Ly\alpha}$ for different EW cuts by computing the EW probability distribution as a function of the UV luminosity (see Fig. 6.11). We propose an EW - UV luminosity distribution which is given by the LAE observations of Kashikawa et al. (2011). Starting from the Schechter functions $\Phi^{UV}_{LAE}(M_{UV})$ for the UV LF of the LAEs and $\Phi^{\alpha}_{LAE}(L_\alpha)$ for the Lyα LF, we express the Lyα luminosity, L_α, in terms of the Lyα equivalent width, $EW = L_\alpha/L_c$, and the UV magnitude, M_{UV}. By multiplying these two distribution functions, we derive a probability distribution for the EW-$\mathrm{M_{UV}}$ plane which is shown in Fig. 6.11.

$$\begin{aligned} P(EW, M_{UV}) &= \Phi^{UV}_{LAE}(M_{UV}) \times \Phi^{\alpha}_{LAE}(L_\alpha) \\ &= \Phi^{UV}_{LAE}(M_{UV}) \times \Phi^{\alpha}_{LAE}(EW, M_{UV}) \end{aligned} \tag{6.4}$$

From this Figure we find that firstly the probability decreases the higher the UV luminosity and/or the EW of a galaxy is (according to a power law), and secondly the probability contours are very similar to the lines of equal luminosity. If probability contours and isohyphenluminosity lines agreed, the Lyα EW would not depend on the Lyα luminosity as it was found in Stanway et al. (2007), Nilsson et al. (2009) and Zheng et al. (2014), while a disagreement favouring higher probabilities for larger EW at constant Lyα luminosity would correspond to the so-called "Ando" effect (Ando et al., 2006), i.e. a deficiency of luminous LBGs with large EW of Lyα emission or a dependency of the EW on the Lyα luminosity. Although the probability contours in Fig. 6.11 are close to the isoluminosity lines, they favour/support an "Ando" effect like distribution.

In order to estimate the number of LBGs showing Lyα emission ($X_{Ly\alpha}$) as a function of the EW cut (EW_{cut}), we firstly determine the number of LAEs for a chosen EW cut and secondly compute

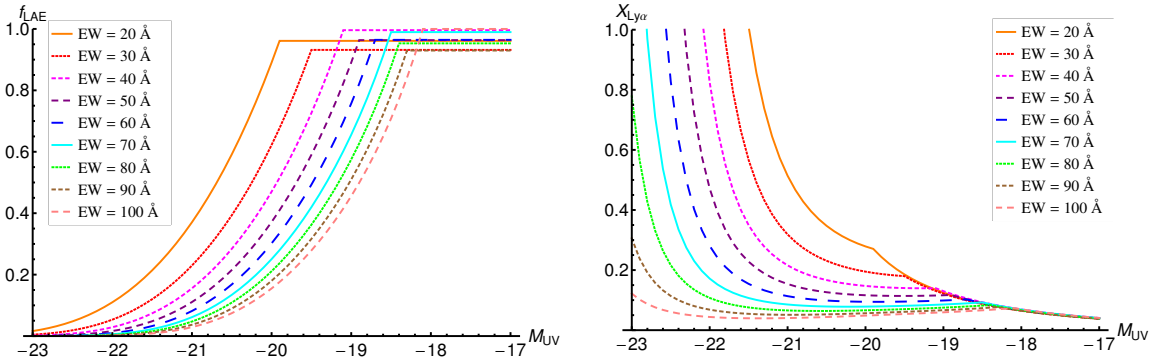

(a) **(b)**

Figure 6.12: Left: The fraction of LAEs with $EW > EW_{cut}$ as a function of UV luminosity. The different lines show the fractions for different EW_{cut}. **Right:** The fraction of LBGs showing Lyα emission as a function of UV luminosity. $X_{Ly\alpha}$ is calculated via the fitted Schechter functions to the observed LAE and LBG UV LFs, $f_{LAE}\Phi^{UV}_{LAE}/\Phi^{UV}_{LBG}$

the resulting $X_{Ly\alpha}$ by using the ratio of the observed LAE and LBG UV LFs and the corresponding fraction of identified LAEs with $EW > EW_{cut}$. To perform the first step we derive the number of LAEs for each UV luminosity that correspond to the measured Lyα LF, i.e. assuming a lower limit EW_i that corresponds to the luminosity limit $L \leq 10^{42}$erg s^{-1} and an upper limit EW_f of 600Å.

$$N_{tot} = \int_{EW_i}^{EW^f} P(EW)\, \mathrm{d}EW \tag{6.5}$$

Under the same assumptions we calculate the number of LAEs for a specified EW cut, i.e. considering all galaxies with $EW > EW_{cut}$ as LAEs.

$$N = \int_{EW_{cut}}^{EW^f} P(EW)\, \mathrm{d}EW \tag{6.6}$$

By evaluating $f_{LAE} = N/N_{tot}$ we determine the fraction of LAEs with $EW > EW_{cut}$. We multiply the latter with Φ_{LAE} and obtain the LAE number density as a function of UV luminosity for a chosen EW cut, i.e. a LAE UV LF ($EW > EW_{cut}$). To yield $X_{Ly\alpha}$ as a function of UV luminosity (M_{UV}) the LAE UV LF for a chosen EW cut is divided by the LBG UV LF (Φ^{UV}_{LBG})

$$X_{Ly\alpha} = f_{LAE}\frac{\Phi^{UV}_{LAE}}{\Phi^{UV}_{LBG}}. \tag{6.7}$$

In Fig. 6.12a we show the fraction of LAEs, $f_{LAE}(M_{UV})$, for different EW cuts (ranging from $EW \geq 20$Å to$EW_{cut} \leq 100$Å). For all EW cuts f_{LAE} increases towards lower UV magnitudes, until it reaches unity; in the following we will refer to this saturation point as the break M^{break}_{UV}. The increasing probability towards lower UV luminosities (see Fig. 6.11) causes the rise in f_{LAE}, while if the luminosity limit exceeds the chosen EW cut f_{LAE} saturates to unity. With increasing EW_{cut} value the fraction f_{LAE} shifts towards lower UV luminosities: as the Lyα LF declines towards lower Lyα luminosities, the probability distribution $P(EW, M_{UV})$ drops accordingly towards higher EW values. Thus a higher EW_{cut} value corresponds to a lower probability in $P(EW, M_{UV})$.

The fraction of LBGs showing Lyα emission ($X_{Ly\alpha}$) is shown in Fig. 6.12b, assuming for Φ^{UV}_{LAE} the Schechter fit of the LAE UV LF from Kashikawa et al. (2011) and for Φ^{UV}_{LBG} the Schechter fit of the LBG UV LF from Bouwens et al. (2011). Surprisingly the increasing trend towards fainter UV luminosities that we found for f_{LAE} is inverted. This inversion results from the ratio of the LAE and LBG UV LFs: firstly, for bright UV luminosities ($M_{UV} < -20.8$) the number of LAEs exceeds the number of LBGs, and secondly, this excess of LAEs rises towards higher UV luminosities (following a power law).

Since this resulting trend of $X_{Ly\alpha}$ is contrary to the observational trend (Stark et al., 2010, 2011), we vary the Schechter parameters of the LBG UV LF to examine whether the observational trend

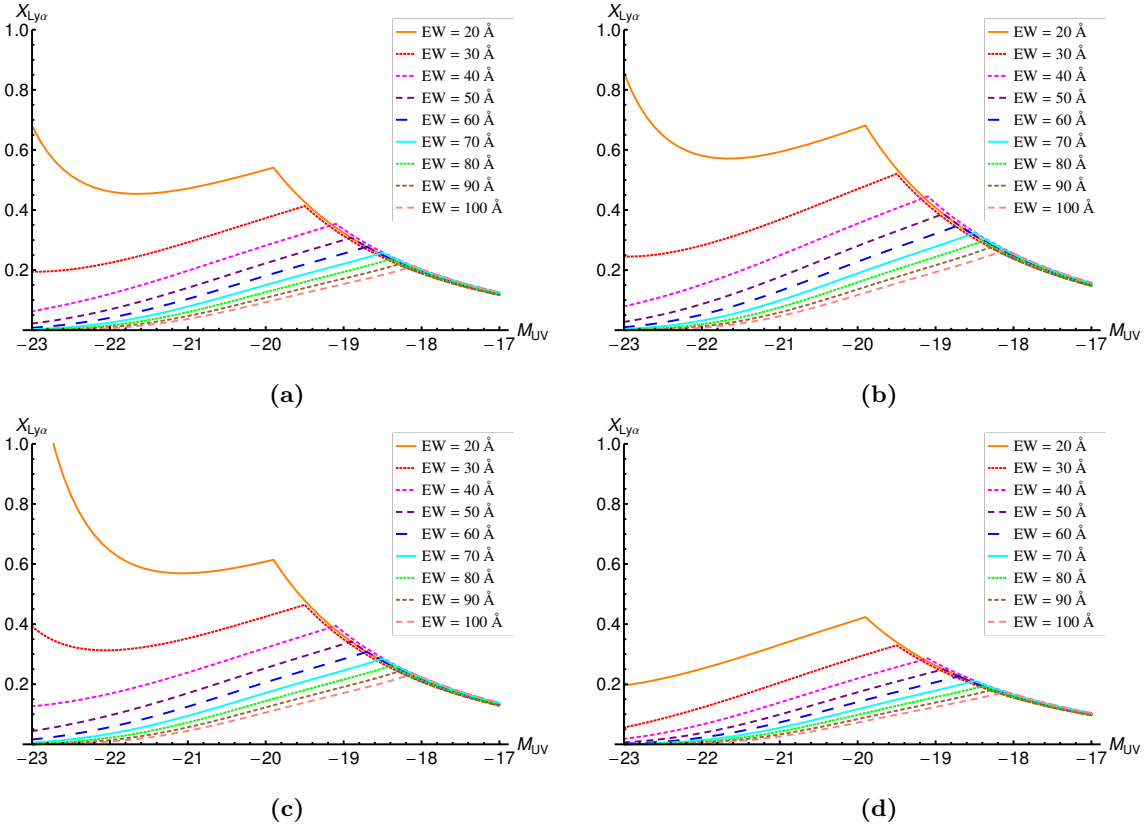

Figure 6.13: The fraction of LBGs showing Lyα emission as a function of UV luminosity. $X_{Ly\alpha}$ is calculated via the fitted Schechter functions to the observed LAE and LBG UV LFs, $f_{LAE}\Phi^{UV}_{LAE}/\Phi^{UV}_{LBG}$. In each panel the resulting $X_{Ly\alpha}$ are shown for EW cuts ranging from $EW > 20$Å to $EW > 100$Å. The Schechter parameters of the LBG UV LF have been adapted to reproduce the observational M_{UV}-trend of $X_{Ly\alpha}$. The Schechter parameters are $\phi^* = (-3.9, -4.0, -3.9, -3.9)$, $M^* = (-21.00, -21.00, -21.90, -21.20)$, $\alpha = -2.0$ for panels a,b,c,d respectively. Changing the Schechter parameters slightly can result in noticeable changes. The decrease of X_{Lya} after the break towards fainter UV luminosities is caused by the assumed minimum Lyα luminosity of 10^{42}erg s^{-1}.

can be recovered. Shifting the LBG UV LF towards higher UV luminosities (shifting the Schechter parameters from $\mathrm{Log}(\phi^*) = -3.07$, $M^* = -20.14$ to $\mathrm{Log}(\phi^*) = -3.90$, $M^* = -21.00$), which leads to a decrease in the difference between LAE and LBG UV LFs, the decreasing trend of X_{Lya} towards fainter UV luminosities can be inverted (see Fig. 6.13a). However, the rising and declining nature of X_{Lya} depends on the EW cut even for fixed Schechter parameters. While in Fig. 6.13a the trend for $EW_{cut} \geq 30$Å is continuously rising until M^{break}_{UV}, we find a declining and then rising trend with decreasing UV luminosity for $EW_{cut} = 20$Å. This complex dependencies are due to the increasing f_{LAE} and the difference of the LAE and LBG UV LFs. For $M_{UV} < -22$ the LAE UV LF exceeds the LBG UV LF by an higher amount than a decrease in f_{LAE} can compensate, while for $-22 < M_{UV} < -20$ the trend of f_{LAE} dominates.

The trend and values of $X_{Ly\alpha}$ are very sensitive to small changes in the LBG UV LF. In Figures 6.13b, 6.13c and 6.13d the Schechter parameters have been varied by small amounts, but the resulting $M_{UV} - X_{Ly\alpha}$ relations vary by amplitude and shape considerably. As a general trend we find that the more the LAE UV LF exceeds the LBG UV LF at higher UV magnitudes, the higher is $X_{Ly\alpha}$ and the more a declining trend with decreasing UV magnitudes is found. This applies when decreasing the value of M^* (compare Figs 6.13a, 6.13c and 6.13d) or the value of $\mathrm{Log}(\phi^*)$ (compare Figs 6.13a and 6.13b).

In summary the fraction of LBGs showing Lyα emission depends sensitively on the observed LBG and LAE UV LFs, the Lyα LF and the assumed EW cut: the more the LBG UV LF deviates from the LAE UV LF, the more sensitive is the M_{UV}-dependency and amplitude of $X_{Ly\alpha}$ on small variations of the Schechter parameters. Given the observational uncertainties on the LFs there is a large range of possible trends of $X_{Ly\alpha}$.

6.6 Conclusions

In this Chapter we employ our model for high-redshift LAEs based on numerical hydrodynamical and radiative transfer simulations to predict the equivalent distribution and the fraction of LBGs showing Lyα emission. As our model has three free parameters, the escape fraction of ionizing photons ($f_{\rm esc}$), the mean amount of neutral hydrogen ($\langle\chi_{HI}\rangle$) and the ratio of the escape fractions of Lyα photons and UV continuum photons (f_α/f_c), we search for those combination of parameters that reproduce the observed Lyα LF (Kashikawa et al., 2011) within a 1σ limit (see Chapter 4) and LAE ACF (Kashikawa et al., 2006) within a 4σ limit (see Chapter 5) at $z \simeq 6.6$. For these combinations we compare model results for the EW distribution and the fraction of LBGs identified as LAEs with observations (Kashikawa et al., 2011; Stark et al., 2010, 2011).

In the first model we assume a constant ratio between the escape fraction of Lyα and UV continuum photons, f_α/f_c, consistent with Chapters 4 and 5. Reproducing the observational trend of the EW-$M_{\rm UV}$ distribution, we find that the mean EW increases with fainter UV luminosities due to the decreasing age for lower stellar masses, leading to an enhanced ratio between the number of UV ionizing and UV continuum photons. Although our model maps the observational trend of an increasing EW towards fainter UV luminosities, our model encounters two issues: Firstly, there is a deficiency of high EW values, and secondly, the EW values and thus the Lyα luminosities of the UV bright galaxies are too high. The first issue, the lack of high EW values, is caused by the averaging of the transmission across 48 lines of sight as the transmission of UV fainter galaxies varies strongly across different lines of sight due to the inhomogeneous ionization field. Due to the second issue (the enhanced Lyα luminosity of the UV bright galaxies) the $M_{\rm UV}$ trend of the fraction of LBG showing Lyα emission ($X_{Ly\alpha}$) - decreasing towards fainter UV luminosities - is in opposition to the observations (Stark et al., 2010, 2011). As $X_{Ly\alpha}$ depends sensitively on the EW cut, we find that when the EW cut value is increased above the value where LBGs are identified as LAEs, the found trend of $X_{Ly\alpha}$ with the UV magnitude (M_{UV}) is inverted and approaches the observational trend. To improve our model we assume that the ratio f_α/f_c decreases exponentially with halo mass and recompute the ACFs, the EW-$M_{\rm UV}$ relations and $X_{Ly\alpha}$. The ACFs remain the same for $f_{\rm esc} = 0.5$ and decrease only marginally towards lower $f_{\rm esc}$ values (0.25, 0.05). The modified f_α/f_c ratio does not alter the previous constraints on the parameter space by the ACFs, but decreases the Lyα luminosities and EW values of the UV bright galaxies. Hence, not only the EW-$M_{\rm UV}$ relation of the modified model is in a better agreement with the observation, but also $X_{Ly\alpha}$; the observations by (Stark et al., 2010) are reproduced for an EW cut of 55Å.

Nevertheless, even the modified f_α/f_c model does not allow us to simultaneously reproduce the observed Lyα LF at $z \simeq 6.6$ and predict sufficiently low Lyα fluxes for UV bright galaxies. The problem we encounter in our model when fitting to observations can be summarised as follows: the UV brightest galaxies coincide with the Lyα brightest galaxies in our model. Decreasing the Lyα luminosities of the UV brightest galaxies to fit the low observed EW values leads to a lack of high Lyα luminosities that are required by the observed Lyα LF. This issue might be caused by either an inconsistency of the observations or our modeling. In the latter case our findings suggest that in the real universe the UV brightest galaxies are not the Lyα brightest, but UV fainter galaxies show the highest Lyα fluxes. Several caveats of our model could explain the disagreement with observations:

- The excessive Lyα luminosities of the UV bright galaxies may be due to the amount of SN energy (50%) that powers winds. Massive galaxies show fewer inflows (as it is the case in other hydrodynamical simulations exploited in other theoretical works Dayal et al. (2011)), this leads to an increasing rather then a constant transmission with rising halo mass.

- Our dust model assumes global values within each galaxy, e.g. the time averaged star formation rate or the distribution of dust and its corresponding extinction. As the ISM is not resolved in the hydrodynamical simulation used, we cannot take inhomogeneous distributions of dust along different line of sights into account. As such our resulting averaged dust-attenuated luminosities might not reflect the observations due to this inhomogeneous emission (Zheng et al., 2010). To solve this issue a detailed treatment of the Lyα radiative transport in the ISM is required.

- As has been shown by Bolton and Haehnelt (2013) self-shielded systems (i.e. Lyman limit systems) can decrease the transmission of Lyα radiation considerably. Since our model does not include self-shielded systems and reionization proceeds inside-out, our Lyα transmission values,

especially of massive and luminous galaxies, might be too high due to this lack of Lyα absorbing systems.

- Although global values for the evolution of the stellar mass and the star formation rate density of our hydrodynamical simulation are consistent with observations, the detailed star formation history of the galaxies might not reflect galaxy formation: as massive galaxies show too much star formation at later times, the mean age of their stellar population is lower. Since younger stellar populations emit an increased amount of Lyα radiation, the reduced mean age of the galaxies leads to a higher fraction between Lyα and UV continuum luminosities. Observationally a correlation between the EW values and the UV slope β has been found by Schenker et al. (2014), i.e. the steeper the slope, the higher the EW values. As a steep UV slope hints towards young galaxies, the most UV luminous galaxies should be the oldest (Meurer et al., 1999; McLure et al., 2011; Bouwens et al., 2012).

Although our model suffers some caveats, the problem of excessive EW values towards higher UV luminosities could also arise from the inconsistency between the different observations. If we derive the fraction of LBGs showing Lyα emission using the observed Lyα and LBG UV LF, the resulting trend is contrary to the observed one. This leads to the question whether these different observations can be used to constrain a LAE model or whether the different selection biases are too strong to be neglected. Due to the observational techniques, different biases might govern LBGs, LAEs or LBGs with strong Lyα emission (Schaerer, 2014). While LBGs are identified by the drop-out technique using the rapid flux decrease in the UV continuum emission shortwards of the Lyman limit, LAEs are selected by the excess in narrowband filters compared to the continuum. According to Ouchi et al. (2008) LAEs are more prevalent at the faint-end of the luminosity function when comparing LBG UV LF with narrowband-selected LAEs. This is supported by the fact that for a number of LAEs the UV continuum luminosity cannot be estimated (Kashikawa et al., 2011) and thus only upper limits can be given. Furthermore when selecting LBGs showing Lyα emission, galaxies that would have been identified as LAEs using a LAE selection method might be missed (Schaerer, 2014). In addition, to date the sample of high-redshift LAEs and LBGs are not sufficient to probe the corresponding luminosity functions definitively. As we have seen in Section 6.4 small uncertainties in the luminosity functions can have a considerable effect on the predicted $X_{Ly\alpha}$.

In summary, although our model suffers from multiple caveats, it is difficult to resolve the tension with observations entirely, since LAE and LBG observations at high redshifts underlie uncertainties and their selection effects on the galaxy properties are not well known. Despite these uncertainties our model provides an excellent tool to illustrate how different parameters, the escape fraction of ionizing photons, the amount of neutral hydrogen in the IGM or the ratio between the escape fraction of Lyα and UV continuum photons, affect the observables and thus which parameter are crucial for the different observations, i.e. while the Lyα LF and the equivalent width distribution depend on the galaxy properties and the IGM Lyα transmission, the ACF is primarily altered by the large scale ionization structure.

Chapter

7

Summary & Conclusions

In this thesis I have focused on the Epoch of Reionization, its progress and possible constraints by observations. By means of a self-consistent cosmological numerical reionization simulation we have studied the growth and distribution of ionized regions, investigated the effect of source properties on the extent of ionized regions, and followed the topology of reionization revealing an inside-out character, in which reionization started in high density regions near sources and ended in low density regions far from sources. In order to constrain reionization we have used high-redshift galaxies showing excess Lyman-α (Lyα) radiation, so-called Lyman Alpha emitters (LAEs). With the help of a number of reionization scenarios, simulated Lyα luminosity functions (Lyα LFs) are compared to observations at $z \simeq 6.6$; a three-dimensional degeneracy between reionization, the escape fraction of ionizing photons from the galaxy, and dust distribution inside the galaxy is revealed, which still remains when we account for observed LAE clustering at $z \simeq 6.6$. The main conclusions which can be drawn from this result is that reionization can not be constrained exclusively by LAEs, and other observational information as the 21cm signal are needed. Nevertheless, the 3D degeneracy indicates also that LAEs are not only tracers of reionization, but also of the escape fraction of ionizing photons and the distribution of dust in the interstellar medium. The degeneracy is also seen in the duty cycle of LBGs with Lyα emission as well as in the Lyα equivalent width distribution and the LAE-fraction of LBGs. The main results of this thesis are summarised in the following and future prospects are given.

- **Analysis of overlapping spheres:**
  Revisiting Strömgren's analysis of ionized spheres around sources emitting hydrogen ionizing photons (Strömgren, 1939), the profile of the H I photoionization rate in terms of Strömgren radii is analyzed regarding its dependency on the number of ionizing photons, the H II recombination rate and the hydrogen density. Being dependent on these parameters, the distance from the source in terms of Strömgren radii is found where the H I photoionization rate drops below (exceeds) the value which corresponds to a H I ionization fraction of 0.99 (0.01), above (below) this value the ionization (neutral) fraction changes marginally. In terms of Strömgren radii the corresponding distance of these "critical photoionization rates" from the source are determined and its dependency on parameters is estimated: the more luminous the source and the less dense the medium, the larger is the "critical distance". We have found that as long as the intersection of the overlapping occurs within the "critical distance" and we account simultaneously for the increase of ionizing photon density (corresponding to photons needed to ionize the overlapping volume) when spheres merge, the photoionization rate of two overlapping ionized spheres can be sufficiently described by the sum of the photoionization rates of two single ionized spheres. Since ionization fronts are sharp, ionization equilibrium is a fair assumption for most distances from the source and photoionization rates can directly be converted to H II fractions. This analysis provides a valuable tool to find fast solutions for the ionized distribution of two sources without performing numerical 3D radiative transfer.

- **Development of a fast mapping-ionized-spheres-scheme:**
  Since the ionization regions carved by galaxies in the intergalactic medium (IGM) can be well approximated by spherical bubbles, a fast approximate scheme of radiative transfer similar to Thomas and Zaroubi (2008) has been developed. In a first step a one-dimensional radiative transfer code solving for H II, He II, He III and temperature is implemented, where the modified Patankar-Runge-Kutta scheme provides a numerically robust, unconditionally positive and conservative solution to the stiff system of production-destruction equations. The code reproduces the analytical solution of an H II Strömgren sphere, as well as the H II, He II, He III and temperature profiles of an emitting source in a homogeneous density field gained with the 3D radiative transfer code pCRASH (Partl et al., 2011). In a second step, based on the mapping-Strömgren-sphere-scheme developed by Adrian Partl (private communication), a MPI-parallelized code is developed, which solves for the ionized regions of multiple sources in a density field by mapping their ionized spheres. Firstly it computes the underlying density and temperature profiles for each source, secondly it calculates the ionization and temperature profiles based on the spectra of the sources, thirdly it accounts for the overlapping of the ionized spheres, and fourthly it maps the spheres on a grid. This mapping-sphere scheme cannot account for angular inhomogeneities around sources in the density field. Compared to 3D radiative transfer calculations the ionized volume is slightly larger as density profiles are underestimated due to averaging over all lines of sight. Its computing time scales with the number of sources. Nevertheless, the ionization distributions of sources in a cosmological density field computed with the mapping-sphere-scheme and pCRASH are very similar. Hence, the mapping-sphere scheme provides a useful tool for the fast computation of an ionization field at the earlier stages of reionization.

- **Enabling reionization simulations with pCRASH:**
  In order to perform self-consistent reionization simulation the Monte-Carlo long characteristic continuum radiative transfer scheme pCRASH, which exploits ray-tracing technique on a 3D grid (Partl et al., 2011), has been extended by a number of features: the possibility of an arbitrary number of spectra, the inclusion of a local and thus spatially-dependent clumping factor and photon tracking from previous snapshots. To carry out a complete reionization simulation with pCRASH the snapshots of the hydrodynamical simulation are consecutively post-processed by firstly using density and temperature distributions of the hydrodynamical simulation as input for the radiative transfer calculations, secondly modelling identified halos as sources whose properties depend on star particle characteristics (stellar mass, age, metallicity), and thirdly running pCRASH for each snapshot. Source properties deduced from the star particles in the hydrodynamical simulation can be reflected in the input spectra of the radiative transfer runs. Inhomogeneities in the IGM within each cell are accounted for by a local clumping factor, whereas IGM clumpiness can only be resolved on the level of the resolution of the underlying hydrodynamical simulation. The memory of propagating photons from the respective previous snapshot ensures a consequential photon propagation when simulations are restarted. These changes allow us to perform self-consistent reionization simulations as the evolution of galaxy spectra can be followed, the clumpiness of the IGM is accounted for to ensure a realistic propagation of the ionization front, and photons are propagated until they are absorbed.

- **Reionization simulation:**
  The Epoch of Reionization is self-consistently simulated by post-processing a hydrodynamical simulation of an 80Mpc/h box with 3D radiative transfer: ionizing radiation of galaxies is modelled according to respective stellar masses, ages and metallicities given by the star particles in the hydrodynamical simulation. The simulation tracks the evolution of the ionization fractions H II, He II, He III and the IGM temperature. Hydrogen ionization starts late at $z \simeq 11$ when the first resolved halos with $M_h > 10^9\,\mathrm{M}_\odot$ appear, and it ends at $z \simeq 6$ when the overall neutral hydrogen fraction drops below 10^{-2}. Reionization shows an inside-out character, i.e. high density regions near sources ionize first while low density regions far from sources ionize last, in agreement with multiple other works (Iliev et al., 2006; Battaglia et al., 2013). Hints of this inside-out character of reionization are given by the cross correlation between density and redshift of H I ionization, and the larger mass-weighed than volume-weighed H I ionization fraction. The sizes of the ionized regions depend primarily on the evolution time and the stellar masses of the enclosed sources; stellar ages and metallicities of galaxies have negligible impact. The IGM thermal state follows the progress of ionization: behind ionization fronts the IGM temperature is lower than in the interior of ionized regions where final ionizing emissivity has

been reached. In regions of ionization equilibrium the temperature-density relation is inverted ($T \propto T_0(1+\delta)^{\gamma-1}$ with $\gamma - 1 = -0.2$) as cooling in denser regions becomes more efficient due to an increased number of recombinations, in agreement with the findings in Trac et al. (2008). Including IGM clumpiness self-consistently by a spatially dependent clumping factor leads to partially neutral patches in regions of high density and clumpiness, which represent self-shielded regions as e.g. Lyman limit systems. In contrast to other works (Bolton and Haehnelt, 2013; Mesinger et al., 2015) an additional model for self-shielding is not invoked. Nevertheless the occurrence of self-shielded regions depends sensitively on the resolution of the radiative transfer calculations; a resolution of 156kpc/h as chosen in this simulation approximates two times the virial radii of the most massive halos in the simulation, while coarser resolutions will not map self-shielded high density peaks sufficiently.

The Thomson optical depth of the reionization simulation falls below the observational constraints from the CMB. This indicates that resolving small scale high density peaks leading to the formation of minihalos and first stars is needed. Inlcuding the ionizing radiation of minihalos forming at high redshifts will shift the start of reionization to higher redshifts and increase the Thomson optical depth, which is required to reproduce the observations. While at the beginning of reionization galaxies form in minihalos and contribute to reionization, their formation will be suppressed by radiative feedback in ionized regions and the halo mass needed to form galaxies will be increased. To trace the effects of radiative feedback on reionization radiation hydrodynamical simulations of reionization are needed, directly following the effect of ionizing radiation on galaxy formation. Combined with a sufficient spatial resolution, reionization history could be accurately mapped, leading to a reionization beginning earlier and an increased suppression of low-mass sources as reionization proceeds. Such simulations represent a valuable tool to resolve the question of self-regulated reionization. While in common post-processing simulations the escape fraction of ionizing photons plays a crucial role for the duration of reionization, radiative feedback might lead to a self-regulation: low escape fractions lead to slow-growing ionized regions and consequentially to a late suppression of galaxies in low-mass halos. In contrast high escape fractions cause a faster growth of ionized regions and radiative feedback, which suppresses galaxy formation in low-mass halos earlier. In both scenarios the duration of reionization could be the same; while in the first scenario reionization is accelerated at the end of reionization, reionization is accelerated at the beginning of reionization in the second scenario. Forthcoming 21cm observations can reveal the reionization topology and which reionization scenario of the described ones applies. To compare simulations to observations it is essential to take observational effects such as foreground radiation and instrumental response into account, which could be done for this reionization scenario in future work. Furthermore, as the 21cm radiation is sensitive to neutral hydrogen, an anticorrelation between galaxies and 21cm radiation should be expected.

- **Constraining the escape fraction of ionizing photons, reionization and dust using Lyman Alpha emitters at $z \simeq 6.6$:**
  We have coupled state of the art cosmological simulations run using GADGET-2 with a dust model and a radiative transfer code (pCRASH) to build a physical model of $z \simeq 6.6$ LAEs to simultaneously constrain the IGM reionization state, the escape fraction of H I ionizing photons and ISM dust distribution (homogeneous/clumped). Identifying simulated galaxies with dust-attenuated UV magnitudes of $M_{UV} \leq -17$ as LBGs, we have validated our simulations by comparing with observed LBG ultraviolet luminosity functions (UV LFs), stellar mass functions, stellar mass densities (SMD) and specific star formation rates (sSFR) at $z \simeq 6-8$. Due to the poor constraints available on the escape fraction of H I ionizing photons ($f_{\rm esc}$) from galaxies, we have used five different values $f_{\rm esc} = 0.05, 0.25, 0.5, 0.75, 0.95$ to post-process the cosmological simulation with pCRASH; starting from a completely neutral Universe, pCRASH is run until reionization is complete for an average H I fraction of $\langle \chi_{HI} \rangle \simeq 10^{-4}$. Then, the only free-parameter left to match model results to the observed Lyα and UV luminosity functions of LAEs at $z \simeq 6.6$ (Kashikawa et al., 2011) is the relative escape of Lyman Alpha (Lyα) and continuum photons from the galactic environment (f_α / f_c) which depends on the clumpiness of the dust in the galaxies. We have found a *three-dimensional* degeneracy such that the theoretical model can be reconciled with observations for an IGM Lyα transmission $\langle T_\alpha \rangle_{LAE} \simeq 38-50\%$ (which translates to $\langle \chi_{HI} \rangle \simeq 0.5 - 10^{-4}$ for Gaussian emission lines), $f_{\rm esc} \simeq 0.05 - 0.50$ and $f_\alpha / f_c \simeq 0.6 - 1.8$, i.e., if dust is clumped in the interstellar medium of high-redshift galaxies,

we can not differentiate between a Universe which is either completely ionized or half neutral, or has an $f_{\rm esc}$ ranging between 5-50%.

Focusing on combinations of $f_{\rm esc}$, $\langle\chi_{HI}\rangle$ and f_α/f_c that have reproduced the observed Lyα LF at $z \simeq 6.6$ we have attempted to break this three-dimensional degeneracy by comparing model results to the observed large scale clustering of LAEs at $z \simeq 6.6$ (Kashikawa et al., 2006). Our results show that reionization has the largest impact on the amplitude of the angular correlation functions (ACFs), and its imprints are clearly distinguishable from those of $f_{\rm esc}$ and f_α/f_c. To reconcile the observations within a 3σ limit we have found $f_{\rm esc} = 0.05 - 0.5$, $\langle T_\alpha\rangle_{LAE} \simeq 45 - 50\%$ (which translates to $\langle\chi_{HI}\rangle = 10^{-4} - 0.01$ for Gaussian emission lines) and $f_\alpha/f_c = 0.6 - 1.2$. Although the parameter $\langle\chi_{HI}\rangle$ can be constrained further by LAE clustering, the three-dimensional degeneracy between $f_{\rm esc}$, $\langle T_\alpha\rangle_{LAE}$ (or $\langle\chi_{HI}\rangle$) and f_α/f_c persists.

Hence, to conclude, the redshift evolution of the Lyα luminosity function can not be solely attributed to reionization, since Lyα visibility depends also on the escape fraction of ionizing photons and dust distribution in the ISM. Although this degeneracy restricts constraints on reionization using LAEs, it implies that LAEs are not only tracers of reionization but also tracers of the escape fraction of ionizing photons and the dust distribution in the ISM. Thus with the help of LAE visibility both the large scale properties of the IGM and properties of the ISM on galactic scales can be studied.

However, on the one hand the IGM Lyα transmission depends on the reionization topology, but on the other hand it depends also on the peculiar velocities around galaxies and the assumed initial Lyα line profile. While different assumptions on the initial line profile change the IGM Lyα transmissions and thus the constrained f_α/f_c values shift accordingly to higher or lower values, the degeneracy between $f_{\rm esc}$, $\langle T_\alpha\rangle_{LAE}$ (or $\langle\chi_{HI}\rangle$) and f_α/f_c remains.

A basic remaining question is how the escape fraction of Lyα photons depends on the escape fraction of UV continuum photons from galaxies, and whether or how it can be attributed to the dust distribution in the ISM. In our model we have assumed that a larger f_α/f_c fraction corresponds to more clumpy ISM, as it has been suggested by Neufeld (1991) who explained the occurrence of large Lyα EW values with the enhanced scattering of Lyα in a clumpy ISM. Nevertheless it has been shown by Laursen et al. (2013) that this scenario is quite unrealistic for expected parameters, thus an alternative explanation might be anisotropic Lyα emission (Zheng and Wallace, 2014; Behrens et al., 2014). How anisotropy might change with halo mass and UV brightness of galaxies is an open question and requires detailed computation of Lyα radiative transfer within the ISM including effects of in- and outflows. Furthermore, although the value of $f_{\rm esc}$ and its dependence on galaxy properties (such as the stellar mass) are only poorly known, recent work hints at an $f_{\rm esc}$ that decreases with increasing mass (Ferrara and Loeb, 2013; Paardekooper et al., 2011). If $f_{\rm esc}$ is indeed higher for low-mass galaxies, the ionization topology would become more homogeneous with the H II regions being built by low-mass (high-mass) galaxies being larger (smaller) than for the constant $f_{\rm esc}$ case. This would have two effects: on the one hand the IGM Lyα transmission would be enhanced (decrease) for low-mass (high-mass) galaxies, leading to a steeper Lyα LF. On the other hand, due to its direct dependence on $f_{\rm esc}$, the intrinsic Lyα luminosity would decrease (increase) for low-mass (high-mass) galaxies, leading to a flattening of the Lyα LF. The relative importance of these two effects is the subject of future work.

A crucial question is whether there are other observations that can break the degeneracy between $f_{\rm esc}$, $\langle\chi_{HI}\rangle$ and f_α/f_c. The solution may be to combine LAE and 21cm observations e.g. by computing the cross-correlation, as the 21cm line follows hydrogen ionization sensitively. As the 21cm signal vanishes in ionized regions, an anticorrelation between LAEs and the 21cm brightness temperature is expected. Lower $f_{\rm esc}$ values cause lower equilibrium ionization fractions within ionized regions, leading to higher 21cm brightness temperatures; due to enhanced neutral density fluctuations the anticorrelation can be expected to be stronger. However, it remains an open question whether there also exists a degeneracy for the cross-correlation between LAEs and the 21cm brightness temperature, since a reduced Lyα transmission in the IGM due to a lower escape fraction could be compensated by not identifying the galaxy as a LAE or by an increased intrinsic Lyα emission from the galaxy.

- **Duty cycle of LBGs showing Lyα emission:**
  In order to investigate when a galaxy is identified as a LBG and/or LAE in its life time, we have analyzed the averaged time evolution and the duty cycle of a galaxy. We have found that: (1) including the effects of dust and IGM attenuation galaxies with a critical stellar mass of $M_\star = 10^{8.5}(10^{9.5})\,\mathrm{M}_\odot$ produce enough luminosity to stay visible as LBGs (LAEs); (2) defining the duty cycle as the fraction of its lifetime a galaxy spends as a LBG with ($f_{LBG\alpha}$) or without Lyα emission (f_{LBG}), $f_{LBG\alpha}$ is always smaller than f_{LBG} due to the more stringent luminosity and equivalent width constraints imposed on identifying galaxies as LAEs; (3) both the intrinsic and dust and IGM-attenuated $f_{LBG\alpha}$ and f_{LBG} rise with increasing UV luminosity (and hence $M_\star$), revealing that in our model the brightest (most massive) LBGs most often show Lyα emission; and (4) the LAE duty cycles of all our models that reproduce the observed Lyα LF and LAE ACFs are independent of the chosen set of parameters: a larger f_α/f_c compensates a decrease in $\langle T_\alpha \rangle_{LAE}$, or an increase in f_{esc}, underlining the 3D degeneracy found in Chapter 4.

  Nevertheless, these estimates on the LAE duty cycles for average galaxies with different final masses or UV luminosities are approximate, as we assume dust attenuation and IGM transmission to be equal to the values at $z \simeq 6.6$. While the dust mass (and hence attenuation) would be expected to be lower at earlier times, tracing this buildup would require tracking the dust growth in the progenitors of our simulated galaxies. This is beyond the scope of this thesis. Furthermore, $f_{LBG\alpha}$ would be expected to decrease with z as a result of an increase in $\langle \chi_{HI} \rangle$ (leading to a decrease in T_α). However, properly accounting for the latter effect requires modelling the entire history of reionization.

- **Reconciling simulated with observed Lyα equivalent width and LAE/LBG fractions:**
  We have used our model for high-redshift LAEs to predict Lyα equivalent distributions and fractions of LBGs showing Lyα emission at $z \simeq 6.6$. We only considered those models that have reconciled the observed Lyα LF and LAE ACF at $z \simeq 6.6$ within a 1σ and 4σ limit respectively. The observed trend of the Lyα equivalent widths (EW) of LAEs which are increasing towards fainter UV luminosities is reconciled, as galaxies with lower stellar masses show lower ages and thus have an enhanced ratio between emitted Lyα and UV continuum photons. However, the Lyα EW values of our simulated UV bright galaxies surpass/exceed the observed values by (Kashikawa et al., 2011). Hence, we expand our LAE model by altering the assumed dust distribution with halo mass (the ratio f_α/f_c is assumed to decline exponentially with halo mass), such that the Lyα emissions of UV bright galaxies are more suppressed than of fainter galaxies and the observed Lyα LF and LAE ACF at $z \simeq 6.6$ are still reproduced. With help of the expanded LAE model we firstly have been able to decrease the Lyα EW of the simulated UV bright galaxies, and secondly to reproduce the observed trend of the LAE/LBG fraction by Stark et al. (2010) for a LAE EW selection criterion of > 55Å: the fraction of LBGs showing Lyα emission increases towards lower UV luminosities.

  However, attempts to improve our LAE model by changing the ratio f_α/f_c have only been partially successful. The global relation of f_α/f_c can not be changed to such a degree that EW values of UV bright galaxies become as low as observed, since otherwise the bright end of the Lyα LF is not reproduced sufficiently. The problem of our LAE model is that UV brightest galaxies coincide with the Lyα brightest galaxies which may not be correct. Possible problems may be due to the properties of the simulation used, in particular the amount of SN energy powering winds, which determines the strength of outflows, or the prescription for star formation, our simplified dust model, or the lack of Lyα absorbing systems in the IGM in our simulation. High resolution hydrodynamical and radiative transfer simulations of galaxies could give inside into the correct modelling of escape fractions of Lyα and UV continuum photons from the galaxy. Furthermore they could enable us to derive also the respective escape fraction of ionizing photons and possible dependencies on H I mass, or Lyα and UV continuum escape fractions. Although a mass dependency of f_{esc} could theoretically alter the EW values of LAEs, it is questionable whether an f_{esc} increasing (decreasing) with halo mass causes a lower observed Lyα luminosity considering the intrinsic Lyα luminosity is reduced (enhanced) but the IGM transmission enhanced (reduced).

- **Lack of UV bright galaxies with low Lyα equivalent widths due to uncertainties in LAE and LBG observations?**
  Since our model for high-redshift LAEs is based on determining parameters by fitting to observed LBG UV LFs, LAE Lyα and UV LFs and imposing EW criterion for LAE selection, we have studied how sensitively the LAE-fraction of LBGs depends on different EW criteria and LBG UV LFs. For this purpose we have computed the probability distribution of the EW values at different UV luminosities and derived the LAE-fraction of LBGs ($X_{Ly\alpha}$). We have found that (1) the higher the value of the EW criterion, the lower the LAE-fraction of LBGs and the more likely it increases towards fainter UV luminosities; (2) the higher the number of LBGs, the lower the LAE-fraction of LBGs; and (3) the shallower the LBG UV LF, i.e. the higher the fraction of UV bright galaxies, the more $X_{Ly\alpha}$ increases towards lower UV luminosities. In this respect our LAE model is sensitive to the detailed course of the observed luminosity functions; uncertainties in the observations are possible to cause an overestimation of the EW values for UV bright galaxies. Nevertheless an essential problem of our model might be the coincidence of UV and Lyα bright galaxies, which may be caused by our approximate modelling of the escape fractions of Lyα and UV continuum photons, or the underlying hydrodynamical simulation. In the hydrodynamical simulation star formation in massive galaxies might be too high and the resulting stellar populations too young, and/or outflows from galaxies are too prevalent due to the high percentage of SN energy used to power outflows. Both effects result in an increase in the observed Lyα flux.

  Future work can include the analysis of the EW distribution produced by our LAE model at $z \simeq 5.7$ when IGM effects on the transmission are insignificant since the universe is assumed to be fully ionized. Furthermore applying our LAE model to a different hydrodynamical simulation could give hints whether the issue of the high EW values for UV bright galaxies arise from the hydrodynamical simulation. Nevertheless, a more detailed model to derive escape fractions of Lyα and UV continuum photons from the galaxy is needed. By following Yajima et al. (2014) who performed hydrodynamical simulations of galaxies and radiative transfer, escape fractions could be computed in detail.

Appendix

A

pCRASH

A.1 Method

In this Section we describe the detailed implementation of radiative transfer in pCRASH (**p**arallelized **C**osmological **RA**diative transfer **S**cheme for **H**ydrodynamics). First we elaborate on the description of different radiation sources (e.g. point sources, diffuse radiation) by photon packets; secondly we specify the propagation of the emitted photon packets, their absorption by neutral atoms and the subsequent updating of physical quantities (e.g. ionization fractions, temperature); and thirdly we describe the conditions for a sufficient numerical resolution in this Monte-Carlo scheme.

Point sources Each source is considered to be a point source with a luminosity L_s and a spectral shape $L_s(\nu_j)$. During the simulation time t_{sim} the total energy emitted by the source is

$$E_s = \int_0^{t_{sim}} L_s(t)\mathrm{d}t. \tag{A.1}$$

This energy is distributed into N_p photon packets, while the energy of each photon package is distributed into the different frequency bins ν_j according to the arbitrary spectrum $E(\nu_j)$, i.e. the number of photons of frequency ν_j is given by $N_{\gamma,j} = E(\nu_j)/h\nu_j$.

Diffuse radiation Recombinations produce diffuse ionizing radiation in the IGM. The implementation includes the following recombination processes

$$\mathrm{HII} + e^- \rightarrow \mathrm{HI} + h\nu \tag{A.2}$$
$$\mathrm{HeII} + e^- \rightarrow \mathrm{HeI} + h\nu \tag{A.3}$$
$$\mathrm{HeIII} + e^- \rightarrow \mathrm{HeII} + h\nu. \tag{A.4}$$

The diffuse radiation is also described by photon packets, whereas their propagation directions are in conformance with the angular distribution and their energy is distributed within the frequency bins according to the spectral shape of the diffuse radiation. Since the recombination is isotropic, propagation directions are randomly selected. In the local thermal equilibrium the spectral emissivity of an arbitrary recombining atom is described by (Mihalas, 1978; Osterbrock, 1989)

$$\eta_i \propto \sigma_i(\nu)\nu^3 e^{-(h\nu - h\nu_{th,i})/k_B T} \tag{A.5}$$

where σ_i is the photoionization cross-section and $h\nu_{th,i}$ the ionization potential of the recombined atom i, k_B is the Boltzmann konstant while T is the kinetic temperature of the recombining electrons.

To evaluate the intensity of the diffuse radiation the number of recombinations in each cells within a time step $t_k - t_{k-1} = \Delta t$ are calculated

$$\Delta N_{rec} = \alpha(T_{k-1}) n_{e,k-1} n_{i,k-1} \Delta t V_c \tag{A.6}$$

where $\alpha(T_{k-1})$ is the recombination coefficient at temperature T_{k-1} of the previous timestep $k-1$, $n_{e,k-1}$ and $n_{i,k-1}$ the respective electron and specie (i = HII, HeII, HeIII) number densities and V_c the volume of the cell. Thus the total number of recombinations is obtained $N_{rec,k} = N_{rec,k-1} + \Delta N_{rec}$. At fixed time intervals Δt_{rec} the number of recombinations in each cell is checked whether it excess a certain threshold. If $N_{rec,k} > f_{rec} N_i$ a packet with $N_\gamma = N_{reck}$ photons is emitted and $N_{rec,k}$ is set to zero. Here N_i describes the number of atoms of specie i and f_{rec} is an adjustable parameter.

In case of recombination, the relation $\alpha_1(T)/\alpha$ is calculated, whereas $\alpha_1(T)$ represents the recombination to the ground level. If recombination occurs to the ground level, the sepctrum for all three re-emission processes are computed. Since for hydrogen only a recombination to the first energy level produces an ionizing photon, only these recombinations are taken into account. For helium the following processes are considered: For HeI $2s \rightarrow 1s$ (19.8eV) and $2p \rightarrow 1s$ (21.2eV) and for HeII $2p \rightarrow 1s$ (40.7eV).

Propagation of photon packets

For each photon packet a propagation direction (r, θ, ϕ) is determined according to the angular emission probability distribution function of the source. Starting at the emission cell, i.e. the source location, (x_E, y_E, z_E) the packet is propagated along

$$x = x_E + r \sin\theta \cos\phi \tag{A.7}$$
$$y = y_E + r \sin\theta \sin\phi \tag{A.8}$$
$$z = z_E + r \cos\theta. \tag{A.9}$$

In each cell c that the photon packet crosses, the length of its path δl and its optical depth calculated

$$\tau_c(\nu_j) = \sum_{i=\mathrm{HI,HeI,HeII}} \tau_i(\nu_j) = \sum_i \delta l \times \sigma_i(\nu_j) n_i \tag{A.10}$$

where the contributions of the different species HI, HeI and HeII are summed up. With help of the optical depth $\tau_c(\nu_j)$ the number of absorbed photons in each frequency bin ν_j are given by

$$N^{(c)}_{A,\gamma}(\nu_j) = N^{(c-1)}_{T,\gamma}(\nu_j) \left[1 - e^{-\tau_c(\nu_j)}\right] \tag{A.11}$$

with $N^{(c)}_{A,\gamma}(\nu_j)$ being the number of absorbed photons in the current cell c and $N^{(c-1)}_{T,\gamma}(\nu_j)$ the number of photons transmitted in the previous cell $c-1$ to the current cell c. In a next step the absorbed photons from each frequency bin $N_{A,\gamma}(\nu_j)$ are distributed among the absorber species i. The fraction of absorbed photons that is assigned to specie i is proportional to the corresponding pabsorption probability of specie i

$$P_i(\nu_j) = 1 - e^{-\tau_i(\nu_j)} \tag{A.12}$$

respective to the total probability

$$P_c(\nu_i) = \sum_i P_i(\nu_j). \tag{A.13}$$

Thus a photon packet ionizes a number of atoms of specie i given by

$$N_{A_i,\gamma}(\nu_j) = N_{A,\gamma} \frac{P_i(\nu_j)}{P_c(\nu_j)} \tag{A.14}$$

and the ionization fraction in the considered cell is increased by

$$\Delta\chi_{i^+} = \frac{\sum_j N_{A_i,\gamma}(\nu_j)}{N_i} \tag{A.15}$$

where i^+ is the singly ionized state of specie i (HI, HeI, HeII) and N_i is the total number of nuclei of the i^{th} specie in the current cell. If the number of ionization events of specie i exceed the number of present non-ionized atoms (HI, HeI, HeII), the remaining photons stay in the photon packet and propagate further. The photon packet is propagated to the next cell and so forth until it is completely absorbed or leaves the simulation box. In case of periodic boundaries it exits the simulation box and re-enters on the other side.

Updating physical quantities

In each cell the time evolution of the ionization fractions $\chi_{\rm HII} = n_{\rm HII}/n_{\rm H}$, $\chi_{\rm HeII} = n_{\rm HeII}/n_{\rm He}$, $\chi_{\rm HeIII} = n_{\rm HeIII}/n_{\rm He}$ and the gas temperature T are followed by coupled rate equations:

$$\frac{{\rm d}n_{\rm HII}}{{\rm d}t} = \Gamma_{\rm HI} n_{\rm HI} + \beta_{\rm HI} n_e n_{\rm HI} - \alpha_{\rm HII} n_e n_{\rm HII} \tag{A.16}$$

$$\frac{{\rm d}n_{\rm HeII}}{{\rm d}t} = \Gamma_{\rm HeI} n_{\rm HeI} + \beta_{\rm HeI} n_e n_{\rm HeI} - \alpha_{\rm HeII} n_e n_{\rm HeII} - \beta_{\rm HeII} n_e n_{\rm HeII} + \alpha_{\rm HeIII} n_e n_{\rm HeIII} - \Gamma_{\rm HeII} n_{\rm HeII} \tag{A.17}$$

$$\frac{{\rm d}n_{\rm HeIII}}{{\rm d}t} = \Gamma_{\rm HeII} n_{\rm HeII} + \beta_{\rm HeII} n_e n_{\rm HeII} - \alpha_{\rm HeIII} n_e n_{\rm HeIII} \tag{A.18}$$

$$\frac{{\rm d}T}{{\rm d}t} = \frac{2}{3 k_B n} \left[k_B T \frac{{\rm d}n}{{\rm d}t} + H(T, \chi_i) - \Lambda(T, \chi_i) \right]. \tag{A.19}$$

While the ionization fractions are determined by the photoionization rates Γ_i, the collisional ionization rates β_i and the recombination rates α_i, the evolution of the temperature is determined by various heating $H(T, \chi_i)$ and cooling $\Lambda(T, \chi_i)$ processes and the variation of the free particles ${\rm d}n/{\rm d}t$.

By solving the rate equations A.19 these quantities are updated each time when a photon packet crosses the cell. Due to the statistical description of the photon emission and absorption processes the integration time-step Δt is not constant and depends on the time passed since a photon packet has crossed the cell. Thus Δt can become larger than the characteristic timescales of ionization, recombination and cooling processes, $\Delta t > t_{min} = min[t_{rec}, t_{coll}, t_{cool}]$. In this case the integration is split into more steps in such a way as the resulting time-step is smaller than any characteristic time-scale.

While collisional ionization, recombination and cooling are treated as continuous processes, photoionization and photoheating are discrete processes in this implementation due to the discretization of the radiation filed into photon packets. Nevertheless, to recover continuous quantities the respective rates are evaluated by means of the discretized contributions. Hence, the changes in the ionization fractions due to photoionization are given by

$$\Delta\chi_{\rm HII} = \Gamma_{\rm HI} \frac{n_{\rm HII}}{n_{\rm H}} \Delta t = \frac{\sum_j N_{A_{\rm HI},\gamma}(\nu_j)}{N_{\rm H}} \tag{A.20}$$

$$\Delta\chi_{\rm HeII} = \Gamma_{\rm HeI} \frac{n_{\rm HeII}}{n_{\rm He}} \Delta t = \frac{\sum_j N_{A_{\rm HeI},\gamma}(\nu_j)}{N_{\rm He}} \tag{A.21}$$

$$\Delta\chi_{\rm HeIII} = \Gamma_{\rm HeII} \frac{n_{\rm HeIII}}{n_{\rm He}} \Delta t = \frac{\sum_j N_{A_{\rm HeII},\gamma}(\nu_j)}{N_{\rm He}} \tag{A.22}$$

and in temperature due to photoheating

$$\Delta T_{i^+} = \frac{2}{3 k_B n_c} \frac{\sum_j N_{A_i,\gamma}(h\nu_j - h\nu_{th,i})}{V_c} \tag{A.23}$$

and the variation of free particles by

$$\Delta T_n = -\frac{2}{3} T_c \frac{\Delta n_e}{n_c} \tag{A.24}$$

$$\frac{\Delta n_e}{n_c} = \Delta\chi_e = f_H \times \Delta\chi_{\rm HII} + f_{He} \times (\Delta\chi_{\rm HeII} + 2\Delta\chi_{\rm HeIII}) \tag{A.25}$$

where $\nu_{th,i}$ is the ionization threshold for photoionization of specie i, n_c is the number density of free particles and Δn_e its variation.

Numerical resolution

To follow the ionization and temperature fields adequately, several numerical conditions must be fulfilled. In the following N_p is the number of photons emitted per source, N_c^3 the number of grid cells, N_s the number of sources, N_γ the number of photons in a packet and N_i the mean number of atoms in each cell:

- Each cell needs to be crossed and updated a sufficient number of times to ensure an accurate sampling of the frequency and time distribution. The mean number of updates during a simulation is given by

$$N_{cr} = \frac{N_s N_p f_d N_c}{N_c^3} = f_c \frac{N_s N_p}{N_c^2}. \tag{A.26}$$

  where f_c represents a parameter ranging from N_c^{-1} to 1: $f_c \approx 1$ for an optically thin medium and $f_c \approx N_c^{-1}$ for an optically thin medium.

- Δt must be smaller than the time scales of the processes that are treated as continuous, i.e. recombination, collisional ionization and cooling.

$$\langle \Delta t \rangle = \frac{t_{sim}}{N_{cr}} << t_{min} \tag{A.27}$$

- The ratio N_γ / N_i reflects/depicts the mean number of photon packets that are necessary to ionize a cell. The lower this ratio is, the better is the continuity of photoionization and photoheating represented.

A.2 Clumping Factor

The gas density ϱ at position $\vec{r_i}$ of particle i is estimated by the SPH algorithm. The corresponding number density is computed by $n = X\varrho/m_p$, where X is the primordial abundance of the subject specie and m_p the proton mass. If we assign a volume $V_i \approx m_i/\varrho_i$ to particle i, we can express the terms $\langle n^2 \rangle$, $\langle n \rangle$ and the total volume V, with N_{part} being the total number of particles in V, as follows (assuming all particles have the same mass $m_i = m$)

$$\begin{aligned}
\langle n^2 \rangle &= \sum_i^{N_{part}} n_i^2 V_i = \sum_i^{N_{part}} \left(\frac{X\varrho_i}{m_p}\right)^2 \frac{m_i}{\varrho_i} = \sum_i^{N_{part}} \left(\frac{X}{m_p}\right)^2 \varrho_i m_i = \sum_i^{N_{part}} \frac{m_i X^2}{m_p^2} \frac{m_p}{X} n_i \\
&= \sum_i^{N_{part}} \frac{m_i X}{m_p} n_i \overset{m_i=m}{=} \frac{mX}{m_p} \sum_i^{N_{part}} n_i
\end{aligned} \tag{A.28}$$

$$\langle n \rangle = \sum_i^{N_{part}} n_i V_i = \sum_i^{N_{part}} \frac{X\varrho_i}{m_p} \frac{m_i}{\varrho_i} = \sum_i^{N_{part}} \frac{m_i X}{m_p} \overset{m_i=m}{=} \frac{mX}{m_p} N_{part} \tag{A.29}$$

$$V = \sum_i^{N_{part}} V_i = \sum_i^{N_{part}} \frac{m_i}{\varrho_i} = \sum_i^{N_{part}} \frac{m_i X}{m_p} \frac{1}{n_i} \overset{m_i=m}{=} \frac{mX}{m_p} \sum_i^{N_{part}} \frac{1}{n_i}, \tag{A.30}$$

and derive the clumping factor as

$$\begin{aligned}
C &= \frac{\langle n^2 \rangle}{\langle n \rangle^2} V = \frac{\frac{mX}{m_p} \sum_i^{N_{part}} n_i}{\left(\frac{mX}{m_p} N_{part}\right)^2} \left(\frac{Xm}{m_p} \sum_i^{N_{part}} \frac{1}{n_i}\right) \\
&= \frac{1}{N_{part}^2} \sum_i^{N_{part}} n_i \sum_i^{N_{part}} \frac{1}{n_i}.
\end{aligned} \tag{A.31}$$

Appendix

B

LAE visibility

B.1 Cosmic variance

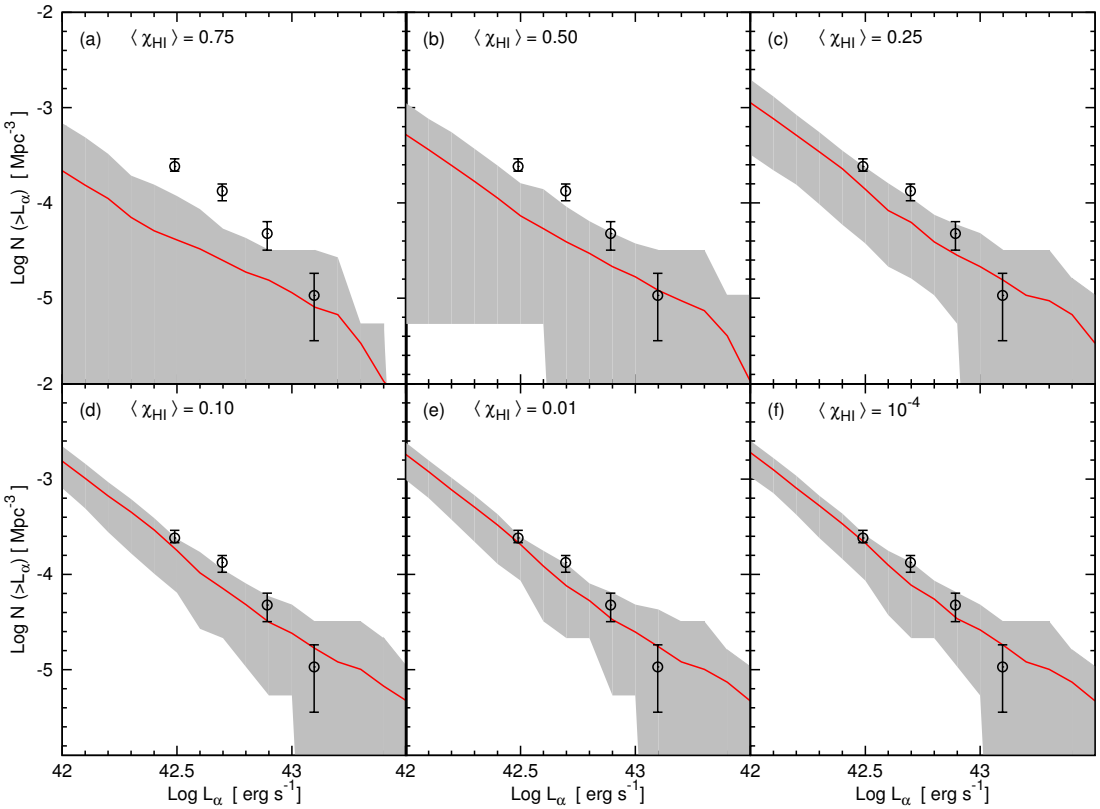

Figure B.1: Simulated cumulative LAE LFs and the associated cosmic variance for homogeneous dust ($f_\alpha/f_c = 0.68$) and $f_{\rm esc} = 0.05$. The panels show the results for different neutral hydrogen fractions, $\langle \chi_{HI} \rangle \simeq$ 0.90, 0.75, 0.50, 0.25, 0.10, 0.01, 10^{-4}, as marked. In each panel, the solid red line shows the LAE LF for the whole simulation box of volume $(80h^{-1}{\rm Mpc})^3$ with the gray shaded areas showing the associated cosmic variance obtained by splitting the entire simulation box into 8 equal sub-volumes. In each panel, the open circles show the Lyα LFs observed by Kashikawa et al. (2011). As the IGM becomes more ionized, the value of T_α increases in all sub-volumes, leading to a decrease in the cosmic variance at the faint-end of the LF; the variance at the bright-end arises due to the low numbers of massive galaxies found in any given sub-volume.

In Fig. B.1 we show the cosmic variance associated with the simulated LAE Lyα LFs. The cosmic variance is estimated by computing the LAE Lyα LFs for 8 sub-volumes of our simulation volume, such that each sub-volume is 1.87×10^5 Mpc^3 and thus comparable to the volume observed by Kashikawa et al. (2011). As $\langle \chi_{HI} \rangle$ evolves from an IGM which is predominantly neutral at $\langle \chi_{HI} \rangle \simeq 0.75$ to one wherein reionization is complete ($\langle \chi_{HI} \rangle \simeq 10^{-4}$), the value of T_α increases in all sub-volumes, leading to a decrease in the cosmic variance at the faint-end of the LF; the variance at the bright-end arises due to few objects being massive/luminous enough to occupy these bins in any given sub-volume.

Appendix

C

LAE clustering & duty cycle

C.1 Dependence of clustering on Line-Of-Sight depth and Field-of-View

The angular correlation function (ACF) depends on the sizes of the volumes that are considered. Firstly, as the ACF is the 3D correlation function projected along the line of sight, it depends substantially on the depth of the volume along the line of sight. With increasing depth more galaxies that are part of clusters and sheets are projected on the plane, leading to a more homogeneous distribution. For a distribution of galaxies that is on average homogeneous, Peebles (1980) has shown that the correlation function depends on the depth D as

$$w(\theta) \quad = \quad \frac{1}{D} W(\theta D) \tag{C.1}$$

where W is the intrinsic correlation function. As can be seen from the solid (depth 30 Mpc/h) and dashed (depth 80 Mpc/h) lines in Figure C.1 we also find this increasing trend of $w(\theta)$ with decreasing

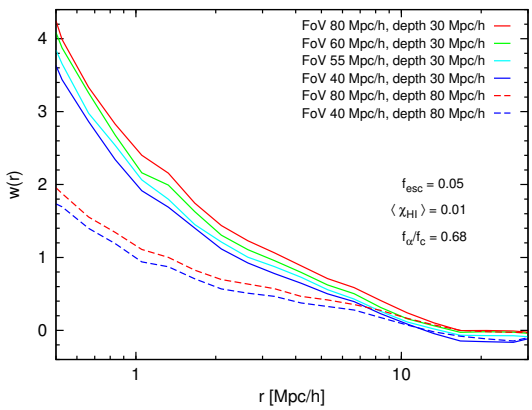

Figure C.1: Angular correlation function of the LAEs for $f_{esc} = 0.05$ and $\langle \chi_{HI} \rangle \simeq 0.01$, assuming depth of 30 Mpc/h (solid) or 80 Mpc/h (dashed) along the line of sight and varying field of view (colors). Due to the projection along the lineof sight the angular correlation function increases for decreasing depths. A declining field of view causes the angular correlation function to be increasingly subject to cosmic variance, leading to more homogeneous distributions.

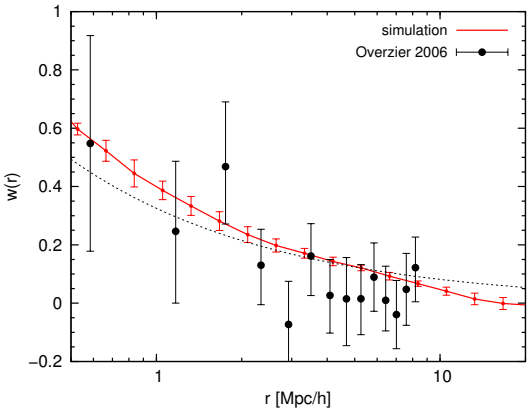

Figure C.2: Angular correlation function of the LBGs. Red line shows the ACF for the identified LBGs in the hydrodynamical simulation (taking the whole 80 Mpc/h simulation box into account) and error bars tha variance across the different realizations, while black points show observations and the black dotted line the respective fit by Overzier et al. (2006).

depth D. Secondly, the ACF depends on the field of view (FoV) for areas that cover cosmic variance not sufficiently. Although the ACF does not change for sufficient large FoVs, for non-sufficient FoVs the ACF declines for decreasing FoV. As the FoV becomes so small that only a clustered region or a void is detected, the distribution appears more homogeneous and the amplitude of the ACF declines respectively (see solid lines in Fig. C.1).

C.2 LBG clustering

In Figure C.2 we show the angular correlation function for all LBGs identified in the hydrodynamical simulation with $M_{UV} < -17$, together with the observations by Overzier et al. (2006). Since the redshifts of the observed LBGs lie between $z \simeq 5.5$ and 6.5, we estimated the the ACF by taking the full 80 Mpc/h simulation box into account. Computing the mean ACF and its variance from the mock catalogues along the different direction $\hat{x}$, $\hat{y}$ and $\hat{z}$, we find that the ACF increases towards smaller scales, i.e. the distribution of the LBGs on smaller scales is more clumpy and less homogeneous than on larger scales, which is in agreement with the observations.

C.3 LAE clustering

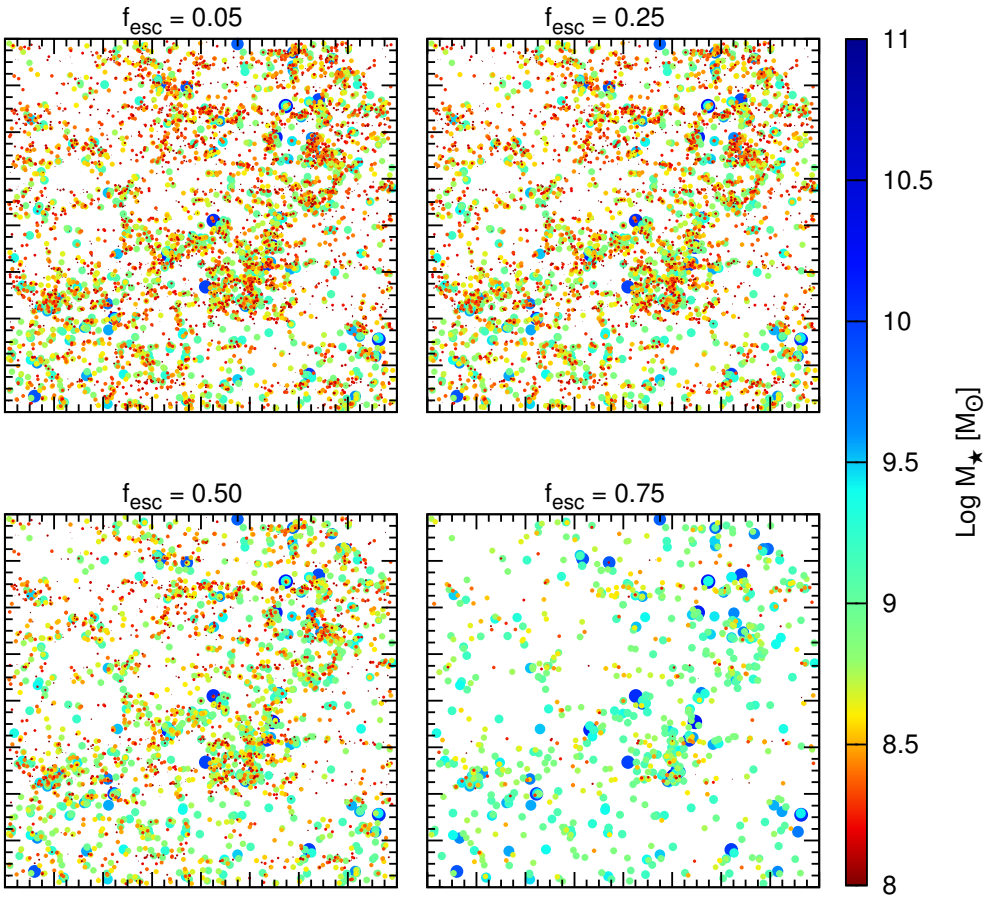

Figure C.3: Spatial distribution of the LAEs for $f_\alpha/f_c = 0.68$ and $\langle \chi_{HI} \rangle \simeq 0$ of the 80Mpc/h box projected onto the x-y plane. Each panel shows the identified LAEs a choosen escape fractions $f_{esc} = 0.05$, 0.25, 0.5 and 0.75. The higher f_{esc}, the lower the number of LAEs. The stellar mass of the LAEs is encoded in the color and the size of the points in the plot.

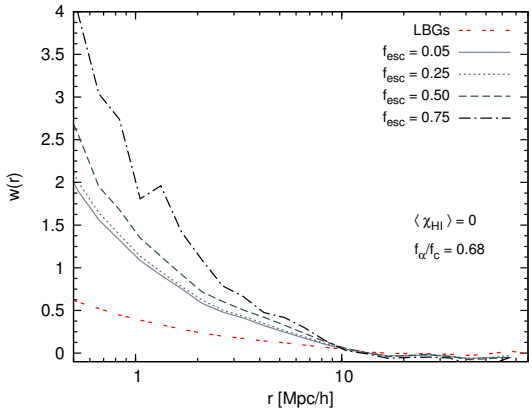

Figure C.4: Angular correlation function of the LAEs for $f_\alpha/f_c = 0.68$ and $\langle \chi_{HI} \rangle \simeq 0$, assuming a depth of 30 Mpc/h and a FoV of $\sim 3 \times 10^4 \mathrm{Mpc}^2/\mathrm{h}^2$. Solid, dotted, dashed, dash-dotted lines show the ACFs for the different escape fractions $f_{esc} = 0.05$, 0.25, 0.5 and 0.75. The higher f_{esc}, the stronger the correlation on small scales; less LAEs are identified for increasing f_{esc}.

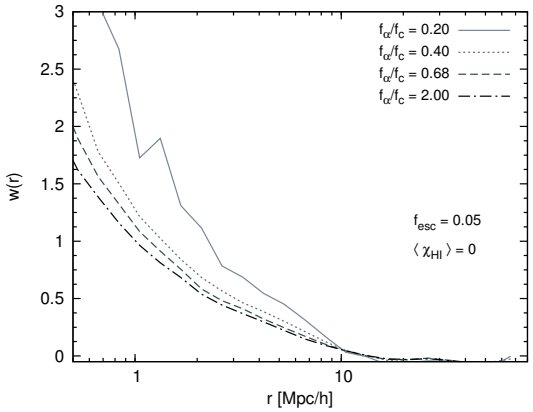

Figure C.5: Angular correlation function of the LAEs for $f_{esc} = 0.05$ and $\langle \chi_{HI} \rangle \simeq 0$, assuming a depth of 30 Mpc/h and a FoV of $\sim 3 \times 10^4 \mathrm{Mpc}^2/\mathrm{h}^2$. Solid, dotted, dashed, dash-dotted lines show the ACFs for the different Lyα escape fractions $f_\alpha/f_c = 0.4$, 0.6, 0.68 and 2.0. The lower f_α/f_c, the stronger the correlation on small scales; less LAEs are identified for decreasing f_α/f_c.

C.3.1 Escape fraction of ionizing photons f_{esc}

To understand the effect of the escape fraction of ionizing photons (f_{esc}) on the ACF, we generate 36 mock catalogues (12 along each of x, y, z directions) for over-lapping volumes comparable to that observed by Kashikawa et al. (2006), corresponding to a redshift distance $\Delta z \sim 0.1$ at $z \simeq 6.5$ and a field of view (FoV) of $\sim 3 \times 10^4 \mathrm{Mpc}^2/\mathrm{h}^2$. The mean ACFs are calculated using the Landy-Szalay estimator with respect to the mean LAE number density $\overline{n}$ of the complete simulation box. In Fig. C.4 we assume the IGM to be completely ionized ($T_\alpha = 1$) and the ratio between the escape fraction of Lyα and UV continuum photons to be $f_\alpha/f_c = 0.68$; we show the ACFs for different values for f_{esc}. We find that the amplitude of the ACF increases towards higher f_{esc} values. In order to understand this trend, we plot the positions (projected on the x-y plane) of all LAEs in the simulation box in Fig. C.3; each galaxy is represented by a point which is colour-coded and sized by its stellar mass. From Fig. C.3 we find that the mean stellar mass of the LAEs increases with rising f_{esc}. As f_{esc} increases, the intrinsic Lyα luminosity decreases and only the most luminous (massive) galaxies are identified as LAEs, leading to an increasing amplitude of the ACF (Zehavi et al., 2005; Wake et al., 2011): the higher the mean stellar mass of the LAEs, the stronger the clustering.

C.3.2 Ratio of Lyα and UV continuum escape fraction f_α/f_c

For the same mock catalogues we assume a completely ionized IGM ($T_\alpha = 1$) and $f_{esc} = 0.05$, and vary the value of f_α/f_c whereas f_c remains the same. Since the Lyα luminosity is proportional to $f_\alpha(1 - f_{esc})$, we find the opposite trend compared to that of f_{esc}: with increasing values f_α/f_c the amplitude of the ACFs decreases.

C.3.3 Spatial distribution of LBGs and LAEs for best fit models

For our best fit models we show ths spatial distribution of the identified LAEs and LBGs in Fig. C.6; the galaxies within our 80 Mpc/h simulation box have been projected on the x-y plane. Grey points represent LBGs, while colored points show the position of the LAEs. The size of the point encodes the halo masses of the respective galaxies and the color the stellar masses of the LAEs. In each of the panels we note that the distribution of LBGs is more homogeneous than the distribution of LAEs which is in agreement with the computed correlation functions (shown in Fig. 5.1). We find that the distribution of LAEs are very similar for all best fit cases; thus their angular correlation function are also in good agreement (see Fig. 5.1).

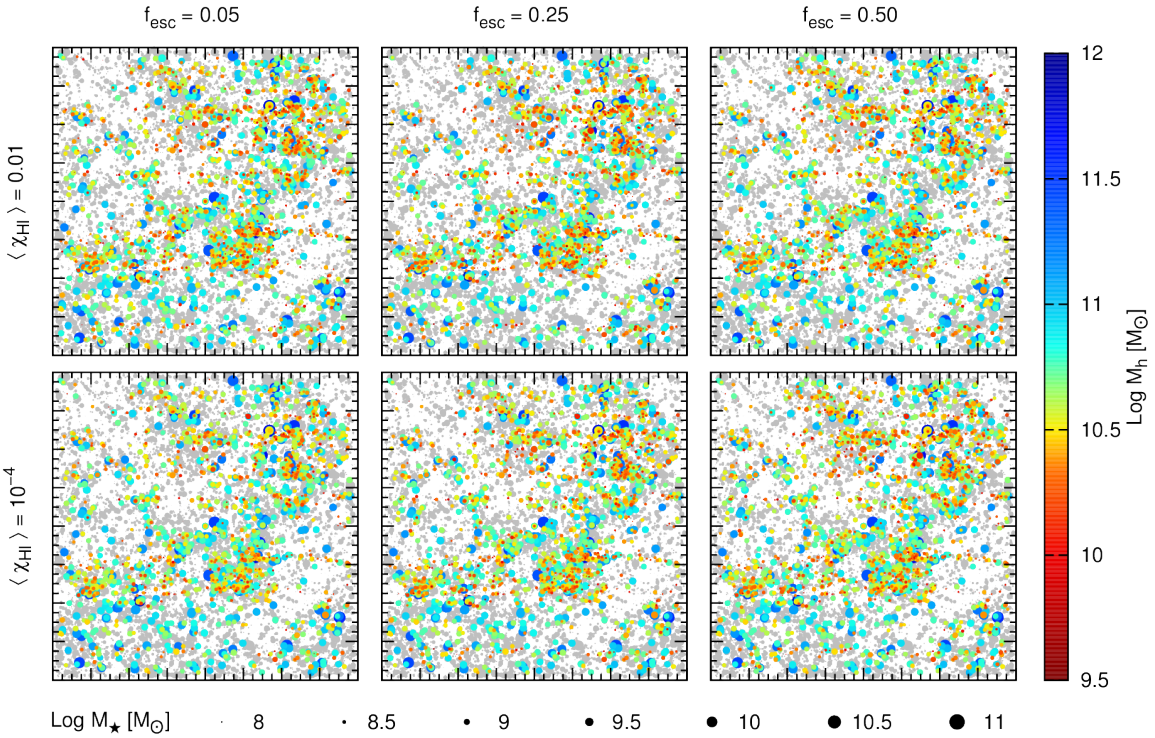

Figure C.6: Spatial distribution of the LAEs for $f_{esc} = 0.05$, 0.25, 0.5 and $\langle \chi_{HI} \rangle \simeq 10^{-4}$, 0.01, 0.1 of the 80Mpc/h box projected onto the x-y plane. Colored point represent LAEs and their stellar and halo mass are encoded in the size and colour of the points in the plot. LBGs are shown as gray points; the pointsize encodes their stellar mass.

C.4 Time evolution & duty cycle of LBGs w/o Lyα emission

In this section we comment on details on the buildup of stellar mass, Lyα and UV luminosity of galaxies and their Lyα equivalent width, whereas we focus on the time evolution of the *intrinsic* luminosities for galaxies in three final stellar mass bins: $10^{7.9-8.1}\,M_\odot$, $10^{8.9-9.1}\,M_\odot$, $10^{9.9-10.1}\,M_\odot$ (see also Sec. 5.4).

C.4.1 Stellar mass, Lyα and UV luminosities

From the black lines in the first row in Fig. 5.3 we find that galaxies gradually build up their stellar mass. Since emission scales with stellar mass, the UV (blue lines) and Lyα luminosity (red lines) increase while the galaxies grow. In contrast to the time evolution of the stellar mass we find that the UV and especially the Lyα luminosity are subject to larger variations: Each time a new star particle is formed our model assumes the occurrence of a starburst; as the luminosity of a starburst decays quickly, its Lyα and UV luminosity is only 7% and 50% of the initial value after 6 Myr, respectively. Thus with each star particle that is formed, the luminosity increases gradually but with a peak in time, leading to the larger variations for UV and Lyα luminosities. The increased sensitivity of the Lyα luminosity with respect to the age of stellar particles compared to the UV luminosity lies in the substantial changes of a starburst spectrum with time. While the spectrum is hard in the beginning and exhibits a large number of ionizing photons, it becomes softer and shows lower numbers of ionizing photons as time proceeds. Since the number of ionizing photons considers all photons with $h\nu \geq 13.6$eV, the decrease is higher than considering the non ionizing UV at 1505Å.

C.4.2 Lyα equivalent widths

In the lower row of Figure 5.3 we show the time evolution of the intrinsic (yellow) and observed (green) Lyα equivalent width ($EW = L_\alpha / L_c$). The shaded areas depict the variance from the mean EW within the respective stellar mass bin. We find that the mean EW increases with stellar mass.

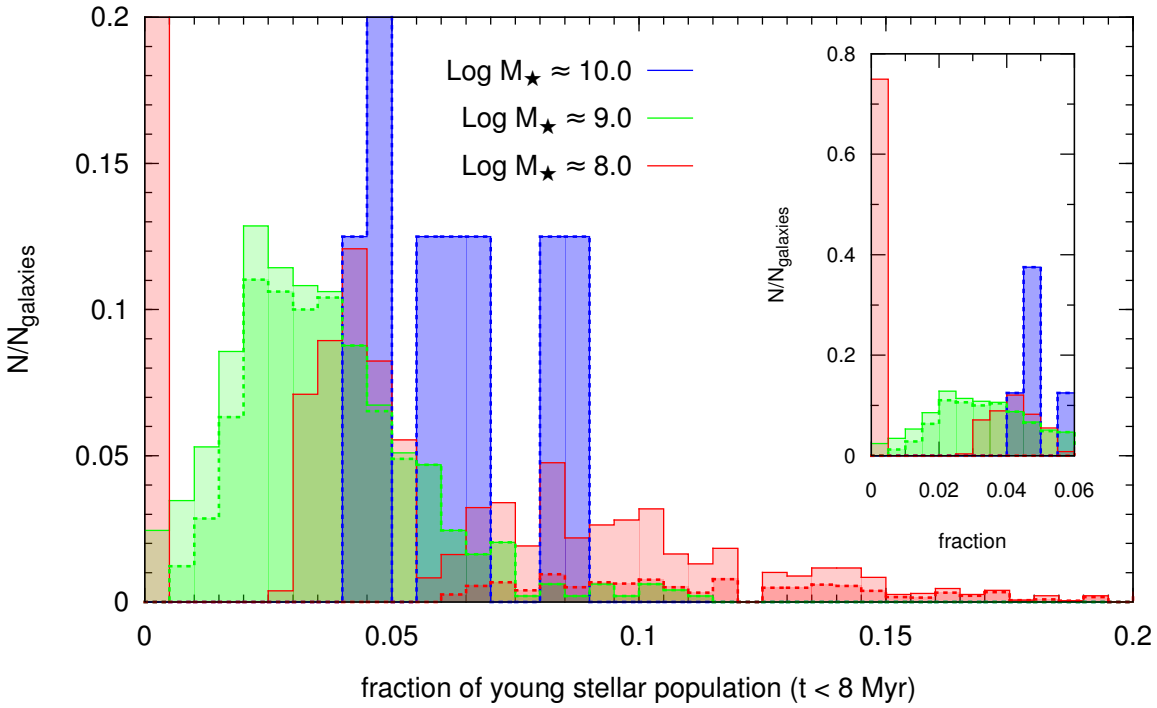

Figure C.7: Distribution of the fraction of young stars ($t < 8$ Myrs) for galaxies in the stellar mass bins $10^{7.9-8.1}\,M_\odot$ (red), $10^{8.9-9.1}\,M_\odot$ (green) and $10^{9.9-10.1}\,M_\odot$ (blue). The distributions are shown for all galaxies (solid lines) and LAEs (dashed lines), whereas $N_{galaxies}$ represents the total number of galaxies in the respective stellar mass bin.

The EW of each galaxy depends strongly on the age of the stellar population or more precisely it increases with a rising fraction of young stellar population ($t < 8$ Myr). Although small galaxies with stellar masses of $\sim 10^8\,M_\odot$ possess either very old stellar populations or a large fraction of young stars, their mean EW is lower than of the large galaxies ($10^{10}\,M_\odot$) that have smaller but also non-zero fractions of young stellar populations. Thus the increase in EW with stellar mass is directly linked to a rising mean fraction of young stellar population in galaxies.

Furthermore, we notice that the variance of the EW changes for different stellar mass bins. While it is similarly high at early times, it decreases to lower values for galaxies with higher stellar masses at later times. This evolution and the different values of variances for different stellar masses are due to different distributions of the fractions of young stellar populations. When the first galaxies and thus stars form, young stellar population determine their luminosity. Due to their starburst character their luminosities can vary considerably as new stars form. Low stellar mass galaxies show either a very low or a high fraction of young stellar population, as they either have already formed stars in the past or they are in the phase of building up stellar mass. Gradually as galaxies grow and form more stellar mass, their fraction of young stellar population at the high end declines since they also posses older stellar populations. Considering this evolution we can understand the different values of variances for different stellar masses: for $10^8\,M_\odot$ the stellar mass is low enough to exhibit a bimodal distribution but their overall distribution of fractions of young stellar populations also decreases with time, leading to a decline of the EW variance. While during the first few 100 Myrs the EW variance decreases considerably, its decrease saturates as the considered galaxies reach their final stellar mass. This trend applies also to higher stellar masses but their EW variances decrease to lower values as their final stellar mass is higher and thus their distribution of fraction of young stellar population decreases to lower values. Furthermore their distribution also sharpens, leading to more similar stellar mass averaged ages of the galaxies.

C.4.3 Life time as LBG or LAE

We use the time evolution of the *intrinsic* UV luminosity that we have computed for each galaxy in the simulation to determine the fraction of time it has spend as a LBG ($M_{UV} \leq -17$), f_{LBG},

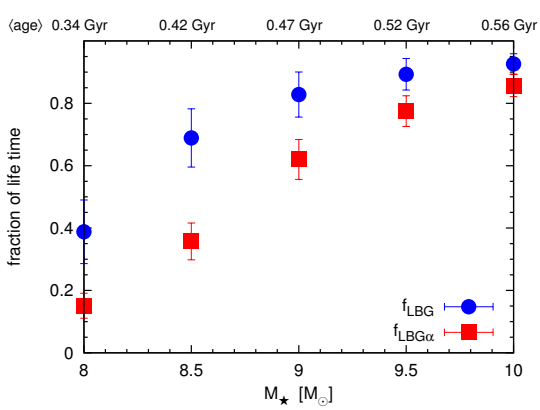

Figure C.8: Fraction of life time that galaxies spend as LBGs (f_{LBG}, blue filled circles) or as LBGs and LAEs ($f_{LBG\alpha}$, red filled squares) as a function of the stellar mass. The fractions are computed as the mean of the galaxies within mass bins k ranging from $10^{k-0.1}\,M_\odot$ to $10^{k+0.1}\,M_\odot$ for $k = 8, 8.5, 9, 9.5, 10$. Error bars show the standard deviations of the mean values. On the top horizontal axis the mean age of the selected galaxies is denoted.

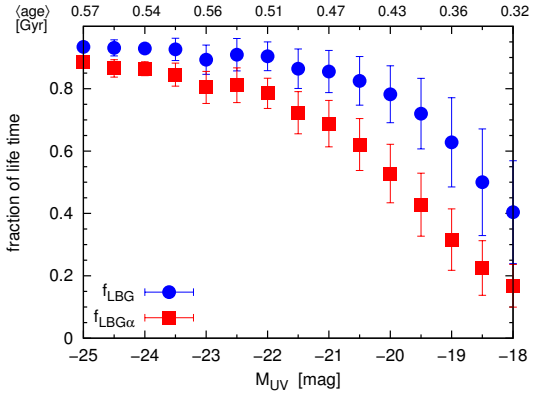

Figure C.9: Fraction of life time that galaxies spend as intrinsic LBGs (f_{LBG}, blue filled circles) or as intrinsic LBGs and LAEs ($f_{LBG\alpha}$, red filled squares) as a function of the intrinsic UV luminosity. The fractions are computed as the mean of the galaxies within M_{UV} bins k ranging from $k - 0.25$ to $k + 0.25$ for $k = -25$ .. -18 in steps of 0.5. Error bars show the standard deviations of the mean values. On the top horizontal axis the mean age of the selected galaxies is denoted.

until $z \simeq 6.6$. By analogy the fraction of time a galaxy spends as an LBG ($M_{UV} \leq -17$) and LAE ($L_\alpha \geq 10^{42}$erg s^{-1} and EW$\geq$ 20Å), $f_{LBG\alpha}$, simultaneously is deduced from the time evolution of its *intrinsic* Lyα luminosity and *intrinsic* EW. As for the time evolution of the UV and Lyα luminosities, we show the mean values of f_{LBG} and $f_{LBG\alpha}$ for different final stellar mass bins in Figure C.8. First we note that the mean age of galaxies is increasing with stellar mass, i.e. massive galaxies are older. Secondly, we find that the mean fraction of time a galaxy spends as a LBG (f_{LBG}) increases with stellar mass (cf. Fig. C.8) and UV luminosity (cf. Fig. C.9). Since a galaxy needs to exceed a critical UV luminosity, $M_{UV} \leq -17$, to be identified as a LBG and the UV luminosity correlates with the stellar mass of the galaxies (see Section C.4), a galaxy is not a LBG for its first part of life time but as soon as it becomes massive enough (roughly about $10^{7.5}\,M_\odot$) it is detectable as a LBG. As larger galaxies are older, they have spent more time as a LBG (having passed the UV luminosity (mass) limit) leading to higher f_{LBG}. Due to the evolution in the stellar population there is not a sharp mass limit above which a galaxy is a LBG but a mass range in which a galaxy is switching between the states of being and not being a LBG. Thirdly, the fraction of time a LBG is also detectable as a LAE rises with stellar mass as well, i.e. galaxies with higher stellar mass are more likely to be identified as LAEs. The explanation for this trend is in line with the rising trend for f_{LBG} just that the additional selection criteria, $L_\alpha \geq 10^{42}$erg s^{-1} and EW$\geq$ 20Å, apply and the critical stellar mass is increased to a higher value of about $10^8\,M_\odot$. Thus $f_{LBG\alpha}$ is always smaller than f_{LBG}, implying that LAEs might be a luminous subsample of LBGs. An interesting fact is that $f_{LBG\alpha}$ approaches f_{LBG} towards higher stellar masses: As the time spent as non-LAE is roughly similar for all galaxies, more massive galaxies have been a LAE for a longer time while less massive galaxies just turned into LAEs, leading to higher $f_{LBG\alpha}$ or lower $f_{LBG\alpha}$ respectively.

Bibliography

T. Abel, G. L. Bryan, and M. L. Norman. The Formation of the First Star in the Universe. *Science*, 295:93–98, January 2002. doi: 10.1126/science.295.5552.93.

A. Aguirre, L. Hernquist, J. Schaye, N. Katz, D. H. Weinberg, and J. Gardner. Metal Enrichment of the Intergalactic Medium in Cosmological Simulations. ApJ, 561:521–549, November 2001. doi: 10.1086/323370.

A. Aguirre, J. Schaye, L. Hernquist, S. Kay, V. Springel, and T. Theuns. Confronting Cosmological Simulations with Observations of Intergalactic Metals. ApJ, 620:L13–L17, February 2005. doi: 10.1086/428498.

K. Ahn, P. R. Shapiro, I. T. Iliev, G. Mellema, and U.-L. Pen. The Inhomogeneous Background Of H_2-Dissociating Radiation During Cosmic Reionization. ApJ, 695:1430–1445, April 2009. doi: 10.1088/0004-637X/695/2/1430.

K. Ahn, I. T. Iliev, P. R. Shapiro, G. Mellema, J. Koda, and Y. Mao. Detecting the Rise and Fall of the First Stars by Their Impact on Cosmic Reionization. ApJ, 756:L16, September 2012. doi: 10.1088/2041-8205/756/1/L16.

S. S. Ali, S. Bharadwaj, and J. N. Chengalur. Foregrounds for redshifted 21-cm studies of reionization: Giant Meter Wave Radio Telescope 153-MHz observations. MNRAS, 385:2166–2174, April 2008. doi: 10.1111/j.1365-2966.2008.12984.x.

M. Ando, K. Ohta, I. Iwata, M. Akiyama, K. Aoki, and N. Tamura. Deficiency of Large Equivalent Width Lyα Emission in Luminous Lyman Break Galaxies at z $\sim$ 5-6? ApJ, 645:L9–L12, July 2006. doi: 10.1086/505652.

D. Aubert and R. Teyssier. A radiative transfer scheme for cosmological reionization based on a local Eddington tensor. MNRAS, 387:295–307, June 2008. doi: 10.1111/j.1365-2966.2008.13223.x.

J. M. Bardeen, J. R. Bond, N. Kaiser, and A. S. Szalay. The statistics of peaks of Gaussian random fields. ApJ, 304:15–61, May 1986. doi: 10.1086/164143.

R. Barkana and A. Loeb. The Photoevaporation of Dwarf Galaxies during Reionization. ApJ, 523: 54–65, September 1999. doi: 10.1086/307724.

R. Barkana and A. Loeb. In the beginning: the first sources of light and the reionization of the universe. Phys. Rep., 349:125–238, July 2001. doi: 10.1016/S0370-1573(01)00019-9.

R. Barkana and A. Loeb. A Method for Separating the Physics from the Astrophysics of High-Redshift 21 Centimeter Fluctuations. ApJ, 624:L65–L68, May 2005. doi: 10.1086/430599.

J. Barnes and G. Efstathiou. Angular momentum from tidal torques. ApJ, 319:575–600, August 1987. doi: 10.1086/165480.

M. R. Bate and A. Burkert. Resolution requirements for smoothed particle hydrodynamics calculations with self-gravity. MNRAS, 288:1060–1072, July 1997.

N. Battaglia, H. Trac, R. Cen, and A. Loeb. Reionization on Large Scales. I. A Parametric Model Constructed from Radiation-hydrodynamic Simulations. ApJ, 776:81, October 2013. doi: 10.1088/0004-637X/776/2/81.

G. D. Becker, J. S. Bolton, P. Madau, M. Pettini, E. V. Ryan-Weber, and B. P. Venemans. Evidence of patchy hydrogen reionization from an extreme Lyα trough below redshift six. *ArXiv e-prints*, 1407.4850, July 2014.

C. Behrens and J. Niemeyer. Effects of Lyman-alpha scattering in the IGM on clustering statistics of Lyman-alpha emitters. A&A, 556:A5, August 2013. doi: 10.1051/0004-6361/201321172.

C. Behrens, M. Dijkstra, and J. C. Niemeyer. Beamed Lyα emission through outflow-driven cavities. A&A, 563:A77, March 2014. doi: 10.1051/0004-6361/201322949.

C. L. Bennett, A. J. Banday, K. M. Gorski, G. Hinshaw, P. Jackson, P. Keegstra, A. Kogut, G. F. Smoot, D. T. Wilkinson, and E. L. Wright. Four-Year COBE DMR Cosmic Microwave Background Observations: Maps and Basic Results. ApJ, 464:L1, June 1996. doi: 10.1086/310075.

F. Bertoldi and P. Cox. Dust emission and star formation toward a redshift 5.5 QSO. A&A, 384: L11–L14, March 2002. doi: 10.1051/0004-6361:20020120.

S. Bianchi and R. Schneider. Dust formation and survival in supernova ejecta. MNRAS, 378:973–982, July 2007. doi: 10.1111/j.1365-2966.2007.11829.x.

V. Biffi and U. Maio. Statistical properties of mass, star formation, chemical content and rotational patterns in early z $\gtrsim$ 9 structures. MNRAS, 436:1621–1638, December 2013. doi: 10.1093/mnras/stt1678.

J. S. Bolton and M. G. Haehnelt. The observed ionization rate of the intergalactic medium and the ionizing emissivity at z >= 5: evidence for a photon-starved and extended epoch of reionization. MNRAS, 382:325–341, November 2007. doi: 10.1111/j.1365-2966.2007.12372.x.

J. S. Bolton and M. G. Haehnelt. On the rapid demise of Ly α emitters at redshift z $\gtrsim$ 7 due to the increasing incidence of optically thick absorption systems. MNRAS, 429:1695–1704, February 2013. doi: 10.1093/mnras/sts455.

R. Bouwens, L. Bradley, A. Zitrin, D. Coe, M. Franx, W. Zheng, R. Smit, O. Host, M. Postman, L. Moustakas, I. Labbe, M. Carrasco, A. Molino, M. Donahue, D. D. Kelson, M. Meneghetti, S. Jha, N. Benitez, D. Lemze, K. Umetsu, T. Broadhurst, J. Moustakas, P. Rosati, M. Bartelmann, H. Ford, G. Graves, C. Grillo, L. Infante, Y. Jiminez-Teja, S. Jouvel, O. Lahav, D. Maoz, E. Medezinski, P. Melchior, J. Merten, M. Nonino, S. Ogaz, and S. Seitz. A Census of Star-Forming Galaxies in the z$\sim$9-10 Universe based on HST+Spitzer Observations Over 19 CLASH clusters: Three Candidate z$\sim$9-10 Galaxies and Improved Constraints on the Star Formation Rate Density at z$\sim$9.2. *ArXiv e-prints*, November 2012.

R. J. Bouwens, G. D. Illingworth, M. Franx, and H. Ford. UV Luminosity Functions at z$\sim$4, 5, and 6 from the Hubble Ultra Deep Field and Other Deep Hubble Space Telescope ACS Fields: Evolution and Star Formation History. ApJ, 670:928–958, December 2007. doi: 10.1086/521811.

R. J. Bouwens, G. D. Illingworth, P. A. Oesch, I. Labbé, M. Trenti, P. van Dokkum, M. Franx, M. Stiavelli, C. M. Carollo, D. Magee, and V. Gonzalez. Ultraviolet Luminosity Functions from 132 z $\sim$ 7 and z $\sim$ 8 Lyman-break Galaxies in the Ultra-deep HUDF09 and Wide-area Early Release Science WFC3/IR Observations. ApJ, 737:90, August 2011. doi: 10.1088/0004-637X/737/2/90.

L. D. Bradley, M. Trenti, P. A. Oesch, M. Stiavelli, T. Treu, R. J. Bouwens, J. M. Shull, B. W. Holwerda, and N. Pirzkal. The Brightest of Reionizing Galaxies Survey: Constraints on the Bright End of the z $\sim$ 8 Luminosity Function. ApJ, 760:108, December 2012. doi: 10.1088/0004-637X/760/2/108.

V. Bromm, P. S. Coppi, and R. B. Larson. The Formation of the First Stars. I. The Primordial Star-forming Cloud. ApJ, 564:23–51, January 2002. doi: 10.1086/323947.

Hans Burchard, Eric Deleersnijder, and Andreas Meister. A High-order Conservative Patankar-type Discretisation for Stiff Systems of Production-destruction Equations. *Appl. Numer. Math.*, 47(1): 1–30, October 2003. ISSN 0168-9274. doi: 10.1016/S0168-9274(03)00101-6. URL `http://dx.doi.org/10.1016/S0168-9274(03)00101-6`.

R. G. Carlberg, H. K. C. Yee, and E. Ellingson. The Average Mass and Light Profiles of Galaxy Clusters. ApJ, 478:462–475, March 1997.

J. Caruana, A. J. Bunker, S. M. Wilkins, E. R. Stanway, S. Lorenzoni, M. J. Jarvis, and H. Ebert. Spectroscopy of z $\sim$ 7 candidate galaxies: using Lyman α to constrain the neutral fraction of hydrogen in the high-redshift universe. MNRAS, 443:2831–2842, October 2014. doi: 10.1093/mnras/stu1341.

R. Cen. A hydrodynamic approach to cosmology - Methodology. ApJS, 78:341–364, February 1992. doi: 10.1086/191630.

R. Cen and J. P. Ostriker. Cosmic Chemical Evolution. ApJ, 519:L109–L113, July 1999. doi: 10.1086/312123.

E. Chapman, F. B. Abdalla, G. Harker, V. Jelić, P. Labropoulos, S. Zaroubi, M. A. Brentjens, A. G. de Bruyn, and L. V. E. Koopmans. Foreground removal using FASTICA: a showcase of LOFAR-EoR. MNRAS, 423:2518–2532, July 2012. doi: 10.1111/j.1365-2966.2012.21065.x.

E. Chapman, F. B. Abdalla, J. Bobin, J.-L. Starck, G. Harker, V. Jelić, P. Labropoulos, S. Zaroubi, M. A. Brentjens, A. G. de Bruyn, and L. V. E. Koopmans. The scale of the problem: recovering images of reionization with Generalized Morphological Component Analysis. MNRAS, 429:165–176, February 2013. doi: 10.1093/mnras/sts333.

W. A. Chiu, N. Y. Gnedin, and J. P. Ostriker. The Expected Mass Function for Low-Mass Galaxies in a Cold Dark Matter Cosmology: Is There a Problem? ApJ, 563:21–27, December 2001. doi: 10.1086/323685.

T. R. Choudhury and A. Ferrara. Experimental constraints on self-consistent reionization models. MNRAS, 361:577–594, August 2005. doi: 10.1111/j.1365-2966.2005.09196.x.

T. R. Choudhury and A. Ferrara. Updating reionization scenarios after recent data. MNRAS, 371: L55–L59, September 2006. doi: 10.1111/j.1745-3933.2006.00207.x.

T. R. Choudhury and A. Ferrara. Searching for the reionization sources. MNRAS, 380:L6–L10, September 2007. doi: 10.1111/j.1745-3933.2007.00338.x.

B. Ciardi and A. Ferrara. The First Cosmic Structures and Their Effects. Space Sci. Rev., 116: 625–705, February 2005. doi: 10.1007/s11214-005-3592-0.

B. Ciardi, A. Ferrara, S. Marri, and G. Raimondo. Cosmological reionization around the first stars: Monte Carlo radiative transfer. MNRAS, 324:381–388, June 2001. doi: 10.1046/j.1365-8711.2001.04316.x.

B. Ciardi, J. S. Bolton, A. Maselli, and L. Graziani. The effect of intergalactic helium on hydrogen reionization: implications for the sources of ionizing photons at z>6. MNRAS, 423:558–574, June 2012. doi: 10.1111/j.1365-2966.2012.20902.x.

D. Clowe, M. Bradač, A. H. Gonzalez, M. Markevitch, S. W. Randall, C. Jones, and D. Zaritsky. A Direct Empirical Proof of the Existence of Dark Matter. ApJ, 648:L109–L113, September 2006. doi: 10.1086/508162.

S. Cole, C. G. Lacey, C. M. Baugh, and C. S. Frenk. Hierarchical galaxy formation. MNRAS, 319: 168–204, November 2000. doi: 10.1046/j.1365-8711.2000.03879.x.

L. L. Cowie and E. M. Hu. High-z Lyalpha Emitters. I. A Blank-Field Search for Objects near Redshift Z = 3.4 in and around the Hubble Deep Field and the Hawaii Deep Field SSA 22. AJ, 115:1319–1328, April 1998. doi: 10.1086/300309.

E. Curtis-Lake, R. J. McLure, H. J. Pearce, J. S. Dunlop, M. Cirasuolo, D. P. Stark, O. Almaini, E. J. Bradshaw, R. Chuter, S. Foucaud, and W. G. Hartley. A remarkably high fraction of strong Lyα emitters amongst luminous redshift 6.0 ¡ z ¡ 6.5 Lyman-break galaxies in the UKIDSS Ultra-Deep Survey. MNRAS, 422:1425–1435, May 2012. doi: 10.1111/j.1365-2966.2012.20720.x.

K. K. Datta, M. M. Friedrich, G. Mellema, I. T. Iliev, and P. R. Shapiro. Prospects of observing a quasar H II region during the epoch of reionization with the redshifted 21-cm signal. MNRAS, 424: 762–778, July 2012. doi: 10.1111/j.1365-2966.2012.21268.x.

P. Dayal and A. Ferrara. Lyα emitters and Lyman-break galaxies: dichotomous twins. MNRAS, 421: 2568–2579, April 2012. doi: 10.1111/j.1365-2966.2012.20486.x.

P. Dayal, A. Ferrara, and S. Gallerani. Signatures of reionization on Lyα emitters. MNRAS, 389: 1683–1696, October 2008. doi: 10.1111/j.1365-2966.2008.13721.x.

P. Dayal, A. Ferrara, A. Saro, R. Salvaterra, S. Borgani, and L. Tornatore. Lyman alpha emitter evolution in the reionization epoch. MNRAS, 400:2000–2011, December 2009. doi: 10.1111/j.1365-2966.2009.15593.x.

P. Dayal, A. Ferrara, and A. Saro. The cool side of Lyman alpha emitters. MNRAS, 402:1449–1457, March 2010. doi: 10.1111/j.1365-2966.2009.15995.x.

P. Dayal, A. Maselli, and A. Ferrara. The visibility of Lyman α emitters during reionization. MNRAS, 410:830–843, January 2011. doi: 10.1111/j.1365-2966.2010.17482.x.

P. Dayal, J. S. Dunlop, U. Maio, and B. Ciardi. Simulating the assembly of galaxies at redshifts z = 6-12. MNRAS, 434:1486–1504, September 2013. doi: 10.1093/mnras/stt1108.

M. Dijkstra and J. S. B. Wyithe. An empirical study of the relationship between Lyα and UV-selected galaxies: do theorists and observers 'select' the same objects? MNRAS, 419:3181–3193, February 2012. doi: 10.1111/j.1365-2966.2011.19958.x.

M. Dijkstra, Z. Haiman, and A. Loeb. A Limit from the X-Ray Background on the Contribution of Quasars to Reionization. ApJ, 613:646–654, October 2004a. doi: 10.1086/422167.

M. Dijkstra, Z. Haiman, M. J. Rees, and D. H. Weinberg. Photoionization Feedback in Low-Mass Galaxies at High Redshift. ApJ, 601:666–675, February 2004b. doi: 10.1086/380603.

M. Dijkstra, A. Lidz, and J. S. B. Wyithe. The impact of The IGM on high-redshift Lyα emission lines. MNRAS, 377:1175–1186, May 2007. doi: 10.1111/j.1365-2966.2007.11666.x.

M. Dijkstra, A. Mesinger, and J. S. B. Wyithe. The detectability of Lyα emission from galaxies during the epoch of reionization. MNRAS, 414:2139–2147, July 2011. doi: 10.1111/j.1365-2966.2011.18530.x.

M. Dijkstra, S. Wyithe, Z. Haiman, A. Mesinger, and L. Pentericci. Evolution in the escape fraction of ionizing photons and the decline in strong Lyα emission from z > 6 galaxies. MNRAS, 440: 3309–3316, June 2014. doi: 10.1093/mnras/stu531.

M. A. Dopita and R. S. Sutherland. *Astrophysics of the diffuse universe*. Springer, 2003. ISBN 3540433627.

J. Dunkley, E. Komatsu, M. R. Nolta, D. N. Spergel, D. Larson, G. Hinshaw, L. Page, C. L. Bennett, B. Gold, N. Jarosik, J. L. Weiland, M. Halpern, R. S. Hill, A. Kogut, M. Limon, S. S. Meyer, G. S. Tucker, E. Wollack, and E. L. Wright. Five-Year Wilkinson Microwave Anisotropy Probe Observations: Likelihoods and Parameters from the WMAP Data. ApJS, 180:306–329, February 2009. doi: 10.1088/0067-0049/180/2/306.

F. Duval, D. Schaerer, G. Östlin, and P. Laursen. Lyman α line and continuum radiative transfer in a clumpy interstellar medium. A&A, 562:A52, February 2014. doi: 10.1051/0004-6361/201220455.

E. Dwek, F. Galliano, and A. P. Jones. The Evolution of Dust in the Early Universe with Applications to the Galaxy SDSS J1148+5251. ApJ, 662:927–939, June 2007. doi: 10.1086/518430.

S. M. Faber and J. S. Gallagher. Masses and mass-to-light ratios of galaxies. ARA&A, 17:135–187, 1979. doi: 10.1146/annurev.aa.17.090179.001031.

X. Fan, V. K. Narayanan, R. H. Lupton, M. A. Strauss, G. R. Knapp, R. H. Becker, R. L. White, L. Pentericci, S. K. Leggett, Z. Haiman, J. E. Gunn, Ž. Ivezić, D. P. Schneider, S. F. Anderson, J. Brinkmann, N. A. Bahcall, A. J. Connolly, I. Csabai, M. Doi, M. Fukugita, T. Geballe, E. K. Grebel, D. Harbeck, G. Hennessy, D. Q. Lamb, G. Miknaitis, J. A. Munn, R. Nichol, S. Okamura, J. R. Pier, F. Prada, G. T. Richards, A. Szalay, and D. G. York. A Survey of z>5.8 Quasars in the Sloan Digital Sky Survey. I. Discovery of Three New Quasars and the Spatial Density of Luminous Quasars at z∼6. AJ, 122:2833–2849, December 2001. doi: 10.1086/324111.

X. Fan, M. A. Strauss, R. H. Becker, R. L. White, J. E. Gunn, G. R. Knapp, G. T. Richards, D. P. Schneider, J. Brinkmann, and M. Fukugita. Constraining the Evolution of the Ionizing Background and the Epoch of Reionization with z∼6 Quasars. II. A Sample of 19 Quasars. AJ, 132:117–136, July 2006. doi: 10.1086/504836.

A. Ferrara and A. Loeb. Escape fraction of the ionizing radiation from starburst galaxies at high redshifts. MNRAS, 431:2826–2833, May 2013. doi: 10.1093/mnras/stt381.

A. Ferrara, M. Pettini, and Y. Shchekinov. Mixing metals in the early Universe. MNRAS, 319: 539–548, December 2000. doi: 10.1046/j.1365-8711.2000.03857.x.

G. B. Field. Excitation of the Hydrogen 21-CM Line. *Proceedings of the IRE*, 46:240–250, January 1958. doi: 10.1109/JRPROC.1958.286741.

G. B. Field. The Spin Temperature of Intergalactic Neutral Hydrogen. ApJ, 129:536, May 1959a. doi: 10.1086/146653.

G. B. Field. The Time Relaxation of a Resonance-Line Profile. ApJ, 129:551, May 1959b. doi: 10.1086/146654.

S. L. Finkelstein, J. E. Rhoads, S. Malhotra, and N. Grogin. Lyman Alpha Galaxies: Primitive, Dusty, or Evolved? ApJ, 691:465–481, January 2009. doi: 10.1088/0004-637X/691/1/465.

K. Finlator, F. Özel, R. Davé, and B. D. Oppenheimer. The late reionization of filaments. MNRAS, 400:1049–1061, December 2009. doi: 10.1111/j.1365-2966.2009.15521.x.

J. E. Forero-Romero, G. Yepes, S. Gottlöber, S. R. Knollmann, A. J. Cuesta, and F. Prada. CLARA's view on the escape fraction of Lyman α photons in high-redshift galaxies. MNRAS, 415:3666–3680, August 2011. doi: 10.1111/j.1365-2966.2011.18983.x.

J. E. Forero-Romero, G. Yepes, S. Gottlöber, and F. Prada. Modelling the fraction of Lyman break galaxies with strong Lyman α emission at $5 \leq z \leq 7$. MNRAS, 419:952–958, January 2012. doi: 10.1111/j.1365-2966.2011.19744.x.

A. Fujita, C. L. Martin, M.-M. Mac Low, and T. Abel. The Influence of Supershells and Galactic Outflows on the Escape of Ionizing Radiation from Dwarf Starburst Galaxies. ApJ, 599:50–69, December 2003. doi: 10.1086/379276.

P. M. Geil, J. S. B. Wyithe, N. Petrovic, and S. P. Oh. The effect of Galactic foreground subtraction on redshifted 21-cm observations of quasar HII regions. MNRAS, 390:1496–1504, November 2008. doi: 10.1111/j.1365-2966.2008.13798.x.

P. M. Geil, B. M. Gaensler, and J. S. B. Wyithe. Polarized foreground removal at low radio frequencies using rotation measure synthesis: uncovering the signature of hydrogen reionization. MNRAS, 418: 516–535, November 2011. doi: 10.1111/j.1365-2966.2011.19509.x.

N. Y. Gnedin. Cosmological Reionization by Stellar Sources. ApJ, 535:530–554, June 2000. doi: 10.1086/308876.

N. Y. Gnedin. Cosmic Reionization On Computers I. Design and Calibration of Simulations. *ArXiv e-prints*, March 2014.

N. Y. Gnedin and T. Abel. Multi-dimensional cosmological radiative transfer with a Variable Eddington Tensor formalism. New Astronomy, 6:437–455, October 2001. doi: 10.1016/S1384-1076(01)00068-9.

N. Y. Gnedin, A. V. Kravtsov, and H.-W. Chen. Escape of Ionizing Radiation from High-Redshift Galaxies. ApJ, 672:765–775, January 2008. doi: 10.1086/524007.

V. González, I. Labbé, R. J. Bouwens, G. Illingworth, M. Franx, M. Kriek, and G. B. Brammer. The Stellar Mass Density and Specific Star Formation Rate of the Universe at $z \sim 7$. ApJ, 713:115–130, April 2010. doi: 10.1088/0004-637X/713/1/115.

V. González, I. Labbé, R. J. Bouwens, G. Illingworth, M. Franx, and M. Kriek. Evolution of Galaxy Stellar Mass Functions, Mass Densities, and Mass-to-light Ratios from z $\sim$ 7 to z $\sim$ 4. ApJ, 735: L34, July 2011. doi: 10.1088/2041-8205/735/2/L34.

J. Goodman. Geocentrism reexamined. Phys. Rev. D, 52:1821–1827, August 1995. doi: 10.1103/PhysRevD.52.1821.

J. E. Gunn and B. A. Peterson. On the Density of Neutral Hydrogen in Intergalactic Space. ApJ, 142:1633–1641, November 1965. doi: 10.1086/148444.

F. Haardt and P. Madau. Radiative Transfer in a Clumpy Universe. II. The Ultraviolet Extragalactic Background. ApJ, 461:20, April 1996. doi: 10.1086/177035.

M. Hansen and S. P. Oh. Lyman α radiative transfer in a multiphase medium. MNRAS, 367:979–1002, April 2006. doi: 10.1111/j.1365-2966.2005.09870.x.

G. Harker, S. Zaroubi, G. Bernardi, M. A. Brentjens, A. G. de Bruyn, B. Ciardi, V. Jelić, L. V. E. Koopmans, P. Labropoulos, G. Mellema, A. Offringa, V. N. Pandey, A. H. Pawlik, J. Schaye, R. M. Thomas, and S. Yatawatta. Power spectrum extraction for redshifted 21-cm Epoch of Reionization experiments: the LOFAR case. MNRAS, 405:2492–2504, July 2010. doi: 10.1111/j.1365-2966.2010.16628.x.

E. R. Harrison. Fluctuations at the Threshold of Classical Cosmology. Phys. Rev. D, 1:2726–2730, May 1970. doi: 10.1103/PhysRevD.1.2726.

K. Hasegawa and M. Umemura. START: smoothed particle hydrodynamics with tree-based accelerated radiative transfer. MNRAS, 407:2632–2644, October 2010. doi: 10.1111/j.1365-2966.2010.17100.x.

G. Hinshaw, D. Larson, E. Komatsu, D. N. Spergel, C. L. Bennett, J. Dunkley, M. R. Nolta, M. Halpern, R. S. Hill, N. Odegard, L. Page, K. M. Smith, J. L. Weiland, B. Gold, N. Jarosik, A. Kogut, M. Limon, S. S. Meyer, G. S. Tucker, E. Wollack, and E. L. Wright. Nine-year Wilkinson Microwave Anisotropy Probe (WMAP) Observations: Cosmological Parameter Results. ApJS, 208:19, October 2013. doi: 10.1088/0067-0049/208/2/19.

E. M. Hu, L. L. Cowie, A. J. Barger, P. Capak, Y. Kakazu, and L. Trouille. An Atlas of z = 5.7 and z = 6.5 Lyα Emitters. ApJ, 725:394–423, December 2010. doi: 10.1088/0004-637X/725/1/394.

A. Hutter, P. Dayal, A. M. Partl, and V. Müller. The visibility of Lyman α emitters: constraining reionization, ionizing photon escape fractions and dust. MNRAS, 441:2861–2877, July 2014. doi: 10.1093/mnras/stu791.

I. T. Iliev, E. Scannapieco, and P. R. Shapiro. The Impact of Small-Scale Structure on Cosmological Ionization Fronts and Reionization. ApJ, 624:491–504, May 2005. doi: 10.1086/429083.

I. T. Iliev, G. Mellema, U.-L. Pen, H. Merz, P. R. Shapiro, and M. A. Alvarez. Simulating cosmic reionization at large scales - I. The geometry of reionization. MNRAS, 369:1625–1638, July 2006. doi: 10.1111/j.1365-2966.2006.10502.x.

I. T. Iliev, G. Mellema, P. R. Shapiro, and U.-L. Pen. Self-regulated reionization. MNRAS, 376: 534–548, April 2007. doi: 10.1111/j.1365-2966.2007.11482.x.

I. T. Iliev, P. R. Shapiro, P. McDonald, G. Mellema, and U.-L. Pen. The effect of the intergalactic environment on the observability of Lyα emitters during reionization. MNRAS, 391:63–83, November 2008. doi: 10.1111/j.1365-2966.2008.13879.x.

I. T. Iliev, B. Moore, S. Gottlöber, G. Yepes, Y. Hoffman, and G. Mellema. Reionization of the Local Group of galaxies. MNRAS, 413:2093–2102, May 2011. doi: 10.1111/j.1365-2966.2011.18292.x.

I. T. Iliev, G. Mellema, P. R. Shapiro, U.-L. Pen, Y. Mao, J. Koda, and K. Ahn. Can 21-cm observations discriminate between high-mass and low-mass galaxies as reionization sources? MNRAS, 423:2222–2253, July 2012. doi: 10.1111/j.1365-2966.2012.21032.x.

I. T. Iliev, G. Mellema, K. Ahn, P. R. Shapiro, Y. Mao, and U.-L. Pen. Simulating cosmic reionization: how large a volume is large enough? MNRAS, 439:725–743, March 2014. doi: 10.1093/mnras/stt2497.

I. Iwata, K. Ohta, N. Tamura, M. Akiyama, K. Aoki, M. Ando, G. Kiuchi, and M. Sawicki. Differential evolution of the UV luminosity function of Lyman break galaxies from z $\sim$ 5 to 3. MNRAS, 376: 1557–1576, April 2007. doi: 10.1111/j.1365-2966.2007.11557.x.

M. Iye, K. Ota, N. Kashikawa, H. Furusawa, T. Hashimoto, T. Hattori, Y. Matsuda, T. Morokuma, M. Ouchi, and K. Shimasaku. A galaxy at a redshift z = 6.96. Nature, 443:186–188, September 2006. doi: 10.1038/nature05104.

J. H. Jeans. The Stability of a Spherical Nebula. *Royal Society of London Philosophical Transactions Series A*, 199:1–53, 1902. doi: 10.1098/rsta.1902.0012.

V. Jelić, S. Zaroubi, P. Labropoulos, R. M. Thomas, G. Bernardi, M. A. Brentjens, A. G. de Bruyn, B. Ciardi, G. Harker, L. V. E. Koopmans, V. N. Pandey, J. Schaye, and S. Yatawatta. Foreground simulations for the LOFAR-epoch of reionization experiment. MNRAS, 389:1319–1335, September 2008. doi: 10.1111/j.1365-2966.2008.13634.x.

H. Jensen, K. K. Datta, G. Mellema, E. Chapman, F. B. Abdalla, I. T. Iliev, Y. Mao, M. G. Santos, P. R. Shapiro, S. Zaroubi, G. Bernardi, M. A. Brentjens, A. G. de Bruyn, B. Ciardi, G. J. A. Harker, V. Jelić, S. Kazemi, L. V. E. Koopmans, P. Labropoulos, O. Martinez, A. R. Offringa, V. N. Pandey, J. Schaye, R. M. Thomas, V. Veligatla, H. Vedantham, and S. Yatawatta. Probing reionization with LOFAR using 21-cm redshift space distortions. MNRAS, 435:460–474, October 2013a. doi: 10.1093/mnras/stt1341.

H. Jensen, P. Laursen, G. Mellema, I. T. Iliev, J. Sommer-Larsen, and P. R. Shapiro. On the use of Lyα emitters as probes of reionization. MNRAS, 428:1366–1381, January 2013b. doi: 10.1093/mnras/sts116.

J. L. Johnson, T. H. Greif, and V. Bromm. Local Radiative Feedback in the Formation of the First Protogalaxies. ApJ, 665:85–95, August 2007. doi: 10.1086/519212.

N. Kaiser. On the spatial correlations of Abell clusters. ApJ, 284:L9–L12, September 1984. doi: 10.1086/184341.

N. Kashikawa, K. Shimasaku, M. A. Malkan, M. Doi, Y. Matsuda, M. Ouchi, Y. Taniguchi, C. Ly, T. Nagao, M. Iye, K. Motohara, T. Murayama, K. Murozono, K. Nariai, K. Ohta, S. Okamura, T. Sasaki, Y. Shioya, and M. Umemura. The End of the Reionization Epoch Probed by Lyα Emitters at z = 6.5 in the Subaru Deep Field. ApJ, 648:7–22, September 2006. doi: 10.1086/504966.

N. Kashikawa, K. Shimasaku, Y. Matsuda, E. Egami, L. Jiang, T. Nagao, M. Ouchi, M. A. Malkan, T. Hattori, K. Ota, Y. Taniguchi, S. Okamura, C. Ly, M. Iye, H. Furusawa, Y. Shioya, T. Shibuya, Y. Ishizaki, and J. Toshikawa. Completing the Census of Lyα Emitters at the Reionization Epoch. ApJ, 734:119, June 2011. doi: 10.1088/0004-637X/734/2/119.

H.-S. Kim, J. S. B. Wyithe, S. Raskutti, C. G. Lacey, and J. C. Helly. The structure of reionization in hierarchical galaxy formation models. MNRAS, 428:2467–2479, January 2013. doi: 10.1093/mnras/sts206.

T. Kimm and R. Cen. Escape Fraction of Ionizing Photons during Reionization: Effects due to Supernova Feedback and Runaway OB Stars. ApJ, 788:121, June 2014. doi: 10.1088/0004-637X/788/2/121.

S. R. Knollmann and A. Knebe. AHF: Amiga's Halo Finder. ApJS, 182:608–624, June 2009. doi: 10.1088/0067-0049/182/2/608.

M. A. R. Kobayashi, T. Totani, and M. Nagashima. Lyα Emitters in Hierarchical Galaxy Formation. II. Ultraviolet Continuum Luminosity Function and Equivalent Width Distribution. ApJ, 708: 1119–1134, January 2010. doi: 10.1088/0004-637X/708/2/1119.

E. Komatsu, J. Dunkley, M. R. Nolta, C. L. Bennett, B. Gold, G. Hinshaw, N. Jarosik, D. Larson, M. Limon, L. Page, D. N. Spergel, M. Halpern, R. S. Hill, A. Kogut, S. S. Meyer, G. S. Tucker, J. L. Weiland, E. Wollack, and E. L. Wright. Five-Year Wilkinson Microwave Anisotropy Probe Observations: Cosmological Interpretation. ApJS, 180:330–376, February 2009. doi: 10.1088/0067-0049/180/2/330.

E. Komatsu, K. M. Smith, J. Dunkley, C. L. Bennett, B. Gold, G. Hinshaw, N. Jarosik, D. Larson, M. R. Nolta, L. Page, D. N. Spergel, M. Halpern, R. S. Hill, A. Kogut, M. Limon, S. S. Meyer, N. Odegard, G. S. Tucker, J. L. Weiland, E. Wollack, and E. L. Wright. Seven-year Wilkinson Microwave Anisotropy Probe (WMAP) Observations: Cosmological Interpretation. ApJS, 192:18, February 2011. doi: 10.1088/0067-0049/192/2/18.

A. Konno, M. Ouchi, Y. Ono, K. Shimasaku, T. Shibuya, H. Furusawa, K. Nakajima, Y. Naito, R. Momose, S. Yuma, and M. Iye. Accelerated Evolution of Lyα Luminosity Function at z>7 Revealed by the Subaru Ultra-Deep Survey for Lyα Emitters at z=7.3. *ArXiv e-prints*, April 2014.

K. A. Kornei, A. E. Shapley, D. K. Erb, C. C. Steidel, N. A. Reddy, M. Pettini, and M. Bogosavljević. The Relationship between Stellar Populations and Lyα Emission in Lyman Break Galaxies. ApJ, 711:693–710, March 2010. doi: 10.1088/0004-637X/711/2/693.

I. Labbé, V. González, R. J. Bouwens, G. D. Illingworth, M. Franx, M. Trenti, P. A. Oesch, P. G. van Dokkum, M. Stiavelli, C. M. Carollo, M. Kriek, and D. Magee. Star Formation Rates and Stellar Masses of z = 7-8 Galaxies from IRAC Observations of the WFC3/IR Early Release Science and the HUDF Fields. ApJ, 716:L103–L108, June 2010a. doi: 10.1088/2041-8205/716/2/L103.

I. Labbé, V. González, R. J. Bouwens, G. D. Illingworth, P. A. Oesch, P. G. van Dokkum, C. M. Carollo, M. Franx, M. Stiavelli, M. Trenti, D. Magee, and M. Kriek. Ultradeep Infrared Array Camera Observations of Sub-L* z $\sim$ 7 and z $\sim$ 8 Galaxies in the Hubble Ultra Deep Field: the Contribution of Low-Luminosity Galaxies to the Stellar Mass Density and Reionization. ApJ, 708: L26–L31, January 2010b. doi: 10.1088/2041-8205/708/1/L26.

I. Labbé, P. A. Oesch, R. J. Bouwens, G. D. Illingworth, D. Magee, V. González, C. M. Carollo, M. Franx, M. Trenti, P. G. van Dokkum, and M. Stiavelli. The Spectral Energy Distributions of z $\sim$ 8 Galaxies from the IRAC Ultra Deep Fields: Emission Lines, Stellar Masses, and Specific Star Formation Rates at 650 Myr. ApJ, 777:L19, November 2013. doi: 10.1088/2041-8205/777/2/L19.

D. Larson, J. Dunkley, G. Hinshaw, E. Komatsu, M. R. Nolta, C. L. Bennett, B. Gold, M. Halpern, R. S. Hill, N. Jarosik, A. Kogut, M. Limon, S. S. Meyer, N. Odegard, L. Page, K. M. Smith, D. N. Spergel, G. S. Tucker, J. L. Weiland, E. Wollack, and E. L. Wright. Seven-year Wilkinson Microwave Anisotropy Probe (WMAP) Observations: Power Spectra and WMAP-derived Parameters. ApJS, 192:16, February 2011. doi: 10.1088/0067-0049/192/2/16.

R. B. Larson. Effects of supernovae on the early evolution of galaxies. MNRAS, 169:229–246, November 1974.

P. Laursen, J. Sommer-Larsen, and A. O. Razoumov. Intergalactic Transmission and Its Impact on the Lyα Line. ApJ, 728:52, February 2011. doi: 10.1088/0004-637X/728/1/52.

P. Laursen, F. Duval, and G. Östlin. On the (Non-)Enhancement of the Lyα Equivalent Width by a Multiphase Interstellar Medium. ApJ, 766:124, April 2013. doi: 10.1088/0004-637X/766/2/124.

C. Ledoux, J. Bergeron, and P. Petitjean. Dust depletion and abundance pattern in damped Lyalpha systems: A sample of Mn and Ti abundances at z ¡ 2.2. A&A, 385:802–815, April 2002. doi: 10.1051/0004-6361:20020198.

C. Leitherer, D. Schaerer, J. D. Goldader, R. M. González Delgado, C. Robert, D. F. Kune, D. F. de Mello, D. Devost, and T. M. Heckman. Starburst99: Synthesis Models for Galaxies with Active Star Formation. ApJS, 123:3–40, July 1999. doi: 10.1086/313233.

C. D. Levermore. Relating Eddington factors to flux limiters. J. Quant. Spec. Radiat. Transf., 31: 149–160, February 1984. doi: 10.1016/0022-4073(84)90112-2.

A. Lidz, O. Zahn, M. McQuinn, M. Zaldarriaga, S. Dutta, and L. Hernquist. Higher Order Contributions to the 21 cm Power Spectrum. ApJ, 659:865–876, April 2007. doi: 10.1086/511670.

P. Madau and M. J. Rees. The Earliest Luminous Sources and the Damping Wing of the Gunn-Peterson Trough. ApJ, 542:L69–L73, October 2000. doi: 10.1086/312934.

U. Maio, S. Khochfar, J. L. Johnson, and B. Ciardi. The interplay between chemical and mechanical feedback from the first generation of stars. MNRAS, 414:1145–1157, June 2011. doi: 10.1111/j.1365-2966.2011.18455.x.

R. Maiolino, T. Nagao, A. Marconi, R. Schneider, S. Bianchi, M. Pedani, A. Pipino, F. Matteucci, P. Cox, and P. Caselli. Metals and dust in high redshift AGNs. Mem. Soc. Astron. Italiana, 77:643, 2006.

S. Malhotra, J. E. Rhoads, N. Pirzkal, Z. Haiman, C. Xu, E. Daddi, H. Yan, L. E. Bergeron, J. Wang, H. C. Ferguson, C. Gronwall, A. Koekemoer, M. Kuemmel, L. A. Moustakas, N. Panagia, A. Pasquali, M. Stiavelli, J. Walsh, R. A. Windhorst, and S. di Serego Alighieri. An Overdensity of Galaxies at z = 5.9 +/- 0.2 in the Hubble Ultra Deep Field Confirmed Using the ACS Grism. ApJ, 626:666–679, June 2005. doi: 10.1086/430047.

M. Malloy and A. Lidz. Identifying Ionized Regions in Noisy Redshifted 21 cm Data Sets. ApJ, 767: 68, April 2013. doi: 10.1088/0004-637X/767/1/68.

Y. Mao, M. Tegmark, M. McQuinn, M. Zaldarriaga, and O. Zahn. How accurately can 21cm tomography constrain cosmology? Phys. Rev. D, 78(2):023529, July 2008. doi: 10.1103/PhysRevD.78.023529.

Y. Mao, P. R. Shapiro, G. Mellema, I. T. Iliev, J. Koda, and K. Ahn. Redshift-space distortion of the 21-cm background from the epoch of reionization - I. Methodology re-examined. MNRAS, 422: 926–954, May 2012. doi: 10.1111/j.1365-2966.2012.20471.x.

A. Maselli, A. Ferrara, and B. Ciardi. CRASH: a radiative transfer scheme. MNRAS, 345:379–394, October 2003. doi: 10.1046/j.1365-8711.2003.06979.x.

A. Maselli, B. Ciardi, and A. Kanekar. CRASH2: coloured packets and other updates. MNRAS, 393: 171–178, February 2009. doi: 10.1111/j.1365-2966.2008.14197.x.

R. J. McLure, M. Cirasuolo, J. S. Dunlop, S. Foucaud, and O. Almaini. The luminosity function, halo masses and stellar masses of luminous Lyman-break galaxies at redshifts 5 ¡ z ¡ 6. MNRAS, 395: 2196–2209, June 2009. doi: 10.1111/j.1365-2966.2009.14677.x.

R. J. McLure, J. S. Dunlop, M. Cirasuolo, A. M. Koekemoer, E. Sabbi, D. P. Stark, T. A. Targett, and R. S. Ellis. Galaxies at z = 6-9 from the WFC3/IR imaging of the Hubble Ultra Deep Field. MNRAS, 403:960–983, April 2010. doi: 10.1111/j.1365-2966.2009.16176.x.

R. J. McLure, J. S. Dunlop, L. de Ravel, M. Cirasuolo, R. S. Ellis, M. Schenker, B. E. Robertson, A. M. Koekemoer, D. P. Stark, and R. A. A. Bowler. A robust sample of galaxies at redshifts 6.0¡z¡8.7: stellar populations, star formation rates and stellar masses. MNRAS, 418:2074–2105, December 2011. doi: 10.1111/j.1365-2966.2011.19626.x.

R. J. McLure, J. S. Dunlop, R. A. A. Bowler, E. Curtis-Lake, M. Schenker, R. S. Ellis, B. E. Robertson, A. M. Koekemoer, A. B. Rogers, Y. Ono, M. Ouchi, S. Charlot, V. Wild, D. P. Stark, S. R. Furlanetto, M. Cirasuolo, and T. A. Targett. A new multifield determination of the galaxy luminosity function at z = 7-9 incorporating the 2012 Hubble Ultra-Deep Field imaging. MNRAS, 432: 2696–2716, July 2013. doi: 10.1093/mnras/stt627.

M. McQuinn. Constraints on X-ray emissions from the reionization era. MNRAS, 426:1349–1360, October 2012. doi: 10.1111/j.1365-2966.2012.21792.x.

M. McQuinn, L. Hernquist, M. Zaldarriaga, and S. Dutta. Studying reionization with Lyα emitters. MNRAS, 381:75–96, October 2007a. doi: 10.1111/j.1365-2966.2007.12085.x.

M. McQuinn, A. Lidz, O. Zahn, S. Dutta, L. Hernquist, and M. Zaldarriaga. The morphology of HII regions during reionization. MNRAS, 377:1043–1063, May 2007b. doi: 10.1111/j.1365-2966.2007.11489.x.

A. Meiksin. Constraints on the ionization sources of the high-redshift intergalactic medium. MNRAS, 356:596–606, January 2005. doi: 10.1111/j.1365-2966.2004.08481.x.

A. Mesinger and S. Furlanetto. Efficient Simulations of Early Structure Formation and Reionization. ApJ, 669:663–675, November 2007. doi: 10.1086/521806.

A. Mesinger, S. Furlanetto, and R. Cen. 21CMFAST: a fast, seminumerical simulation of the high-redshift 21-cm signal. MNRAS, 411:955–972, February 2011. doi: 10.1111/j.1365-2966.2010.17731.x.

A. Mesinger, A. Aykutalp, E. Vanzella, L. Pentericci, A. Ferrara, and M. Dijkstra. Can the intergalactic medium cause a rapid drop in Lyα emission at z $>$ 6? MNRAS, 446:566–577, January 2015. doi: 10.1093/mnras/stu2089.

G. R. Meurer, T. M. Heckman, and D. Calzetti. Dust Absorption and the Ultraviolet Luminosity Density at z $\sim$ 3 as Calibrated by Local Starburst Galaxies. ApJ, 521:64–80, August 1999. doi: 10.1086/307523.

D. Mihalas. *Stellar atmospheres*. W. H. Freeman and Co., 2nd edition, 1978.

J. Miralda-Escude. Reionization of the Intergalactic Medium and the Damping Wing of the Gunn-Peterson Trough. ApJ, 501:15, July 1998. doi: 10.1086/305799.

S. Mitra, A. Ferrara, and T. R. Choudhury. The escape fraction of ionizing photons from high-redshift galaxies from data-constrained reionization models. MNRAS, 428:L1–L5, January 2013. doi: 10.1093/mnrasl/sls001.

H. J. Mo and S. D. M. White. An analytic model for the spatial clustering of dark matter haloes. MNRAS, 282:347–361, September 1996.

H. J. Mo, S. Mao, and S. D. M. White. The formation of galactic discs. MNRAS, 295:319–336, April 1998. doi: 10.1046/j.1365-8711.1998.01227.x.

K. Nagamine, M. Ouchi, V. Springel, and L. Hernquist. Lyman-α Emitters and Lyman-Break Galaxies at z = 3-6 in Cosmological SPH Simulations. PASJ, 62:1455–, December 2010.

J. F. Navarro, C. S. Frenk, and S. D. M. White. The Structure of Cold Dark Matter Halos. ApJ, 462:563, May 1996. doi: 10.1086/177173.

E. Neistein and A. Dekel. Constructing merger trees that mimic N-body simulations. MNRAS, 383:615–626, January 2008. doi: 10.1111/j.1365-2966.2007.12570.x.

D. A. Neufeld. The escape of Lyman-alpha radiation from a multiphase interstellar medium. ApJ, 370:L85–L88, April 1991. doi: 10.1086/185983.

K. K. Nilsson, O. Möller-Nilsson, P. Møller, J. P. U. Fynbo, and A. E. Shapley. On the dependence between UV luminosity and Lyα equivalent width in high-redshift galaxies. MNRAS, 400:232–237, November 2009. doi: 10.1111/j.1365-2966.2009.15439.x.

M. L. Norman, D. R. Reynolds, G. C. So, and R. P. Harkness. Direct Numerical Simulation of Reionization in Large Cosmological Volumes I: Numerical Methods and Tests. *ArXiv e-prints*, 1306.0645, June 2013.

P. A. Oesch, R. J. Bouwens, G. D. Illingworth, C. M. Carollo, M. Franx, I. Labbé, D. Magee, M. Stiavelli, M. Trenti, and P. G. van Dokkum. z $\sim$ 7 Galaxies in the HUDF: First Epoch WFC3/IR Results. ApJ, 709:L16–L20, January 2010. doi: 10.1088/2041-8205/709/1/L16.

T. Okamoto and C. S. Frenk. The origin of failed subhaloes and the common mass scale of the Milky Way satellite galaxies. MNRAS, 399:L174–L178, October 2009. doi: 10.1111/j.1745-3933.2009.00748.x.

T. Okamoto, L. Gao, and T. Theuns. Mass loss of galaxies due to an ultraviolet background. MNRAS, 390:920–928, November 2008. doi: 10.1111/j.1365-2966.2008.13830.x.

A. Omont, P. Cox, F. Bertoldi, R. G. McMahon, C. Carilli, and K. G. Isaak. A 1.2 mm MAMBO/IRAM-30 m survey of dust emission from the highest redshift PSS quasars. A&A, 374: 371–381, August 2001. doi: 10.1051/0004-6361:20010721.

Y. Ono, M. Ouchi, K. Shimasaku, J. Dunlop, D. Farrah, R. McLure, and S. Okamura. Stellar Populations of Lyα Emitters at z $\sim$ 6-7: Constraints on the Escape Fraction of Ionizing Photons from Galaxy Building Blocks. ApJ, 724:1524–1535, December 2010. doi: 10.1088/0004-637X/724/2/1524.

Y. Ono, M. Ouchi, B. Mobasher, M. Dickinson, K. Penner, K. Shimasaku, B. J. Weiner, J. S. Kartaltepe, K. Nakajima, H. Nayyeri, D. Stern, N. Kashikawa, and H. Spinrad. Spectroscopic Confirmation of Three z-dropout Galaxies at z = 6.844-7.213: Demographics of Lyα Emission in z $\sim$ 7 Galaxies. ApJ, 744:83, January 2012. doi: 10.1088/0004-637X/744/2/83.

B. D. Oppenheimer and R. Davé. Cosmological simulations of intergalactic medium enrichment from galactic outflows. MNRAS, 373:1265–1292, December 2006. doi: 10.1111/j.1365-2966.2006.10989.x.

A. Orsi, C. G. Lacey, C. M. Baugh, and L. Infante. The clustering of Lyα emitters in a ΛCDM Universe. MNRAS, 391:1589–1604, December 2008. doi: 10.1111/j.1365-2966.2008.14010.x.

D. E. Osterbrock. *Astrophysics of gaseous nebulae and active galactic nuclei.* University Science Books, 1989.

M. Ouchi, K. Shimasaku, M. Akiyama, C. Simpson, T. Saito, Y. Ueda, H. Furusawa, K. Sekiguchi, T. Yamada, T. Kodama, N. Kashikawa, S. Okamura, M. Iye, T. Takata, M. Yoshida, and M. Yoshida. The Subaru/XMM-Newton Deep Survey (SXDS). IV. Evolution of Lyα Emitters from z=3.1 to 5.7 in the 1 deg^2 Field: Luminosity Functions and AGN. ApJS, 176:301–330, June 2008. doi: 10.1086/527673.

M. Ouchi, B. Mobasher, K. Shimasaku, H. C. Ferguson, S. M. Fall, Y. Ono, N. Kashikawa, T. Morokuma, K. Nakajima, S. Okamura, M. Dickinson, M. Giavalisco, and K. Ohta. Large Area Survey for z = 7 Galaxies in SDF and GOODS-N: Implications for Galaxy Formation and Cosmic Reionization. ApJ, 706:1136–1151, December 2009. doi: 10.1088/0004-637X/706/2/1136.

M. Ouchi, K. Shimasaku, H. Furusawa, T. Saito, M. Yoshida, M. Akiyama, Y. Ono, T. Yamada, K. Ota, N. Kashikawa, M. Iye, T. Kodama, S. Okamura, C. Simpson, and M. Yoshida. Statistics of 207 Lyα Emitters at a Redshift Near 7: Constraints on Reionization and Galaxy Formation Models. ApJ, 723:869–894, November 2010. doi: 10.1088/0004-637X/723/1/869.

R. A. Overzier, R. J. Bouwens, G. D. Illingworth, and M. Franx. Clustering of i_{775} Dropout Galaxies at z $\sim$ 6 in GOODS and the UDF. ApJ, 648:L5–L8, September 2006. doi: 10.1086/507678.

J.-P. Paardekooper, C. J. H. Kruip, and V. Icke. SimpleX2: radiative transfer on an unstructured, dynamic grid. A&A, 515:A79, June 2010. doi: 10.1051/0004-6361/200913821.

J.-P. Paardekooper, F. I. Pelupessy, G. Altay, and C. J. H. Kruip. The escape of ionising radiation from high-redshift dwarf galaxies. A&A, 530:A87, June 2011. doi: 10.1051/0004-6361/201116841.

H. Park, P. R. Shapiro, E. Komatsu, I. T. Iliev, K. Ahn, and G. Mellema. The Kinetic Sunyaev-Zel'dovich Effect as a Probe of the Physics of Cosmic Reionization: The Effect of Self-regulated Reionization. ApJ, 769:93, June 2013. doi: 10.1088/0004-637X/769/2/93.

A. R. Parsons, D. C. Backer, G. S. Foster, M. C. H. Wright, R. F. Bradley, N. E. Gugliucci, C. R. Parashare, E. E. Benoit, J. E. Aguirre, D. C. Jacobs, C. L. Carilli, D. Herne, M. J. Lynch, J. R. Manley, and D. J. Werthimer. The Precision Array for Probing the Epoch of Re-ionization: Eight Station Results. AJ, 139:1468–1480, April 2010. doi: 10.1088/0004-6256/139/4/1468.

A. M. Partl, A. Maselli, B. Ciardi, A. Ferrara, and V. Müller. Enabling parallel computing in CRASH. MNRAS, 414:428–444, June 2011. doi: 10.1111/j.1365-2966.2011.18401.x.

A. H. Pawlik, M. Milosavljević, and V. Bromm. The First Galaxies: Assembly under Radiative Feedback from the First Stars. ApJ, 767:59, April 2013. doi: 10.1088/0004-637X/767/1/59.

P. J. E. Peebles. *The large-scale structure of the universe*. Princeton University Press, 1980.

U.-L. Pen, T.-C. Chang, J. B. Peterson, J. Roy, Y. Gupta, and K. Bandura. The GMRT Search for Reionization. In R. Minchin and E. Momjian, editors, *The Evolution of Galaxies Through the Neutral Hydrogen Window*, volume 1035 of *American Institute of Physics Conference Series*, page 75–81, August 2008. doi: 10.1063/1.2973618.

L. Pentericci, A. Grazian, A. Fontana, M. Castellano, E. Giallongo, S. Salimbeni, and P. Santini. The physical properties of Lyα emitting galaxies: not just primeval galaxies? A&A, 494:553–561, February 2009. doi: 10.1051/0004-6361:200810722.

L. Pentericci, A. Fontana, E. Vanzella, M. Castellano, A. Grazian, M. Dijkstra, K. Boutsia, S. Cristiani, M. Dickinson, E. Giallongo, M. Giavalisco, R. Maiolino, A. Moorwood, D. Paris, and P. Santini. Spectroscopic Confirmation of z $\sim$ 7 Lyman Break Galaxies: Probing the Earliest Galaxies and the Epoch of Reionization. ApJ, 743:132, December 2011. doi: 10.1088/0004-637X/743/2/132.

L. Pentericci, E. Vanzella, A. Fontana, M. Castellano, T. Treu, A. Mesinger, M. Dijkstra, A. Grazian, M. Bradač, C. Conselice, S. Cristiani, J. Dunlop, A. Galametz, M. Giavalisco, E. Giallongo, A. Koekemoer, R. McLure, R. Maiolino, D. Paris, and P. Santini. New Observations of z $\sim$ 7 Galaxies: Evidence for a Patchy Reionization. ApJ, 793:113, October 2014. doi: 10.1088/0004-637X/793/2/113.

M. Persic, P. Salucci, and F. Stel. The universal rotation curve of spiral galaxies - I. The dark matter connection. MNRAS, 281:27–47, July 1996.

M. Pettini, L. J. Smith, R. W. Hunstead, and D. L. King. Metal enrichment, dust, and star formation in galaxies at high redshifts. 3: Zn and CR abundances for 17 damped Lyman-alpha systems. ApJ, 426:79–96, May 1994. doi: 10.1086/174041.

Planck Collaboration, P. A. R. Ade, N. Aghanim, C. Armitage-Caplan, M. Arnaud, M. Ashdown, F. Atrio-Barandela, J. Aumont, C. Baccigalupi, A. J. Banday, and et al. Planck 2013 results. XVI. Cosmological parameters. A&A, 571:A16, November 2014a. doi: 10.1051/0004-6361/201321591.

Planck Collaboration, P. A. R. Ade, N. Aghanim, C. Armitage-Caplan, M. Arnaud, M. Ashdown, F. Atrio-Barandela, J. Aumont, C. Baccigalupi, A. J. Banday, and et al. Planck 2013 results. XV. CMB power spectra and likelihood. A&A, 571:A15, November 2014b. doi: 10.1051/0004-6361/201321573.

W. H. Press and P. Schechter. Formation of Galaxies and Clusters of Galaxies by Self-Similar Gravitational Condensation. ApJ, 187:425–438, February 1974. doi: 10.1086/152650.

J. R. Pritchard and A. Loeb. Evolution of the 21cm signal throughout cosmic history. Phys. Rev. D, 78(10):103511, November 2008. doi: 10.1103/PhysRevD.78.103511.

M. Raičević and T. Theuns. Modelling recombinations during cosmological reionization. MNRAS, 412:L16–L19, March 2011. doi: 10.1111/j.1745-3933.2010.00993.x.

A. O. Razoumov and C. Y. Cardall. Fully threaded transport engine: new method for multi-scale radiative transfer. MNRAS, 362:1413–1417, October 2005. doi: 10.1111/j.1365-2966.2005.09409.x.

A. O. Razoumov and J. Sommer-Larsen. Escape of Ionizing Radiation from Star-forming Regions in Young Galaxies. ApJ, 651:L89–L92, November 2006. doi: 10.1086/509636.

A. O. Razoumov and J. Sommer-Larsen. Ionizing Radiation from z = 4-10 Galaxies. ApJ, 710: 1239–1246, February 2010. doi: 10.1088/0004-637X/710/2/1239.

M. J. Rees and J. P. Ostriker. Cooling, dynamics and fragmentation of massive gas clouds - Clues to the masses and radii of galaxies and clusters. MNRAS, 179:541–559, June 1977.

M. Ricotti and J. M. Shull. Feedback from Galaxy Formation: Escaping Ionizing Radiation from Galaxies at High Redshift. ApJ, 542:548–558, October 2000. doi: 10.1086/317025.

V. C. Rubin, N. Thonnard, and W. K. Ford, Jr. Extended rotation curves of high-luminosity spiral galaxies. IV - Systematic dynamical properties, SA through SC. ApJ, 225:L107–L111, November 1978. doi: 10.1086/182804.

V. C. Rubin, W. K. J. Ford, and N. . Thonnard. Rotational properties of 21 SC galaxies with a large range of luminosities and radii, from NGC 4605 /R = 4kpc/ to UGC 2885 /R = 122 kpc/. ApJ, 238:471–487, June 1980. doi: 10.1086/158003.

Barbara Ryden. *Introduction to Cosmology*. Addison-Wesley, 2006. ISBN 0-8053-8912-1.

E. E. Salpeter. The Luminosity Function and Stellar Evolution. ApJ, 121:161, January 1955. doi: 10.1086/145971.

R. Salvaterra, F. Haardt, and A. Ferrara. Cosmic backgrounds from miniquasars. MNRAS, 362: L50–L54, September 2005. doi: 10.1111/j.1745-3933.2005.00074.x.

R. Salvaterra, F. Haardt, and M. Volonteri. Unresolved X-ray background: clues on galactic nuclear activity at z > 6. MNRAS, 374:761–768, January 2007. doi: 10.1111/j.1365-2966.2006.11195.x.

R. Salvaterra, A. Ferrara, and P. Dayal. Simulating high-redshift galaxies. MNRAS, 414:847–859, June 2011. doi: 10.1111/j.1365-2966.2010.18155.x.

R. Salvaterra, U. Maio, B. Ciardi, and M. A. Campisi. Simulating high-z gamma-ray burst host galaxies. MNRAS, 429:2718–2726, March 2013. doi: 10.1093/mnras/sts541.

S. Samui, R. Srianand, and K. Subramanian. Understanding the redshift evolution of the luminosity functions of Lyman α emitters. MNRAS, 398:2061–2068, October 2009. doi: 10.1111/j.1365-2966.2009.15245.x.

M. R. Santos. Probing reionization with Lyman α emission lines. MNRAS, 349:1137–1152, April 2004. doi: 10.1111/j.1365-2966.2004.07594.x.

E. Scannapieco and T. Broadhurst. The Role of Heating and Enrichment in Galaxy Formation. ApJ, 549:28–45, March 2001. doi: 10.1086/319043.

E. Scannapieco, A. Ferrara, and T. Broadhurst. The Influence of Galactic Outflows on the Formation of Nearby Dwarf Galaxies. ApJ, 536:L11–L14, June 2000. doi: 10.1086/312725.

C. Scarlata, J. Colbert, H. I. Teplitz, N. Panagia, M. Hayes, B. Siana, A. Rau, P. Francis, A. Caon, A. Pizzella, and C. Bridge. The Effect of Dust Geometry on the Lyα Output of Galaxies. ApJ, 704:L98–L102, October 2009. doi: 10.1088/0004-637X/704/2/L98.

D. Schaerer. Lyman alpha emitting and related star-forming galaxies at high redshift. *ArXiv e-prints*, 1407.2796, July 2014.

D. Schaerer and S. de Barros. On the physical properties of z $\approx$ 6-8 galaxies. A&A, 515:A73, June 2010. doi: 10.1051/0004-6361/200913946.

M. A. Schenker, D. P. Stark, R. S. Ellis, B. E. Robertson, J. S. Dunlop, R. J. McLure, J.-P. Kneib, and J. Richard. Keck Spectroscopy of Faint 3 ¡ z ¡ 8 Lyman Break Galaxies: Evidence for a Declining Fraction of Emission Line Sources in the Redshift Range 6 ¡ z ¡ 8. ApJ, 744:179, January 2012. doi: 10.1088/0004-637X/744/2/179.

M. A. Schenker, R. S. Ellis, N. P. Konidaris, and D. P. Stark. Line-emitting Galaxies beyond a Redshift of 7: An Improved Method for Estimating the Evolving Neutrality of the Intergalactic Medium. ApJ, 795:20, November 2014. doi: 10.1088/0004-637X/795/1/20.

S. F. Shandarin and Y. B. Zeldovich. The large-scale structure of the universe: Turbulence, intermittency, structures in a self-gravitating medium. *Reviews of Modern Physics*, 61:185–220, April 1989. doi: 10.1103/RevModPhys.61.185.

P. R. Shapiro, I. T. Iliev, and A. C. Raga. Photoevaporation of cosmological minihaloes during reionization. MNRAS, 348:753–782, March 2004. doi: 10.1111/j.1365-2966.2004.07364.x.

A. E. Shapley, C. C. Steidel, M. Pettini, and K. L. Adelberger. Rest-Frame Ultraviolet Spectra of z∼3 Lyman Break Galaxies. ApJ, 588:65–89, May 2003. doi: 10.1086/373922.

R. K. Sheth and G. Tormen. Large-scale bias and the peak background split. MNRAS, 308:119–126, September 1999. doi: 10.1046/j.1365-8711.1999.02692.x.

K. Shimasaku, N. Kashikawa, M. Doi, C. Ly, M. A. Malkan, Y. Matsuda, M. Ouchi, T. Hayashino, M. Iye, K. Motohara, T. Murayama, T. Nagao, K. Ohta, S. Okamura, T. Sasaki, Y. Shioya, and Y. Taniguchi. Lyα Emitters at z = 5.7 in the Subaru Deep Field. PASJ, 58:313–334, April 2006.

Y. Shioya, Y. Taniguchi, S. S. Sasaki, T. Nagao, T. Murayama, T. Saito, Y. Ideue, A. Nakajima, K. Matsuoka, J. Trump, N. Z. Scoville, D. B. Sanders, B. Mobasher, H. Aussel, P. Capak, J. Kartaltepe, A. Koekemoer, C. Carilli, R. S. Ellis, B. Garilli, M. Giavalisco, M. G. Kitzbichler, C. Impey, O. LeFevre, E. Schinnerer, and V. Smolcic. Photometric Properties of Lyα Emitters at z $\approx$ 4.86 in the COSMOS 2 Square Degree Field. ApJ, 696:546–561, May 2009. doi: 10.1088/0004-637X/696/1/546.

J. M. Shull and M. E. van Steenberg. X-ray secondary heating and ionization in quasar emission-line clouds. ApJ, 298:268–274, November 1985. doi: 10.1086/163605.

B. Siana, H. I. Teplitz, H. C. Ferguson, T. M. Brown, M. Giavalisco, M. Dickinson, R.-R. Chary, D. F. de Mello, C. J. Conselice, C. R. Bridge, J. P. Gardner, J. W. Colbert, and C. Scarlata. A Deep Hubble Space Telescope Search for Escaping Lyman Continuum Flux at z $\sim$ 1.3: Evidence for an Evolving Ionizing Emissivity. ApJ, 723:241–250, November 2010. doi: 10.1088/0004-637X/723/1/241.

E. Sobacchi and A. Mesinger. How does radiative feedback from an ultraviolet background impact reionization? MNRAS, 432:3340–3348, July 2013a. doi: 10.1093/mnras/stt693.

E. Sobacchi and A. Mesinger. The depletion of gas in high-redshift dwarf galaxies from an inhomogeneous reionization. MNRAS, 432:L51, May 2013b. doi: 10.1093/mnrasl/slt035.

A. Sokasian, T. Abel, L. Hernquist, and V. Springel. Cosmic reionization by stellar sources: Population II stars. MNRAS, 344:607–624, September 2003. doi: 10.1046/j.1365-8711.2003.06847.x.

A. Sokasian, N. Yoshida, T. Abel, L. Hernquist, and V. Springel. Cosmic reionization by stellar sources: population III stars. MNRAS, 350:47–65, May 2004. doi: 10.1111/j.1365-2966.2004.07636.x.

V. Springel. The cosmological simulation code GADGET-2. MNRAS, 364:1105–1134, December 2005. doi: 10.1111/j.1365-2966.2005.09655.x.

V. Springel and L. Hernquist. Cosmological smoothed particle hydrodynamics simulations: a hybrid multiphase model for star formation. MNRAS, 339:289–311, February 2003. doi: 10.1046/j.1365-8711.2003.06206.x.

J. A. Srbinovsky and J. S. B. Wyithe. Constraining the quasar contribution to the reionization of cosmic hydrogen. MNRAS, 374:627–633, January 2007. doi: 10.1111/j.1365-2966.2006.11173.x.

E. R. Stanway, A. J. Bunker, K. Glazebrook, R. G. Abraham, J. Rhoads, S. Malhotra, D. Crampton, M. Colless, and K. Chiu. The GLARE Survey - II. Faint z $\sim$ 6 Lyα line emitters in the HUDF. MNRAS, 376:727–738, April 2007. doi: 10.1111/j.1365-2966.2007.11469.x.

D. P. Stark, R. S. Ellis, A. Bunker, K. Bundy, T. Targett, A. Benson, and M. Lacy. The Evolutionary History of Lyman Break Galaxies Between Redshift 4 and 6: Observing Successive Generations of Massive Galaxies in Formation. ApJ, 697:1493–1511, June 2009. doi: 10.1088/0004-637X/697/2/1493.

D. P. Stark, R. S. Ellis, K. Chiu, M. Ouchi, and A. Bunker. Keck spectroscopy of faint 3 ¡ z ¡ 7 Lyman break galaxies - I. New constraints on cosmic reionization from the luminosity and redshift-dependent fraction of Lyman α emission. MNRAS, 408:1628–1648, November 2010. doi: 10.1111/j.1365-2966.2010.17227.x.

D. P. Stark, R. S. Ellis, and M. Ouchi. Keck Spectroscopy of Faint 3>z>7 Lyman Break Galaxies: A High Fraction of Line Emitters at Redshift Six. ApJ, 728:L2, February 2011. doi: 10.1088/2041-8205/728/1/L2.

D. P. Stark, M. A. Schenker, R. Ellis, B. Robertson, R. McLure, and J. Dunlop. Keck Spectroscopy of 3 ¡ z ¡ 7 Faint Lyman Break Galaxies: The Importance of Nebular Emission in Understanding the Specific Star Formation Rate and Stellar Mass Density. ApJ, 763:129, February 2013. doi: 10.1088/0004-637X/763/2/129.

M. Steinmetz and M. Bartelmann. On the spin parameter of dark-matter haloes. MNRAS, 272: 570–578, February 1995.

M. Stiavelli. *From First Light to Reionization: The End of the Dark Ages*. 2009.

G. Stratta, R. Maiolino, F. Fiore, and V. D'Elia. Dust Properties at z = 6.3 in the Host Galaxy of GRB 050904. ApJ, 661:L9–L12, May 2007. doi: 10.1086/518502.

B. Strömgren. The Physical State of Interstellar Hydrogen. ApJ, 89:526, May 1939. doi: 10.1086/144074.

R. S. Sutherland and M. A. Dopita. Cooling functions for low-density astrophysical plasmas. ApJS, 88:253–327, September 1993. doi: 10.1086/191823.

Y. Taniguchi, M. Ajiki, T. Nagao, Y. Shioya, T. Murayama, N. Kashikawa, K. Kodaira, N. Kaifu, H. Ando, H. Karoji, M. Akiyama, K. Aoki, M. Doi, S. S. Fujita, H. Furusawa, T. Hayashino, F. Iwamuro, M. Iye, N. Kobayashi, T. Kodama, Y. Komiyama, Y. Matsuda, S. Miyazaki, Y. Mizumoto, T. Morokuma, K. Motohara, K. Nariai, K. Ohta, Y. Ohyama, S. Okamura, M. Ouchi, T. Sasaki, Y. Sato, K. Sekiguchi, K. Shimasaku, H. Tamura, M. Umemura, T. Yamada, N. Yasuda, and M. Yoshida. The SUBARU Deep Field Project: Lymanα Emitters at a Redshift of 6.6. PASJ, 57:165–182, February 2005.

C. Tapken, I. Appenzeller, S. Noll, S. Richling, J. Heidt, E. Meinköhn, and D. Mehlert. Lyα emission in high-redshift galaxies. A&A, 467:63–72, May 2007. doi: 10.1051/0004-6361:20065825.

E. Tescari, M. Viel, V. D'Odorico, S. Cristiani, F. Calura, S. Borgani, and L. Tornatore. Cosmic evolution of the C IV in high-resolution hydrodynamic simulations. MNRAS, 411:826–848, February 2011. doi: 10.1111/j.1365-2966.2010.17761.x.

T. Theuns, M. Viel, S. Kay, J. Schaye, R. F. Carswell, and P. Tzanavaris. Galactic Winds in the Intergalactic Medium. ApJ, 578:L5–L8, October 2002. doi: 10.1086/344521.

R. M. Thomas and S. Zaroubi. Time-evolution of ionization and heating around first stars and miniqsos. MNRAS, 384:1080–1096, March 2008. doi: 10.1111/j.1365-2966.2007.12767.x.

R. M. Thomas, S. Zaroubi, B. Ciardi, A. H. Pawlik, P. Labropoulos, V. Jelić, G. Bernardi, M. A. Brentjens, A. G. de Bruyn, G. J. A. Harker, L. V. E. Koopmans, G. Mellema, V. N. Pandey, J. Schaye, and S. Yatawatta. Fast large-scale reionization simulations. MNRAS, 393:32–48, February 2009. doi: 10.1111/j.1365-2966.2008.14206.x.

S. J. Tingay, R. Goeke, J. D. Bowman, D. Emrich, S. M. Ord, D. A. Mitchell, M. F. Morales, T. Booler, B. Crosse, R. B. Wayth, C. J. Lonsdale, S. Tremblay, D. Pallot, T. Colegate, A. Wicenec, N. Kudryavtseva, W. Arcus, D. Barnes, G. Bernardi, F. Briggs, S. Burns, J. D. Bunton, R. J. Cappallo, B. E. Corey, A. Deshpande, L. Desouza, B. M. Gaensler, L. J. Greenhill, P. J. Hall, B. J. Hazelton, D. Herne, J. N. Hewitt, M. Johnston-Hollitt, D. L. Kaplan, J. C. Kasper, B. B. Kincaid, R. Koenig, E. Kratzenberg, M. J. Lynch, B. Mckinley, S. R. Mcwhirter, E. Morgan, D. Oberoi, J. Pathikulangara, T. Prabu, R. A. Remillard, A. E. E. Rogers, A. Roshi, J. E. Salah, R. J. Sault, N. Udaya-Shankar, F. Schlagenhaufer, K. S. Srivani, J. Stevens, R. Subrahmanyan, M. Waterson, R. L. Webster, A. R. Whitney, A. Williams, C. L. Williams, and J. S. B. Wyithe. The Murchison Widefield Array: The Square Kilometre Array Precursor at Low Radio Frequencies. PASA, 30: e007, January 2013. doi: 10.1017/pasa.2012.007.

P. Todini and A. Ferrara. Dust formation in primordial Type II supernovae. MNRAS, 325:726–736, August 2001. doi: 10.1046/j.1365-8711.2001.04486.x.

H. Trac, R. Cen, and A. Loeb. Imprint of Inhomogeneous Hydrogen Reionization on the Temperature Distribution of the Intergalactic Medium. ApJ, 689:L81–L84, December 2008. doi: 10.1086/595678.

M. Trenti and M. Stiavelli. Formation Rates of Population III Stars and Chemical Enrichment of Halos during the Reionization Era. ApJ, 694:879–892, April 2009. doi: 10.1088/0004-637X/694/2/879.

T. Treu, M. Trenti, M. Stiavelli, M. W. Auger, and L. D. Bradley. Inferences on the Distribution of Lyα Emission of z $\sim$ 7 and z $\sim$ 8 Galaxies. ApJ, 747:27, March 2012. doi: 10.1088/0004-637X/747/1/27.

T. Treu, K. B. Schmidt, M. Trenti, L. D. Bradley, and M. Stiavelli. The Changing Lyα Optical Depth in the Range 6 ¡ z ¡ 9 from the MOSFIRE Spectroscopy of Y-dropouts. ApJ, 775:L29, September 2013. doi: 10.1088/2041-8205/775/1/L29.

J. A. Tyson, R. A. Wenk, and F. Valdes. Detection of systematic gravitational lens galaxy image alignments - Mapping dark matter in galaxy clusters. ApJ, 349:L1–L4, January 1990. doi: 10.1086/185636.

R. Valiante, R. Schneider, S. Bianchi, and A. C. Andersen. Stellar sources of dust in the high-redshift Universe. MNRAS, 397:1661–1671, August 2009. doi: 10.1111/j.1365-2966.2009.15076.x.

M. P. van Haarlem, M. W. Wise, A. W. Gunst, G. Heald, J. P. McKean, J. W. T. Hessels, A. G. de Bruyn, R. Nijboer, J. Swinbank, R. Fallows, M. Brentjens, A. Nelles, R. Beck, H. Falcke, R. Fender, J. Hörandel, L. V. E. Koopmans, G. Mann, G. Miley, H. Röttgering, B. W. Stappers, R. A. M. J. Wijers, S. Zaroubi, M. van den Akker, A. Alexov, J. Anderson, K. Anderson, A. van Ardenne, M. Arts, A. Asgekar, I. M. Avruch, F. Batejat, L. Bähren, M. E. Bell, M. R. Bell, I. van Bemmel, P. Bennema, M. J. Bentum, G. Bernardi, P. Best, L. Bîrzan, A. Bonafede, A.-J. Boonstra, R. Braun, J. Bregman, F. Breitling, R. H. van de Brink, J. Broderick, P. C. Broekema, W. N. Brouw, M. Brüggen, H. R. Butcher, W. van Cappellen, B. Ciardi, T. Coenen, J. Conway, A. Coolen, A. Corstanje, S. Damstra, O. Davies, A. T. Deller, R.-J. Dettmar, G. van Diepen, K. Dijkstra, P. Donker, A. Doorduin, J. Dromer, M. Drost, A. van Duin, J. Eislöffel, J. van Enst, C. Ferrari, W. Frieswijk, H. Gankema, M. A. Garrett, F. de Gasperin, M. Gerbers, E. de Geus, J.-M. Grießmeier, T. Grit, P. Gruppen, J. P. Hamaker, T. Hassall, M. Hoeft, H. A. Holties, A. Horneffer, A. van der Horst, A. van Houwelingen, A. Huijgen, M. Iacobelli, H. Intema, N. Jackson, V. Jelic, A. de Jong, E. Juette, D. Kant, A. Karastergiou, A. Koers, H. Kollen, V. I. Kondratiev, E. Kooistra, Y. Koopman, A. Koster, M. Kuniyoshi, M. Kramer, G. Kuper, P. Lambropoulos, C. Law, J. van Leeuwen, J. Lemaitre, M. Loose, P. Maat, G. Macario, S. Markoff, J. Masters, R. A. McFadden, D. McKay-Bukowski, H. Meijering, H. Meulman, M. Mevius, E. Middelberg, R. Millenaar, J. C. A. Miller-Jones, R. N. Mohan, J. D. Mol, J. Morawietz, R. Morganti, D. D. Mulcahy, E. Mulder, H. Munk, L. Nieuwenhuis, R. van Nieuwpoort, J. E. Noordam, M. Norden, A. Noutsos, A. R. Offringa, H. Olofsson, A. Omar, E. Orrú, R. Overeem, H. Paas, M. Pandey-Pommier, V. N. Pandey, R. Pizzo, A. Polatidis, D. Rafferty, S. Rawlings, W. Reich, J.-P. de Reijer, J. Reitsma, G. A. Renting, P. Riemers, E. Rol, J. W. Romein, J. Roosjen, M. Ruiter, A. Scaife, K. van der Schaaf, B. Scheers, P. Schellart, A. Schoenmakers, G. Schoonderbeek, M. Serylak, A. Shulevski, J. Sluman, O. Smirnov, C. Sobey, H. Spreeuw, M. Steinmetz, C. G. M. Sterks, H.-J. Stiepel, K. Stuurwold, M. Tagger, Y. Tang, C. Tasse, I. Thomas, S. Thoudam, M. C. Toribio, B. van der Tol, O. Usov, M. van Veelen, A.-J. van der Veen, S. ter Veen, J. P. W. Verbiest, R. Vermeulen, N. Vermaas, C. Vocks, C. Vogt, M. de Vos, E. van der Wal, R. van Weeren, H. Weggemans, P. Weltevrede, S. White, S. J. Wijnholds, T. Wilhelmsson, O. Wucknitz, S. Yatawatta, P. Zarka, A. Zensus, and J. van Zwieten. LOFAR: The LOw-Frequency ARray. A&A, 556:A2, August 2013. doi: 10.1051/0004-6361/201220873.

E. Vanzella, M. Giavalisco, M. Dickinson, S. Cristiani, M. Nonino, H. Kuntschner, P. Popesso, P. Rosati, A. Renzini, D. Stern, C. Cesarsky, H. C. Ferguson, and R. A. E. Fosbury. Spectroscopic Observations of Lyman Break Galaxies at Redshifts $\sim$4, 5, and 6 in the Goods-South Field. ApJ, 695:1163–1182, April 2009. doi: 10.1088/0004-637X/695/2/1163.

A. Verhamme, D. Schaerer, and A. Maselli. 3D Lyα radiation transfer. I. Understanding Lyα line profile morphologies. A&A, 460:397–413, December 2006. doi: 10.1051/0004-6361:20065554.

A. Verhamme, D. Schaerer, H. Atek, and C. Tapken. 3D Lyα radiation transfer. III. Constraints on gas and stellar properties of z $\sim$ 3 Lyman break galaxies (LBG) and implications for high-z LBGs and Lyα emitters. A&A, 491:89–111, November 2008. doi: 10.1051/0004-6361:200809648.

L. M. J. S. Volders. Neutral hydrogen in M 33 and M 101. Bull. Astron. Inst. Netherlands, 14:323, September 1959.

D. A. Wake, K. E. Whitaker, I. Labbé, P. G. van Dokkum, M. Franx, R. Quadri, G. Brammer, M. Kriek, B. F. Lundgren, D. Marchesini, and A. Muzzin. Galaxy Clustering in the NEWFIRM Medium Band Survey: The Relationship Between Stellar Mass and Dark Matter Halo Mass at 1 ¡ z ¡ 2. ApJ, 728:46, February 2011. doi: 10.1088/0004-637X/728/1/46.

J. Wang, H. Xu, T. An, J. Gu, X. Guo, W. Li, Y. Wang, C. Liu, O. Martineau-Huynh, and X.-P. Wu. Exploring the Cosmic Reionization Epoch in Frequency Space: An Improved Approach to Remove the Foreground in 21 cm Tomography. ApJ, 763:90, February 2013. doi: 10.1088/0004-637X/763/2/90.

S. D. M. White and C. S. Frenk. Galaxy formation through hierarchical clustering. ApJ, 379:52–79, September 1991. doi: 10.1086/170483.

S. D. M. White and M. J. Rees. Core condensation in heavy halos - A two-stage theory for galaxy formation and clustering. MNRAS, 183:341–358, May 1978.

T. Wiklind, B. Mobasher, and V. Bromm, editors. *The First Galaxies*, volume 396 of *Astrophysics and Space Science Library*, 2013. doi: 10.1007/978-3-642-32362-1.

S. M. Wilkins, A. Bunker, W. Coulton, R. Croft, T. D. Matteo, N. Khandai, and Y. Feng. Interpreting the observed UV continuum slopes of high-redshift galaxies. MNRAS, 430:2885–2890, April 2013. doi: 10.1093/mnras/stt096.

J. H. Wise and T. Abel. Resolving the Formation of Protogalaxies. I. Virialization. ApJ, 665:899–910, August 2007. doi: 10.1086/520036.

J. H. Wise and T. Abel. Resolving the Formation of Protogalaxies. III. Feedback from the First Stars. ApJ, 685:40–56, September 2008. doi: 10.1086/590417.

J. H. Wise and T. Abel. ENZO+MORAY: radiation hydrodynamics adaptive mesh refinement simulations with adaptive ray tracing. MNRAS, 414:3458–3491, July 2011. doi: 10.1111/j.1365-2966.2011.18646.x.

J. H. Wise and R. Cen. Ionizing Photon Escape Fractions From High-Redshift Dwarf Galaxies. ApJ, 693:984–999, March 2009. doi: 10.1088/0004-637X/693/1/984.

J. H. Wise, V. G. Demchenko, M. T. Halicek, M. L. Norman, M. J. Turk, T. Abel, and B. D. Smith. The birth of a galaxy - III. Propelling reionization with the faintest galaxies. MNRAS, 442:2560–2579, August 2014. doi: 10.1093/mnras/stu979.

S. A. Wouthuysen. On the excitation mechanism of the 21-cm (radio-frequency) interstellar hydrogen emission line. AJ, 57:31–32, 1952. doi: 10.1086/106661.

K. K. S. Wu, O. Lahav, and M. J. Rees. The large-scale smoothness of the Universe. Nature, 397:225–230, January 1999. doi: 10.1038/16637.

J. S. B. Wyithe and A. Loeb. Was the Universe Reionized by Massive Metal-free Stars? ApJ, 588:L69–L72, May 2003. doi: 10.1086/375682.

J. S. B. Wyithe and A. Loeb. A suppressed contribution of low-mass galaxies to reionization due to supernova feedback. MNRAS, 428:2741–2754, January 2013. doi: 10.1093/mnras/sts242.

K. Yabe, K. Ohta, I. Iwata, M. Sawicki, N. Tamura, M. Akiyama, and K. Aoki. The Stellar Populations of Lyman Break Galaxies at z $\sim$ 5. ApJ, 693:507–533, March 2009. doi: 10.1088/0004-637X/693/1/507.

H. Yajima and S. Khochfar. Can the 21 cm signal probe Population III and II star formation? *ArXiv e-prints*, 1405.7385, May 2014.

H. Yajima, J.-H. Choi, and K. Nagamine. Escape fraction of ionizing photons from high-redshift galaxies in cosmological SPH simulations. MNRAS, 412:411–422, March 2011. doi: 10.1111/j.1365-2966.2010.17920.x.

H. Yajima, Y. Li, Q. Zhu, T. Abel, C. Gronwall, and R. Ciardullo. Escape of Lyα and continuum photons from star-forming galaxies. MNRAS, 440:776–786, May 2014. doi: 10.1093/mnras/stu299.

T. Yamada, Y. Matsuda, K. Kousai, T. Hayashino, N. Morimoto, and M. Umemura. Profiles of Lyα Emission Lines of the Emitters at z = 3.1. ApJ, 751:29, May 2012. doi: 10.1088/0004-637X/751/1/29.

N. Yoshida, K. Omukai, L. Hernquist, and T. Abel. Formation of Primordial Stars in a ΛCDM Universe. ApJ, 652:6–25, November 2006. doi: 10.1086/507978.

S. Yuma, K. Ohta, K. Yabe, K. Shimasaku, M. Yoshida, M. Ouchi, I. Iwata, and M. Sawicki. Stellar Populations of Lyα Emitters at z = 4.86: A Comparison to z $\sim$ 5 Lyman Break Galaxies. ApJ, 720:1016–1029, September 2010. doi: 10.1088/0004-637X/720/2/1016.

O. Zahn, A. Lidz, M. McQuinn, S. Dutta, L. Hernquist, M. Zaldarriaga, and S. R. Furlanetto. Simulations and Analytic Calculations of Bubble Growth during Hydrogen Reionization. ApJ, 654:12–26, January 2007. doi: 10.1086/509597.

M. Zaldarriaga. Polarization of the microwave background in reionized models. Phys. Rev. D, 55: 1822–1829, February 1997. doi: 10.1103/PhysRevD.55.1822.

S. Zaroubi, A. G. de Bruyn, G. Harker, R. M. Thomas, P. Labropolous, V. Jelić, L. V. E. Koopmans, M. A. Brentjens, G. Bernardi, B. Ciardi, S. Daiboo, S. Kazemi, O. Martinez-Rubi, G. Mellema, A. R. Offringa, V. N. Pandey, J. Schaye, V. Veligatla, H. Vedantham, and S. Yatawatta. Imaging neutral hydrogen on large scales during the Epoch of Reionization with LOFAR. MNRAS, 425: 2964–2973, October 2012. doi: 10.1111/j.1365-2966.2012.21500.x.

I. Zehavi, Z. Zheng, D. H. Weinberg, J. A. Frieman, A. A. Berlind, M. R. Blanton, R. Scoccimarro, R. K. Sheth, M. A. Strauss, I. Kayo, Y. Suto, M. Fukugita, O. Nakamura, N. A. Bahcall, J. Brinkmann, J. E. Gunn, G. S. Hennessy, Ž. Ivezić, G. R. Knapp, J. Loveday, A. Meiksin, D. J. Schlegel, D. P. Schneider, I. Szapudi, M. Tegmark, M. S. Vogeley, D. G. York, and SDSS Collaboration. The Luminosity and Color Dependence of the Galaxy Correlation Function. ApJ, 630:1–27, September 2005. doi: 10.1086/431891.

Y. B. Zel'dovich. Gravitational instability: An approximate theory for large density perturbations. A&A, 5:84–89, March 1970.

Y. B. Zeldovich. A hypothesis, unifying the structure and the entropy of the Universe. MNRAS, 160: 1P, 1972.

Z. Zheng and J. Wallace. Anisotropic Lyman-alpha Emission. ApJ, 794:116, October 2014. doi: 10.1088/0004-637X/794/2/116.

Z. Zheng, R. Cen, H. Trac, and J. Miralda-Escudé. Radiative Transfer Modeling of Lyα Emitters. I. Statistics of Spectra and Luminosity. ApJ, 716:574–598, June 2010. doi: 10.1088/0004-637X/716/1/574.

Z.-Y. Zheng, J.-X. Wang, S. Malhotra, J. E. Rhoads, S. L. Finkelstein, and K. Finkelstein. Lyα equivalent width distribution of Lyα emitting galaxies at redshift z 4.5. MNRAS, 439:1101–1109, March 2014. doi: 10.1093/mnras/stu054.

F. Zwicky. Die Rotverschiebung von extragalaktischen Nebeln. *Helvetica Physica Acta*, 6:110–127, 1933.

F. Zwicky. On the Masses of Nebulae and of Clusters of Nebulae. ApJ, 86:217, October 1937. doi: 10.1086/143864.

Acknowledgement

I am indebted to many people for the support and encouragement which was invaluable for the successful completion of this research work.
Firstly, I would like to thank my supervisor Volker Müller for his advice and patient supervision, without which this work would not have been possible. I also thank the Leibniz-Institute for Astrophysics Potsdam for the scientific and financial support.
I am especially indebted to Pratika Dayal for the wonderfull collaboration with many helpful scientific discussions, valuable ideas and advices, immense motivation and the friendly hospitality during my stays in Edinburgh. I also thank Adrian Partl for introducing and helping me with pCRASH, and valuable discussions.
I would like to thank all members of the AIP cosmology group for stimulating discussions and their support. I am also indebted to Christian and Joseph for introducing me to the world of LAE and LBG observations.

Further I would like to thank all my current and former colleagues at AIP for their support during the recent years, the nice working environment and nice times we had during lunch, barbeques, Gleis 6 and many other occasions.
Thanks to my former and current office mates, Metin and Omar, for your help on various scientific and coding problems, and of course for all the chocolate! A special thanks goes to Peter, Maneenate, Ugur, Isabel and Pierre-Antoine, without your support it would have been much harder. Further I would like to thank Peter for all proofreading and his feedback. Finally, although you are far away, Kristina and Annemarie, I will not forget your support and encouragement you gave me, whenever I was in doubt.

Parts of this work has been performed under the HPC-EUROPA2 project (project number: 228398) with the support of the European Commission - Capacities Area - Research Infrastructures.

Erklärung

Hiermit bestätige ich, dass diese Arbeit bisher an keiner anderen Hochschule eingereicht worden ist und selbständig und ausschließlich mit den angegebenen Mitteln angefertigt wurde.

Potsdam, den